University of Southampton Research Repository

Copyright © and Moral Rights for this thesis and, where applicable, any accompanying data are retained by the author and/or other copyright owners. A copy can be downloaded for personal non-commercial research or study, without prior permission or charge. This thesis and the accompanying data cannot be reproduced or quoted extensively from without first obtaining permission in writing from the copyright holder/s. The content of the thesis and accompanying research data (where applicable) must not be changed in any way or sold commercially in any format or medium without the formal permission of the copyright holder/s.

When referring to this thesis and any accompanying data, full bibliographic details must be given, e.g.

Thesis: Rogers, A. (2019) "The Geometric Scaling of a Developing Scour Hole", University of Southampton, Faculty of Engineering and Physical Sciences, PhD Thesis, p129.

University of Southampton

Faculty of Engineering and Physical Sciences

School of Engineering

The Geometric Scaling of a Developing Scour Hole

by

Ashley Jordan James Rogers

MEng

Thesis for the degree of Doctor of Philosophy

July 2019

University of Southampton

Abstract

Faculty of Engineering and Physical Sciences

School of Engineering

Thesis for the degree of Doctor of Philosophy

The Geometric Scaling of a Developing Scour Hole

by

Ashley Jordan James Rogers

A novel scanning technique using a rotating-head sonar profiler attached to a slider mechanism is presented as a means to directly measure the complex erosion and deposition features of local scour holes developing in clear-water conditions around vertical cylinders mimicking bridge piers. Extensive validation shows that the method produces high-density elevation surfaces to within $\cong \pm 1\%$ accuracy (relative to the flow depth) in a quasi-non-invasive manner. Experimental data from eleven trials, conditioned to vary the flow regime (and therefore the effect of viscosity relative to inertial forces) within the scour hole over a wide range, indicate that monitoring of the whole scour hole in time (instead of only the maximum depth as is commonly isolated in laboratory experiments) can reveal important information about local scour evolution. In particular, results show that the development of the scour hole volume (V_{OL}), within vicinity of the horseshoe vortex, scales with respect to the maximum scour depth (y_s) cubed (i.e.$V_{OL} \sim {y_s}^3$) through three linear regimes. Whilst the first and second regimes are attributable to the initial generation and steady growth of the horseshoe vortex respectively, transition to a third regime after significant scour development was found to represent a step change in the scour evolution process. Following the recent theoretical framework proposed by Manes and Brocchini (2015), this change, termed the *crossover point*, was interpreted as the physical point in time beyond which the production of turbulent kinetic energy plateaus which corresponds to a stabilisation in the erosive power of the horseshoe vortex.

Scour development beyond the crossover point is characterised by a significant reduction in the rate of volumetric scour, relative to the steadily-increasing maximum scour depth. This overall reduction in volume development is attributed to a balance between erosion and deposition characteristics from in-front and around the sides of the pier which was observed using topography analysis. Intriguingly, the sediment erosion and deposition trade-off in the third regime was found to be influenced by the flow regime within the scour hole. While the sediment trade-off for the fully-rough regime was characterised by erosion in front of and deposition around the sides of the pier, the viscosity-dominated hydraulically-smooth regime showed erosion and deposition patterns that are completely the opposite. As such, the presence of a crossover point is physically underwritten by sediment redistribution which varies as a function of the flow regime inside the scour hole.

Under the assumption that at the crossover point the shear stress acting on the scour hole surface (τ) approaches the critical shear stress of the sediment (i.e. $\tau \approx \tau_c$), the crossover depth was modelled using a theoretical approach by Manes and Brocchini (2015) which provided an excellent fitting to the fully-rough crossover data. This model was extended to account for

viscosity effects within the scour hole (owing to a change in flow regime) by considering the dependency of τ and τ_c on the flow regime in turn, following the work by Brownlie (1981) and Batchelor (e.g. Lohse and Muller-Groeling, 1994). The crossover depth was used as a scaling parameter for quantifying other geometric properties of the scour hole at the point of crossover using empirical data-fitting. The final formulae presented are very promising for engineering applications.

The existence of a well-defined crossover point presents itself as an excellent candidate for defining characteristic length and time scales that may effectively describe local scour dynamics and evolution in time, which may be used for modelling purposes. This is extremely relevant because, especially in clear-water conditions, the definition of such scales is still elusive as the equilibrium scour depth and time are well known to be arbitrarily defined.

For completeness, the similarity analysis was extended to defining the evolution of the scour hole boundaries, which were found to develop in proportion with the maximum scour depth and independent of time. The scaling relationships presented within the text for the scour boundaries are suitable for engineering applications as a good estimation of the scour major axes and footprint for a given scour depth.

Table of Contents

List of Tables

List of Tables

List of Figures

Research Thesis: Declaration of Authorship

Print name:	Ashley Jordan James Rogers

Title of thesis:	The Geometric Scaling of a Developing Scour Hole

I declare that this thesis and the work presented in it are my own and has been generated by me as the result of my own original research.

I confirm that:

1. This work was done wholly or mainly while in candidature for a research degree at this University;
2. Where any part of this thesis has previously been submitted for a degree or any other qualification at this University or any other institution, this has been clearly stated;
3. Where I have consulted the published work of others, this is always clearly attributed;
4. Where I have quoted from the work of others, the source is always given. With the exception of such quotations, this thesis is entirely my own work;
5. I have acknowledged all main sources of help;
6. Where the thesis is based on work done by myself jointly with others, I have made clear exactly what was done by others and what I have contributed myself;
7. Parts of this work have been published as:

Rogers, A., Manes, C., and Tsuzaki, T. (2019) “Geometric scaling of a developing scour hole in clear-water conditions using underwater sonar scanning”. Under consideration by the International Journal of Sediment Research.

Manes, C., Coscarella, F., Rogers, A. and Gaudio, R. (2018) “Viscosity effects on local scour around vertical structures in clear-water conditions”. Paper presented at 9th International Conference on Fluvial Hydraulics - River Flow 2018, Lyon-Villeurbanne, France.

Signature:		Date:	

Acknowledgements

The author would like to send individual gratitude to the following people:

Dr. Costantino Manes – We have had a rollercoaster ride, with some real highs and many lows. However, something that has never changed is your enthusiasm and positivity towards my work. You have guided me throughout and I cannot thank you enough for that.

Dr. Toru Tsuzaki – The assistance you have provided me with goes above and beyond any normal colleague. Both as a lab technician sorting out anything and everything, to being a real supportive figure on all fronts of my work, and someone I can say is a good friend from this process.

Bryanna McGregor – You were so supportive of me throughout the major write up stages of my thesis. You have had to listen to me stress over all sorts of problems, as well as successes, and have really kept me going when in the really low times.

To all my laboratory assistants – Those overnight experiments would have not been the same without your moral support and for keeping me sane throughout those long and cold nights. Thank you for giving that amount of time up to assist.

Gratitude is also extended to Prof. David Richards, Dr. Gustavo De Almeida and Dr. Athanasios Paschalis for your feedback at key periods of the process. This gratitude is extended to Sergio Maldonado and Oscar Link for taking the time to read this thesis in depth and providing excellent feedback and suggestions during the PhD viva.

Definitions and Abbreviations

A_f	Area of the Scour Hole Footprint
A_S	Wetted Surface of the Scour Hole Parallel to the Viscous sub-layer Peaks
a	Effective Pier Width or Diameter
B	Widths of Depth-Averaged Channel
b	Length of the Pier (used in Aspect Ratio computation), or Constant ≈ 5.8
C	Constant Applied to the Brownlie (1981) equation (C= 52)
C_D	Coefficient of Drag within the Vicinity of the Scour Hole
$D(l)$	Batchelor's Second-Order Structure Function
d_{50}	Mean Sediment Diameter
$d(x)$	Distance along the abscissa from the point of interest to another point
d_*	Dimensionless Sediment Diameter defined by Lança *et al.* (2016)
F_D	Drag Force Applied by HS Vortex to the Frontal Face of the Pier
Fr, Fr_1	Upstream Froude Number
f	Function Describing the Dependency of the Scour Depth on d_{50}/η
f_1, f_2, f_3	Sheppard-Melville Factors for the Flow field, Flow Intensity and Relative Coarseness
$f[R_e^*]$	Dependency of Dimensionless Shear Stress on Particle Reynolds Number
g	Gravitational Acceleration
K_{ya}, K_I, K_{d50}	Melville (1997) Correction Factors for Flow Depth and Pier Width, Flow Intensity and Non-Uniformity
K_s, K_θ, K_G	Melville (1997) Correction Factors for Shape Effects, Pier Alignment and Channel Geometry
K_1, K_2, K_3	HEC-18 Correction Factors for Pier Shape, Angle of Attack and Bed State
k_s	Equivalent Sand Roughness from Nikuradse

L	Characteristic Length Scale of the Largest Eddies
L, L_e	Scour Hole Length at time t and at equilibrium
L_L	Kernel Bound Limit
l	Characteristic Length Scale of an Eddy within the Inertial Sub-Range
M	Mass of Water Contained in the Spatial Volume of the Largest Scale Eddy
P	Power Associated with the Large Scale Eddies, and Pressure in Figure 2.4
Q	Flow Rate and Direction
Re	Reynolds Number
R_e^*, Re_P	Particle Boundary and Pier Reynolds Number
r, r_r	Kernel Radius of Large Kernel and Reduced Kernel
r_1, r_2	Location of Velocity Measurements Separated by the Vector **r**
s_d	Spearman Rank Correlation Coefficient
T	Time $\sim L/V_1$ which characterises the flow field
t	(a) Time and (b) Turnover Time for an Eddy of Characteristic Length l
t_{end}, t_{ssd}	Length of Experimental Trial and Crossover Time
U_*	Bed Shear Velocity
u, v, w	Stream-wise, Lateral and Bed Normal Velocity Components
$\overline{u'}, \overline{w'}$	Time-Averaged Stream-wise and Bed Normal Velocity Components
$u_{d_{50}}, u_l, u_\eta$	Characteristic Velocity of Eddies of Length Scale d_{50}, l and η
$u_t, u_t{}'$	Velocity and Fluctuation at a Given Point
V	Characteristic Velocity of the Largest Scale Eddies
V_1	Depth-Averaged Approach Flow Velocity
V_c	Incipient Threshold Velocity of the Bed Sediment
V_{lp}	Live-Bed Peak

V_{ol}	Scour Hole Volume at time t
$V_{ol,\ end}, V_{ol,\ ssd}$	Scour Hole Volume at the End of Trial and at the Crossover Point
V_{SH}	Depth-Averaged Velocity Profile within the vicinity of the Scour Hole
W, W_e	Scour Hole Width at time t and at equilibrium
w_i	Regression weight for point i
X_H	Length of the Turbulent Boundary Layer
$x/x_P, x_i$	Abscissa Values for the Point of Interest, i, and the Nearest Neighbours
Δx	Horizontal Distance Between Adjacent Sonar Line Scans
y	Undisturbed Upstream
y_P, y_i	Ordinates for Point of Interest and Point i
$y_s,$	Maximum Scour Depth at time t
$y_{s,\ end}, y_{ssd}$	Maximum Scour Depth at the End of Trial and at the Crossover Point
y_{se}	Maximum Equilibrium Local Scour Depth
z	Bed elevation relative to the flat-bed state in Figure 2.4
z_P, z_i	Depth Elevations of the Point of Interest and Point i
z_{nP}	Depth Elevation of the Replacing Small-Kernel Weighted Average
$z_{w,av}$	Depth Elevation of the Large-Kernel Weighted Average
γ	Boundary Layer Constant ($= 0.33$)
Δ	Ratio between sediment and fluid densities
δ	Thickness of the Boundary Layer
$\varepsilon, \varepsilon_{ssd}$	Rate of Production of TKE at time t and at the Point of Crossover
η	Kolmogorov Length Scale
θ	Effective Angle of Attack, and angle from Axis of Scour Hole Symmetry
μ	Molecular Dynamic Viscosity of Water, and Mean Measurement Error

Definitions and Abbreviations

υ	Kinematic Viscosity of Water
ρ, ρ_s	Averaged Density of Water and the Bed Sediment
σ	Standard Deviation of Measurement Errors
σ_g	Sediment Geometric Standard Deviation of the Particle Size Distribution
τ	Bed Shear Stress at the Point of Scour Hole Equilibrium
τ_b	Localised Bed Shear Stress
τ_c	Threshold Critical Shear Stress of the Bed Sediment
$\overline{\omega}$	Fluid Vorticity
∞	'Infinity'
$\sim$	'Scales As'
ADV	Acoustic Doppler Velocimeter
ASCII	American Standard Code for Information Interchange
CSU	California-State University
FHWA	US Federal Highway Administration
GIS	Geographic Information Systems
HEC-18	Hydraulic Engineering Circular No. 18
HS	Horseshoe
HVS	Horseshoe Vortex System
LSPIV	Particle Image Velocimetry
NCHRP	National Cooperative Highway Research Program
PG1, PG2, PG3	Point Gauges Located Upstream of the Test Area and Scour Hole Apex, and At the Location of Maximum Scour Depth

PVC	Polyvinyl Chloride
S/M	Sheppard/Melville
SMC	Smart Motion Controller
SNR	Sound-to-Noise Ratio
TKE	Turbulent Kinetic Energy
UKCP	UK Climate Predictions
USB	Universal Serial Bus
W.S.	Water Surface
WVS	Wake Vortex System

Chapter 1: Introduction

1.1 Relevance and Context

Local scour is the erosion of sediment around the base of a foundation caused by turbulent vortices that are impinged by a flowing current (Melville and Coleman, 2000). The erosive action results in a depression of the local bed, a *scour hole*, that can lead to foundation undermining and collapse if the critical depth of the foundation is exceeded (Kirby *et al.*, 2015). It is well documented that flood-induced local scouring is responsible for the majority of hydraulic-structure failures worldwide (Benn, 2013; Lagasse *et al.*, 2013; Deng *et al.*, 2015). Hydraulic structures such as bridges are fundamental components of infrastructure systems for rail and road networks; a global aim to reduce unsustainable energy consumption has also seen major offshore development in the form of windfarms (Whitehouse *et al.*, 2011). While bridges are exposed to both general and more localised scour degradation, seabed monopile installations are susceptible to local scour development under wave action and hydrodynamic processes concerning seabed ripples and currents (Harris *et al.*, 2010). With an increase in intense floods and sea level anticipated from recent climatic reports (e.g. see Eddowes *et al.*, 2003; Jenkins *et al.*, 2009; Met Office *et al.*, 2018), it is imperative that scour risk assessment procedures are able to reliably identify high-risk structures so that resources are correctly allocated to those requiring maintenance or preventative measures (Tubaldi *et al.*, 2017). This assessment requires formulae that enable a straightforward but reliable computation of local scour.

1.2 Scour Computation

Local scour is a time-dependent phenomenon. However, the main parameter that governs the outcome of any structural assessment concerning scour risk is the computation of an equilibrium scour depth. This length scale characterises the maximum perceivable scour depth for a given flow return period, and is crucial for modelling scour development over time as it is directly comparable to the critical depth of the foundation (Ettema *et al.*, 2011). Having a quick and reliable method to predict this length scale is therefore vital for assessing scour risk, and its computation has been the main focus of laboratory work for the past 60 years.

Laboratory work is used to study the behaviour of scour development to changes in key physical parameters thought to influence the evolution process. Measured changes in the scour depth with each parameter are then compounded into a predictive framework that can estimate the magnitude of the equilibrium scour depth for the experiment test range. The observed behavioural trends are subsequently extrapolated using fitting techniques to extend their application to full scale problems for use in risk categorisation.

The dependency of the equilibrium scour depth on key physical parameters influencing the scour development process is well documented in the literature. However, a more general description of the scour hole geometry both at equilibrium and during its evolution in time is equally important as this knowledge feeds into other essential aspects of the scour risk assessment process.

Firstly, whilst knowledge of the maximum perceivable depth is used to categorise scour risk for a structure, an ability to quantify the corresponding scour hole geometry both at equilibrium conditions and during its development over time allows quantification of the scour hole footprint and its volume. This has important repercussions, in particular, for the design of scour countermeasures based on armouring material or scour aprons which may be promptly required at structures categorised as high-risk. Therefore, having a reliable method to evaluate the geometry of the scour hole and its scaling with time can provide valuable information for effective countermeasure design.

Secondly, the scour hole development in time provides data that can be used for advancements in numerical modelling. Scour is a complex phenomenon. Physical models are critically limited in measurement ability due to equipment invasiveness; as such, numerical models provide a flexible alternative. In the literature, numerical methods have been used mainly for simulating the complex flow field that develops around a structure during scour generation (e.g. Kirkil *et al.*, 2008, 2009; Kirkil and Constantinescu, 2012). However, simulations require extensive validation in order to verify the capabilities of the applied local scour model in reproducing an accurate scour hole profile (Alemi and Maia, 2018). Verification is typically achieved by using bathymetry that is known *a priori* from physical model outputs (e.g. Kirkil *et al.*, 2009). Therefore, being able to quantify the scour development process in time provides a useful tool that can be used both as boundary conditions for model calibration and as a cross-reference check for output validation. This is particularly relevant as numerical models provide a platform for advancements in this field which, in turn, can shed light on fundamental aspects of the erosion process that may be poorly understood using a physical model alternative.

Finally, measuring geometric evolution allows for the validation and improvement of recently-derived predictive equations for the equilibrium scour depth which are more theoretically-based (Manes and Brocchini, 2015) than those available from the literature that are mostly of an empirical nature. As it will be discussed in the literature review (next Chapter), empirical frameworks are notably unreliable and often produce overly-conservative depth estimates as the true underlying behaviour of key behavioural trends are incorrectly captured when extrapolating from laboratory to field scales (e.g. Ettema *et al.*, 2006; Deng *et al.*, 2015). Whilst laboratory estimations have produced many important results towards quantifying local scour behaviour, physical characteristics of local scour at field scales are not well understood and are poorly integrated within existing predictive models. The concept of deriving a reliable predictive model governed by theoretical principles can provide a baseline for improving the correlation between small-scale studies and full scale problems.

These are all important aspects to consider when bridging the gap between laboratory and full-scale problems.

To quantify the development of the scour geometry with time up to the state of equilibrium, laboratory measurements of the scouring bed need to be captured in a dynamic state at set intervals. This has only been attempted directly by a handful of studies, using techniques that typically fall into one of three categories; laser-scanning, photogrammetry and echo-sounder monitoring.

In the literature, laser scanning is performed non-invasively to the scour process by installing a laser distance sensor inside a transparent test-pier (e.g. Link and Zanke, 2004). The laser scanner functions by performing sweeping scans of the surrounding bed in large radial increments, configured by a stepper motor to capture the development of the geometry with time. However, quasi-dynamic measurements of the scouring profile can only be achieved by performing a few radial rotations around the circumference of the test pier. Whilst major scour boundaries can be measured, capturing the entire bed surface using laser scanning is susceptible to overlooking or simplifying important topographical details due to the requirement of high post-experiment interpolation.

Photogrammetry is an alternative non-invasive option which involves making measurements of the scoured bed using photographs from multiple cameras focussed on the test area. This technique had been tested with promising results (e.g. Sumer *et al.*, 2013). However, the method has a time-consuming post-processing requirement, and yields results that can be inaccurate due to difficulties with including a modelling correction for refraction between air and water. The technique is also only suitable for end-of-trial measurements as it cannot be used to capture scour geometry while the flume is running (Porter *et al.*, 2014).

Echo-sounders (*sonar*) are extensively used to model the bathymetry of watercourses in the field, and are often fixed to high-risk structures for the monitoring and alerting of critical bed levels. As such, they provide a plausible option for equivalent laboratory monitoring. Within the literature, only single-beam sonars have been used for this purpose. These sonars are attached to a transverse motorised platform that can manoeuvre the device in two-dimensions so that full coverage of the scouring bed is possible (e.g. Porter *et al.*, 2014). However, an acoustic transducer requires constant submersion during operation, meaning that full capture of the scour development can only be achieved very intrusively. A single scan using a two-directional mobilisation platform is also completed over a long measurement duration, meaning that snapshots of the dynamic scouring bed are difficult to capture accurately.

Issues with invasiveness and measurement accuracy has therefore limited many investigations into characterising the scoured footprint by isolating the equilibrium scour hole footprint and volume through measurements of the drained equilibrium scour surface profile. This is somewhat documented (e.g. Khwairakpam *et al.*, 2012; Das *et al.*, 2014a; Das *et al.*, 2014c). However, owing to invasiveness and issues with capturing the scour geometry in a quasi-dynamic state, the development of the bulk scour hole geometry with time is far from being understood.

1.3 Project Aims and Objectives

Within this context, the main aim of this thesis is to develop a reliable experimental methodology that allows for scour geometric measurements to be made in real-time. Experiment data gathered using the proposed technique will be presented to investigate the similarity of the scour hole forming with time around three isolated piers of different sizes and positioned in different flow regimes. This will be achieved through the following series of objectives:

1. To develop and validate an experimental methodology for measuring the geometry of a developing local scour hole in a quasi-dynamic non-invasive manner;
2. To investigate the scaling relationships between the geometric properties of a scour hole as it develops with time and interpret them using the theoretical framework proposed by Manes and Brocchini (2015);
3. To assess whether a change in flow regime within the scour hole, governed by a change in the importance of viscosity relative to inertial forces , has an influence on the scour development process; and
4. To provide quantitative analysis of the relationships between important geometric properties of the scour hole for use in engineering applications.

1.4 Structural Overview of Thesis

To achieve the above aim, the thesis is organised as follows. Chapter 2 presents the current understanding of local scour in a physical sense. The principles of scour dynamics and development are presented, detailing how key parameters influence the magnitude of the equilibrium scour depth and how this is captured by empirical predictive models. Scour computation using the theoretical framework of Manes and Brocchini (2015) is also summarised. The influence of key parameters is extended to the scour geometry, where a review of past studies and their key outputs are presented.

Leading on from the literature, Chapters 3 describes the experimental methodology used to measure the three-dimensional development of the scour hole with time. Details of the experiment trial conditions are provided. The validation of the experimental methodology (Obj. 1) is presented in Chapter 4, which covers the invasiveness of the technique and its measurement accuracy and repeatability. Chapter 5 covers the scaling relationships between key geometric properties of the scour hole; namely, the scour depth, width, length, footprint and volume (Obj. 2). This section provides an interpretation of the scaling relationships using erosion-deposition patterns and energetic considerations. The effect of viscosity on the observed trends, owing to a change in flow regime (Obj. 3), is integrated within the analysis. Quantitative analysis of the observed key relationships (Obj. 4) are covered in Chapter 6. Chapter 7 gives concluding remarks and suggested avenues for further work, based on the findings of the study.

The thesis includes two Appendices. Appendix A presents the structural drawings of the laboratory setup described in Chapter 3. The post-processing methodology, used to convert raw measurement outputs into a three-dimensional scour hole surface for analysis, is presented in Appendix B.

Chapter 2: Literature Review

2.1 Introduction to Scour

Scour is the process of mobilisation and removal of sediment from the bed and banks of a watercourse by the action of flowing water (Kirby *et al.*, 2015). There are three main types of scour that can form around a structure; *natural scour, contraction scour* and *local scour*.

Natural scour is a long-term phenomenon, evolving over the order of years, that characterises river bed degradation, lateral channel migration, bend and confluence scouring that would occur independently of any unnatural obstruction (Arneson *et al.*, 2012; Kirby *et al.*, 2015). Where the flow regime becomes confined, such as through a bridge or channel narrowing, contraction scour (in addition to natural scour) can occur due to the local fluvial dynamics around the obstruction being altered which results in additional bed erosion across the channel width *(Umbrell et al., 1998)*. While contraction scour results in removal of bed material from across the entire channel width through the constriction, local scour by its very definition occurs in immediate vicinity of the feature that is obstructing the flow field. The presence of the obstruction induces a significant local increase in flow velocity which promotes the development of a powerful inhomogeneous three-dimensional vortex system around its base and sides (Melville, 1975; Chang *et al.*, 2013). The vortex system exerts a high shearing stress upon interaction with the immediate bed material, resulting in concentrated bed erosion forming around the obstruction (a localised *scour hole*) and aggradation further downstream in the obstructions' wake (a *deposition mound*) provided by the eroded sediment. Local scour differs in nature from contraction scour as this phenomena occurs solely around the circumference of the obstruction, whereas contraction scour affects the entire channel width through the constriction. The dominance of one over the other is determined by the degree of contraction and the obstruction characteristics (Sturm *et al.*, 2011).

Many scour-related bridge collapses result from the presence of local scour, owing to the concentrated natural of this scour phenomenon (Benn, 2013; Kirby *et al.*, 2015). Thus, this research focusses on the development of local scour around isolated pier foundations, up to an equilibrium state. This Chapter reviews the current knowledge on scour development dynamics, features perceived to influence its occurrence, and how this understanding is used towards assessing the risk of scour at candidate bridge structures.

2.2 Mechanisms of Local Scour

Our physical understanding of the development process of local scour, based on small-scale laboratory analysis, is now presented. The physical flow mechanism underlying the phenomenon of local scour around a blunt-nosed narrow pier obstruction is associated with the development of a localised turbulent spectrum of three-dimensional flow field vortices (Melville, 1975; Chang *et al.*, 2013), as shown in Figure 2.1. As the flow impinges the face of the foundation pier, the blockage produces a negative stagnation pressure gradient acting vertical and away from the free surface along the pier face (Dey and Raikar, 2007; Das *et al.*, 2013b; Schanderl *et al.*, 2017b). The pressure gradient results in up and down flow velocities developing longitudinally along the pier face about a stagnation pressure point[1] (Unger and Hager, 2007).

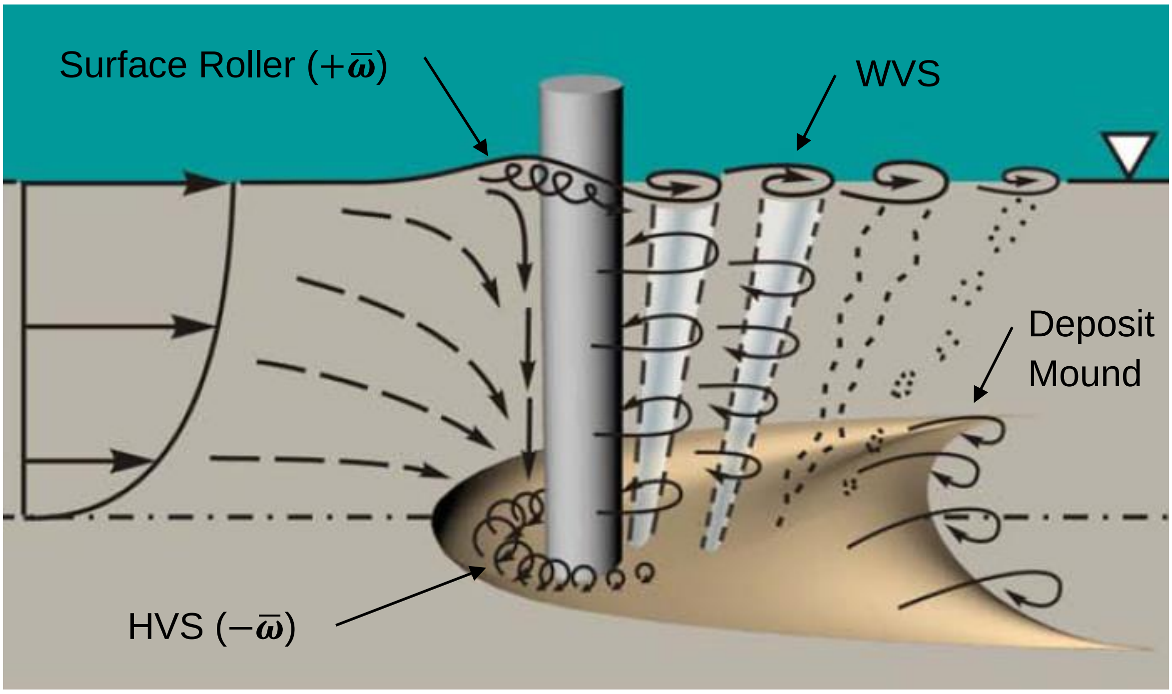

Figure 2.1 Three-dimensional flow field around a cylindrical pier foundation with high flow depth relative to pier width (Ettema et al., 2011: Adapted). HVS is the horseshoe vortex system, whilst WVS is the wake vortex system (defined within the subsequent text).

---

[1] The up flow jet component attains a height approximating to the stagnation head and, along with the formation of a bow wave, induces anticlockwise vorticity ($+\bar{\omega}$) in the proximity of the free surface, known as a surface roller. Anticlockwise vorticity is viewed as entering from left to right as shown in Figure 2.1. The influence of the surface roller on scour generation is only realised in shallow flow conditions, where the approach flow depth is of a similar order of magnitude to, or smaller than, the effective pier width (Ettema et al., 2011).

The down flow velocity component impinges the river bed around the front of the pier and is deflected in the upstream direction. This gives rise to a strong pressure field that promotes a localised flow acceleration and substantial increase in bed shear stress within the pier vicinity, leading to localised flow separation around the pier flanks (Melville, 1975; Tritton, 1988; Dargahi, 1990; Dey, 1996). Initial scouring occurs within this region (Dargahi, 1990; Oliveto and Hager, 2002). After a short duration (of the order of minutes), a coupled vortex system is generated which extends rapidly around the pier face upstream and promotes the development of a minor bed depression around the pier with a roughly constant sloped profile[2] (Figure 2.2) (Melville and Raudkivi, 1977; Baker, 1980a). Consequently, the incoming boundary layer undergoes three-dimensional separation as the edge of the bed depression is reached, causing the shear layer to roll up into an elliptical vortex core of high turbulent kinetic energy (Kirkil *et al.*, 2008). The overall result is a re-organisation of turbulent vorticity which migrates around the upstream face and pier flanks forming a necklace-like turbulent structure, commonly termed the *horseshoe vortex system* (HVS) (Melville, 1975; Baker, 1980b; Tritton, 1988; Dey, 1996; Das *et al.*, 2014b). This vortex system is characterised by negative vorticity ($-\overline{\omega}$), relative to the upper surface roller (Melville, 1975), and flow within it is solely circulatory (Dey and Bose, 1994).

The vorticity of the horseshoe creates an instantaneous bed shearing stress between the boundary of the vortex system and the surrounding bed (Baker, 1980a). The magnitude of this applied bed stress is substantially higher than the threshold stress for sediment motion, and therefore results in the rapid dislodging of sediment particles through local bed-load transport (Dargahi, 1990; Dey, 1996). Whilst the average kinetic energy is strongest in the approach flow that is not affected by the scour hole, the strongest turbulence intensity forms at the upstream head of the main HS vortex (Guan *et al.*, 2019). The vorticity of the HVS deflects the down flow jet underneath the HVS and upstream where it undergoes deceleration and gives rise to strong production in turbulent kinetic energy (Schanderl *et al.*, 2017b). As such, the horseshoe vortex is well known to dictate bed mobilisation and entrainment of sediment within a local scour hole (Shen *et al.*, 1966; Melville, 1975; Dargahi, 1990). As such, the location of maximum scour is translated from around the pier flanks to the front of the pier where the energetic vortex core is generated and dominates the flow field (Unger and Hager, 2007). The development of the HVS dictates the shape of the scour hole which remains approximately constant during the scour development process. This shape is distinguished by three regions Figure 2.2; a circular portion close to the pier base, a steep slope in the deeper area of the scour hole, and a milder upper slope (Gobert *et al.*, 2010).

---

[2] The generated slope is at an angle of around 10-20% greater than the angle of repose of the bed material in still water.

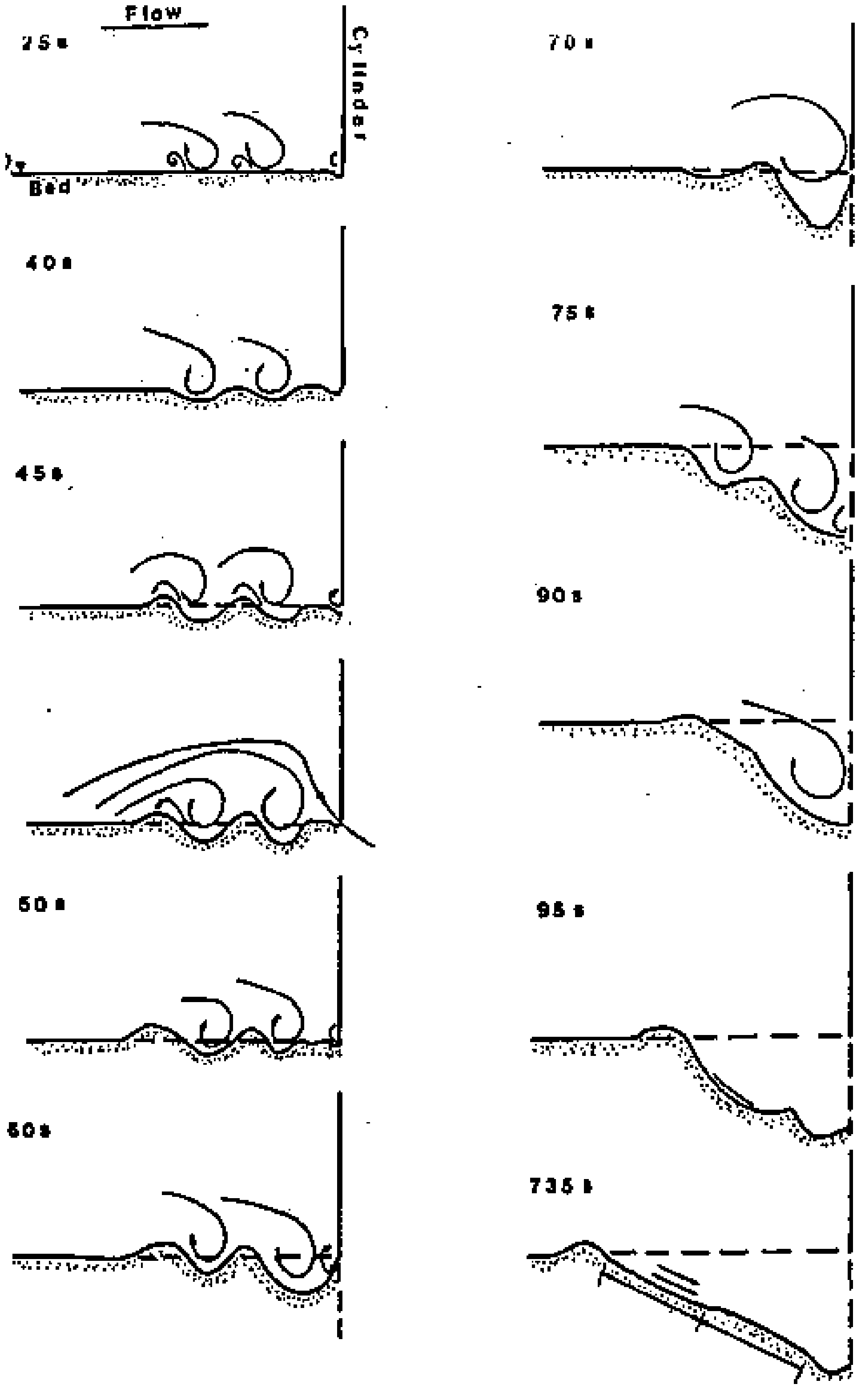

Figure 2.2 Early scour development process around a narrow pier (Dargahi, 1990).

Downstream, further separation of unstable shear layers around the pier flanks promotes three-dimensional shedding of attached eddies within the piers' wake (Melville, 1975; Stevens *et al.*, 1991). The eddy shedding immediately downstream of the pier is collectively known as the *wake vortex system* (WVS), which dissipates as it extends downstream (Stevens *et al.*, 1991). The wake is characterised as a low-pressure region where the vertical velocity component is upward-dominated. Thus, the role of a turbulent WVS in the scouring process is to lift any sediment mobilised by the HVS into the upper region of the flow to transport the entrained particles downstream (Melville, 1975). Wake vortex visualisations (see Figure 2.3b) show that the trajectories of entrained particles follow spiralled paths due to the ”tornado-like” structure of the WVS, where sediment follow the flow (i.e. as if they are mass-less) and can be lifted as high as 80% of the wake flow depth (Ettema *et al.*, 2006). Further downstream, where the energetic wake eddies have significantly dissipated, sediment particles can no longer be transported further and are subsequently deposited. Early scour deposition occurs in the immediate vicinity of the pier wake (Dargahi, 1990). However, as more sediment is removed and the scour hole develops, the deposition region forms a sediment mound which stretches over a significant area downstream beyond the scoured zone (Unger and Hager, 2007). The shedding, dissipation, and interaction of the WVS with the HVS depends on the pier Reynolds number (discussed later in Section 2.3.1.3).

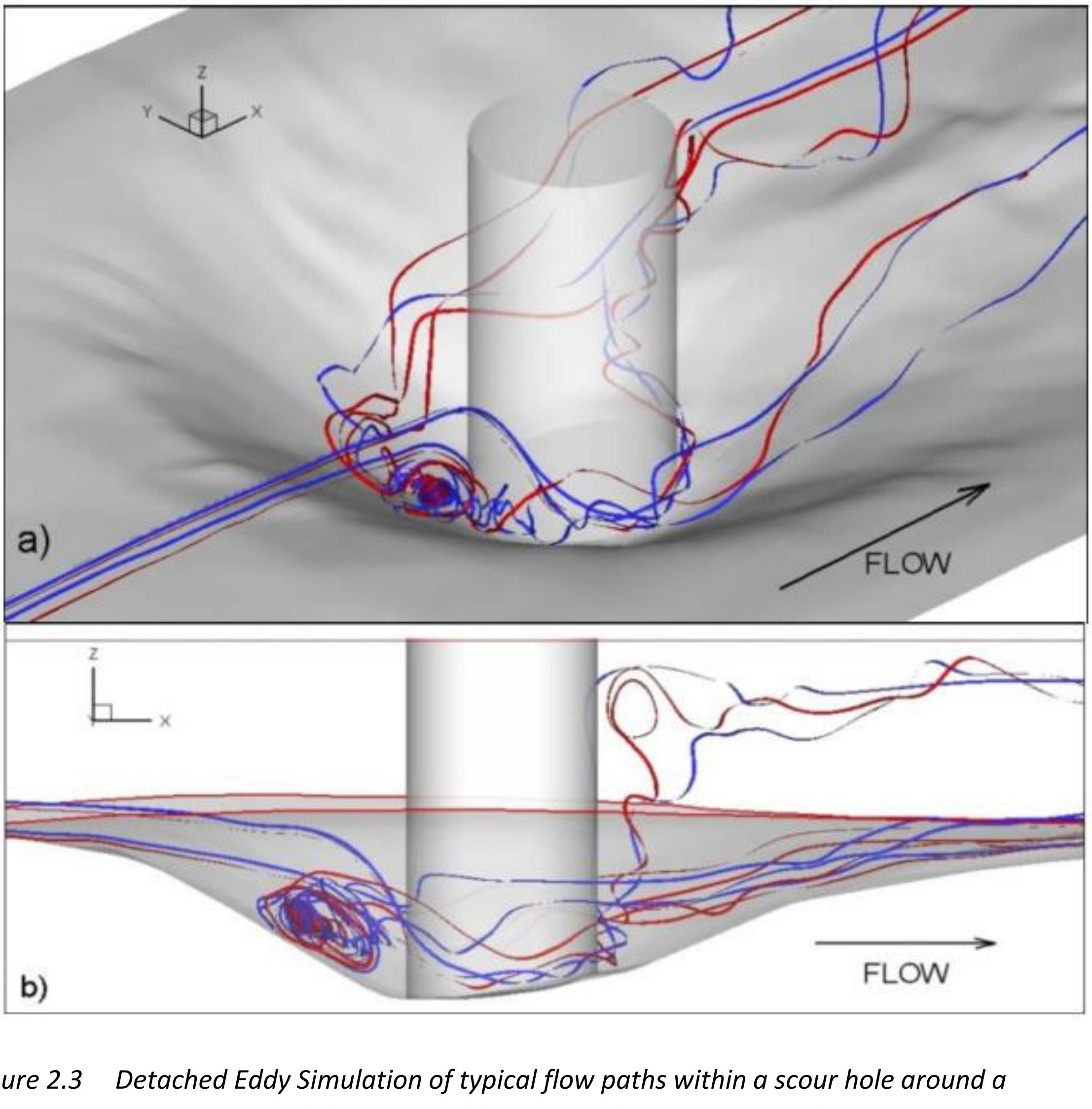

Figure 2.3 Detached Eddy Simulation of typical flow paths within a scour hole around a cylindrical pier; (a) overview, (b) elevation (Kirkil et al., 2008).

Initially, the HVS is known to be geometrically small as its size is perceived to stably scale with the development of the scour hole volume (Figure 2.3b) (Melville, 1975; Muzzammil and Gangadhariah, 2003; Link *et al.*, 2008a). Based on Large Eddy Simulations (LES) from Schanderl *et al.* (2017b), the wall shear stress is largest between the main horeshoe vortex and the pier. This is governed by the strong downflow presence in front of the cylinder as turbulent stresses are relatively small in this zone (Schanderl *et al.*, 2017a; Schanderl *et al.*, 2017b). As the scour hole enlarges, the overall shape of the horseshoe vortex expands and extends further radially around the pier as more of the approaching flow obtains a larger downward component. Extension of the HVS around the pier coincides with a significant magnitude attenuation of the vortex system core in this region (Melville, 1975).

As the scour hole develops further the HVS rapidly increases in vorticity whilst the concentrated turbulent kinetic energy core sinks into the hole (Melville, 1975; Baker, 1980a). As the HVS is buried in the scour hole as it develops over time, sediment is mobilised and transported by erosion of the bed and continuous sliding of sediment along the scour hole due to the lower scour hole bed slope exceeding the repose angle of the sediment which gives rise to instability (Gobert *et al.*, 2010). Depending upon the fluvial conditions, a second steeper scour rim forms lower within the scour hole (Melville and Raudkivi, 1977) that houses a secondary horseshoe vortex[3] (Baker, 1980b; Dargahi, 1990). The location of this rim oscillates as the horseshoe vortex expands and contracts (Lee and Sturm, 2009), owing to the vortex core being located between this rim and the pier (Guan *et al.*, 2019). The increased steepness results in regular avalanche-type collapses that, in combination with the negative vorticity of the HVS, forces dislodged sediment to move up the slope in intermittent bursts and transported to the pier wake for deposition downstream (Melville and Raudkivi, 1977; Baker, 1980a; Ettema *et al.*, 2006).

After significant development, the vortex upstream of the scour hole evolves into two inter-connected vortices in the form of a main and smaller vortex (Guan *et al.*, 2019). This expansion of the HS vortex is coupled with a localised vortex that forms at the base of the scour hole, referred to as the *base vortex*, which is characterised with an positive vorticity opposing the HVS (Kirkil *et al.*, 2008; Guan *et al.*, 2019). The base vortex (Figure 2.4) presumably acts to mobilise particles in the vicinity of the bed that are piled up against the face of the cylinder or held in suspension. The vorticity of the base vortex is weak compared with the main HS vortex, though an increase in turbulence intensity is observed very locally within its vicinity (Guan *et al.*, 2019). The presence

---

[3] This secondary lower inner slope below the primary vortex is steeper as it is affected by a combination of down flow and HVS vorticity, rather than solely induced by the action of the primary vortex (Lee & Sturm, 2009).

and action of the base vortex leads to a scour hole base which is substantially reduced in gradient and approaches a flat-bed (Dargahi, 1990; Link *et al.*, 2008a; Diab *et al.*, 2010; Guan *et al.*, 2019).

Enlargement of the scour hole sees the overall geometry of the HVS increase, whilst the strength of the energetic core decreases and is translated further away from the pier (Das *et al.*, 2013a) and approaches a stable position (Guan *et al.*, 2019). A reduced core strength results in a reduced rate of sediment mobilisation around the pier base, consequential of a reduced magnitude of bed shear stresses induced by the HVS. Moreover, the expanding HVS causes the down flow along the pier face to be more frequently deflected upwards, reducing both the scouring caused by the down flow component and the rate of increase in HVS vorticity (Melville, 1975; Melville and Raudkivi, 1977).

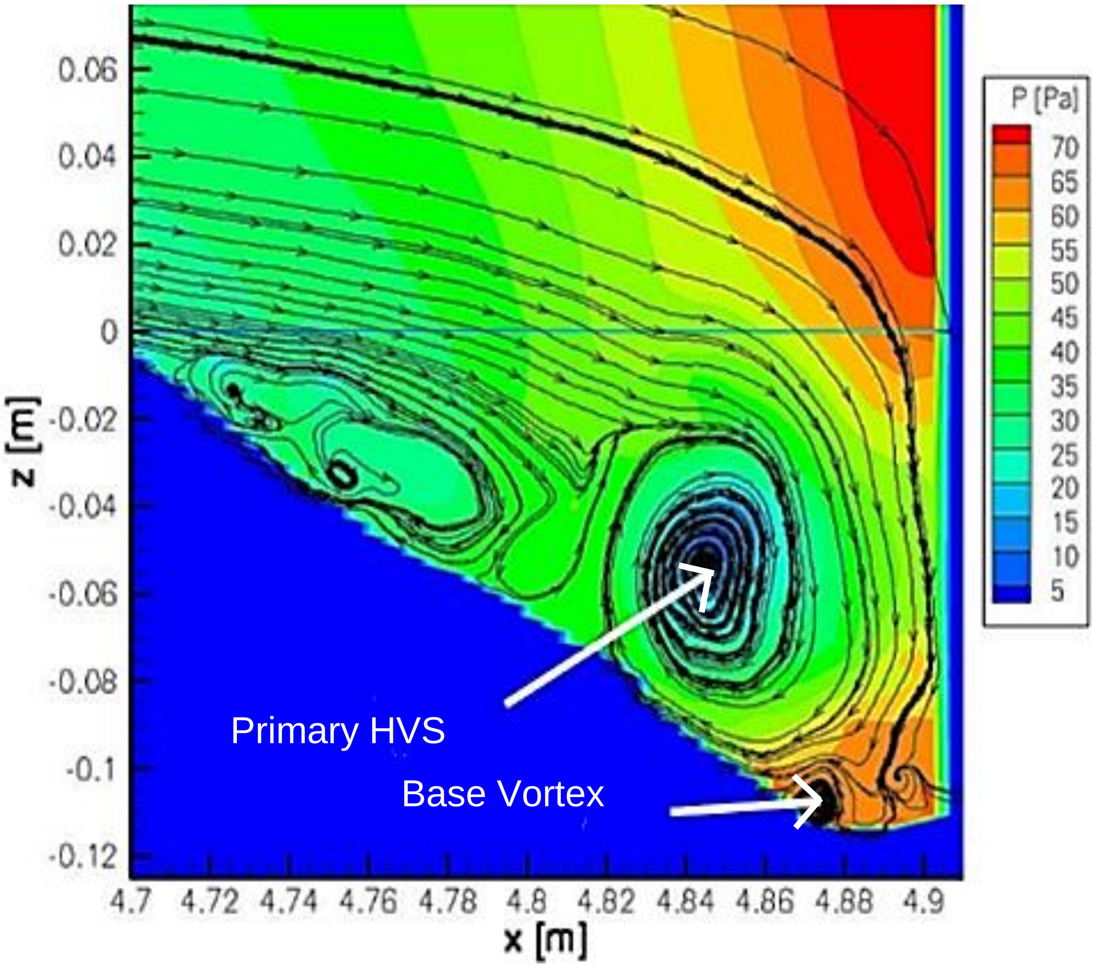

Figure 2.4 *Local scour vortices. Elevation taken of the upstream axis of symmetry (Link et al., 2006: Adapted). z is the bed elevation relative to the flat-bed state, and x is the stream-wise location measured from the flume inlet.*

Upon approaching an equilibrium state, the magnitude of the down flow velocity near the bottom of the hole decreases due to the size of the HVS. When scour hole equilibrium is reached, the primary horseshoe vortex core the rate of increase in horseshoe vortex vorticity plateaus (Melville, 1975; Unger and Hager, 2007). As a result, the vortex system is thought to be in a state of equipoise with the down flow along the pier face, whereby only intermittent bursts of sediment up the scour hole slope remain due to fluctuations in turbulent kinetic energy.

For sharp-nosed piers, three-dimensional boundary layer separation upstream cannot be induced due to the incapability of developing a significantly large pressure field at the base of the pier. Thus the formation of a horseshoe vortex does not occur (Shen *et al.*, 1966; Chiew, 1984). Initial high rates of scouring instead occur within the pier wake as the sharp edges are able to form relatively strong roller vortices which can maintain their coherence until they reach the bed surface, conveying significant bed shear velocities in the near wake region (Ettema *et al.*, 2011). At equilibrium, the maximum scour depth for a sharp-nosed pier is smaller in magnitude to that of a blunt-nosed foundation, assuming the pier is positioned parallel to the direction of flow. If the pier inclination is not parallel, the sharp-nosed pier would behave like a blunt-nose type due to an increase in effective pier width (Melville and Coleman, 2000). Within this context, blunt-nosed piers are the focus of this research.

2.2.1 Types of Local Scour

Local scouring occurs in two different forms; *live-bed* and *clear-water* flow conditions. The presence of one over the other is identifiable from whether sediment is removed with or without replenishment, respectively (Chabert and Engeldinger, 1956; Melville, 1984). The horseshoe vortex is the primary source of significant bed shear stresses that instigate local scour phenomena, regardless of flow regime (clear water or live-bed). As the scour hole expands, there is decay in the erosive strength of the HVS due its own expanding vortex core and thus the magnitude of the shear stresses also reduce. Theoretical clear-water equilibrium conditions are reached when the local mean bed shear stress (τ_b) induced by the HVS is no longer able to mobilise the bed sediment from within the scour hole, i.e. $\tau_b \cong \tau_c$ (Shields, 1936; Vanoni, 1964). Conversely, live-bed equilibrium conditions result when a balance is struck between incoming and outgoing sediment fluxes within the scour hole (Chiew, 1984; Oliveto and Hager, 2002).

The time scale to reach an equilibrium state substantially varies for the two regimes. For live-bed scour conditions, studies have shown (e.g. Chiew, 1984; Melville, 1984) the point of system equilibrium is approached reasonably promptly – of the order of hours. After the maximum scour peak is obtained, the state of physical volumetric equilibrium exhibits a periodic fluctuation about a mean scour depth value (Figure 2.5) resulting from the passage of bed forms through the scour hole from upstream (Chabert and Engeldinger, 1956; Melville, 1984). This understanding of time duration fluctuations during live-bed conditions is well accepted for small-scale experiments (Melville and Coleman, 2000).

Conversely, clear-water equilibrium is approached at a far slower rate (Figure 2.6). This is a result of comparably slower bulk approach flow velocities which are unable to dislodge sediment particles, and erosion is reliant upon the action of the horseshoe vortex system to remove sediment from around the pier base. Due to a lack of sediment inflow, equilibrium can only be obtained if inflow velocities are maintained for a sufficiently long period (Link *et al.*, 2017).

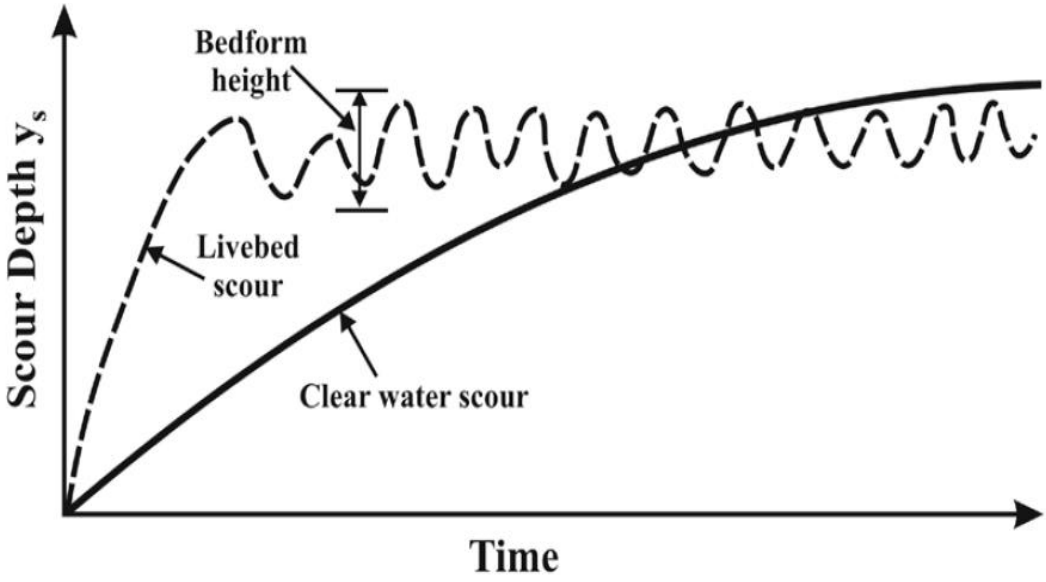

Figure 2.5 Scour Development around a cylindrical pier in clear water peak conditions and live-bed approach flow conditions just beyond the threshold peak (Ettema et al., 2011).

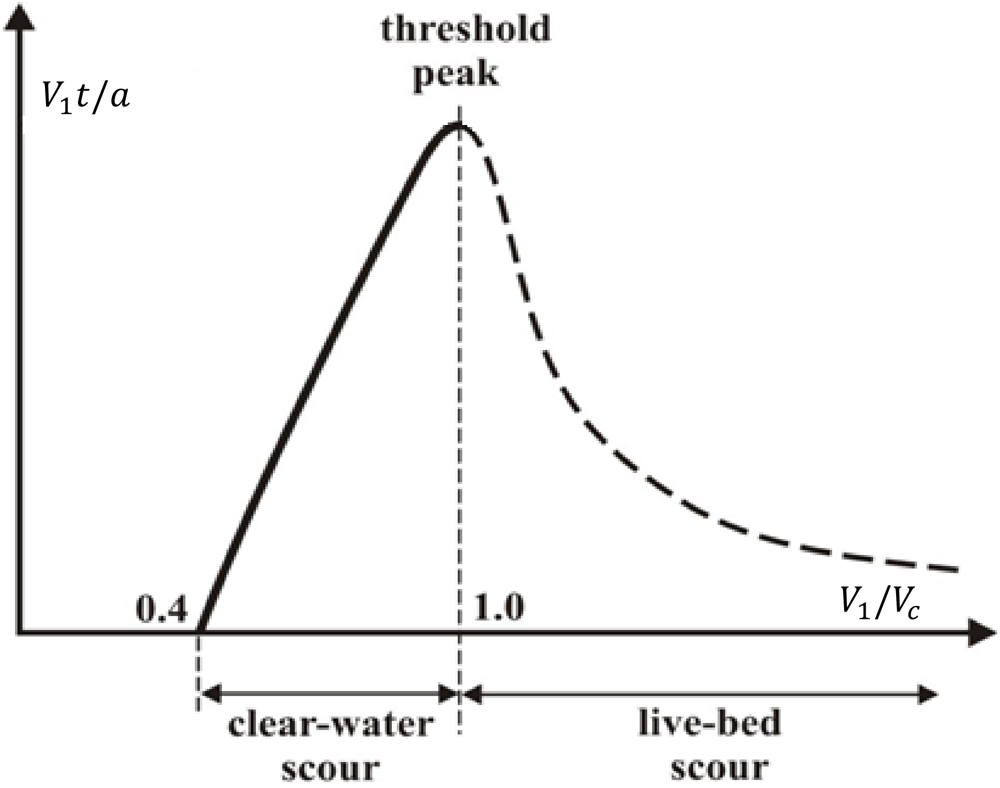

Figure 2.6 Time scale variation for scour hole equilibrium (Adapted, Melville and Chiew, 1999). V_1/V_c defines the flow intensity, which is the ratio between inflow (V_1) and critical sediment velocity (V_c), t is time and a is the pier diameter.

Identifying the timescale to clear-water scour equilibrium predominantly involves monitoring the temporal development of the maximum depth, located at the upstream edge of the narrow pier face. However, this exact time frame is a much more arbitrary concept, relative to live-bed scour behaviour, that is typically research-subjective.

Many scour researchers assume that a state of equilibrium is achieved within a finite time period (Ettema, 1980; Chiew, 1984; Dey and Raikar, 2007; Das *et al.*, 2013a, 2014a; Das *et al.*, 2014d). Most small-scale laboratory experiments use this hypothesis, indicating that the scour hole development begins to level off after a period of 24-36 hours (Melville and Coleman, 2000; Oliveto and Hager, 2005; Hager, 2007). However, large scale and long-term laboratory experiments (e.g. Sheppard *et al.*, 2004) have shown that intermittent fluctuations in the scour depth occurs (Figure 2.7) – presumably from sporadic slope failure of the scour hole caused by eddy impingement (Ettema *et al.*, 2006) – as the scour hole approaches an equilibrium state following experiments lasting in excess of 200 hours. As a result, some researcher hypothesise that equilibrium is approached asymptotically, with a true equilibrium state reached in an infinite timeframe. Several time evolution equations have subsequently been derived (Kothyari *et al.*, 2007; Sheppard and Melville, 2011; Lança *et al.*, 2013) in an attempt to generate a universal definition for the equilibrium timescale. However, these equations have limited applicability outside of the small-scale test range they were derived from and may not reflect the true complexities of field scour development. As a result, a universal definition of clear-water equilibrium is elusive as the physics of reaching its state are poorly understood.

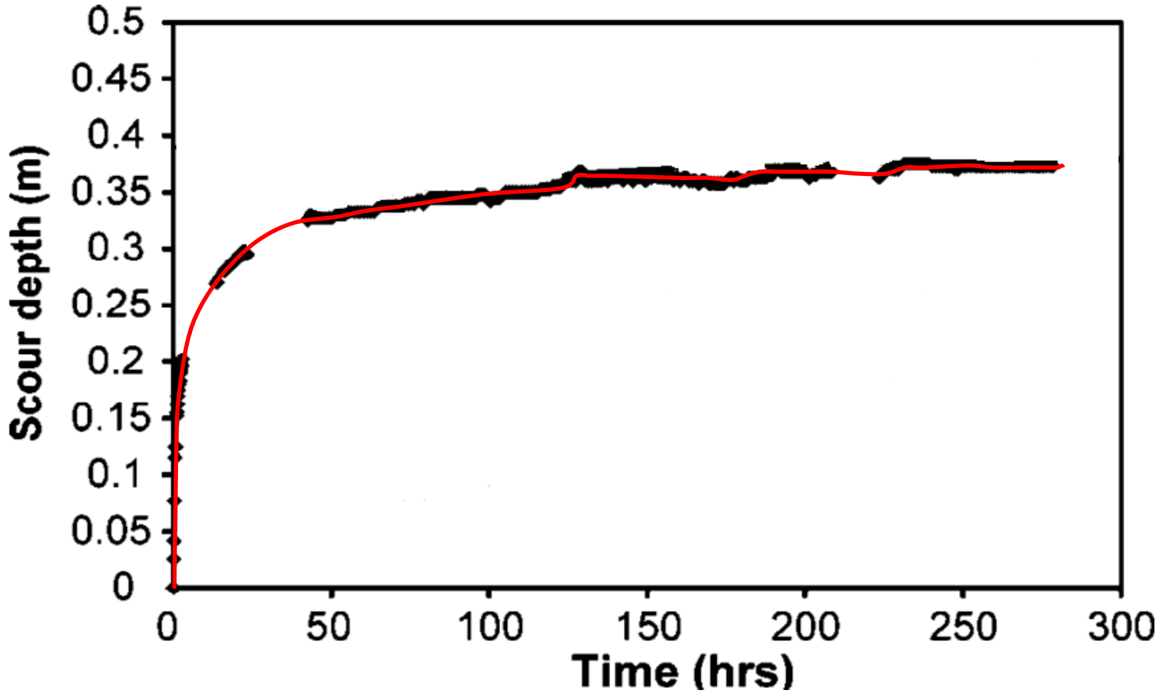

Figure 2.7 Scour depth variation over a substantially long time period. Data taken from large scale experiments by Sheppard et al. (2004). (Adapted)

2.2.2 Scour during Floods

It is well documented that flood-induced local scouring is responsible for the majority of hydraulic structure failures worldwide (Benn, 2013; Lagasse *et al.*, 2013; Deng *et al.*, 2015). As the flood hydrograph begins to dominate the flow, local scour around the structure occurs in the form of intense live-bed scour conditions followed by clear-water scour prior to flood recession (Lee *et al.*, 2004; von Leeuwen and Lamb, 2014). The intensity and duration of the flood hydrograph determines whether previously scoured bed material will become re-entrained, and whether further scour hole development will result. If previously scoured sediment is re-mobilised, this occurs rapidly due to its loose structure (Buffington and Montgomery, 1997). This is particularly important because, as the flood hydrograph recedes, it engenders scour hole refilling by sediment previously entrained within the flow volume due to a diminished sediment transport capability; leaving negligible trace of any flood-related foundation undermining (Figure 2.8) (May *et al.*, 2002). Therefore, our ability to identify the level of previously scoured bed material and the perceived maximum depth for a given hydrodynamic condition is vital for reliably categorising the scour risk at a structure.

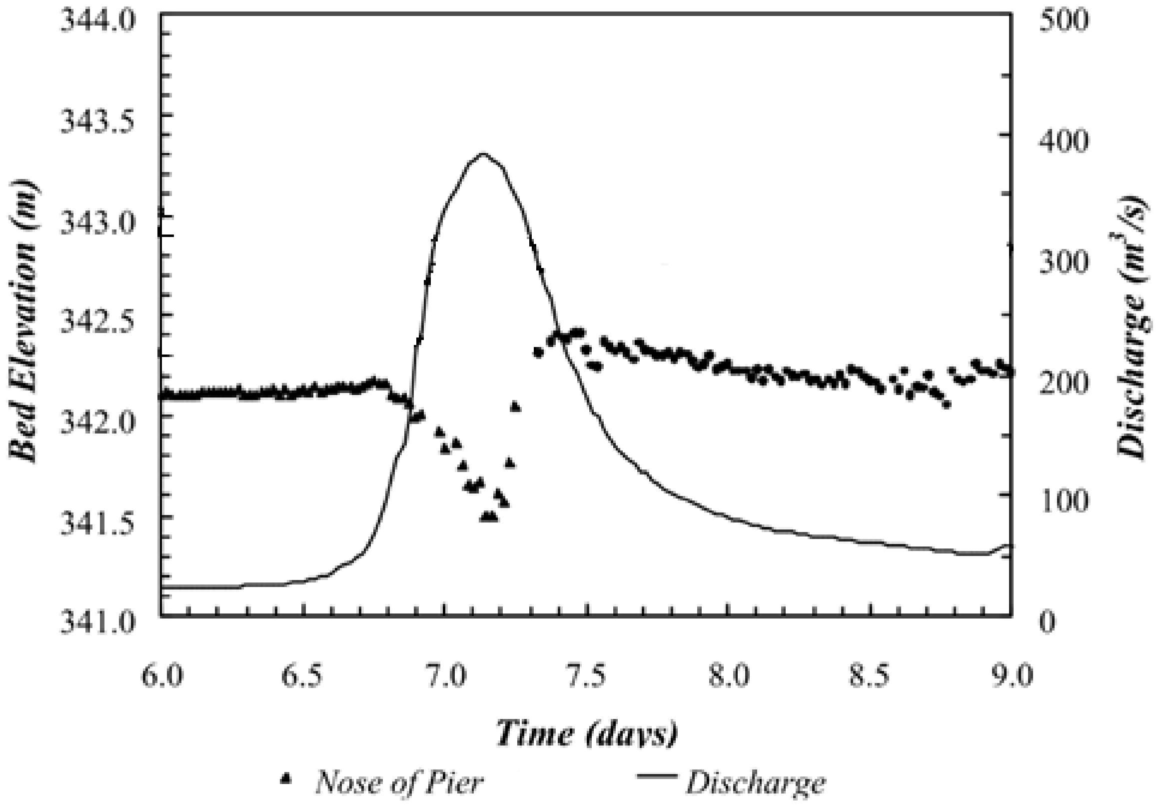

Figure 2.8 Flood Hydrograph, showing the variation of river bed elevation for a flood event around a blunt-nosed pier (Lee et al., 2004) and the location of maximum scour (Nose of Pier).

2.3 Dimensional Analysis

With an increase in future floods and sea level anticipated from recent climatic reports (e.g. see Eddowes et al., 2003; Jenkins et al., 2009), it is imperative that scour risk assessment procedures are able to reliably identify high-risk structures so that resources are correctly allocated to those requiring maintenance or preventative measures (Tubaldi et al., 2017).

Local scour is a notoriously complex and time-dependent phenomenon. However, the main parameter that governs the outcome of any structural assessment concerning scour risk is the computation of an equilibrium scour depth. This length scale characterises the maximum perceivable scour depth for a given flow return period, and its computation has been the main focus of laboratory work for the past 60 years as it is directly comparable to the critical depth of the foundation (Ettema *et al.*, 2011).

Our understanding what physical factors influence scour development has traditionally relied on an empirical approach based on dimensional analysis. Dimensional analysis is used to develop an implicit formulation of criteria for dynamic similarity of the scour phenomenon in a direct manner. The identification of parameters apposite to this phenomena are considered to fall within three categories: attributes of the approach flow, the erodible bed material, and the candidate pier. For this study, we consider the simplest case of a cylindrical pier. Accordingly, the equilibrium local scour depth, y_{se}, can be expressed by the functional relationship (e.g. Olsen and Melaaen, 1993; Ettema *et al.*, 2006)

$$y_{se} = f\begin{bmatrix} Flow\ (V_1, y, g, \rho, \mu);\ Pier\ (a);\ Sediment\ \left(d_{50}, \sigma_g, \rho_s\right); \\ Site\ (B);\ Time\ (t) \end{bmatrix}, \tag{2.1}$$

where V_1 = mean approach velocity; y = upstream depth; g = acceleration of gravity; ρ and μ = fluid density and dynamic viscosity, respectively; a = pier diameter; d_{50} and σ_g = median size and geometric standard deviation of the sediment particle size distribution, respectively; ρ_s = sediment density; B = average channel width; t = time; and f denotes “a function of”. Appropriate physical parameters are illustrated in Figure 2.9.

Typically within the literature, the sediment size distribution is quantified through considering the magnitude of d_{50} and σ_g. This assumes the sediment size can be modelled well using the normal distribution, which is not necessarily the case for all sediment samples. However for a uniform sample, which is the focus of this study, the normal distribution provides a reasonable estimate of the sediment size distribution (McManus, 1988). Details of the variation of y_{se} with σ_g are presented for context in Section 2.3.2 .

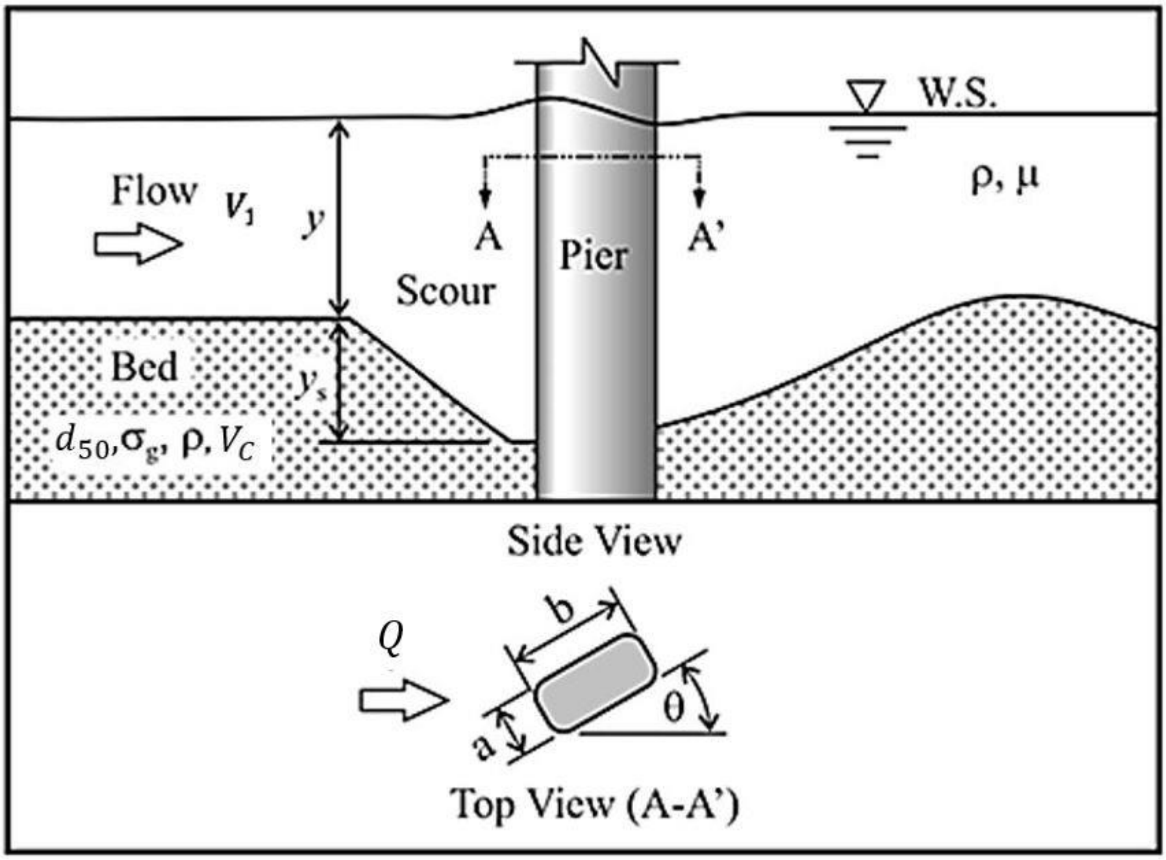

Figure 2.9 Referenced variables known to influence localised scour around a cylindrical pier foundation (Ettema et al., 2011). Θ represents the angle of attack, and b is the effective pier length.

The Buckingham Pi theorem is applied to the parameters given in Eq. (2.1); whereby the pier diameter, flow velocity and fluid density are utilised as repeating variables for implementation. As such, the normalised equilibrium scour depth, y_{se}, can be expressed in terms of

$$\frac{y_{se}}{a} = f\left[\frac{y}{a}, \frac{{V_1}^2}{ga}, \frac{\rho a V_1}{\mu}, \frac{B}{a}, \frac{a}{d_{50}}, \sigma_g, \frac{\rho_s}{\rho}\right]. \tag{2.2}$$

The first four are related to the influence of the flow field scale, whilst the latter three terms describe the influence of the bed sediment characteristics. Along with these terms, many authors have adopted several artificially-introduced functions in an attempt to describe certain observed behavioural trends. An overall collection of key non-dimensional terms from the literature is

$$\frac{y_{se}}{a} = f\left[\frac{y}{a}, \frac{{V_1}^2}{ga}, \frac{\rho a V_1}{\mu}, \frac{B}{a}, \frac{a}{d_{50}}, \sigma_g, \frac{\rho_s - \rho}{\rho}, \frac{V_1}{V_c}, \frac{V_1}{\sqrt{\frac{\rho_s - \rho}{\rho} g d_{50}}}, \frac{B}{y}\right]. \tag{2.3}$$

The parameter V_c defines the critical velocity of incipient sediment motion in the undisturbed channel. The terms to note are flow intensity (V_1/V_c), densimetric Froude number

$(V_1/\sqrt{\frac{\rho_s-\rho}{\rho}gd_{50}})$ and flow shallowness (B/y); all of which are derived using a different dimensional analysis approach to that presented here. The sediment threshold velocity is not included within Eq. (2.1) as it is known to be a function of sediment diameter and density; both of which are adequately captured within the above analysis. The non-dimensional group V_1/V_c is often introduced by researchers to discern between clear-water $(0.4 < V_1/V_c < 1)$ and live-bed $(V_1/V_c > 1)$ conditions. Also note that the specific gravity term (ρ_s/ρ) has been adapted to the more commonly applied form $(\rho_s - \rho)/\rho$.

The importance of each term on the scour process given in Eq. (2.2) is understood by isolating each effect in turn. A significant amount of research has been conducted to this end. Important conclusions from those studies will now be summarised for completeness. Only research focussing on individual foundation piers will be used to disentangle relation intricacies, meaning that the indirect effect of e.g. pile grouping, and hence scour hole superposition, are avoided.

2.3.1 Flow Field

2.3.1.1 Flow Shallowness y/a

Flow shallowness $(\mathrm{y/a})$ quantifies the effect of blockage imposed by the pier. For wide piers, where the flow depth is significant relative to the pier width $(\mathrm{y/a} \lesssim 0.2)$, the scour depth linearly increases with flow depth. At reduced flow depths for a constant pier diameter, the surface roller progressively begins to dominate the flow field and eventually eliminates the horseshoe vortex at very shallow flow conditions (Melville, 2008). As the horseshoe vortex is the dominant source of bed mobilisation, the maximum scour depth is notably reduced (Laursen and Toch, 1956; Raudkivi, 1986) and the location of maximum scour depth typically occurs around the pier flanks.

As $\mathrm{y/a}$ increases, there is less interaction between the opposing vorticities of the surface roller and HVS, leading to the development of the latter and in increase in scour activity around the frontal face of the structure. For $\mathrm{y/a} > 1.4$, the flow field is classified as a narrow pier, where the approach flow is independent of the flow depth as the HVS is able to develop unimpeded by the surface roller (Ettema, 1980; Raudkivi and Ettema, 1983; Melville and Coleman, 2000). Accordingly, the HVS and down flow components are instead a function of the transverse geometry of the foundation, with their geometry seen to scale with pier width.

2.3.1.2 Froude Number V_1^2/ga

The vorticity of wake vortices is thought to be characterised by the Froude number (Ettema *et al.*, 2006). By examining time-averaged wake structures using Particle Image Velocimetry (LSPIV), Ettema *et al.* (2006) identified that smaller cylinders are associated with wake vortices of a far higher vorticity relative to their large scale counterparts. Applying small-scale results to field scales is hindered by an inability to achieve dynamic similitude in three major length scales: sediment diameter, flow depth and pier diameter. Thus, small model piers are seen to have a greater capacity for removing sediment away from the scour hole. Although adjustment factors to account for this eddy scaling concern have been developed, their inclusion has yet to be validated using field data and thus the physics underlying the proposed adjustment are not well understood.

2.3.1.3 Reynolds Number $\rho a V_1/\mu$

The Reynolds number characterises the relationship between inertial and viscous forces. In much of the literature on local scour, the dependence of the equilibrium scour depth on the Reynolds number (Re_p) is assumed to be negligible due to the highly turbulent nature of flow structures around a bridge pier (Manes and Brocchini, 2015). However the strength, evolution and instability of the vortices upstream of the pier are well known to be dependent upon the Reynolds number which dictates momentum transfer mechanisms at the sediment-water interface (Tritton, 1988; Ettema *et al.*, 2011). Early work by Shen *et al.* (1969) identified that the equilibrium scour depth has some dependency on Re_p, owing to its effect on the size and strength of the horseshoe vortex. Ettema *et al.* (2006), who investigated the similitude of large-scale turbulent structures generated during local scouring, observed that vortex dependency on the Reynolds number is extendable to the piers' wake, where they identified that the shedding frequency, and therefore power, of the wake vortex system has a notable dependency on Re_p. They found that the ability of the WVS to move sediment for narrower piers is also enhanced which, in turn, can induce distorted scour depths when scaled to field equivalents.

Much of the scour research to date has largely ignored the implications of viscosity forces on scour development. However, Lança *et al.* (2016) used a dimensional analysis approach that differs from that presented in Section 2.3 to isolate viscosity effects to identify that viscosity does exert a minor, yet important, influence on the scour depth of equilibrium. Their results can be understood through simple theoretical considerations. An assumption of negligible viscosity influence assumes the approach flow regime is in fully-rough turbulent flow conditions where the critical shear stress (see Figure *2.10*), as first introduced by Shields (1936), is independent of the particle Reynolds number $Re^* = U^* d_{50}/\upsilon$, where U^* is the shear velocity (Ettema *et al.*, 1998; Manes and Brocchini, 2015). Fully-rough conditions are applicable to sediments defined as very coarse sand or gravel, however most experimental research into scour has typically used fine-to-medium sands which are defined within the transitionally-rough regime. As such, it is very plausible that there is some dependency of the equilibrium scour depth on viscosity.

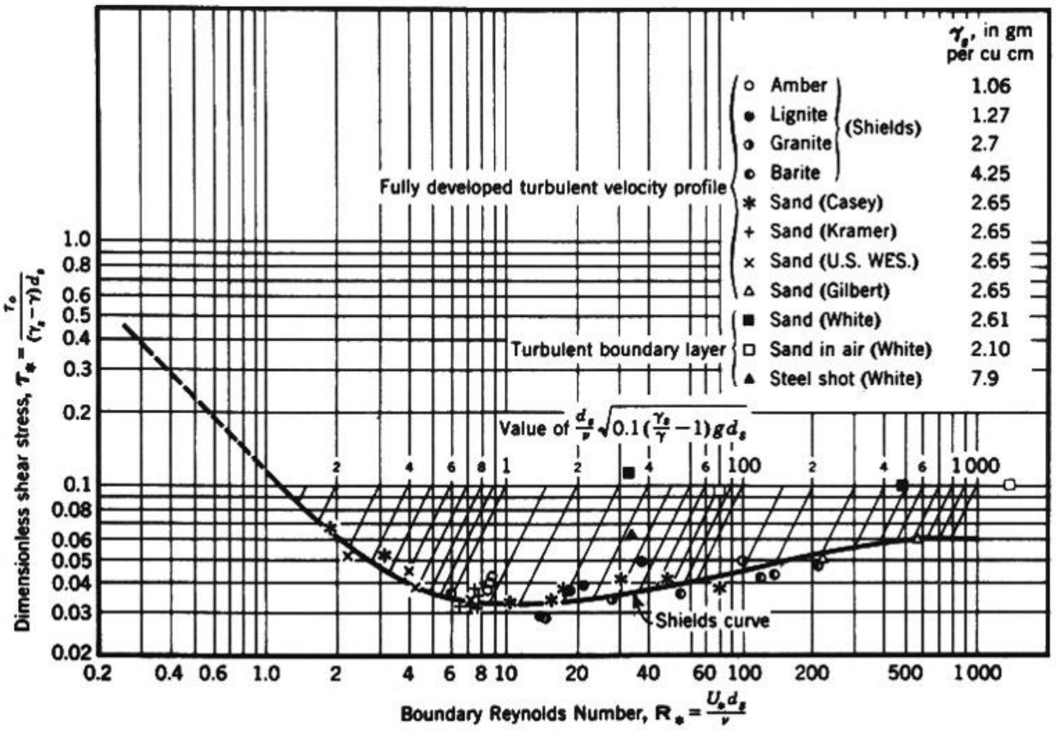

Figure 2.10 Shields curve: shear stress variation with boundary Reynolds number (Vanoni, 1964)

2.3.1.4 Contraction Blockage B/a

Contraction scour is directly considered within the ratio B/a. Due to the limited size of most laboratory test flumes, scale model replicas of entire bridge spans are infeasible. Instead, isolated scaled pier foundations are tested; assuming that the effects of pier spacing at field scale are negligible. In order to avoid the superposition of both local and contraction scour and any associated turbulent eddy interactions, scale models are limited to a maximum pier width relative to the flume width which is captured by B/a.

An increase in the contraction blockage reflects a similar increase in form drag (Qi *et al.*, 2014). Raudkivi and Ettema (1983) suggest that the ratio B/a must exceed 6.25 to minimise any contraction effect on the natural development of local pier scour, whilst Chiew (1984) argues that $B/a > 10$ is required for any changes in form drag to be completely discarded. However, observations by Chiew (1984) were made during live-bed experiments characterised by the passage of dune bed forms which are more likely to be influenced by flow contraction. Bed forms in clear-water conditions are not developed so long as simulations are carried out below threshold conditions (Buffington and Montgomery, 1997). As a result, the threshold value of $B/a > 6.25$ is often accepted for clear-water scour.

2.3.2 Bed Sediment

2.3.2.1 Relative Sediment Coarseness a/d$_{50}$

Early experimental work showed that the influence of sediment size on the developing scour hole has only a measurable impact on the equilibrium scour depth for $\mathrm{a/d_{50}} < 50$ (Ettema, 1980; Raudkivi and Ettema, 1983). Within this range the sediment particles are considered coarse in size, which ultimately reduces the potential for scouring as part of the down flow energy used to mobilise the sediment gets dissipated within the pores of the coarse sediment bed. However, Buffington and Montgomery (1997) state that an increased relative roughness (i.e. lower values of $\mathrm{a/d_{50}}$) promotes an increase in form drag which, in turn, decreases the shear stress available to mobilise sediment due to enhanced bed shear stress partitioning. Consequently, they argue that lower values of $\mathrm{a/d_{50}}$ require a greater total bed shear stress to promote bulk sediment motion.

Later work by Chiew (1984) found that for $50 < \mathrm{a/d_{50}} < 150$ the scour depth decreases marginally and approaches a plateau of $y_{se}/a \cong 2.2 - 2.3$ at around $\mathrm{a/d_{50}} \cong 130$; beyond which the scour depth is deemed independent of sediment coarseness (Raudkivi and Ettema, 1983). However, more recent large scale studies (Sheppard *et al.*, 2004; Sheppard and Miller Jr, 2006) have shown that, for $a/d_{50} > 50$, y_{se}/a decreases significantly and eventually plateaus at $y_{se}/a \cong 1.4$ for $\mathrm{a/d_{50}} > 400$ (Figure *2.11*). The reason for this behaviour as $\mathrm{a/d_{50}}$ increases beyond this range is largely unknown. As field sites have very high values of $\mathrm{a/d_{50}}$ relative to small-scale studies, this lack of interpretation raises concerns that the true behaviour of field scour may be poorly accounted for in empirical predictive models.

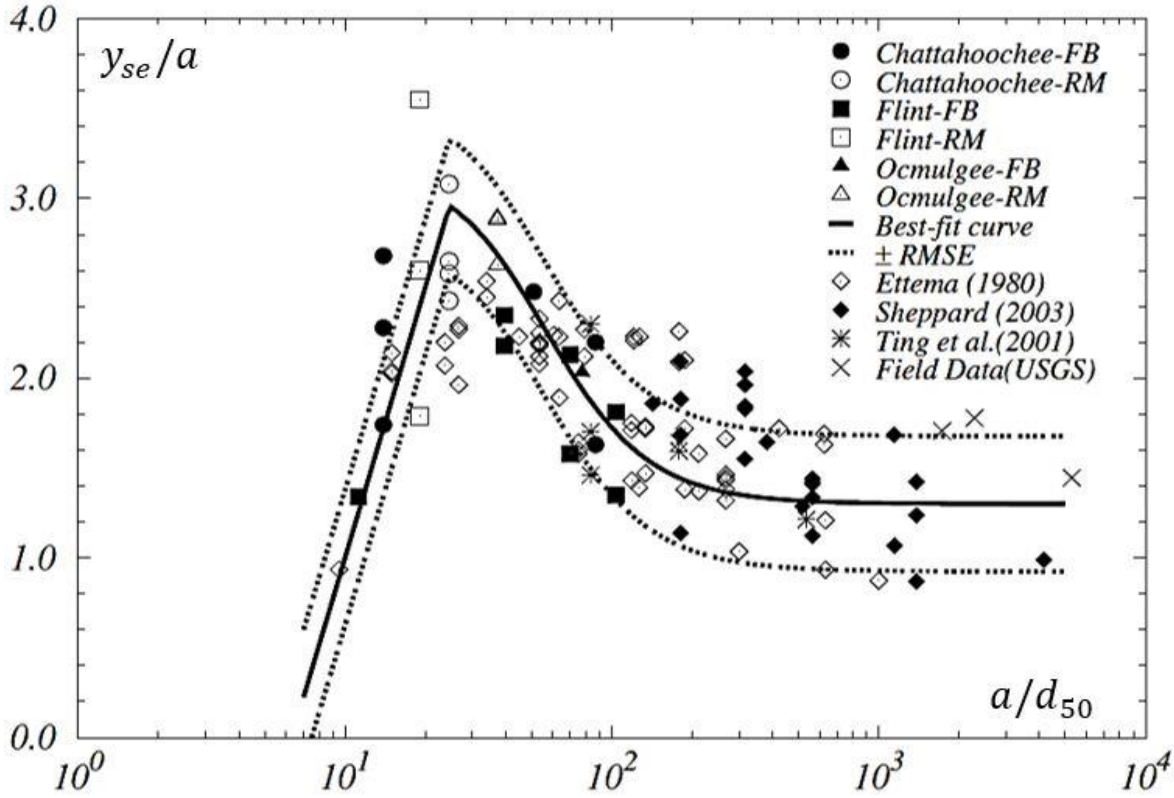

Figure 2.11 Variation of the equilibrium scour depth with relative sediment coarseness (Lee and Sturm, 2009). y_{se} is the end-of-trial maximum scour depth for each data point.

2.3.2.2 Geometric Standard Deviation of Sediment Size Distribution σ_g

The geometric standard deviation of particle size distribution (σ_g) quantifies the variability in size of the sediment within a representative sample of bed sediment, obtained using sediment sieve analysis (Ettema, 1980; Raudkivi and Ettema, 1983)). For sediments with a value of $\sigma_g < 1.5$, the sediment can be considered uniform (Ettema, 1980; Lee and Sturm, 2009). At values greater than this, the sediment is considered non-uniform which promotes the formation of an armour layer on top of the scour hole surface due to the presence of larger grain constituents. This armouring effect significantly reduces the rate of scour development and equilibrium scour depths (see Figure 2.12) in non-ripple forming sediments due to energy dissipation through the larger grains (Raudkivi, 1986), as discussed previously. Therefore for conservativism, most empirical methods apply experiment results using uniform sediment to derive a scour depth predictive formulae and factor in the effects of sediment non-uniformity separately.

2.3.2.3 Sediment Angularity and Specific Density $\rho_s - \rho / \rho$

Buffington and Montgomery (1997) compiled a significant amount of experimental data investigating the incipient motion of sediment. Their analysis identified that greater particle sorting and angularity ensured that the sediment grains were more resistant to movement relative to loose, surface-protruding and highly spherical alternative beds. The effect was found to be an increase in the value of the dimensionless critical shear stress defined by Shields (1936). Ultimately, a greater flow velocity would be required in order to reach the threshold condition of incipient motion.

Due to the tedious nature of varying the density of bed sediment, minimal experimental work has been conducted that examines the effects of specific density on the scour hole. However, by considering the Shields curve (Figure 2.10), it is observed that the dimensionless shear stress defined by $\tau_c/(\rho_s - \rho)gd_{50}$ is approximately constant for a given value of the particle Reynolds number Re^*. The Shields curve was developed using a variety of particle types; therefore, for the value of $\tau_c/(\rho_s - \rho)gd_{50}$ to stay constant for a given Re^*, it is reasonable to assume that the magnitude of the critical shear stress τ_c must be in direct proportion with the sediment density ρ_s.. Accordingly, sediment density should be identical in field and laboratory experiments in order to avoid issues pertaining to sediment scaling.

2.3.2.4 Flow Intensity V_1 / V_c

Flow intensity (V_1/V_c) has an important physical meaning in that it distinguishes between the expected regime of the incoming flow (clear water or live-bed). The observed variation of the scour depth with respect to a change in flow intensity based upon small-scale laboratory experiments is presented in Figure 2.12.

For a constant flow depth and uniform sediment combination, clear water scour starts to occur at $\mathrm{V_1/V_c} \cong 0.4$ (Melville and Coleman, 2000), and varies linearly with the flow intensity up to the *threshold peak* i.e. $\mathrm{V_1/V_c} \cong 1$ (Melville, 2008). At this peak, the largest possible equilibrium scour hole in the clear water regime is formed for a particular flow depth, assuming uniform bed sediment exists (Benn, 2013).

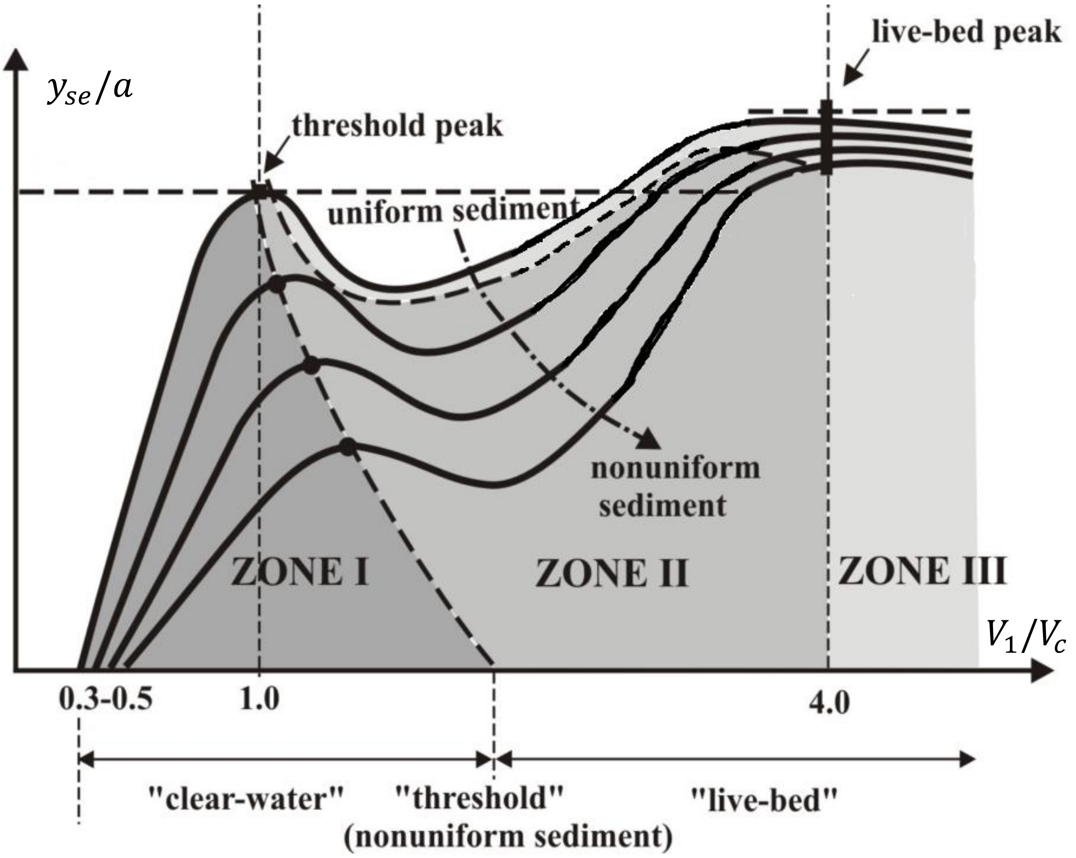

Figure 2.12 Variation of the normalised maximum local scour depth with flow intensity (image adapted from Melville, 2008).

Beyond the threshold peak as the flow velocity increases, dunes form upstream and pass through the scoured region, resulting in the normalised scour depth reducing due to a sediment replenishment (Chiew, 1984; Raudkivi, 1986). Further increase in flow intensity beyond maximum dune height conditions (occurring when y_{se}/a is at a minimum in Zone 2, Figure 2.12) sees a progressive washing out of upstream bed dunes and a resultant increase in y_{se}/a, eventually reaching a second scour depth peak which coincides with a upstream flat-bed stage of sediment transport, known as the *live-bed peak* (Melville, 2008). This peak exceeds the clear-water threshold peak. Beyond this, it is hypothesised that further flow velocity increase leads to the progressive development of anti-dunes, resulting in another gradual decrease in scour depth in proportion with increasing flow intensity (Shen *et al.*, 1966).

For non-uniform sediments (i.e. $\sigma_g > 1.5$), the clear water peak decreases in proportion to an increase in σ_g. The armouring of the scour hole base caused by the presence of larger sediment particles dissipates some of the erosive energy of the scouring down flow, causing a reduction in y_{se}/a. Moreover, the clear water peak occurs at higher flow intensities than during the uniform sediment scenario as non-uniformity increases. Beyond the threshold peak, the value of y_{se}/a loses its dependency on sediment uniformity as it approaches the live-bed peak as the velocities required to reach the live-bed peak ensure a majority of the sediment particles are mobilised.

Hence, the live-bed peak at armoured conditions again exceeds the clear water peak, suggesting that this is also the critical flow condition in non-uniform sediment flow scenarios, albeit at flow rates that far exceed the capabilities of most small-scale hydraulic laboratories. As such, the development of scour upon approach to the clear-water peak is often used as the benchmark for scour studies.

2.3.2.5 Densimetric Froude Number

The effects of sediment density and Froude number can be coupled to form the densimetric Froude number ($V_1 / \sqrt{\frac{\rho_s - \rho}{\rho} g d_{50}}$). Although not explicitly determined through dimensional analysis, many argue that it is the dominant parameter controlling the scour process (Oliveto and Hager, 2002; Kothyari *et al.*, 2007). The parameter essentially compounds the implications of inertial forces and sediment mass r (Khwairakpam *et al.*, 2012) and thus does not provide any additional physical understanding of scour development not already covered above.

2.3.2.6 Side Wall Influence B / y

Excessive flow depths can ultimately influence the naturally-induced flow field. Graf and Altinakar (1998) found that for $\mathrm{B/y} < 3$, the fluvial sides can exert a measurable influence on the velocity distribution, which converts into a three-dimensional flow field stemming transversely from the approach flow direction (Figure 2.13). To achieve uniform approach flow characteristics, the ratio $\mathrm{B/y} > 3$ must hold so that local scour remains strictly unaffected by a three-dimensional flow field (Tafarojnoruz *et al.*, 2010). This parameter is largely unconsidered within predictive formulae as it induces negligible impact on the scour development process (e.g. Melville, 2008).

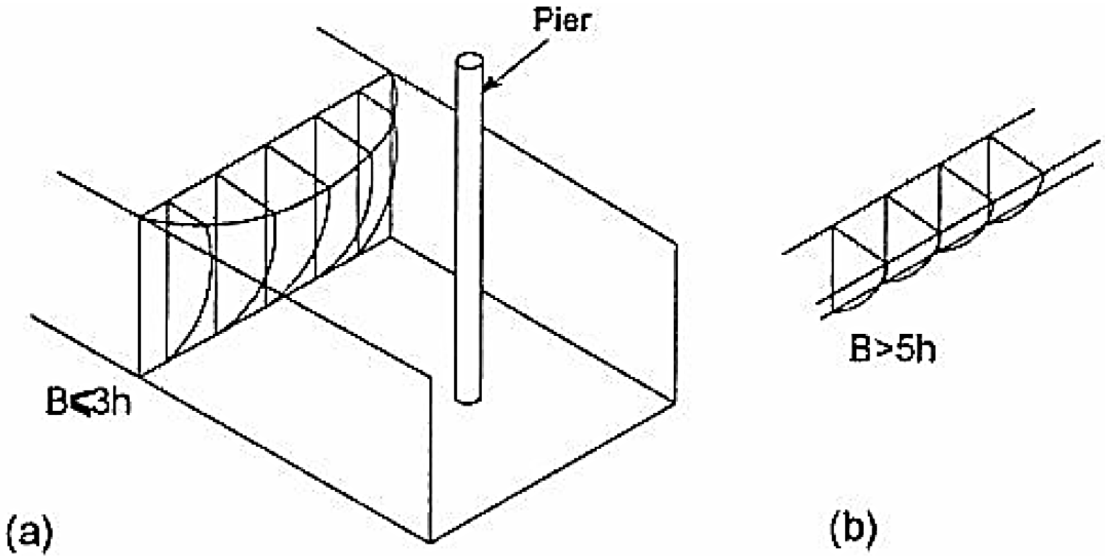

Figure 2.13 Variation of three-dimensional velocity field for (a) B/y<3 and (b) B/y>5 (Tafarojnoruz et al., 2010). Note that, in this figure, the flow depth is defined as h.

2.4 Computing the Equilibrium Depth using Dimensional Analysis

The equilibrium scour depth is considered as the main parameter that ultimately governs the categorisation of scour risk for any structural scour assessment. Thus, having a reliable tool that can compute this length scale quickly and reliably is vital. A vast number of equations aimed at computing the equilibrium local scour depth have been derived, typically by concatenating the functional trends observed for each isolated dimensionless parameter, as according to dimensional analysis in Section 2.3, on the scour development process. The observed trends are subsequently extrapolated from laboratory to field scales using data fitting techniques. The reliability of these tools is well-published (e.g. Deng and Cai (2010), Ettema *et al.* (2011), Sheppard *et al.* (2014)). Here, a short summary of the three leading equations widely accepted for risk assessments and design is presented for completeness.

The Colorado State University (CSU) equation (HEC-18) is adopted by the US Federal Highway Administration (FHWA) for the prediction of scour depth equilibrium (Arneson *et al.*, 2012; Sheppard *et al.*, 2014). The equation as presented in HEC-18 is of the form (Arneson *et al.*, 2012)

$$\frac{y_{se}}{a} = 2K_1K_2K_3\frac{y}{a}^{0.35}\,Fr_1^{0.43},$$

where K_1, K_2, K_3 are correction factors accounting for pier nose shape, angle of attack and bed condition, respectively; and Fr_1 is the upstream Froude number. Originally, the equation was derived from work by Chabert and Engeldinger (1956) and Shen *et al.* (1966) on pier shape effects and the general mechanisms of local pier for simple narrow pier shapes. Correction factors have subsequently been integrated over the years to extend its application to live-bed scour, sediment size and wide pier scenarios. The equation is also being adapted for more complex foundation configurations (Arneson *et al.*, 2012).

For a given flow condition, the Melville (1997) presented the equation

$$y_{se} = K_{ya}K_IK_{d50}K_sK_\theta K_G,$$

where the subscripts of the empirical correction factors K represent: flow depth and pier width (ya), flow intensity and non-uniformity (I), sediment size ($d50$), shape effects (s), pier alignment (θ), and channel geometry (G). The values for each correction factor are derived from envelope curves fitted to empirical datasets of small-scale laboratory work from earlier small-scale scour studies (Data taken from Chabert and Engeldinger, 1956; Laursen and Toch, 1956; Shen *et al.*, 1966; Ettema, 1980; Chiew, 1984; Melville and Raudkivi, 1996). As can be seen, the equation covers the influence of most key dimensional terms using research data where each function has been considered in isolation.

More recently, Sheppard *et al.* (2014) evaluated the reliability of key predictive equations and derived a hybrid equation – incorporating the Melville (1997) and Sheppard and Miller Jr (2006) methods – known as the Sheppard-Melville equation (S/M). Their approach consists of two equations; one each for defining the development behaviour observed for clear water and live bed regimes;

$$\frac{y_{se}}{a} = 2.5 f_1 f_2 f_3, \qquad for\ 0.4 \le \frac{V_1}{V_C} \le 1.0$$

$$\frac{y_{se}}{a} = f_1[2.2\left(\frac{\frac{V_1}{V_C}-1}{\frac{V_1}{V_C}-1}\right) + 2.5 f_3\left(\frac{\frac{V_{lp}}{V_C}-\frac{V_1}{V_C}}{\frac{V_{lp}}{V_C}-1}\right). \qquad for\ 1.0 \le \frac{V_1}{V_C} \le \frac{V_{lp}}{V_C}$$

f_1, f_2, f_3 define the effects of flow field scale (y/a), flow intensity (V_1/V_C) and relative coarseness (a/d_{50}), respectively; V_{lp} denotes the live-bed peak. The equation is based on the three dimensionless parameters perceived by many authors to be critical for describing the physics of the local scour process. Their equation is able to reproduce the functional trends observed from laboratory analysis well, and was extensively validated by Sheppard *et al.* (2014) in comparison with other key predictive equations. The performance of these three formulae for predicting the magnitude of local scour in laboratory and field environments are given in Figure 2.17 and 2.18, respectively.

As both figures show, application of these leading empirical predictive methods results in a significant overestimation of the measured equilibrium scour depth. There are several reasons for this shortcoming. Firstly, data used to derive these predictive tools are obtained mainly from laboratory experiments. As such, the laboratory results suffer from issues scaling to full scale problems (e.g. Ettema *et al.*, 2006) as the real shape of functional relations between the key non-dimensional groups may not reflect full scale behaviours (e.g. changes to the functional relation a/d_{50} provided by large-scale studies). Secondly, measuring the true maximum scour depth at field scales is notoriously difficult as the scour hole that develops predominantly during a storm event is often partly-infilled as the storm recedes. Finally, even where reliable large-scale experiments are available to extend functional relations to field scales, empirical methods are unable to provide a framework for interpreting the data and understanding the physics underpin such behaviour. As such, conservative factors of safety are incorporated in to these predictive models to ensure the risk of scour related failure for detailed design is reduced.

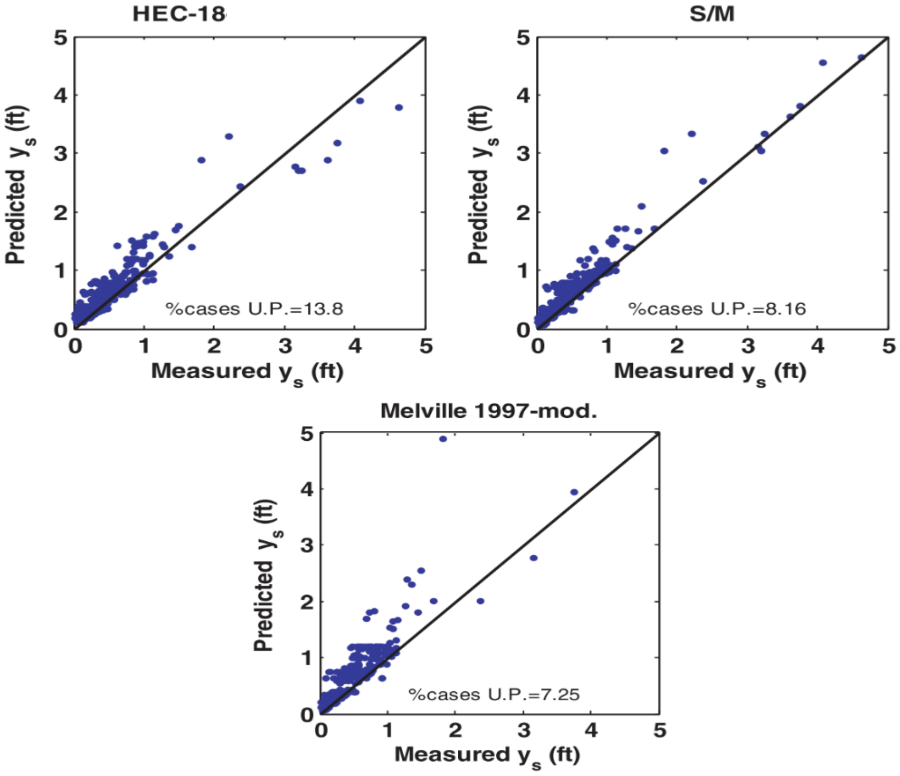

Figure 2.14 Predicted versus measured equilibrium scour depths for three predictive formulae for laboratory data (Taken from Sheppard and Melville, 2011)

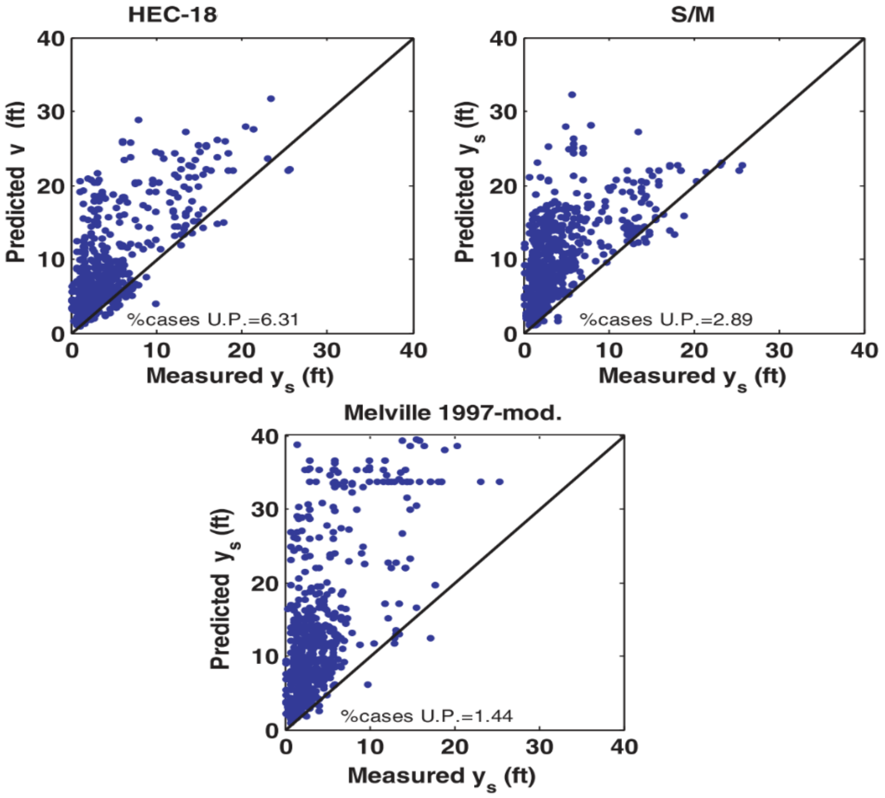

Figure 2.15 Predicted versus measured equilibrium scour depths for the same three predictive formulae for field data. Field data in most cases is unlikely to reflect the equilibrium scour depth. (Taken from Sheppard and Melville, 2011)

2.5 Computing the Equilibrium Depth using a Theoretical Approach

Recently, Manes and Brocchini (2015) developed a predictive equation for the equilibrium scour depth using a more theoretically-based approach. Their theoretical framework is perceived to offer an understanding on the physics of local scour development based on physical arguments, rather than intuitive reasoning through experiment observations. Whilst empirical approaches have provided many important results pertaining to the quantification of local scour, the scaling of prediction frameworks for field application is plagued with uncertainty and conservatism (see Figure 2.15) owing to the physics of scour being poorly integrated within the derived predictive model.

Here, a detailed overview of their framework and validity for equilibrium scour depth predictions is presented. Their approach is derived from the idealisations of Kolmogorov's theory of homogeneous and isotropic turbulence, and the Shields' criterion for sediment entrainment. These aspects are described in turn, before presenting the derivation and final equation of the authors.

2.5.1 Kolmogorov's Theory of Turbulence

For fully developed turbulence, the flow is characterised by an extremely irregular variation of the velocity with time at each point. This irregular motion is analogous to the superposition of turbulent eddies of different sizes; the size depicting the order of magnitude of the distances over which velocity varies appreciably (Landau and Lifshitz, 1959). The largest eddies – of the order of dimensions of the flow field (whose length scale is denoted L) – are characterised by velocities comparable to the variation of the mean velocity (denoted V) which determines the velocity of the turbulent flow. Conversely, smaller eddies participate in the turbulent flow with far smaller length scales, whereby only a relatively small part of the turbulent kinetic energy resides. Thus the variation of velocity in a turbulent flow is described as two-fold (Landau and Lifshitz, 1959); over large distances the variation of the flow velocity is determined by large scale variations (i.e. comparable with V), whilst for smaller distances (relative to L) the velocity variation is small as it is determined by the small scale eddies.

The Reynolds number (Re), which quantifies the ratio between inertial and viscous effects, can be used to qualitatively ascribe turbulent eddy scales. For a given turbulent eddy; whose order of magnitude of size and velocity are l and u_l, respectively; the Reynolds number is given by $u_l l/v$. For large Reynolds numbers which characterises the largest eddies, the viscosity is negligible and therefore there exists negligible depreciation of energy. Thus, a dissipation of energy only occurs when the viscosity becomes important which exists at the smallest characteristic eddy scales (whose length scale is termed the Kolmogorov length scale, η) where the Reynolds number approaches unity (Landau and Lifshitz, 1959). From these idealisations Kolmogorov (1941) presented his paradigm of turbulence; turbulent kinetic energy (TKE), which is introduced at a continuous rate into the flow at scales commensurate of the largest eddies, cascades as a continuous flow of energy from the large to small eddies until the flow of energy begins to dissipate only at the smallest eddy length scales (comparable with η) due to viscosity[4]. Therefore, physical quantities pertaining to eddies of size $l \gg \eta$ are viscous-independent. The continuous rate of turbulent kinetic energy (ε) dissipation scales with the rate of energy production, owing to the principle of energy conservation. Thus, although dissipation ultimately occurs due to viscosity, the order of magnitude of ε can be determined from characteristic length scale eddies where the energy is introduced (i.e. at eddy scales L). From dimensional considerations, Kolmogorov (1941) identified that $\varepsilon \sim V^3/L$, which quantifies the rate of turbulent energy dissipation.

Fundamental eddies of size L are of the order of magnitude of the flow field, and thus are affected by the absolute motion of the flow region as a whole and the presence of solid boundary surfaces. At sufficiently large Reynolds numbers, therein lies a range of eddy scales which are large relative to the smallest eddies where energy dissipation occurs ($l \gg \eta$) but small compared to the fundamental largest scales ($l \ll L$). At these length scales, the properties of the turbulence are described as local (i.e. small-scale turbulence relative to the flow field scale). Kolmogorov (1941) used this analogy to hypothesise that within this range of scales (i.e. $\eta \ll \ l \ll L$), the characteristic eddies of size l take a universal form that can be statistically described by ε alone; this is commonly referred to as the *inertial sub-range*. This description insinuates that the properties of turbulence within this range exhibit a homogeneous and isotropic statistical distribution. Strictly speaking, a flow is considered homogeneous and isotropic if all values of momentum tensors remain unchanged within a spatial co-ordinate system (Barenblatt, 1996). To be considered homogeneous and isotropic, properties of the flow at these local length scales must be independent of the dimensions of the flow as a whole (i.e. L and V), whilst energy cascading occurs inviscidly as $l \gg \eta$. Thus, the variation of the turbulent velocity over a distance l (i.e. u_l) can only be determined from parameters of the eddy and ε, which from dimensional considerations is

$$u_l \sim (\varepsilon l)^{1/3}. \tag{2.4}$$

---

[4] Dissipation at the smallest length scales occurs because at the smallest scales the turbulent viscous stresses are able to work against further fluid element deformation (i.e. eddies splitting into smaller eddies) due to the turbulent strain rate (Saddoughi and Veeravalli, 1994).

This is *Kolmogorov and Obukhov's law*. From Landau and Lifshitz (1959), the velocity variation at a given point over a time interval t (i.e. u_t), which characterises the turnover time for an eddy of size l within the inertial range, is short compared to the time $T \sim L/V_1$ which characterises the flow field. Assuming a net mean flow field prevails (i.e. the velocity fluctuation at a given point, $u_t{}'$, is small relative to u_t), fluid particles are displaced by a distance $V_1 t$ over that turnover time and thus, $u_t \sim (\varepsilon V_1 t)^{1/3}$. Application of Kolmogorov and Obukhov's law ($\varepsilon \sim V^3/L$) finally produces

$$\begin{gathered} u_l \sim V(l/L)^{1/3}, \\ u_t \sim V(t/T)^{1/3}. \end{gathered} \tag{2.5}$$

Kolmogorov's scaling laws given in Eq. (2.5) illustrate the self-similarity property of local turbulence (eddies in the range $\eta \ll l \ll L$); that small-scale turbulent characteristics are universal apart from the scale of length and time. These scaling laws are important results about the nature of local turbulence but their application is strictly valid providing that the local properties of the fully developed flow are homogeneous and isotropic.

2.5.2 Shields' Theory of Sediment Entrainment

Shields (1936) developed a physical explanation for the required conditions of incipient motion of a uniform sediment. By deriving an expression for the shear stress exerted on the sediment surface by the flow (τ), and for the force required to induce sediment motion; Shields identified that at the point of incipient motion, the relationship between the two forces is defined by a universal function of the ratio between the grain size to the thickness of the viscous sub-layer (i.e. d_{50}/δ, where δ is the thickness of the viscous sub-layer which is of the order of magnitude of the Kolmogorov length scale, η). Through plotting the critical dimensionless shear stress ($\tau_c/(\rho_s - \rho)gd_{50}$, where τ_c is the critical shear stress) as a function of the boundary Reynolds number ($U_* d_{50}/\upsilon$, which is analogous to d_{50}/η) using an extensive dataset of particle entrainment studies, the relationship forms a single defined trend. This trend is known as the *Shields' criterion* for sediment entrainment (Figure 2.16).

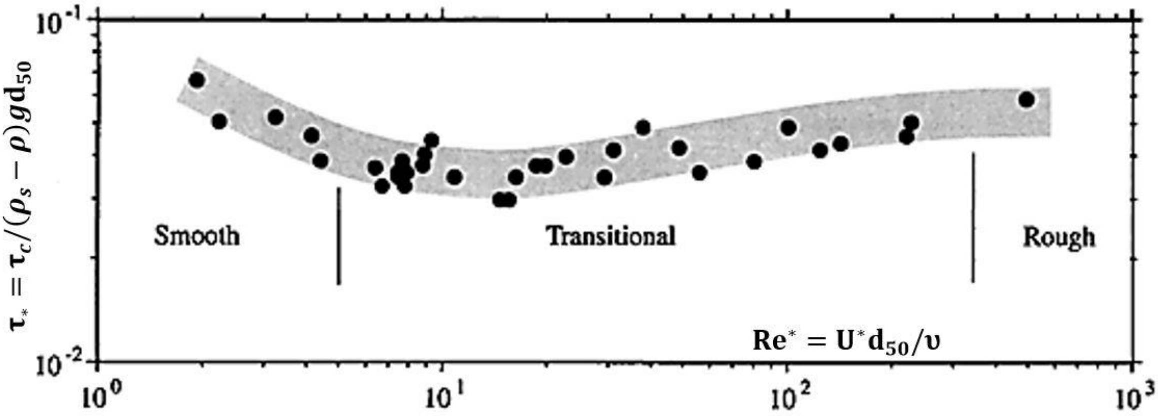

Figure 2.16 Shields criterion for incipient motion (Buffington and Montgomery, 1997).

This Shields criterion describes the initiation of sediment motion based on the mechanism of bulk sediment mobilisation, rather than the isolated erosion of individual particles through rolling or lifting (Miedema, 2010; Dey and Ali, 2017). Data points which lie above the Shields envelope indicate sediment mobilisation ($\tau > \tau_c$), whilst below the curve negligible erosion occurs ($\tau < \tau_c$). The Shields curve has been subjected to extensive validation using sediments of varying geometry and density, and therefore is seen to adequately depict the unique variability of the critical shear stress with flow regime (i.e. hydraulically smooth, transitionally-rough, or fully turbulent flows).

For *hydraulically smooth* boundaries (where $d_{50} < \delta$) the surface acts as a smooth boundary as no additional energy loss is caused by the presence of the sediment roughness.. As the flow regime moves into the *transitionally smooth* flow regime (where d_{50} is of the same order of magnitude as the viscous sub-layer thickness i.e. $d_{50} \sim \delta$), sediment particles protruding out above the viscous boundary layer initiate the development of eddies and a concentration of bed shearing in their location. Further increase in the boundary Reynolds number (where $d_{50} > \delta$) gradually reduces the dependency of sediment entrainment to viscosity effects, as the viscous sub-layer thickness becomes increasingly negligible; this flow regime is termed *transitionally rough*. Flow in this regime is characterised almost uniquely by the development of turbulent eddies from bed sediment protrusions. The transition between smooth and rough coincides with a minimum of the Shields criterion band. The slight increase in Shields parameter (y-axis) beyond the minimum point was described by Shields (1936) and Vanoni (1964) as being due to the resistance coefficient of the sediment decreasing with an increasing Reynolds number, owing to low velocity zones that prevail in the region of the protruding roughness elements that changes the resistance of the grain in the near-wall region.

As the ratio between the sediment diameter and viscous sub-layer thickness increases substantially further (i.e. $d_{50} \gg \delta$), a *fully-rough* regime prevails which results in the shearing force of the flow exerts a constant influence on the sediment bed independent of the flow characteristics. Thus, within this regime the critical shear stress exhibits an independency on the boundary Reynolds number and the non-dimensional shear stress saturates to a constant;

$$\tau_c/(\rho_s - \rho)gd_{50} = const. \tag{2.6}$$

2.5.3 Manes and Brocchini Approach to Scour

Manes and Brocchini (2015) apply the results of Shields' criterion for sediment entrainment and Kolmogorov's theory of turbulence to derive a formula for predicting the local scour depth of equilibrium from a physical rather than empirical basis. The basis of their work stems from that by Gioia and Bombardelli (2002), Gioia and Bombardelli (2005) and Bombardelli and Gioia (2006) in applying the phenomenology of turbulence for deriving classical hydraulic equations using physical reasoning.

Local scour involves the removal of sediment particles from around the pier base due to bed shear stresses which exceed the threshold value of the bed sediment. Clear-water equilibrium is assumed to be reached when the turbulent shear stress acting at the point of maximum scour depth (τ) and the critical shear stress of the sediment (τ_c) are equivalent i.e. $\tau \cong \tau_c$. The point of reaching equilibrium is assumed to be equivalent to Shields' criterion for sediment entrainment. Assuming that the flow within the scour hole is in the fully-rough regime (i.e. Eq. (2.6)), clear-water equilibrium is independent of viscosity and can be simply expressed as

$$\tau \approx \tau_c \sim (\rho_s - \rho)gd_{50}. \tag{2.7}$$

The shear stress (τ) acts over the wetted surface A_S and is heavily influenced by momentum transfer occurring due to the interaction of different size turbulent eddies impinging the surface of the scour hole (shown in Figure 2.17). Directly above the viscous sub-layer the tangential flow velocity to A_S scales as V, the characteristic velocity of the largest energetic eddies forming within the scour hole (presumed to characterise the horseshoe vortex itself). This means that the incoming fluid carries a high horizontal momentum per unit volume of the order $\sim\rho V$ (Gioia and Chakraborty, 2006); eddies of smaller length scales produce negligible characteristic velocities in comparison, as according to Kolmogorov's scaling law (Eq. (2.5)). Momentum transfer per unit volume below the wetted surface A_S defined in Figure 2.17 is comparably lower due to substantially lower flow velocities due to the viscous action of the viscous sub-layer and considerable energy dissipation that occurs between adjacent sediment pores. The rate of momentum transfer across the boundary A_S is determined by the normal velocity component of the eddy w' (Gioia and Bombardelli, 2002). The vorticity of eddies that straddle either side of the wetted surface A_S impose momentum transfer across its boundary; with fluid particles of high horizontal momentum being transferred below this boundary, whilst simultaneously fluid of negligible horizontal momentum is transported above. Thus, the shear stress (τ) scales as $\tau \sim \rho V w'$.

From Gioia and Bombardelli (2002); for a uniform top layer of sediment the normal velocity component $\overline{w'}$ acting across A_S is dominated by eddies of size equivalent to the sediment particle diameter d_{50} (Figure 2.17), owing to geometric considerations and Kolmogorov and Obukhov's law. Thus, it can be summarised that the normal fluctuating velocity component (w') is dominated by u_{d50} (characteristic velocity of eddies scaling with d_{50}), and therefore as $\tau \sim \rho V u_{d50}$. By hypothesising that the sediment diameter belongs in the inertial range of scales (i.e. $\eta \ll d_{50} \ll L$), application of Kolmogorov's scaling law (Eq. (2.5)) gives

$$\tau \sim \rho V^2 \left(\frac{d_{50}}{L}\right)^{1/3}, \tag{2.8}$$

from which a scaling law is required to define the characteristic length (L) and velocity (V) scales of the largest eddies.

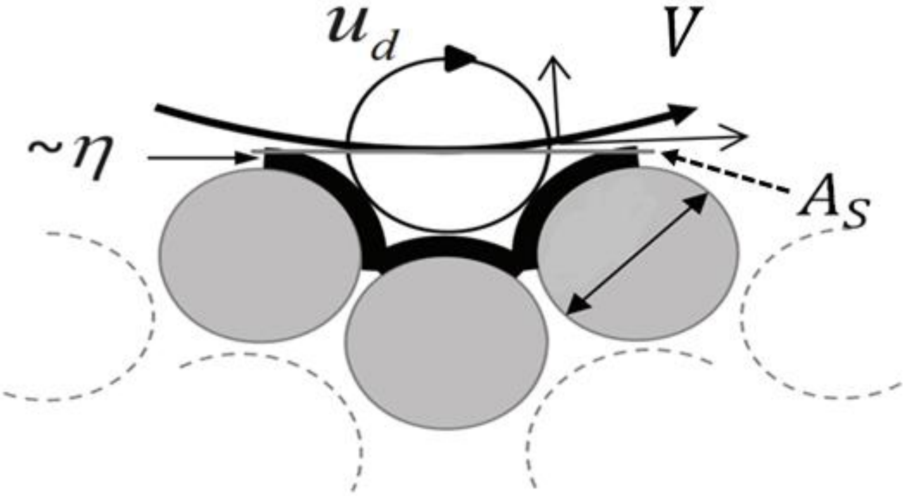

Figure 2.17 The interaction of large-scale eddies and eddies of size d_{50} with the sediment bed (Manes and Brocchini, 2015). A_S denotes the wetted surface over which the bed shear stress acts, which is used to quantify local momentum transfer in the near-bed region.

Their scaling is derived from Kolmogorov and Obukhov's law and from energy principles. Manes and Brocchini (2015) hypothesised that the rate of TKE production (i.e. ϵ) can be estimated as the ratio between the power associated with the horseshoe vortex (P) and the mass of fluid contained with its characteristic volume i.e. $\epsilon \sim P/M$. From considering the role of the HS vortex in scour development, its power is estimated as the work of a drag force (F_D) acting on the face of the pier exposed to scour. Whilst power is assumed to be governed by the drag force of the large-scale eddies (i.e. the HVS) and is computed using[5] $P = F_D V_{SH}$, where[6]

$$F_D = \frac{1}{2}\rho C_D a L {V_{SH}}^2 \sim \frac{1}{2}\rho C_D a L {V_1}^2,$$

where, C_D is the piers coefficient of drag, the mass of the characteristic large-scale following dimensional considerations is assumed to follow the similarity scaling function $M \sim \rho L^3$. Accordingly, a scaling law for V is derived of the form

$$V \sim V_1 \left(\frac{C_d a}{L}\right)^{1/3} \tag{2.9}$$

which, in turn, enables the turbulent shear stress to be defined as

$$\tau \sim \rho V^2 \left(\frac{d_{50}}{L}\right)^{1/3} \sim \rho {V_1}^2 \left(\frac{C_D a}{L}\right)^{2/3} \left(\frac{d_{50}}{L}\right)^{1/3}. \tag{2.10}$$

By hypothesising that the horseshow vortex (which is representative of large scale turbulence) is fully buried within the scour hole, L scales as the scour depth itself (Manes and Brocchini, 2015), at hence at equilibrium conditions $L \sim y_{se}$. At equilibrium conditions, the critical shear stress can be approximated by Eq. (2.7)so that the condition for equilibrium scour $\tau \cong \tau_c$ is defined by

$$y_{se} \sim \frac{\rho}{(\rho_s - \rho)} \frac{{V_1}^2}{g} (C_D)^{2/3} \left(\frac{a}{d_{50}}\right)^{2/3}. \tag{2.11}$$

Eq. (2.11) is the final result of Manes and Brocchini (2015) which represents a scaling function for the clear-water equilibrium scour depth providing the bed sediment diameter lies within the inertial range (i.e. $\eta \ll d_{50} \ll y_{se}$). The order of magnitude of the bulk Kolmogorov length scale, η, is estimated as $\eta \sim (\upsilon^3/\epsilon)^{1/4}$. By assuming that the rate of TKE production scales as $\epsilon \sim P/M$ as before, and the formation of P is that of a drag force, the Kolmogorov length scale can be estimated as

$$\eta \sim \left(\frac{\upsilon^3 L}{C_D V_1^3}\right)^{1/4}. \tag{2.12}$$

At equilibrium, $L \sim y_{se} \cong a$ (e.g. Lee and Sturm, 2009). Thus, the limits of applicability convert to

---

[5] V_{SH} is assumed to scales with the magnitude of the approach flow velocity and therefore $V_{SH} \sim V_1$.

[6] C_D is the foundations' coefficient of drag, and aL is the surface area of the cylinder subject to drag which results from the presence of the horseshoe vortex.

$$\left(\frac{\upsilon^3 a}{C_D V_1^3}\right)^{1/4} \ll d_{50} \ll a,$$

which after some algebra gives

$$1 \ll \frac{a}{d_{50}} \ll {Re_P}^{3/4}. \qquad (2.13)$$

The upper and lower bounds in this form are subjective to interpretation by the user. Thus by using experimental data pertaining to orders of magnitude change in the relative coarseness, Manes & Brocchini (2015) revised the lower and upper bounds given in Eq. (2.13). The lower bound was increased to account for the poor scale separation between the sediment diameter and the large scale eddies (which scale as $L \sim y_{se} \sim a$) as $a/d_{50} \to 1$ which promotes enhanced energy dissipation from the roughness elements and a reduced scour depth. The upper limit was reduced by hypothesising that for $d_{50}/\eta < 5$, the sediment diameter is comparable to the thickness of the viscous sublayer (a common hypothesis, e.g. Pope, 2000) and thus turbulent fluctuations become predominantly viscous, invalidating the applicability of Kolmogorov's turbulence theory. The proposed limits of validity are hence

$$20 < \frac{a}{d_{50}} < 0.2{Re_P}^{3/4}. \qquad (2.14)$$

This is the final result of Manes and Brocchini (2015). Eq. (2.11) which is valid for fully-rough flow conditions around cylindrical piers provided that a/d_{50} lies within the bounds defined by Eq. (2.14).

2.5.4 Experimental Validation

Successful validation of the proposed scaling $y_{se} g/V_1^2 \sim (a/d_{50})^{2/3}$ was achieved using an extensive series of experimental laboratory data (Figure 2.18). Manes and Brocchini (2015) stipulate that the observed variability of the data around the 2/3 power law is associated with inconsistencies in the timescale to clear-water equilibrium used by each of the researchers, which can vary the apparent equilibrium scour depth by as much as 20% (Melville and Chiew, 1999; Lança *et al.*, 2013). Separate analysis of each dataset was thus performed which identified a striking agreement between the proposed theory and experiments through variation of the singular empirical constant (Figure 2.19). The authors hence concluded that the proposed theoretical approach provides a vital insight into deriving a well-rounded physical understanding of local scouring around structures, and can be used to effectively compute the magnitude of the equilibrium local scour depth for a given flow condition provided the limits of applicability defined in Eq. (2.14) are satisfied.

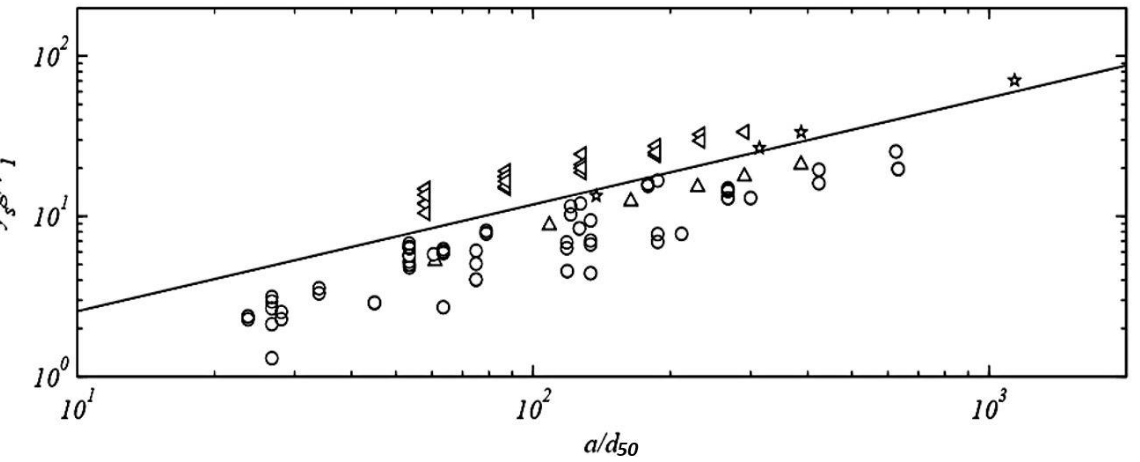

Figure 2.18 Experiment data contained within the limits defined by Eq. (2.14)*; stars, Sheppard et al. (2004); circles, Ettema (1980); up-triangles, (Ettema et al., 2006); left-triangles, Lança et al. (2013). Solid line denotes a 2/3 Power Law (Manes and Brocchini, 2015).*

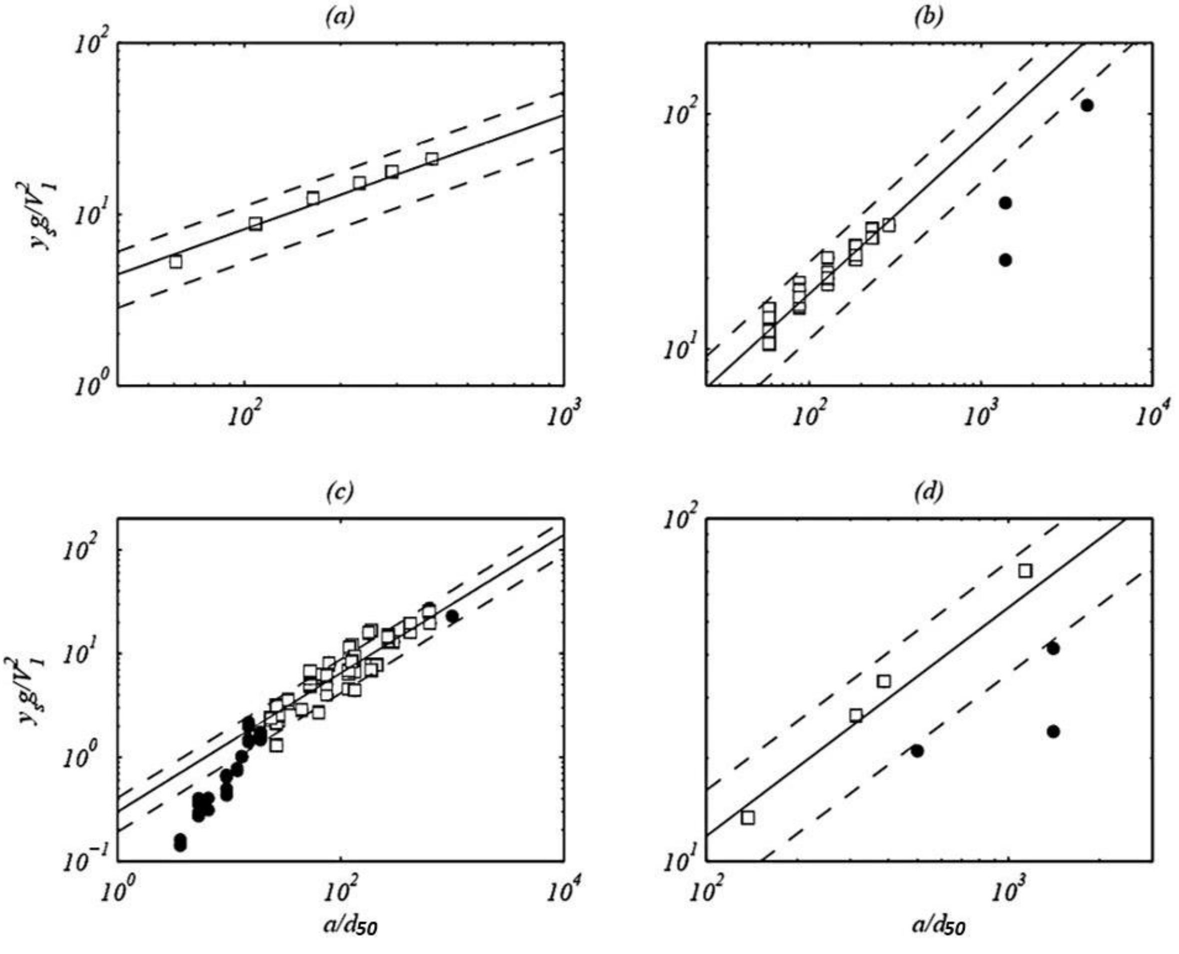

Figure 2.19 Variation of Non-dimensional scour depths with relative coarseness using data from; (a) Ettema et al., (2006); (b) Lanca et al., (2013); (c) Ettema (1980); and (d) Sheppard et al. (2004). Solid and dashed lines denote a 2/3 Power Law and the 36% uncertainty due to τ_c and τ (Manes and Brocchini, 2015). The white squares and black circles refer to values of a/d_{50} that are within and outside the limited imposed by Eq. (2.14).

2.5.4.1 Idealisation of a Characteristic Eddy

It must be noted that the theoretical derivation presented by Manes & Brocchini (2015) idealises the velocity terms of the Reynolds stress, that in turn defines the order of magnitude of the acting shear stress, can be broadly determined by the dominance of two characteristic eddies (of length scales L and d_{50}). Arguments in support of the assumptions made using Kolmogorov's scaling law have been presented by those who originated the approach (e.g. Gioia and Bombardelli, 2005). However the application of Kolmogorov's scaling laws, although a plausible assumption (Moser, 1994; Manes and Brocchini, 2015), rarely holds true for wall-bounded flows such as within a scour hole where the assumption of homogeneity and isotropy break down. Bonetti *et al.* (2017) present an alternative method involving the incorporation of a co-spectral budget model that moves away from the simplifications of the current theoretical approach. However, the experimental validation of the theory (Section 2.5.4) shows the equilibrium scour depth can be predicted using the existing equation with good accuracy. Although the assumption of a single characteristic eddy dominating the quantification of the normal fluctuating velocity represents an idealisation, this is very applicable providing the top layer of sediment is of uniform size.

2.6 Scour Hole Geometry

As shown in the previous sections, the dependency and development of the maximum scour depth with parameters defined in Eq. (2.1) is well researched. However, a more general description of the scour hole geometry both at equilibrium and during its evolution in time as a function of the same parameters is equally important.

Very few researchers have attempted to measure the scour hole development with time directly. Yanmaz and Altinbilek (1991) pioneered scour footprint mapping with time by stopping the flume incrementally to perform measurements of the scoured profile using a gauge, before flattening the surface and restarting the experiment. For early scour development, they found the localised hole can be well modelled by the frustum of a cone, a commonly employed assumption for idealising the scour footprints evolving shape. However, draining and restarting is significantly invasive on the natural scour generation, and can represent different scour processes if the sediment bed is inconsistently compacted (Buffington and Montgomery, 1997). Although an array of gauges has been used to measure scour evolution around spur dikes for deriving a power function for the scoured volume with time (Kuhnle *et al.*, 1999), the time taken to measure the three-dimensional geometry is ineffective for snapshot observations of the bed profile.

Positioning the measurement technique outside the remits of the scour hole flow field can avoid intrusion. Link and Zanke (2004) developed a laser distance sensor to operate inside a transparent

Plexiglas test pier and perform sweeping scans of the surrounding bed in large radial increments. They found that the maximum scour depth develops in direct proportion with the maximum scour hole radius (Figure 2.20), and provided a predictive model for the scour volume as a function of y_{se}. Using the same technique, Link *et al.* (2008b) extended observations of linear scaling between the maximum scour depth with the scour radius for several azimuthal half-planes around the scour hole. This measurement technique was also later applied by the same authors (in Link, 2008) where they observed a stabilisation in the development of the scour volume about significant development that they attributed to a decay in erosive intensity (Figure 2.21).

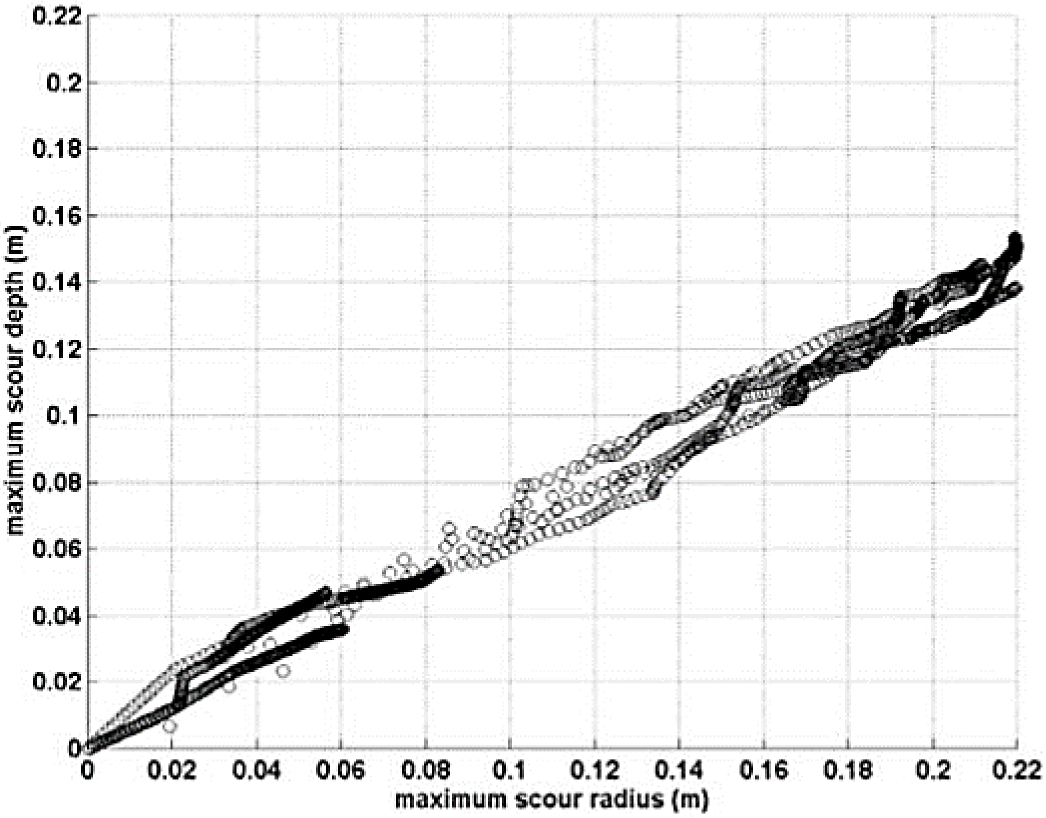

Figure 2.20 Variation of maximum scour depth with maximum scour radius (Taken from Link and Zanke, 2004).

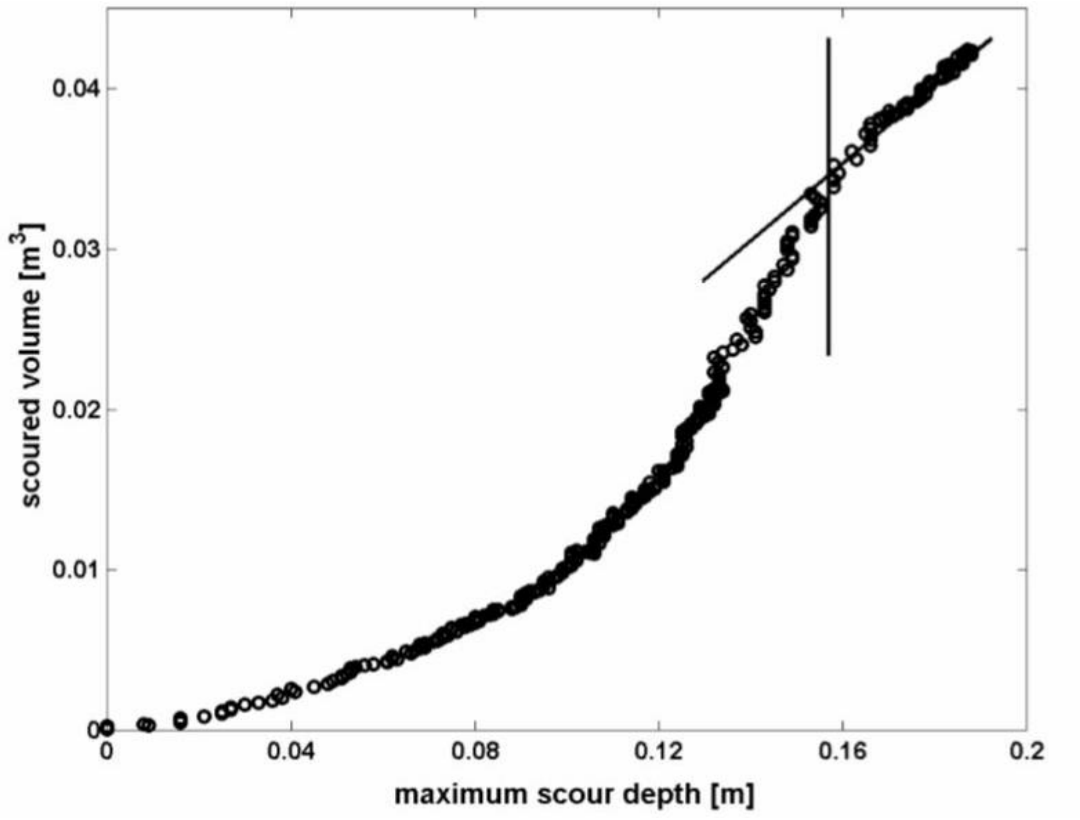

Figure 2.21 Variation of maximum scour volume as a function of maximum scour depth (Taken from Link and Zanke, 2004).

However, quasi-dynamic measurements of the scouring profile were only possible by configuring the laser profiler to perform only a few radial rotations around the circumference of the test pier. Whilst this technique is suitable for measuring vertical profiles of the scoured bed and therefore can be used to map out the major boundaries of the scour hole (Figure 2.20), the interpolated output surface is susceptible to overlooking or simplifying important topographical details as each coarse data grid output is the resultant of high post-experiment interpolation. Evidence of an inflection point in the scour development process (Figure 2.21) therefore requires validation.

Photogrammetry is an alternative physically non-invasive option that has been tested with promising results (Sumer *et al.*, 2013). However, the method has a time-consuming post-processing requirement which yields results that can be inaccurate due to difficulties with including a modelling correction for refraction between air and water. A major drawback using this method is also that scour generation is not measurable while the flume is running (Porter *et al.*, 2014).

Echo-sounders (*sonar*) are extensively used to model the bathymetry of watercourses in the field, and are often fixed to high-risk structures for the monitoring and alerting of critical bed levels. As such, they provide a plausible option for equivalent laboratory monitoring. However, echo-sounders (sonar) produce direct data inaccuracies as the transverse footprint of the acoustic beam enlarges with increasing beam inclination, resulting in measured bed elevations far away from the sonar being averaged over an increasing transverse footprint area.

Porter *et al.* (2014) addressed these inaccuracies by fitting a 1MHz single-beam echo-sounder to a transverse motorised platform that could manoeuvre the device in two-dimensions for full coverage of the bed and produced 3D imagery of the scoured surface. However, owing to the short measuring time at each position (in an attempt to take a snapshot of the developing bed), the accuracy of the echo-sounder using this single-beam technique provided a poor representation of the scoured bed profile. Moreover, an acoustic transducer requires constant submersion which is intrusive to the scour process if used or left in close vicinity to the pier, whilst the range resolution of the sonar is restricted by its beam angle which increases in physical size as range resolution is enhanced (Atherton, 2011). Furthermore, two-directional mobilisation platforms such as those used by Porter *et al.* (2014) restrict the 3D profile snapshots of early scour development being captured due to total measurement duration.

2.7 Summary

Bridges are susceptible to three main types of scour; general, contraction and local. Although not exclusive, the risk of failure from localised scour is the main reason for bridge failures worldwide. Due to its complexity, advancements in our understanding of factors which drive the local scour process have been predominantly made using small-scale empirical methods. In the past, the focus has been on investigating and quantifying the development of the equilibrium scour depth, as this length scale is critical for categorising the structural risk in relation to the depth of the foundation. Thus, having a reliable method that can compute this length scale for a given flood-recurrence interval is vital for risk assessing (Tubaldi *et al.*, 2017).

As shown in this literature review, the dependency and development of the maximum scour depth has been extensively published. However, a more general description of the scour hole geometry both at equilibrium and during its evolution in time is a less focused topic that is also of equal importance. Although techniques have been developed for the purpose of measuring the scour hole geometry as it develops with time, the measurement invasiveness and accuracy of these techniques owing to the need of measuring the scour hole geometry in a quasi-dynamic state is questionable. As such, these concerns have limited our understanding of scour geometry to isolating the equilibrium scoured area and volume using high-density gauge measurements of the drained equilibrium scour surface profile (Khwairakpam *et al.*, 2012; Das *et al.*, 2014a; Das *et al.*, 2014c).

Within this context, this thesis addresses the design and implementation of an experimental methodology that allows for real time measurements of the scour geometry to be made in a quasi-non-invasive manner. The framework by Manes and Brocchini (2015), which provides a theoretical approach to better understand the physics of the local scouring process, represents an experimentally-validated tool that can be used to interpret and understand the results. Results pertaining to the scour hole geometry will be put into the context of assessing scour risk.

Chapter 3: Laboratory Methodology

3.1 Introduction

Measuring the geometry of a developing local scour hole requires an ability to measure the scour development in three-dimensions with time. As discussed in Section 2.6, designing a technique that can measure the development process reliably is challenging due to difficulties of measuring the bed surface in a quasi-dynamic state. This Chapter presents a novel approach to the problem by trialling a new sonar profiling technique for laboratory analysis. A full account of the equipment and associated experimental procedure is given, along with a summary and rationale of the experiment trials carried out.

3.2 Experimental Equipment and Set-Up

3.2.1 Experimental Set-Up

All scour experiments were performed in the controlled environment of a hydraulic flume available at the University of Southampton's Science Park in Chilworth (Figure 3.1a). The internal flume is a 23m long re-circulating hydraulic channel, spanning 1.40m transversely between glass side walls with a working depth of 0.60m. The flume discharge volume is controlled by manually adjusting three independent pump valves (Figure 3.1b). Water is pumped from the flumes' storage sump and fed into the flume through two inlet pumps (Figure 3.1c). The flume water depth is adjusted by a downstream tailgate weir (Figure 3.1d), beyond which overtopping water is recollected in the storage sump and recirculated back through the system.

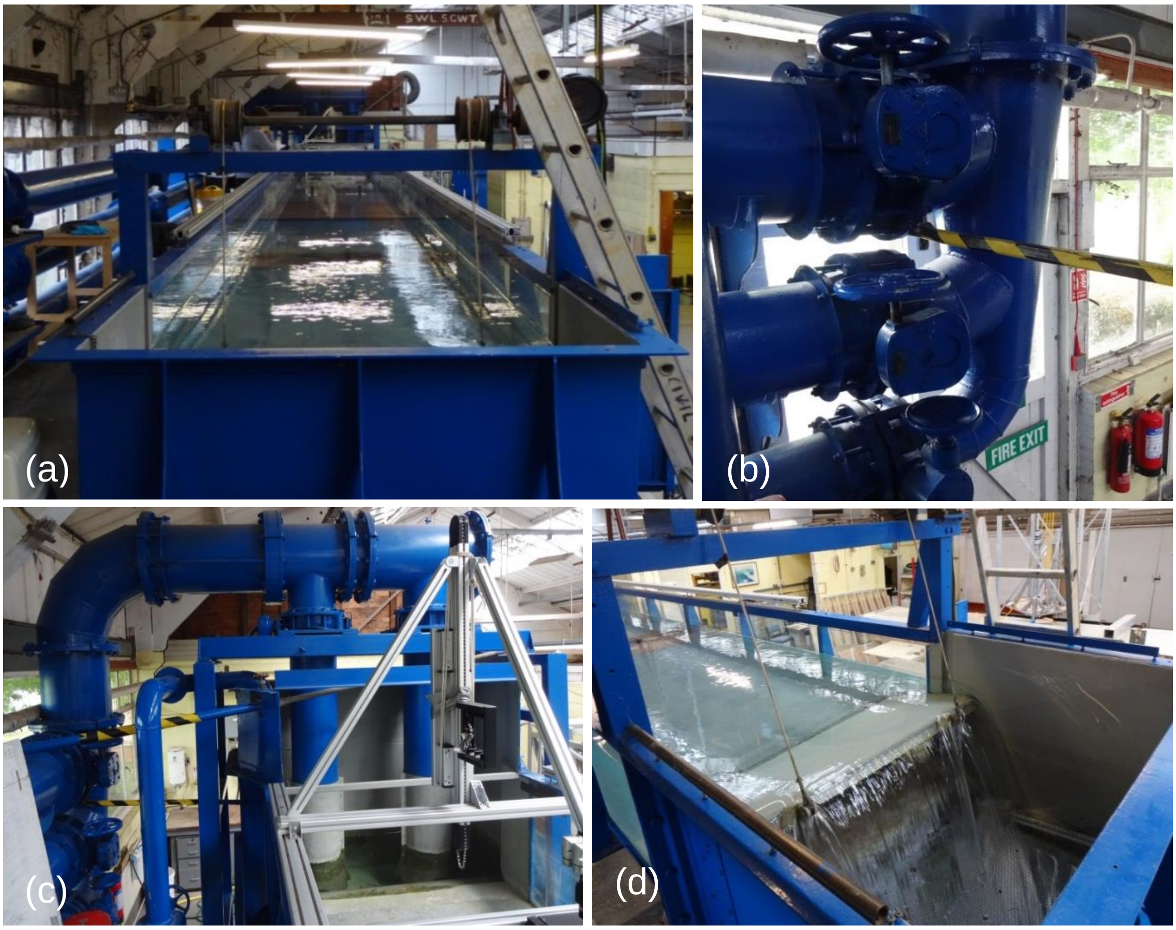

Figure 3.1 (a) Internal flume at Chilworth science park, University of Southampton, (b) Discharge control valves, (c) Flume inlet system, and (d) Downstream weir tailgate.

A structural platform was constructed inside the flume to provide a sufficiently-deep sediment box for investigating scour. The platform upstream of the sediment box consisted of elevating the flume base by 0.25m using a 1:8 slope approach flow ramp near the inlet which was preceded by a 5m span of flooring at constant elevation (referred to as false flooring from here on in) (Figure 3.2). The false flooring was covered with a single layer of uniform coarse gravel deposits (mean thickness = 35mm) to promote fully-developed turbulent flow conditions upon approach to the sediment box test area (see Section 3.3.1 for further details on flow conditioning). The fixed false flooring top further ensured that measurements of localised scour in the test area were not supplemented by general upstream bed scour degradation.

Figure 3.2 Constructed false flooring viewed from upstream.

A 1.5m-long recess area located immediately downstream of the false flooring housed the test sediment. The test area was preceded by a 2m length of false flooring to ensure natural development of the scour hole deposition mound[7]. Sediment transported beyond the deposition mound was stopped from leaving the flume vicinity, entering the storage sump and being recirculated through the system by a downstream fine-mesh sediment trap. A design schematic of the flooring is given in Figure 3.3. Structural drawings of the false flooring and sediment trap are given in Appendix A.

---

[7] Downstream flooring also minimised backwater effects and energy losses that would otherwise be induced by rapidly-varied flow conditions if a return to the natural flume bed level was installed immediately downstream of the recess box.

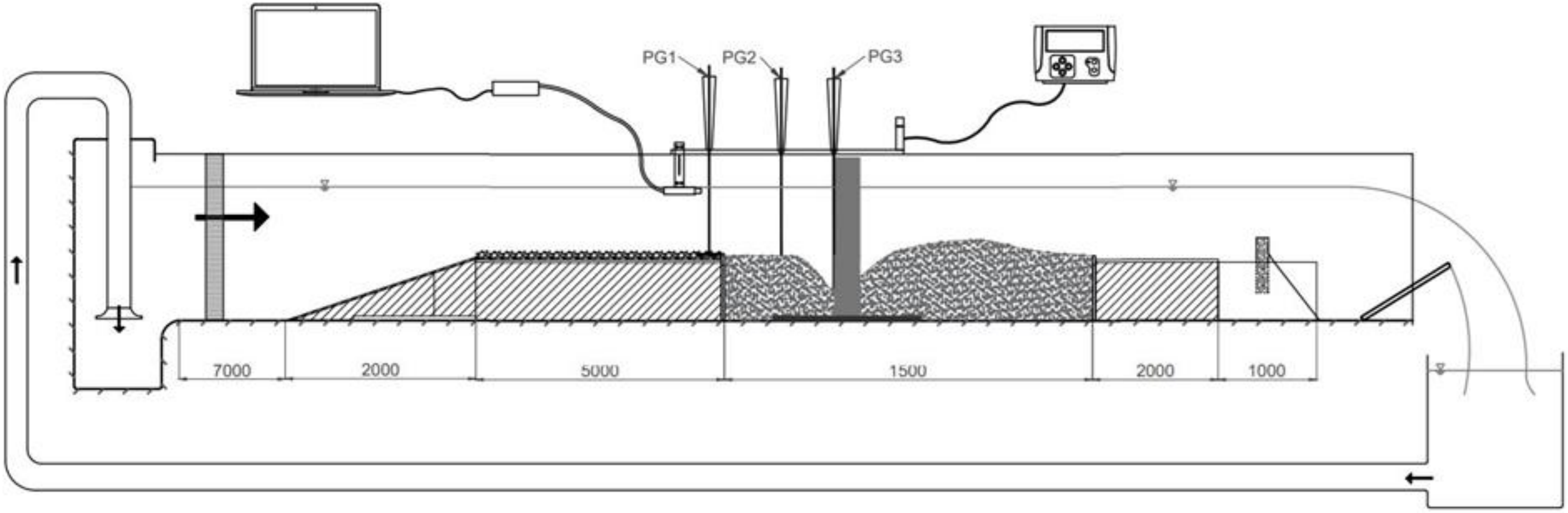

Figure 3.3 Overview of the laboratory experiment setup. PG1, PG2 and PG3 reflect point gauges that were used to measure the bed elevation at key locations. All dimensions stated are in millimetres. Drawing is not to scale

3.2.2 Scour Hole Surface Mapping

Real-time measurements of the scour hole profile were made using a Mini Pipe Profiling Sonar[8] (Figure 3.4); an underwater acoustic swath[9] profiler typically used for the profiling of pipeline interiors. A cable connected to the sonar provides power and the import/export of information to a control box. Exported sonar data is visualised in the sonars Pipe Profiler E software package using an Ethernet connection linking the control box to a remote PC (Figure 3.3).

Figure 3.4 Mini Pipe Profiling Sonar Device (Model 2512).

The sonar operates at an acoustic frequency of 2MHz and transmits the acoustic signal at a 2µs pulse length. The signal transmission produces a high transverse cell resolution of 0.63mm at zero beam inclination (Table 3.1) for the maximum expected acoustic range[10] (~0.42m); sufficiently detailed for visualising fine sediment. The effect of inclination on measurement accuracy is assessed in Section 4.3. The equivalent vertical range resolution[11] of the sonar device is ~1.5mm.

Table 3.1 Profiler resolution at high range setting. Velocity of sound in water is 1500 m/s.

Acoustic Range (m)	Resolution per cell (mm)
0.25	0.375
0.30	0.450
0.35	0.525
0.40	0.600
0.45	0.675
0.50	0.750

---

[8] Mini Pipe Profiler Sonar: Model 2512 USB Underwater Unit from Marine Electronics, Guernsey, UK. The unit is 178mm in length and 50mm in diameter; and mass of 0.4kg (measured in air).

[9] The scanning angle programmed to be covered by the sonar transducer in one steady sweeping motion.

[10] Based on a 101mm diameter pier with maximum scour depth $y_{se} = 2.0a$ (Melville and Coleman, 2000).

[11] Calculated based on the equation: Range Resolution = Pulse length x Speed of Sound/2 (Atherton, 2011)

The sonar is fitted with a small circular transducer element, enclosed within the hermetically sealed oil-filled nose cone of the device, which forms a narrow 1.8^{0} ($\pm$3dB) conical profiling beam. An internal stepper motor rotates the transducer element in 0.9^{0} increments through up to an entire 360^{0} sweep rotation transverse to the sonar's major axis without influencing the pitch or roll of the unit. The motion of the profilers' internal stepper motor is entirely configurable in the associated Pipe Profiler E software package. Upon completing a single sweep rotation, the transducer is returned to its start point and the configured scanning sweep is repeated.

The sonar is a two-dimensional acoustic scanner. Therefore, profiling the scour hole in three-dimensions required the continuous-scanning sonar to be moved at a steady rate parallel to the direction of flow (stream-wise direction). A Konova K5 slider was used for this purpose. The sonar was secured to the base of an oversized slider bracket which in turn was mounted to the Konova sliders' platform (Figure 3.5). The quasi non-intrusive nature of the equipment to the scour development process is analysed later in this thesis in Section 4.4.1.

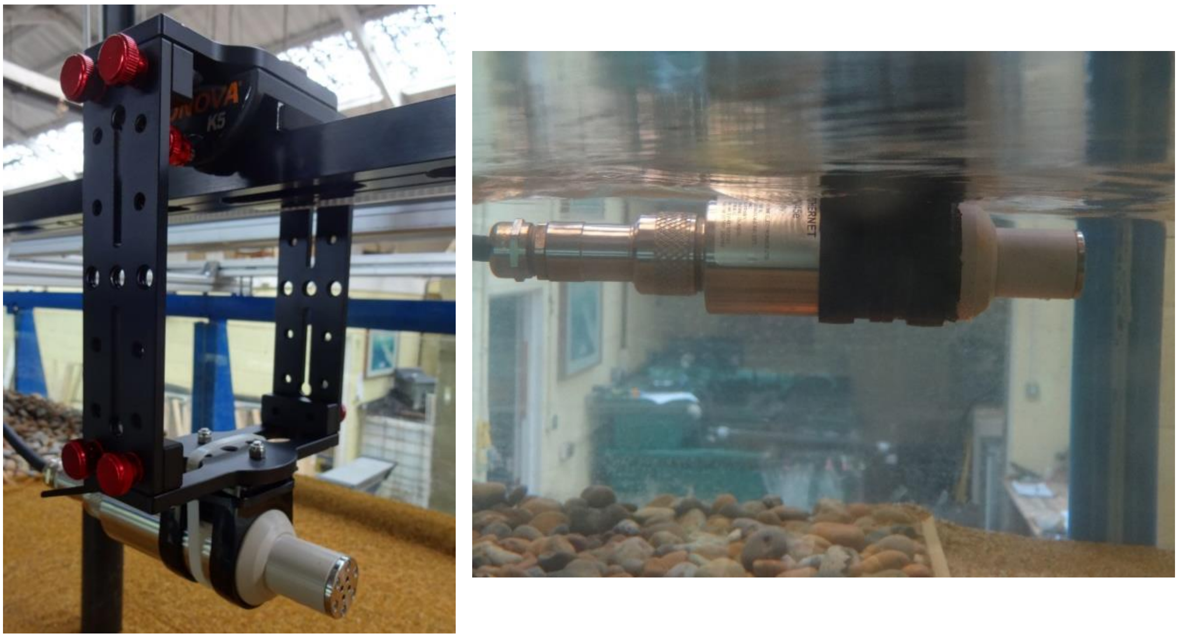

Figure 3.5 Oversized slider bracket (left), and sonar submergence during testing (right). Orientation of transducer rotation is transverse to the direction of motion.

A pulley system (Figure 3.6a) was installed to connect the sliders' platform to a 721:1 gear motor (Figure 3.6b) fixed atop of the slider frame. The gear motor is fully programmable using a Konova Smart Motion Controller (SMC) and can be configured to move the slider automatically or to be controlled manually, enabling precise remote control of the motion and positioning of the sonar device (Figure 3.6c).

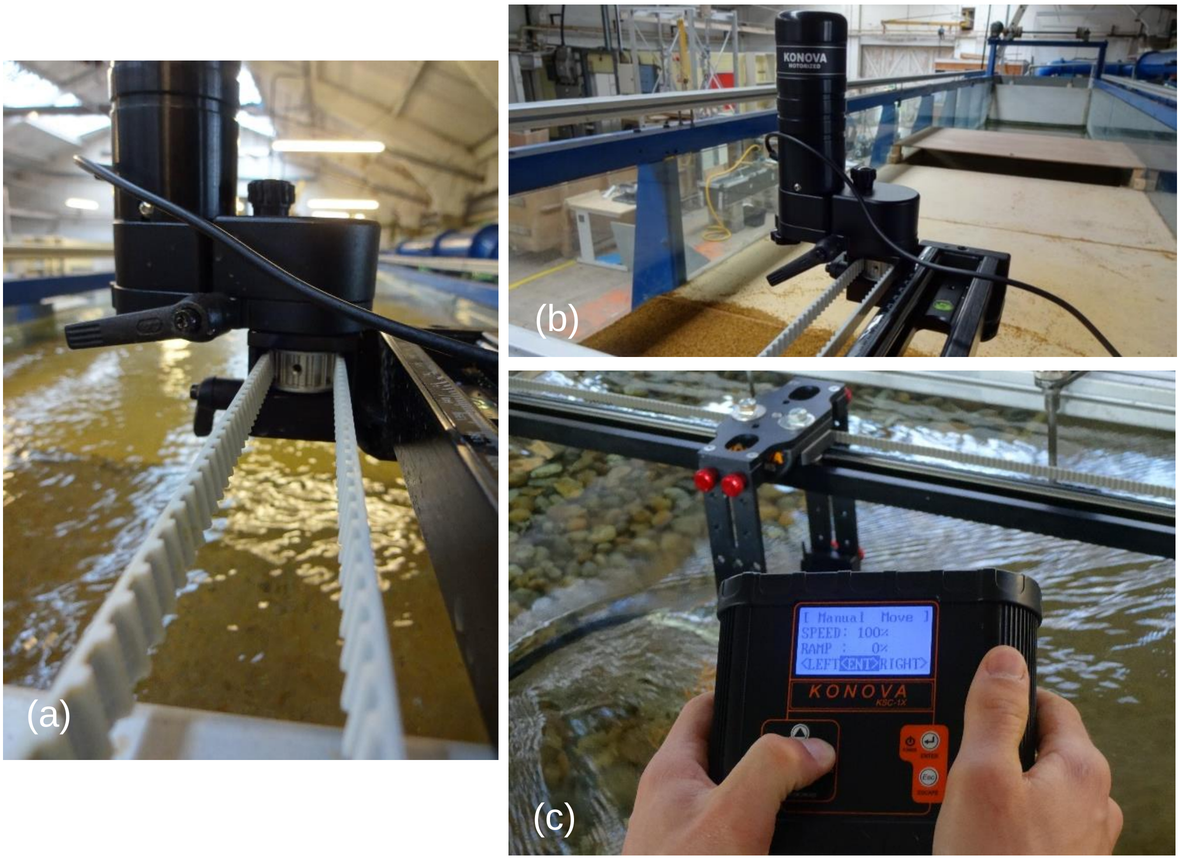

Figure 3.6 (a) Pulley system, (b) 721:1 Geared motor, and (c) Konova smart motion controller.

The oversized slider bracket was used to ensure the transducer head remained fully submerged throughout experimentation. The slider, and therefore the sonar, was offset by 175mm from the flume centre to account for the dimensions of the bracket. This offset distance was minimised to ensure that any profiling of the nearside[12] local scour zone was captured inside an incident angle exceeding 45° to eradicate any dishing effects from conical beam transverse footprint enlargement, which can occur as the beam angle increases away from vertical (Atherton, 2011).

To account for the offset and reduce the time between successive scanning sweeps, the sonar's internal stepper motor was configured to reduce the coverage angle of the acoustic transducer to a 90^{o} swath angle, offset by 30^{o} from the horizontal to focus the profiling on the scoured area of interest (Figure 3.7). This also ensured the time between successive swaths was minimised for capturing quasi-dynamic profiles of the bed.

---

[12] It is well known that a local scour hole is symmetrical about its central axis. As such, the magnitude of the scour hole volume calculated by profiling just half of the scour hole adjacent to the sonar can be doubled with confidence to find the total scour hole volume at that time.

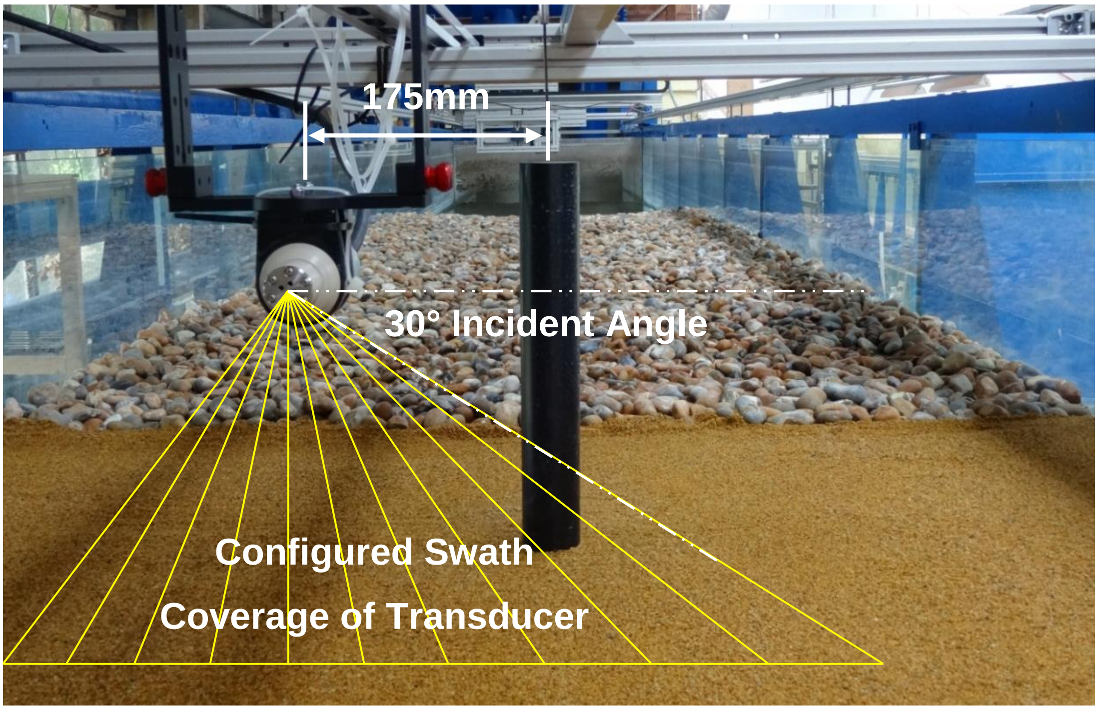

Figure 3.7 Illustration of sonar positioning relative to the test pier and the transverse extents covered by the generated line scan using a 90° swath.

The automated Konova SMC was configured to cover a scan length of 0.75m for each measurement. This scan length spanned the region between a fixed-plate datum located upstream of the test sediment area, to a fixed location one diameter downstream of the test pier[13]. The optimal automated slider speed to cover this distance was determined by identifying the input speed for which the sonar surface output produced the closest match to an equivalent surface output of a high-density manual scan. Manual measurements – moving the sonar to pre-defined locations along the stepper motor axis and allowing it to scan whilst static – were not affected by possible movement errors and therefore provided a true representation of the underlying bed[14]. A slider input speed of 7% (~5mm/s) was selected using this approach (Figure 3.8).

Sonar data was automatically captured by moving the slider at a continuous rate until manually stopped. The time taken to complete one full scan was 150 seconds, producing ~420 acoustic line outputs at an equivalent stream-wise spacing of ~1.78 mm. Using a 90° coverage angle completed in 0.9° step intervals, the two-dimensional line scan consists of 100 individual elevation points, equating to a point cloud of ~42,000 data points per scan. For the flat-bed condition upstream, the output cross-stream spacing between elevation data points is solely a function of

---

[13] The end point downstream was determined by measuring one pier diameter downstream from the trailing edge of the largest test pier (101mm) used.

[14] This form of measurement was time intensive and therefore was not suitable for full experiment operation.

the acoustic beam inclination and as such varied between 3-8mm. However, within the vicinity of the dynamically changing scour hole profile the cross-stream spacing also becomes a function of the distance between the sonar and the bed. This has particular importance for mapping the location of maximum scour depth as this location. As the scoured bed develops with time, by considering simple trigonometric arguments, the lowering bed elevation means that the scour depth is captured at a shallower swath angle relative to the vertical. The implications of this are an increase in the cross-stream resolution around this location. Furthermore, the shallower swath angle is related to a reduced transverse footprint of the sonar beam, meaning that the scour depth in time is measured with reduced geometric distortion owing to possible dishing effects mentioned previously (Atherton, 2011). It must be noted however that the reducing shallower swath angle reaches a plateau as the development of the scour depth approach an equilibrium state. Collectively, the stream-wise and cross-stream resolution provides a comprehensive snapshot of the underlying scoured surface in real-time.

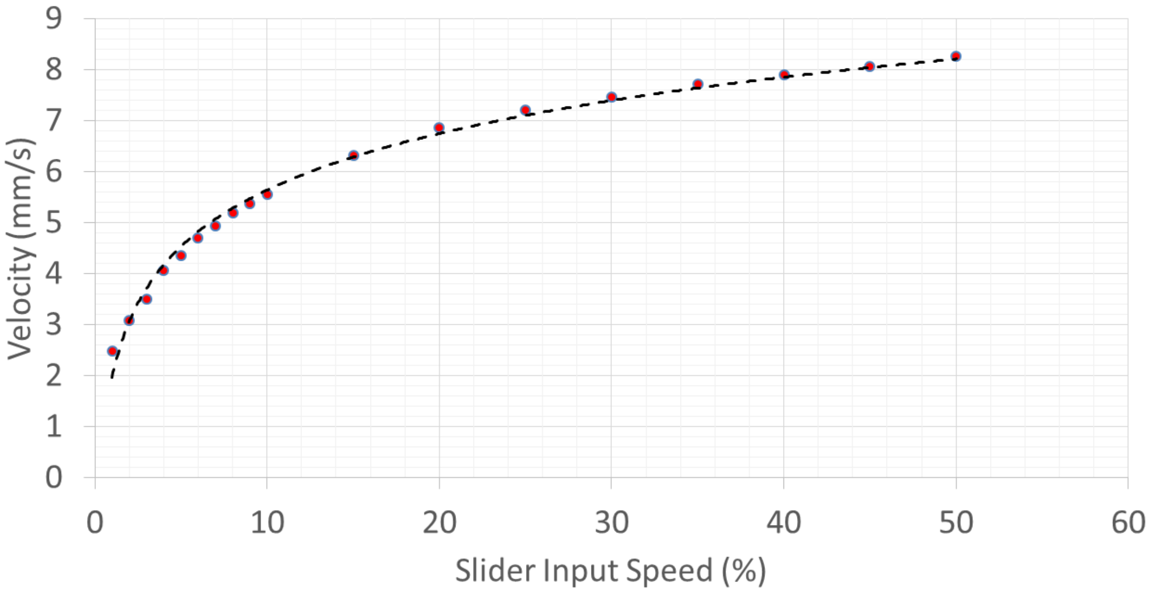

Figure 3.8 *Calibration curve of the Konova 721:1 geared motor.*

3.3 Experimental Procedure

3.3.1 Flow Conditioning

Flow entering through the inlet is dispersed uniformly[15] across the channel width by honeycomb flow straighteners. For a well-developed turbulent boundary layer upstream of the test area, it is vital to ensure that the flow field in the flume simulates a typical open channel flow, and key hydraulic equations are applicable (Chow, 1959). These conditions are developed by a rough upstream boundary layer introducing turbulence to the flow. The rough boundary is developed by adding coarse gravel atop the upstream false flooring. The minimum length of approach false flooring required for a turbulent boundary layer to fully develop can be considered analogous to the length of the boundary layer, X_H, developed for a given boundary layer thickness (δ). For a fully-developed flow field, the boundary layer thickness must extend over the entire flow depth, which for a 1.40m wide channel is limited to 0.28m ($B/y \geq 5$), i.e. $y = \delta \leq 0.28$m.

The boundary layer length is related to the average roughness element thickness using (Monin and Yaglom, 2007)

$$U_* = \left(\frac{y}{\gamma}\right)\left(\frac{V_1}{X_H}\right);$$

where γ is a coefficient equal to 0.33; and , U_* is the bed shear velocity, respectively. For an undisturbed flow over a rough surface, the shear velocity (U_*) can be computed using the Soulsby (1997) friction law relating U_* and V_1 of the form $7U_*/V_1 = (d_{50}/y)^{1/7}$.

For clear water approach flow conditions, the maximum permissible inflow velocity (V_1) for any test sediment is 0.6 m/s. Therefore, turbulent flow conditions fully-developed over the flow depth upon reaching the sediment zone were obtained provided that the single-layer of upstream roughness elements ($d_{50,U}$) placed on the 5m span of false flooring exceeded 11mm (Shields curve, see Shields, 1936). Roughness elements readily available at the laboratory with an average size of 35mm (the mean diameter, taken from 50 independent geometric measurements) were therefore considered sufficiently adequate for flow conditioning purposes (Figure 3.9).

---

[15] For a two-dimensional flow, the mean velocity and all gradients in the cross-stream direction are negligible and the boundary layer develops uniformly over the width of the false flooring. However, if $B/y < 5$ a weak secondary motion in the cross-section may occur which transports low momentum fluid motion towards the central section of the channel, resulting in a three-dimensional flow field where the maximum velocity occurs below the free surface (Chiu, 1987). Assumptions of a uniform approach flow are therefore only applicable to two-dimensional profiles where $B/y \geq 5$.

Figure 3.9 Upstream roughness layer.

3.3.1.1 Acoustic Doppler Velocimeter (ADV) Analysis

An ADV positioned 1m upstream of the sediment recess box was used to verify the flow conditioning within the central region of the flume created by the upstream flow roughness (Figure 3.10). The Vectrino ADV works by transmitting short acoustic pulses through the water column to a 1mm^3 sampling volume target located 5cm away from the transmit probe. Fractions of the transmitted acoustic energy are reflected off of particles suspended in the water within the sampling volume which is recorded by one of four ADV receivers. Each receiver records a velocity component, a signal strength value, SNR (sound-to-noise ratio) and a correlation value. The change in wavelength phase between successive coherent acoustic returns is then converted by the Vectrino software into velocity estimates using the Doppler shift (Voulgaris and Trowbridge, 1998).

ADV seeding was added to the water intermittently to improve the waters acoustic reflectivity, ultimately providing velocity readings to within an accuracy of $\pm$1mm/s. Measurements were taken in 10mm increments in the vertical plane. A total of 24000 velocity readings, sampled at an output rate of 200Hz over a two minute period, were recorded at each increment.

Figure 3.10 Acoustic Doppler Velocimeter support (left) and submerged receiver head (right).

Characteristics of the approach flow 1m upstream of the test pier are illustrated in Figure 3.11. The results reflect the flow conditioning for all laboratory trials. The measured mean flow statistics (Figure 3.11) resembles conditions encountered in canonical open channel flows. This provides confidence that the results obtained from the scour experiments will be of fairly general validity and will be easily reproducible.

In particular, the profiles in Figure 3.11 suggest that a well-developed turbulent boundary layer has been developed (e.g. Kironoto and Graf, 1994; Bomminayuni and Stoesser, 2011). Since the development of the horseshoe vortex system is strongly influenced by bed shear stresses resulting from the impinging flow, the developed turbulent boundary layer provides an adequate and realistic resource from which the HVS can be derived.

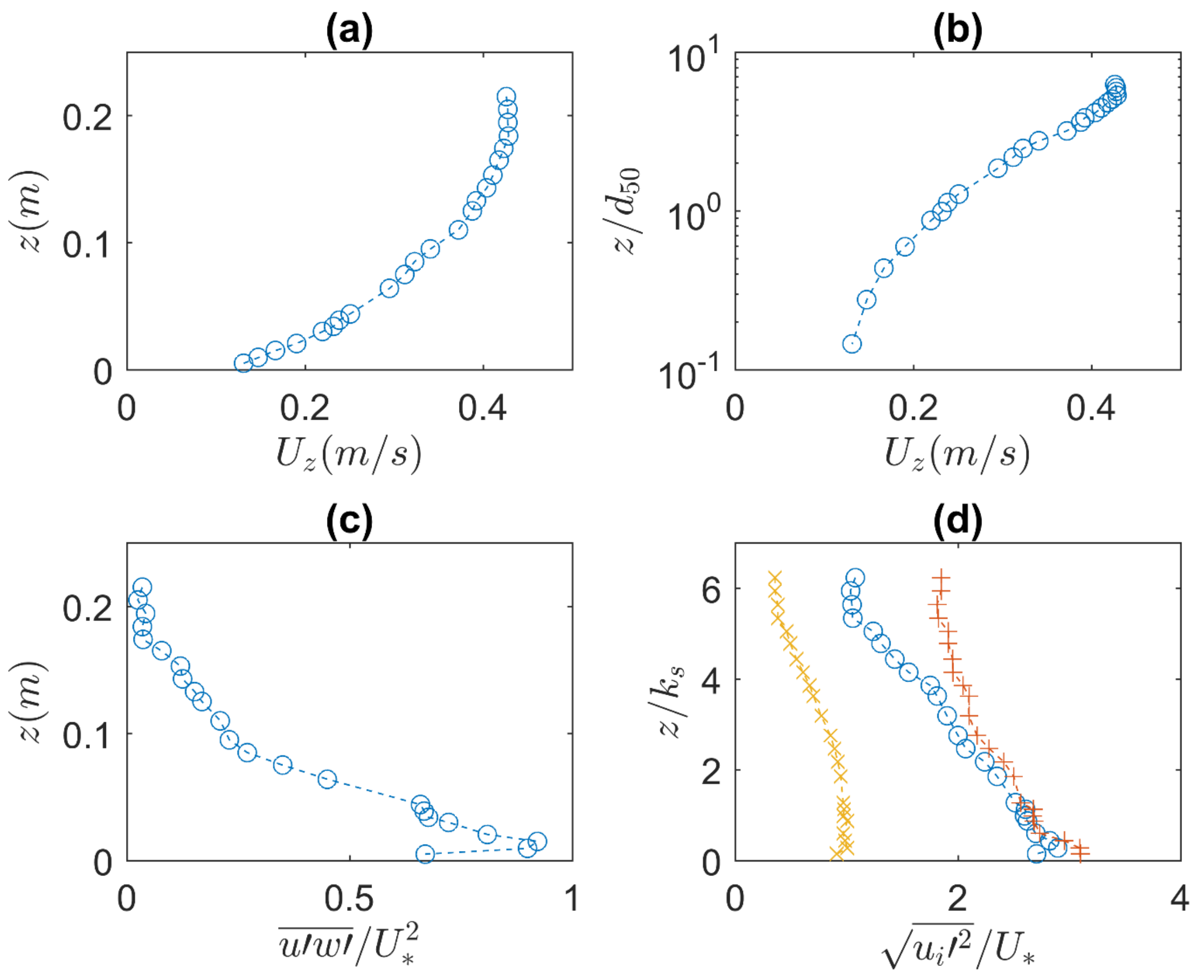

Figure 3.11 *Upstream flow conditioning. (a) Stream-wise flow velocity profile with depth (U_x $vs.$ z); (b) Log-law of the wall (U_x $vs.$ $\ln z/d_{50}$); (c) Variation of the Reynolds stress tensor with depth ($\overline{u'w'}/U_*^2$ vs. z); and (d) Velocity fluctuations normalised with the shear velocity against the normalised depth ($\surd(u'^2_i)/U_*$ $vs.$ z/k_s): blue u'^2, red v'^2, yellow w'^2. In the above, the straight overbar denotes time-averaging, whereas the prime denotes the time fluctuations; u, v, w are the stream-wise, lateral and bed normal velocity components, respectively; k_s is the equivalent sand roughness from Nikuradse which is idealised to be equivalent to the mean sediment diameter, d_{50}.*

3.3.2 Experimental Methodology

To ensure replicability of the local scour simulations, a standardised procedure was used to prepare the test area and perform each real-time measurement of the scour hole volume. The experimental procedure was as follows:

3.3.2.1 Bed Preparation

1. A single test pier – constructed using a solid opaque PVC pipe structurally supported on a PVC plate – was positioned centrally inside the sediment recess box and located 500mm from the upstream edge of its boundary (Figure 3.12a). This location was pre-determined

to accommodate natural scour formation; with a short steep approach upstream, followed by a long shallow downstream slope and accompanying deposition mound further afield;

2. Sediment, thoroughly hand-washed to minimise fine silt levels (Figure 3.12b), was added to the recess box in layers around the test cylinder (Figure 3.12c). For each added layer, the sand was evenly distributed inside the recess box, saturated and subsequently compacted. Layer compaction across the test area and sides of the flume was achieved by hand using a bespoke flat-faced rectangular earth rammer. Compacting reduced the variation in air voids within the sediment layers and simulated the equivalent resistance of the bed material to erosion in the field, which consolidates under the weight of the structure (Benn *et al.*, 2004);
3. As soon as the recess box had been filled to capacity, the downstream overflow weir was closed and the flume slowly filled with water. Stagnant water conditions were subsequently induced for a minimum period of 1 hour to again saturate the bulk sediment;
4. Upon draining the flume, the recess box was further re-compacted to reduce the existence of air voids within the sediment around the pier structure as per Sheppard *et al.* (2000). The sand bed surface was levelled using a spirit level to minimise unwanted bed topography variation that could produce initial bed elevation errors measured by the sonar (Figure 3.12d);

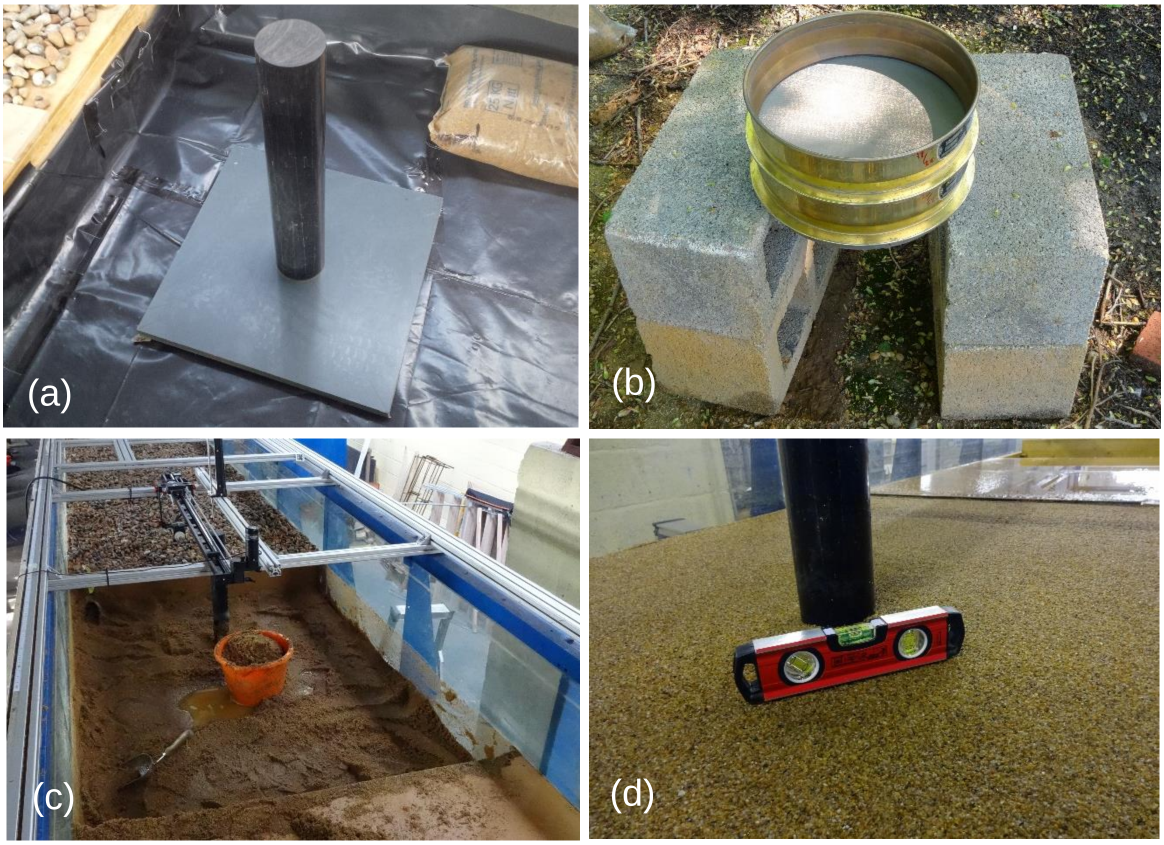

Figure 3.12 (a) Location of the test cylinder, (b) Sieving of sand, (c) Addition of sand in layers, and (d) Test sediment levelling.

3.3.2.2 Flow Preparation and Sonar Measurements

5. Using a low flow rate, the flume was slowly refilled over a long duration (around 2 hours) until the test depth was reached. Slow filling of the flume nullified early local scour generation and the mobilisation of sediment due to bed-load transport (Sheppard *et al.*, 2004);

6. Under static flow conditions, a full topographic profile of the bed using the sonar-slider configuration was performed at an effective time $t = 0$ to generate a 'flat-bed' datum. This datum was used as a reference surface to calculate the volume occupied between it and a scour hole surface measured at time t during the experiment. The initial flow depth and bed elevations were also measured using point-gauges PG2 and PG3 (see Figure 3.13);

7. By quasi-simultaneously opening the pump valves to increase the inflow volume[16] whilst lowering the downstream overflow weir to reduce the tail-water depth, the target flow

---

[16] For velocities within the range 0.3-0.6 m/s, two pumps working in combination were used (Pumps 2 and 3). Sufficient water in the sump was therefore used to avoid air lock becoming present within the pipe system, causing a significant variation in inflow volume.

velocity and depth for each experiment could be set. Upon reaching the required experiment test parameters, the experiment timer was started;

8. Each measurement consisted of performing a fully automated sonar scan, which was immediately succeeded by gauge measurements of the bed elevation using PG2 and PG3. The sonar was then returned to its original position ready for the next interval scan. Real-time measurements of the scour hole profile were performed at predetermined intervals. Measurements were made every 15 minutes for the first 3 hours to capture the initial high rate of scouring (Melville and Chiew, 1999), beyond which the frequency reduced to every 30 minutes. Real-time measurements were recorded hourly after 10 hours had passed. An undisturbed[17] minimum test duration of 36 hours was used for all trials (Figure *3.14*). During periods of inactivity, the idle sonar was positioned far upstream to minimise its invasiveness on the local scour development around the test cylinder (Figure 2.13). A high flow depth of 0.28m was also used for this purpose. Equipment invasiveness is assessed in Section 4.4.1;

9. For each preceding scour trial, the sediment was fully removed from the test area and replaced in accordance with the methodology outlined in Step 2. Measurement repeatability is assessed in Section 4.4.

Flow velocity measurements were monitored hourly throughout the trial duration using a Valeport Model 801 electromagnetic flow meter. An average velocity of the fully developed flow was measured 1m upstream from the apex to the test area. The flow meter was programmed to measure the flow velocity over one-minute intervals to calculate an average value to within ±1 mm/s. Flow measurements were repeated if the standard deviation recorded by the instrument exceeded 0.1 m/s.

---

[17] Pausing the experiment overnight invalidates any results beyond the stoppage due to flume drainage causing a compaction of the sediment layers, whilst refilling the flume results in the scour hole being partially-infilled by upstream sediment.

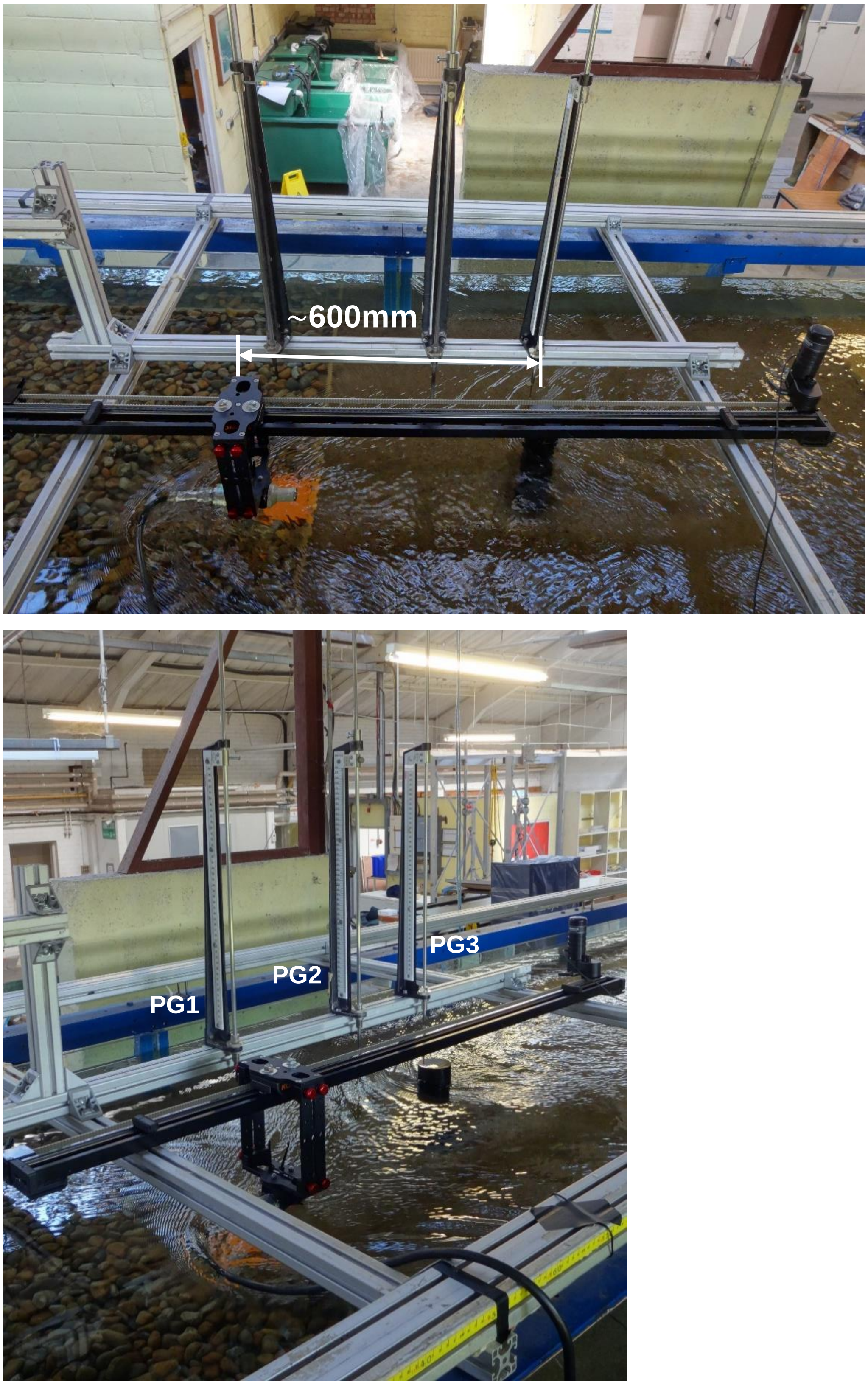

Figure 3.13 Overview of apparatus set-up. Idle sonar is positioned upstream of the test area. PG1, PG2 and PG3 represent point-gauges installed to check the elevation of the sonar outputs.

Figure 3.14 End scour hole extent.

3.3.3 Pre-Scan Preparation

During periods of inactivity, the sonar was positioned far upstream to minimise its interaction with local scour development around the test cylinder. Electrical power to the sonar was also cut when idle to reduce the risk of sonar overheating. Prior to each scan, an average water temperature was measured and used to provide an estimate for the speed of sound[18] in the water column, based on a fifth-order polynomial function based on temperature measurements of the water column from Marczak (1997). The initial speed of sound value was subsequently verified and adjusted by comparing elevation measurements of the fixed upstream baseplate using the sonar device against those measured using the point gauge (location of PG1 shown in Figure 3.13) to correct the propagating sound waves before each scan was carried out (Figure 3.15).

Although sediment saturation was completed for long periods of time during trial preparation, intermittent pockets of air from the sediment became dislodged and built up around the face of the sonar transducer. Due to its high acoustic frequency, small obstacles such as air bubbles are visible to the sonar and cause very strong acoustic reflections within the data output. Therefore, the sonar transducer outer-shell was wiped prior to each scan to minimise this occurrence.

---

[18] The speed of sound in the water body is used to calibrate the sonar's path length from the time to transmit and receive an acoustic signal (Atherton, 2011).

Figure 3.15 A fixed upstream reference point.

3.4 Test Parameters

The experiments were conditioned to vary the flow regime (and therefore the effects of viscosity relative to inertial forces) within the scour hole over a wide range, as this has been shown (e.g. Lança *et al.*, 2016; Manes *et al.*, 2018) to have a measurable effect on the scour development process. Here, the flow regime within the scour hole is classified by the ratio between the mean sediment size and the Kolmogorov length scale i.e. d_{50}/η following the phenomenological approach (as in Manes and Brocchini, 2015). As detailed in Section 2.5, the Kolmogorov scale η can be computed as

$$\eta \sim \left(\frac{\upsilon^3 a}{C_D V_1^3} \right)^{1/4}.$$

To simulate a variety of flow regimes within the scour hole (by means of varying d_{50}/η), both the pier and sediment diameter were adjusted. The physical parameters and non-dimensional groups for all 18 trials are given in Table 3.2 and Table 3.3, respectively.

In order to ascertain a base-line for an inviscid response of the scour generation process (from which the effects of viscosity can be observed), a large sediment diameter ($\rho_s = 2640$ kgm^{-3}, $\sigma_g < 1.5$); $d_{50} = [2.62$ mm$]$ that represents a fully-rough flow case within the scour hole was selected for initial experimentation. Three additional uniform[19] quartz sands[20] were then used to vary the flow regime within the scour hole; one coarse ($\rho_s = 2640$ kgm^{-3}, $\sigma_g < 1.5$); $d_{50} =$ [1.61 mm], one medium ($\rho_s = 2640$ kgm^{-3}, $\sigma_g = 1.28$); $d_{50} =$ [0.87 mm] and one fine fraction ($\rho_s = 2640$ kgm^{-3}, $\sigma_g = 1.38$); $d_{50} =$ [0.28 mm]. Three pier diameters were used throughout; $a = [51, 76, 101$ mm].

Table 3.2 Physical experiments parameters. A repeated trial is denoted with the superscript in the first column^{+}.

Trial	**a (mm)**	**V_1 (ms^{-1})**	**d_{50} (mm)**	**Temp. (°C)**	**Temp. Range (°C)**	**Average ν (10^{-6} m^2/s)**
1	51	0.443	2.62	14.86	11.7 - 17.9	1.143
2	101	0.443	2.62	14.16	10.2 - 16.9	1.164
3	101	0.355	2.62	13.85	11.2 - 16.9	1.174
4	76	0.447	2.62	17.18	13.3 - 20.9	1.075
5	76	0.331	2.62	18.26	17.1 - 18.9	1.046
6	51	0.401	1.61	16.37	13.2 - 20.1	1.098
7	101	0.400	1.61	16.93	12.3 - 19.8	1.082
8	101	0.308	1.61	16.07	15.0 - 16.9	1.107
9	76	0.393	1.61	19.62	16.0 - 21.8	1.012
10	76	0.313	1.61	16.62	15.1 - 18.6	1.091
11^{+}	101	0.455	2.62	13.59	12.0 - 14.9	1.183
12^{+}	76	0.449	2.62	12.2	10.1 - 13.9	1.229
13	101	0.341	0.87	13.35	11.1 - 15.8	1.190
14	76	0.365	0.87	14.85	12.1 - 17.2	1.143
15	51	0.348	0.87	15.58	13.8 - 16.9	1.121
16^{+}	101	0.342	0.87	16.87	14.0 - 19.7	1.084
17	101	0.278	0.28	16.76	14.1 - 19.5	1.087
18	76	0.273	0.28	22.72	19.0 - 25.8	0.939

---

[19] A uniform topsoil minimises armouring effects and hence produces the greatest clear water scour depth.

[20] 1.5 tonnes of each sediment type was procured from Aggregate Industries.

Table 3.3 Non-dimensional groups. Particle Reynolds numbers (R_e^*) is given by $U_* d_{50}/\upsilon$. *A repeated trial is denoted with the superscript$^+$.*

Trial	y/a	a/d_{50}	Re_p (10^4)	Re^*	Fr	V_1/V_c	B/a	η (mm)	d_{50}/η
1	5.5	19.5	1.98	75.16	0.27	0.71	27.5	2.89E-05	90.6
2	2.8	38.5	3.88	73.74	0.27	0.71	13.9	3.48E-05	75.3
3	2.8	38.5	3.06	58.68	0.21	0.57	13.9	4.13E-05	63.4
4	3.7	29.0	3.16	80.57	0.27	0.71	18.4	3.03E-05	86.4
5	3.7	29.0	2.40	61.29	0.20	0.53	18.4	3.72E-05	70.4
6	5.5	31.7	1.86	40.60	0.24	0.82	27.5	3.02E-05	53.2
7	2.8	62.7	3.74	41.10	0.24	0.81	13.9	3.55E-05	45.3
8	2.8	62.7	2.81	30.91	0.19	0.63	13.9	4.40E-05	36.6
9	3.7	47.2	2.95	43.14	0.24	0.80	18.4	3.19E-05	50.4
10	3.7	47.2	2.18	31.89	0.19	0.64	18.4	4.00E-05	40.2
11^+	2.8	38.5	3.84	74.55	0.27	0.72	13.9	3.45E-05	75.9
12^+	3.7	29.0	2.78	70.79	0.27	0.71	18.4	3.34E-05	78.4
13	2.8	116.1	2.89	15.77	0.21	0.93	13.9	4.30E-05	20.2
14	3.7	87.4	2.39	17.57	0.22	0.99	18.4	3.69E-05	23.5
15	5.5	58.6	1.59	17.05	0.21	0.95	27.5	3.42E-05	25.4
16^+	2.8	116.1	3.17	17.34	0.21	0.93	13.9	4.01E-05	21.7
17	2.8	360.7	2.60	3.85	0.17	0.99	13.9	4.69E-05	6.0
18	3.7	271.4	2.18	4.37	0.16	0.98	18.4	3.97E-05	7.1

For completeness, the flow regime in the undisturbed open channel flow upstream of the pier described by Re^* is also reported in Table 3.3. The flow regime upstream of the pier can be characterised from the work by Nikuradse (1950). Nikuradse noted that the fully-rough regime exists for a particle Reynolds number $Re^* > 70$, provided the bed consists of uniform close-packed sand elements[21]. Thorough sand box compaction during experiment preparation, evidenced by values of $y_{s,end}/a$ being comparatively low to the literature (typical range is $y_{s,end}/a = 1 \div 3$) owing to the roughness grains being more resistant to movement[22] (Buffington and Montgomery, 1997), shows the regime criterion is valid for these experiments. Accordingly,

---

[21] The shear velocity used to compute $Re^* = \rho U_*/\upsilon$ was computed using the Soulsby, R. (1997) *Dynamics of marine sands: A manual for practical applications*. Thomas Telford. friction law relating U_* and V_1 of the form $7U_*/V_1 = (d_{50}/y)^{1/7}$.

[22] Buffington and Montgomery (1997) reproduced the original Shields curve for different bed material properties and concluded that loosely packed surface have a far higher grain mobility due to a reduced critical shear stress. This is in contrast to well packed and greater sorted grains that are more resistant to movement and increase the surfaces' critical shear value required for incipient motion.

the hydraulically smooth regime is defined for $Re^* < 5$, whilst the transitionally rough and smooth regimes, naturally, are contained within the range $5 < Re^* < 70$.

Within this context, the dataset contains experimental trials where the upstream boundary layer is characterised by either the fully-rough (7), transitionally rough (5), transitionally smooth (4) or hydraulically smooth (2) flow regime[23]. The influence of flow regime (and therefore the relative importance of viscosity effects) on the scour process is assessed in detail in the forthcoming Chapters.

3.5 Summary

Real-time measurements of the developing scour hole profile were captured using a 2 MHz Marine Electronics 2512 pipe profiling sonar. The two-dimensional sonar was secured to the base of an oversized slider bracket that, in turn, was mounted to a remotely-controllable sliding platform. This set-up enabled three-dimensional bed measurements of the scour hole to be captured by the sonar over time.

The sliding platform was programmed to move at a steady continuous motion at a speed calibrated to match a baseline measurement scanned manually (moving the sonar in steps for static scanning) over a flat-bed surface around the test pier. The automated system was configured to cover a scan length of 0.75 m for each measurement which spanned the region between a fixed-plate datum located upstream of the test sediment area, to one diameter downstream of the test pier. This scan length provided a comprehensive snapshot of the scour hole and the undisturbed bed upstream of the test pier. Bed elevations measured by the sonar were compared against gauged readings at three key locations. This was used to ensure that the measurement accuracy of the sonar was consistent for surveying both flat-bed and sloping scour hole profiles. Measurement validation is reported in the succeeding Chapter.

A total of 18 trials were carried out. The trials were conditioned to vary the flow regime of the upstream boundary layer (and therefore the effects of viscosity relative to inertial forces) within the scour hole as this is known to have a measurable effect on the local scour development (e.g. Lança et al., 2016). The influence of flow regime on the developing scour hole, and therefore the effects of viscosity relative to inertial forces, is assessed in the succeeding Chapters.

---

[23] The number of trials carried out for in each flow regime is stated in brackets.

Chapter 4: Validation of the Experimental Technique

4.1 Introduction

A novel scanning technique using a rotating-head sonar profiler attached to a slider mechanism was presented as a means to directly measure the complex erosion and deposition features of local scour holes developing in clear-water conditions around vertical cylinders mimicking bridge piers. To the best of the author’s knowledge, this technique is the first of its kind that enables the development of the scour hole to be measured in comprehensive detail over time and space. However, an extensive assessment of the technique is required as a pre-requisite to identify the system performance and the accuracy of the data produced. Only then can results be correctly interpreted. This Chapter presents a performance validation of the novel technique covering the accuracy, repeatability and non-invasiveness of implementing the equipment for measuring the geometry of a developing local scour hole in a quasi-non-invasive manner.

4.2 Raw Data Processing Method

For a single sweep of the underlying surface, the sonar produces a raw image file that represents acoustic returns received by the sonar’s transducer in the transverse plane. Each image file was converted into a two-dimensional line profile using the sonar’s Pipe Profiler E software through post-experiment playback. Playback enables the user to configure the acoustic intensity threshold and blanking radius of the line profile generator to minimise the capture of suspended sediment and background noise, respectively, allowing the bed profile to be isolated (Figure 4.1).

Each snapshot of the scoured bed at a time t consists of an array of line profiles. The line profiles are generated by the steady movement of the sonar longitudinally (i.e. in the x-plane, see Figure 4.2) over the scoured bed whilst the sonar performs a swath scan configured to loop continuously. The collection of line profiles generated for each complete bed scan were concatenated to form a single three-dimensional (x-y-z Cartesian co-ordinates, see Figure 4.2) point cloud of the scoured surface. Prior to surface generation, each point cloud was filtered using a two-dimensional locally-weighted quadratic regression model and three-dimensional kernel smoothing. Kriging interpolation then converted each point cloud into a continuous raster surface for similarity analysis (Figure 4.2).

In order to reduce the large amount of data to be analysed, sonar scans were carried out over one half of the scour hole, exploiting its symmetry with respect to the x-z plane through the piers’ centre, where z is the bed-normal direction (see Figure 4.2). Real-time characteristics of the developing scour hole were then computed for each trial using the difference between bed elevations at time interval t and the corresponding flat-bed condition at time $t = 0$. Full details of the bed surface generation process can be found in Appendix B.

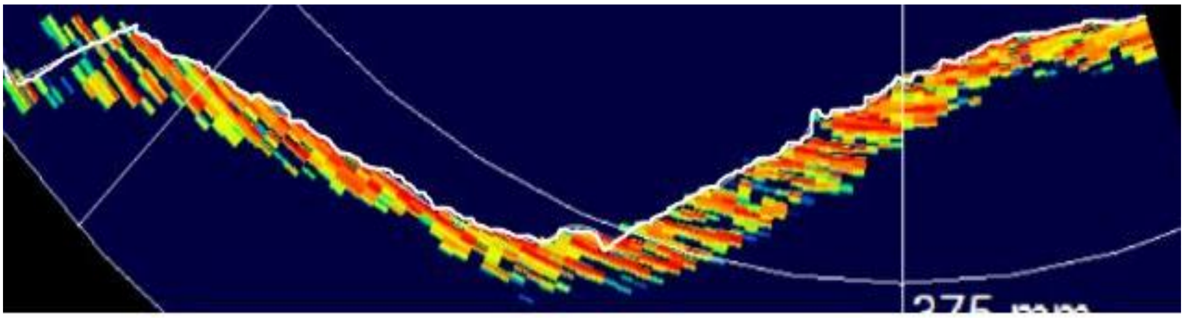

Figure 4.1 Surface profile outline from an individual swath of raw acoustic returns.

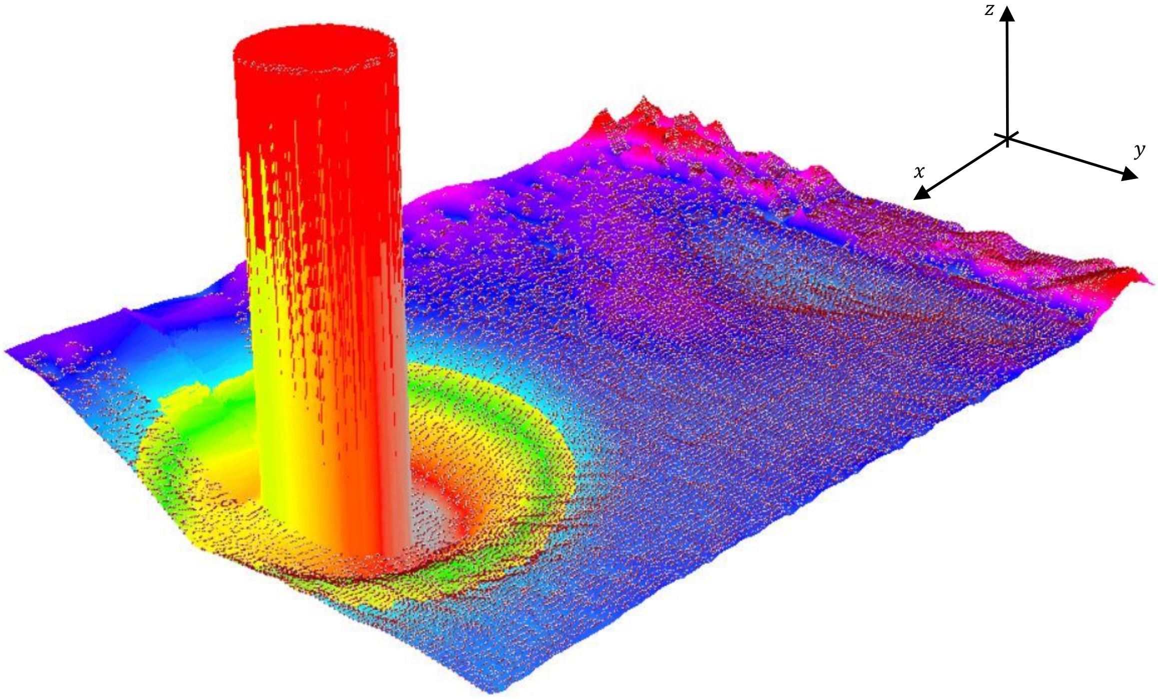

Figure 4.2 Filtered three-dimensional sand bed point cloud overlaying a kriging-interpolated surface.

4.3 Measurement Validation

Due to the sonar being offset from the flume centre-line, the scour development process was captured when the sonar beam was at an incline. Therefore, reference point gauges were installed along the centreline of the flume at critical locations to verify the elevation of the sonar measurements and eventual interpolated bed surfaces. Gauges were installed at three key locations (Figure 4.3); (a) above a small flat-plate datum located upstream of the sediment recess box (PG1, termed *fixed plate* in the subsequent text), (b) upstream of the scour hole apex within the sand recess pit periphery (PG2, termed *approach* in the subsequent text), and (c) above the point of maximum scour depth (PG3). Each gauged measurement is referenced to the centre of the sonar transducer for direct validation of the acoustic measurements. Bed elevations from gauged readings are accurate to within ±0.5mm.

Measurements from all three gauges were performed immediately after each sonar scan had ceased. Table 4.1 presents the difference in elevation recorded by the sonar and point gauge at the approach (PG2) and maximum scour depth (PG3) locations for all trials. The errors are presented (i) relative to the flow depth and (ii) as an absolute error in multiples of the trial sediment diameter. A positive mean value indicates that, on average, the bed elevation was higher according to the sonar-generated surface. The fixed plate elevation measurements (PG1) were used to adjust the speed of sound configured for the sonar prior to each scan being performed, and are therefore not reported here.

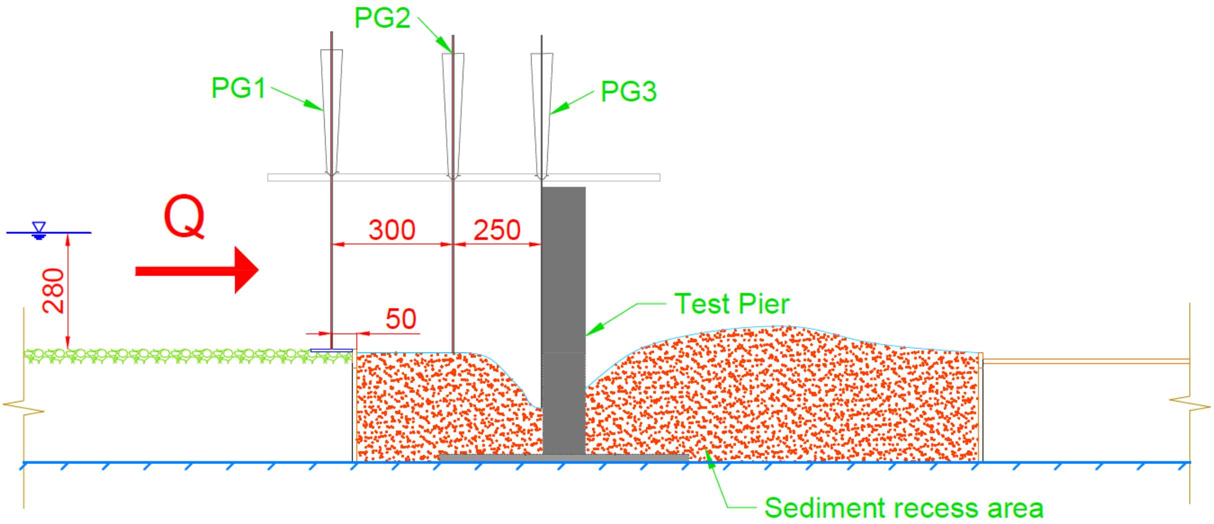

Figure 4.3 Schematic of Point Gauge (PG) measurement locations. PG1 signifies the location of the fixed plate situated atop the false flooring upstream of the sand recess pit. PG2 is located above the sand recess pit upstream of the scour hole apex. PG3 is the location of maximum scour depth which, for a narrow pier, is at its upstream leading edge.

Table 4.1 Elevation errors between sonar and gauge measurements at the approach (PG2) and maximum scour depth (PG3) locations. $\mu \pm 1.96\sigma$ = mean difference ± 95% limits of agreement, with errors presented (i) relative to the water surface and (ii) as an equivalent absolute error normalised by the trial mean sediment diameter; Δy_s = difference between measured maximum scour depths; end of trial Δy_s = the absolute and relative elevation error measured at trial termination – relative error is referenced to the flat-bed datum.

	PG2 Elevation Error (Gauge - Sonar)		PG3 Elevation Error (Gauge - Sonar)		
Trial	(i) Relative to Flow Depth $\mu \pm 1.96\sigma$ (%)	(ii) Absolute Error, as Multiples of Trial d_{50} $\mu \pm 1.96\sigma$	(i) Relative to Flow Depth $\mu \pm 1.96\sigma$ (%)	(ii) Absolute Error, in Multiples of Trial d_{50} $\mu \pm 1.96\sigma$	End of Trial Δy_s
1	-0.47 ± 0.42	-0.51 ± 0.46	0.44 ± 1.71	0.57 ± 2.16	5.64 mm 9.33 %
2	-0.41 ± 0.57	0.44 ± 0.61	0.49 ± 1.29	0.72 ± 1.85	4.41 mm 4.12 %
3	-0.17 ± 0.86	-0.18 ± 0.92	1.78 ± 3.42	2.56 ± 4.85	16.45 mm 20.49 %
4	0.18 ± 0.31	0.20 ± 0.34	0.77 ± 1.99	1.05 ± 2.71	7.75 mm 9.82 %
5	0.58 ± 0.68	0.62 ± 0.73	2.47 ± 2.62	3.33 ± 3.53	15.96 mm 29.38 %
6	-0.53 ± 0.70	-0.92 ± 1.22	1.18 ± 1.85	2.48 ± 3.89	7.27 mm 11.88 %
7	0.34 ± 0.66	0.59 ± 1.15	0.43 ± 1.83	1.02 ± 4.19	7.24 mm 7.47 %
8	0.74 ± 0.62	1.30 ± 1.09	0.69 ± 1.56	1.46 ± 3.25	4.98 mm 7.93 %
9	1.10 ± 0.74	1.96 ± 1.29	-0.06 ± 1.70	-0.10 ± 3.68	1.57 mm 2.02 %
10	-0.14 ± 0.64	-0.24 ± 1.11	0.26 ± 1.72	0.53 ± 3.53	6.93 mm 14.16 %
11	0.24 ± 0.84	0.25 ± 0.90	0.12 ± 0.81	0.18 ± 1.17	0.19 mm 0.17 %
12	0.00 ± 0.87	0.00 ± 0.93	0.93 ± 0.60	1.25 ± 0.83	4.95 mm 6.28 %
13	0.28 ± 0.57	0.90 ± 1.85	0.39 ± 0.76	1.67 ± 3.17	2.27 mm 2.40 %
14	0.10 ± 0.54	0.31 ± 1.75	-0.56 ± 0.91	-2.27 ± 3.73	0.24 mm 0.28 %
15	0.81 ± 0.26	2.63 ± 0.85	0.14 ± 0.72	0.58 ± 2.83	0.99 mm 1.53 %
16	1.58 ± 1.11	5.13 ± 3.61	1.03 ± 1.60	4.43 ± 7.01	7.37 mm 7.56 %
17	-0.06 ± 0.73	-0.67 ± 7.54	1.70 ± 1.80	22.51 ± 25.17	7.87 mm 8.64 %
18	1.26 ± 0.23	13.11 ± 2.38	-0.20 ± 0.92	-2.47 ± 12.10	2.18 mm 2.73 %

It is notable that the errors in the end of trial scour depth for Trials 3, 5, 6 and 10 are significant (>10% relative error). However, this can be explained by the following principle. These four trials represent flow cases where the scour hole footprint produced is smaller in size, owing either to a very low flow intensity (Trials 3, 5 and 10) or small test pier diameter (Trial 6). As the sonar is off-set from the test pier, scanning of the scour hole is completed with the sonar beam at an angle from vertical. The sonars acoustic footprint widens with inclination, meaning that more acoustic returns are considered within the acoustic footprint. From these acoustic returns, the strongest echoed return from within the footprint is used as the estimated range for that step. This is an issue for small scour hole footprints as, for a reduced scour hole footprint where the scour hole width and length are small, the bed topography is more rapidly varied relative to larger pier or higher flow intensity trial-equivalents. As such, a higher percentage of acoustic returns for each acoustic footprint will be affected by acoustic shadow from the smaller scour hole. This ultimately leads to an underestimation of the scoured surface as the echo intensity from the scour slope walls provides a stronger acoustic response when performing a swath over the area of maximum scour. These four trials were therefore removed from further analysis.

The location of PG2 was verified to be above a static flat-bed surface; therefore, the error calculated for PG2 (Table 4.1) represents the random error produced when using the sonar system. A visual representation of the relative error for a sample trial are shown in Figure 4.4. With these four trials removed, the errors produced by the sonar are contained within an discrepancy average of 1%, relative to the flow depth[24], with the majority (8) at an average discrepancy of <0.5%. The 95% confidence limits (1.96σ) are of a similar magnitude (<1%), for all trials. In contrast, the absolute errors for the later trials (13-18) appear significant. However, the increase in error is a direct consequence of the smaller sediment diameter (0.87 and 0.28mm) used to normalise the absolute errors in comparison with the earlier trials (1-12) using coarse sediment (2.62 and 1.61mm). This shows that the survey errors are independent of changes in sediment diameter.

Generally speaking, measurement discrepancies at the location of maximum scour depth appear to be consistent with the flat-bed errors. An improved comparison can be made by considering errors produced for each pier size that provides an improved estimate of the average random error. The mean discrepancy relative to the flow depth for the bed located at PG2 (approach) was found to be 0.33%, 0.51% and 0.06% for pier diameters 101mm, 76mm and 51mm, respectively, whilst the corresponding standard deviations are 0.74%, 0.61% and 0.66%, respectively. The equivalent bulk mean discrepancy at the location of maximum scour depth is 0.52%, 0.16% and

---

[24] Measurement errors are quoted as relative to the flow depth as it is well known that the accuracy of the sonar is dictated by the scanning range (Atherton, 2011).

0.32% for pier diameters 101mm, 76mm and 51mm, respectively, whilst the corresponding standard deviations are 0.74%, 0.91% and 0.72%, respectively. Clearly, there is a striking agreement between both the mean and standard deviations for the two measurement locations. The consistency in random errors for the flat-bed and scour hole locations provides strong evidence that the sonar is absent from systematic errors which might accrue from the combined effect of acoustic footprint widening and scour hole steepness in significantly underestimating the scour profile elevation, as previous research using sonar technology suggests (e.g. Porter *et al.*, 2014). This is provided that the test pier diameter $a > 5\text{cm}$ and the flow intensity $V_1/V_c > 0.6$ are used, based on the presented analysis.

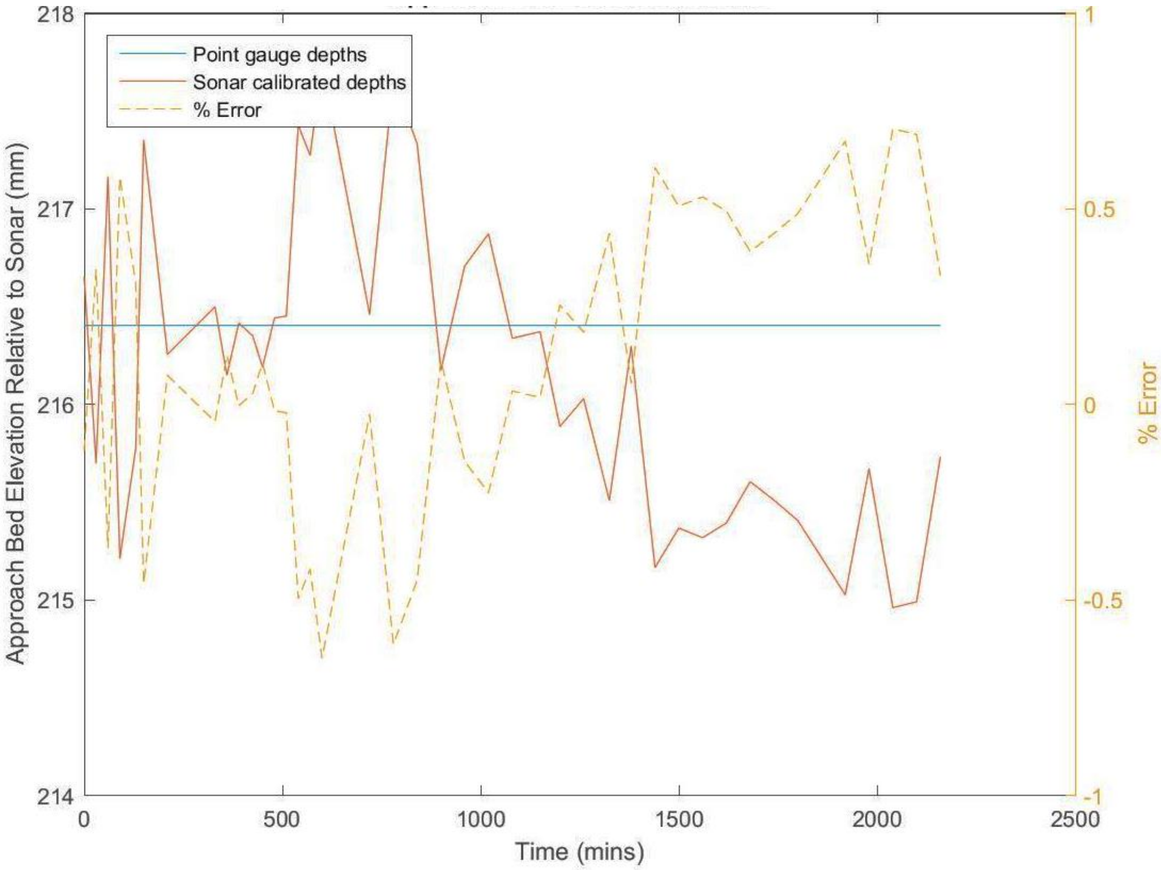

Figure 4.4 Difference between approach elevations for a sample trial measured using sonar and gauge (PG2) equipment, and the corresponding error relative to the scanning distance.

4.4 Output Repeatability

The repeatability of the outputs is a measure of the precision of the sonar technique and the rigour used to carry out scour experiments. Here, repeatability is interpreted by how consistent the time-series behaviour of the scour development process is between two independent trials performed in identical test conditions. Three experiments were replicated for this purpose[25]. A direct comparison of the scour hole volumes calculated for one original dataset and the corresponding replicated trial is shown in Figure 4.5. Changes in the discrepancies with time are observed by plotting the difference between paired time-series outputs against their corresponding mean value (Figure 4.6). As identical test conditions were used, measurement discrepancies between the replicated datasets are normally distributed. Therefore, 95% limits of agreement ($\mu \pm 1.96\sigma$) can be superimposed to observe the output agreement[26].

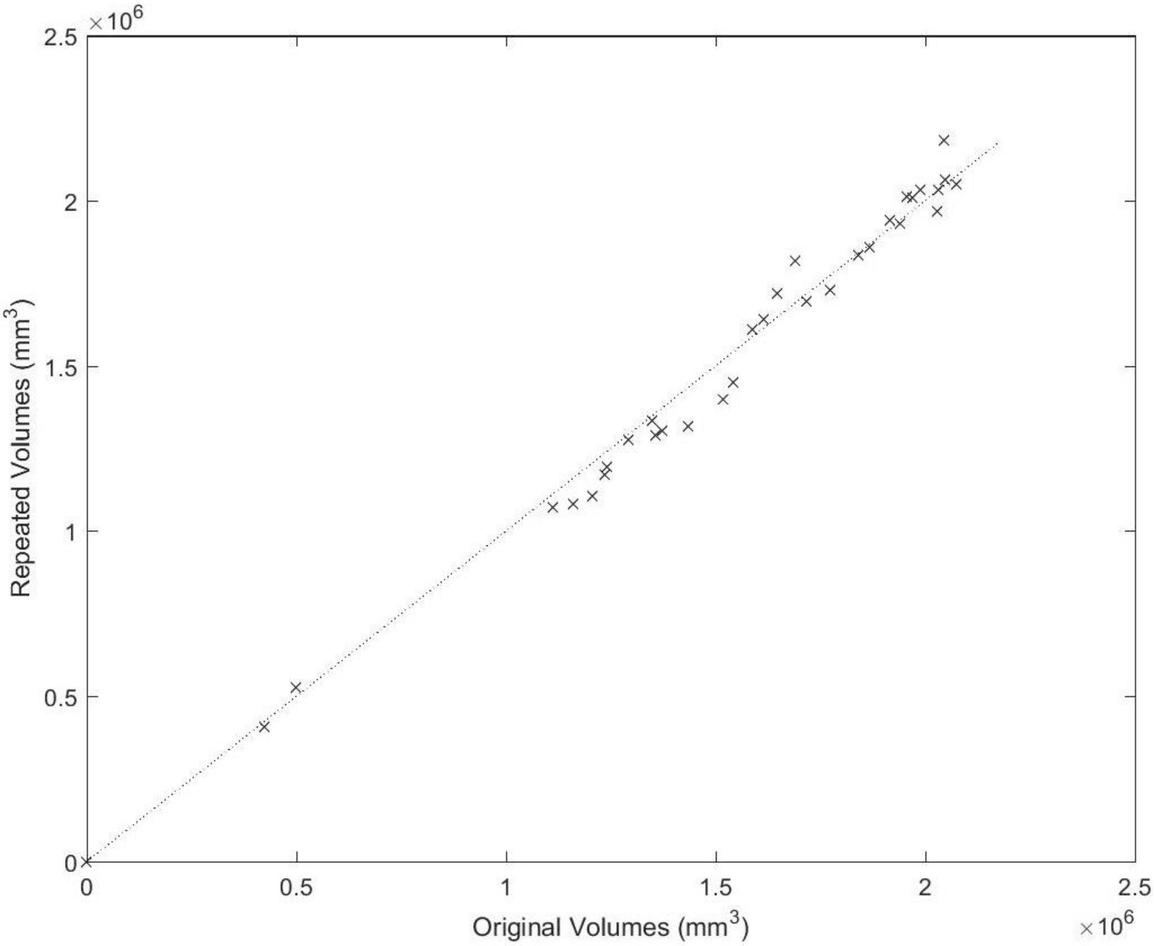

Figure 4.5 Direct comparison between scour hole volumes for a replicated trial.

---

[25] Trials 2, 3 and 13 correspond to replicate trials 11, 12 and 16, respectively.

[26] If the mean significantly deviates from zero, the discrepancy is defined by systematic error.

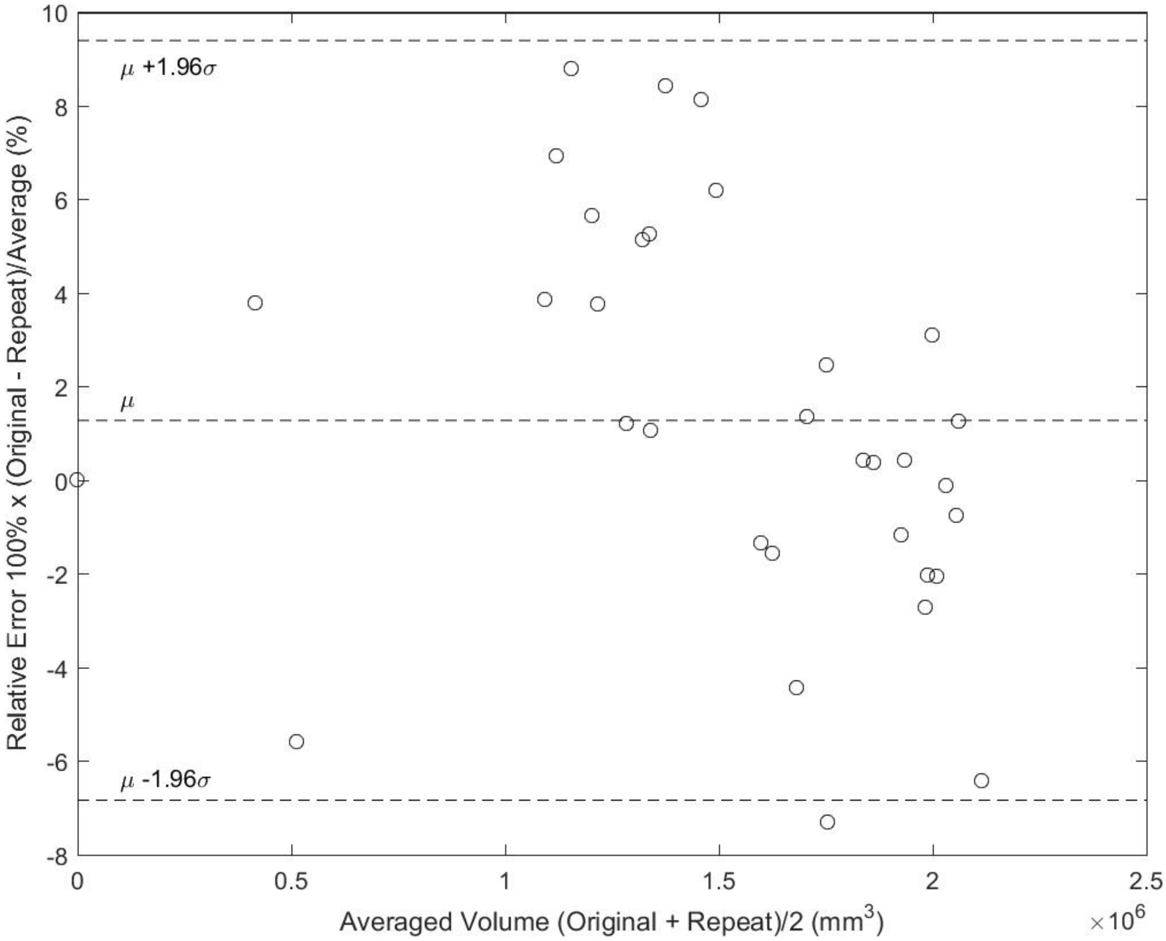

Figure 4.6 Relative differences between paired volumes and their corresponding mean value.

Both measurement sets show a striking agreement over the entire scour development process (Figure 4.5). The variation between the two volume datasets shows an equal deviation of outputs around the theoretical line of equality with time, with a mean error of 1.27% ± 8.11% (95% limits of agreement) relative to the original trials' measured scour volume. The random fluctuations in error around a near-zero mean value (Figure 4.6) shows that the results are removed from significant bias. The non-zero mean is acceptable as the deviation can be accounted for by standard error in the mean, which has a 95% confidence interval range[27] of -0.22% to 2.76% that encapsulates the zero bias criterion (Bland and Altman, 1999).

The relative difference measured at the location of maximum depth for the same replicated trials is presented in Figure 4.7. The mean relative error is 0.12% ± 4.44% (95% limits of agreement), with a corresponding 95% confidence interval in the mean discrepancy of -0.69% to 0.94%. The discrepancies are minor and show good agreement, with negligible deviation from a zero mean. The standard deviation for both comparisons is minor and can be attributed to differences in the measurement times between the coupled data points, most evident during early scour

---

[27] Calculated using the standard error by considering (N-1) degrees of freedom and the Student t-probability distribution for small samples.

development. The variability for the volume measurements are a function of cubic length scale discrepancies and as such are notably higher. These results provide evidence of repeatability in the measuring technique.

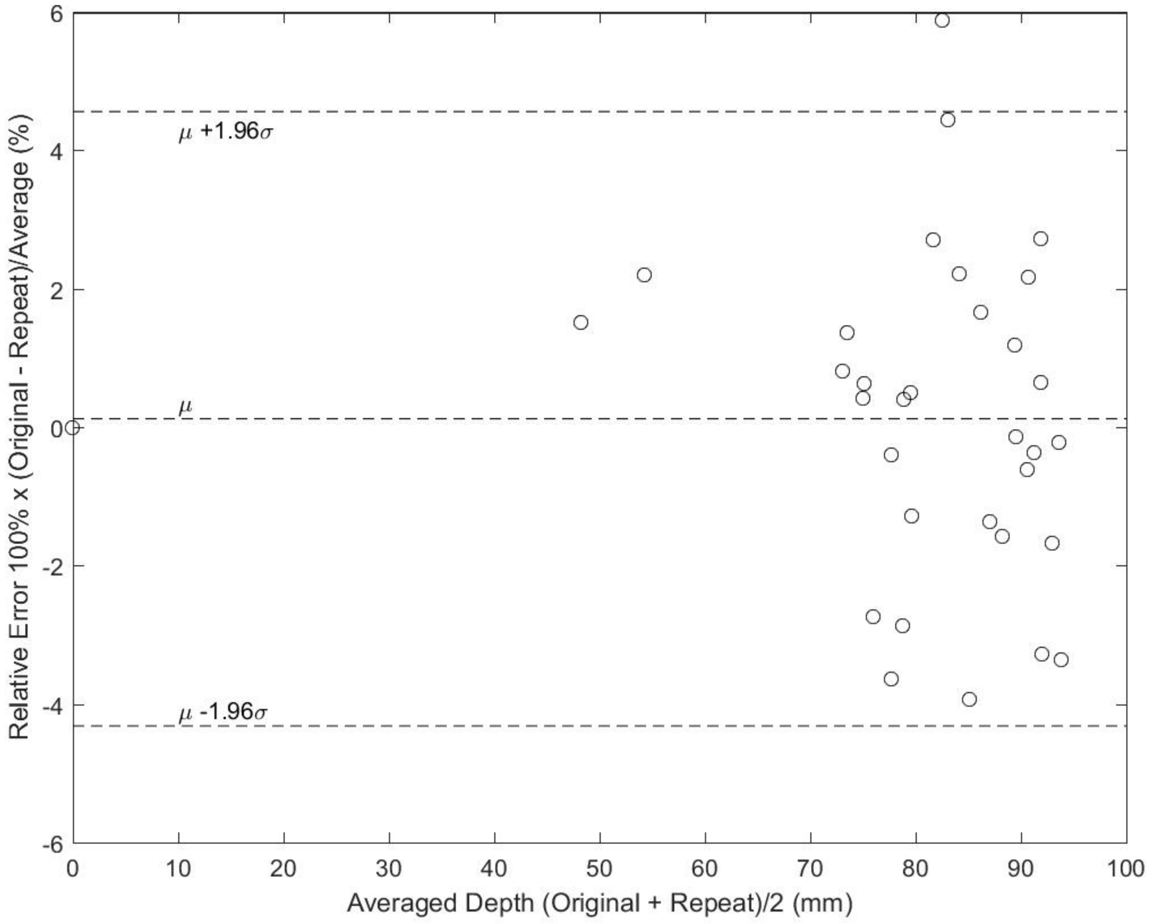

Figure 4.7 Relative differences between paired depths and their corresponding mean value.

4.4.1 Invasiveness of Equipment

The sonar remains fully submerged throughout the experiment phase. To assess whether the equipment had any meaningful impact on the scour process, whilst verifying that the non-zero mean discrepancy found in the repeatability validation was not a product of equipment interaction, its invasiveness was tested by repeating a single trial with the equipment absent. With this setup, invasiveness was examined by monitoring the development of the maximum scour depth (PG3).

The development profile for the maximum scour depth with and without the presence of the sonar equipment shows excellent agreement with time (Figure 4.8). The differences between paired time-series outputs against their corresponding mean value shows a mean discrepancy of -0.96% ± 1.97% (95% limits of agreement), relative to the scour flat-bed datum (Figure 4.9). The small error range infers that the measurements with and without the sonar presence are negligible. This makes the proposed experimental equipment fit for purpose, providing that the flow depth is large relative to the pier diameter. While untested, it should be noted that issues of equipment invasiveness may be encountered when using shallower flow depths as the equipment may impede the natural development of the horseshoe vortex that drives the local scour process; similar to the effect of the surface roller on the horseshoe vortex for flows where $y/a < 1.4$.

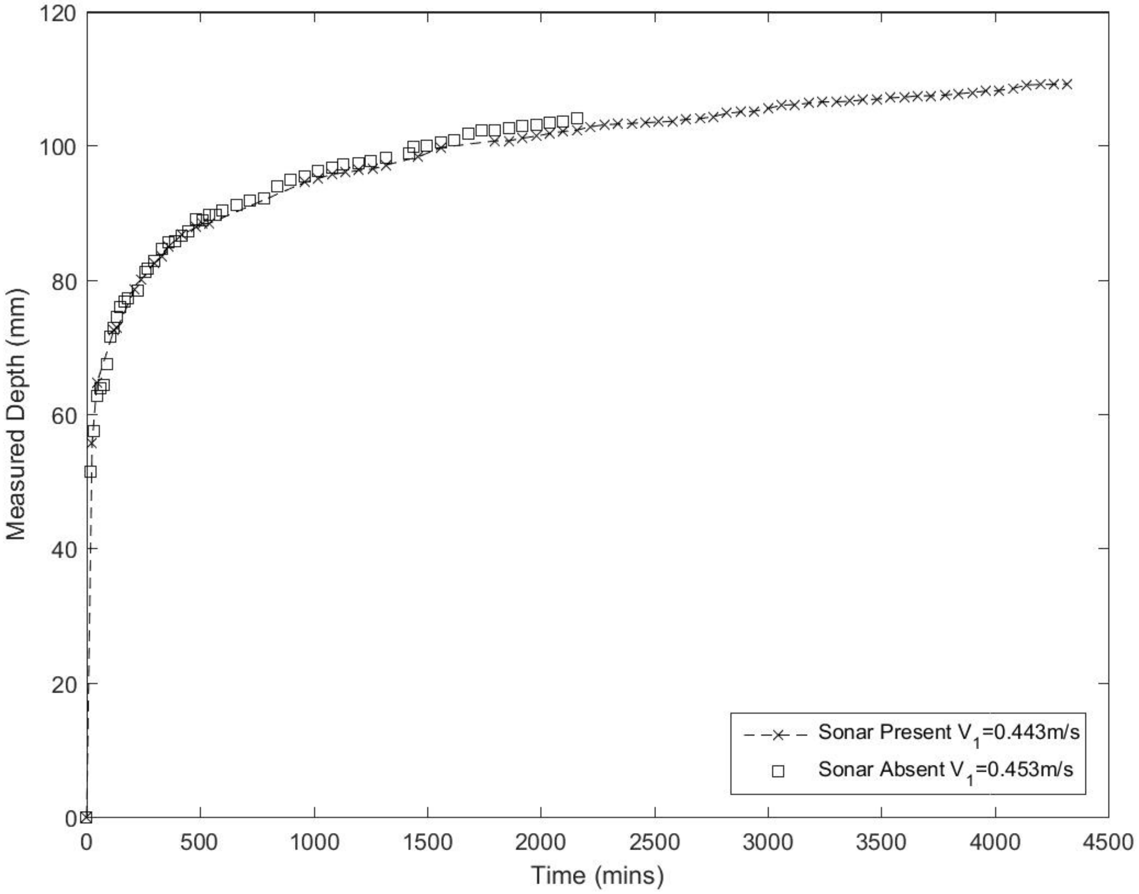

Figure 4.8 Scour depths development with and without the presence of the sonar equipment.

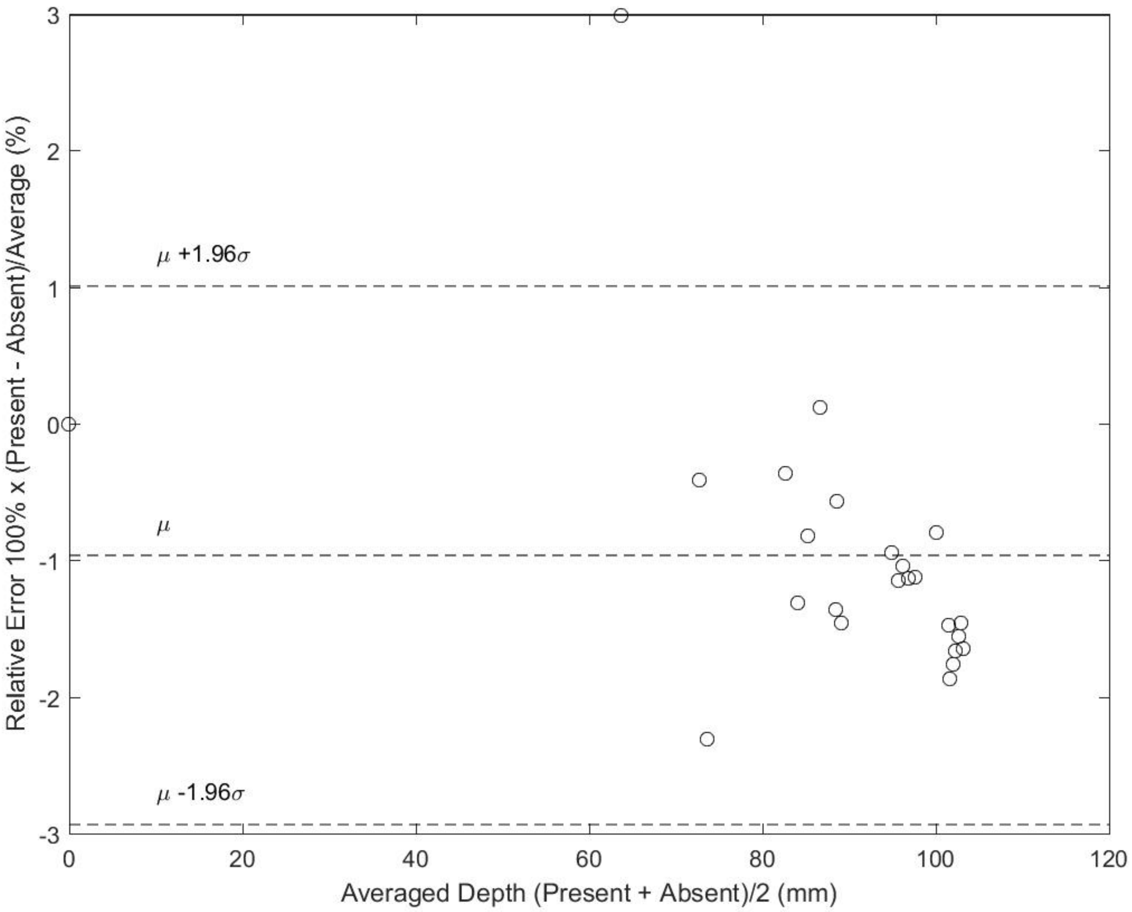

Figure 4.9 Relative scour depth differences between paired time-series outputs from a trial replicated with and without the sonar equipment present.

The upper and lower 95% confidence intervals for the mean during invasiveness tests is -1.39% and -0.54%, respectively, inferring that minor bias exists in the discrepancies. However, the limits of agreement for the full dataset is narrow, with the output values easily contained within the 95% limits of agreement with exception to a single outlier. To assess the influence of this outlier on the calculated confidence intervals, the mean and 95% confidence limits were recalculated excluding this value. Accordingly, the measurement discrepancy converted from -0.96% $\pm$ 1.97% to -1.14% $\pm$ 1.16%. While a negligible change in the mean is observed, the span of the limits of agreement shows a substantial 41% reduction, indicating high sensitivity to this anomaly. This outlier is presumably the result of rapid bed elevation changes during early scour development, which can cause high discrepancies if data points between two compared trials are not measured in the same timeframe.

The notable discrepancy bias in the mean can be accounted for by consideration of the difference in inflow velocity (V_1= 0.44 m/s and 0.45m/s with the sonar present and absent, respectively). To illustrate this, the depths measured with the sonar present were adjusted by the ratio between the measured flow velocities (at time t) for each paired output[28]. With the differences in velocity adjusted between paired measurements (Figure 4.10), the discrepancies convert from -0.96% $\pm$ 1.97% to -0.50% $\pm$ 1.89%. This characterises a mean discrepancy as a similar order of magnitude to the sonars cell resolution (0.42-0.63mm). Interestingly, the Spearman rank correlation (s_d) coefficient converts from s_d=-0.63 to s_d=-0.09, implying that any apparent trend in the discrepancies can largely be accredited to differences in trial flow velocity.

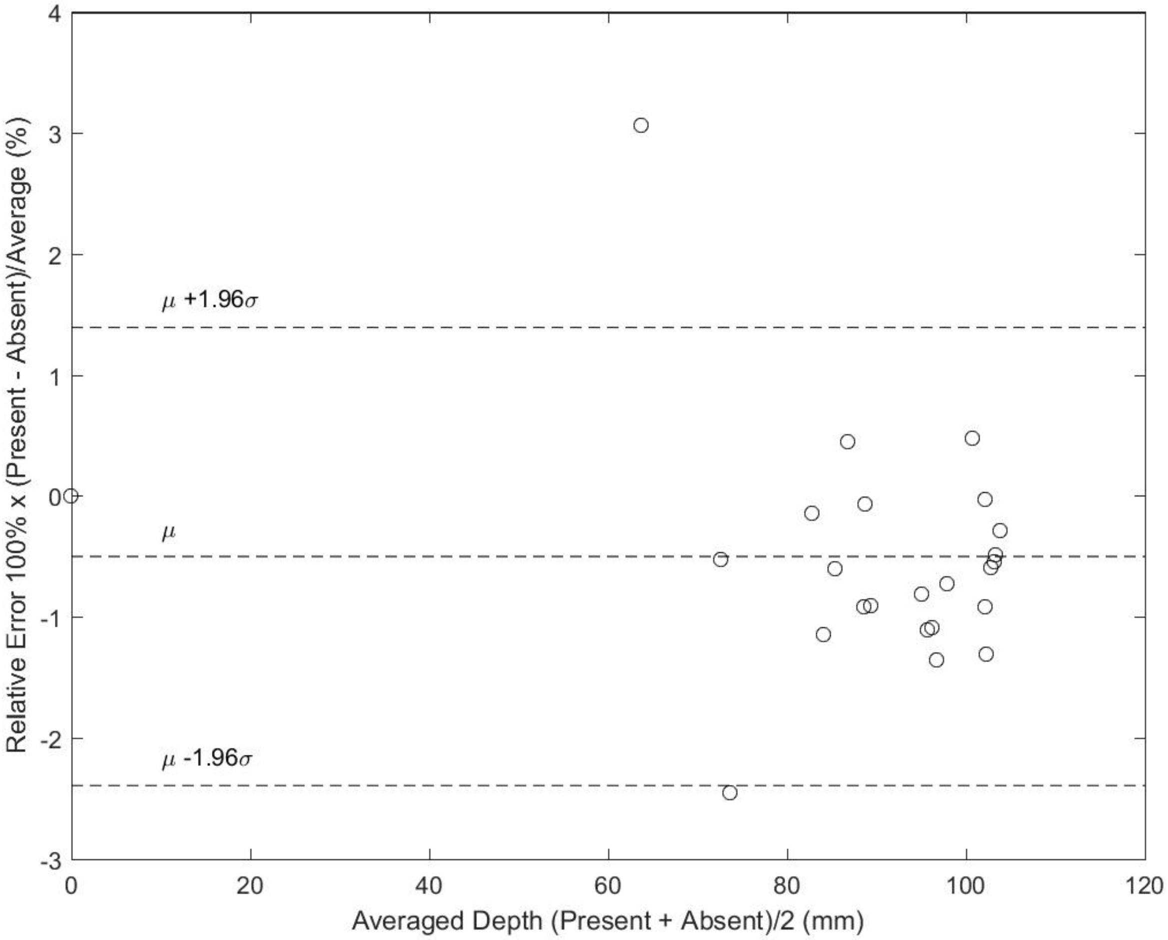

Figure 4.10 Velocity-adjusted differences between paired outputs to assess sonar invasiveness.

4.4.2 Sonar Scanning Precision

The standard error in the volume measurements was calculated by repeating measurements of the same scoured bed profile. Five measurements were recorded in succession at the end of the sonar-absent trial by slowly reducing the inflow rate until standing water conditions prevailed to allow the sonar scanning equipment to be inserted. These outputs are shown in Figure 4.11; consecutive outputs are adjoined using a dashed line. The standard deviation of the relative

---

[28] It is well known that in clear water conditions the scour depth scales linearly with the flow intensity (V_1/V_C) (e.g. Melville, 2008); thus directly scaling the scour depths to accommodate the difference in flow velocities in this instance is not unreasonable.

error[29] for volume and depth measurements is 0.99% and 0.34%, respectively. The measured range of the computed volumes and scour depths was 2.86% and 0.84%, respectively.

The discrepancies are notable, but not significant. The sonar equipment had been shown previously to be non-invasive to the development of scour, suggesting the errors observed here are precision-driven. However, the maximum discrepancy between the values of scour depth recorded here is ~1% of flow depth in magnitude and may be the result of sediment mobilisation within the scour hole which is not unreasonable as equilibrium trial conditions were not reached.

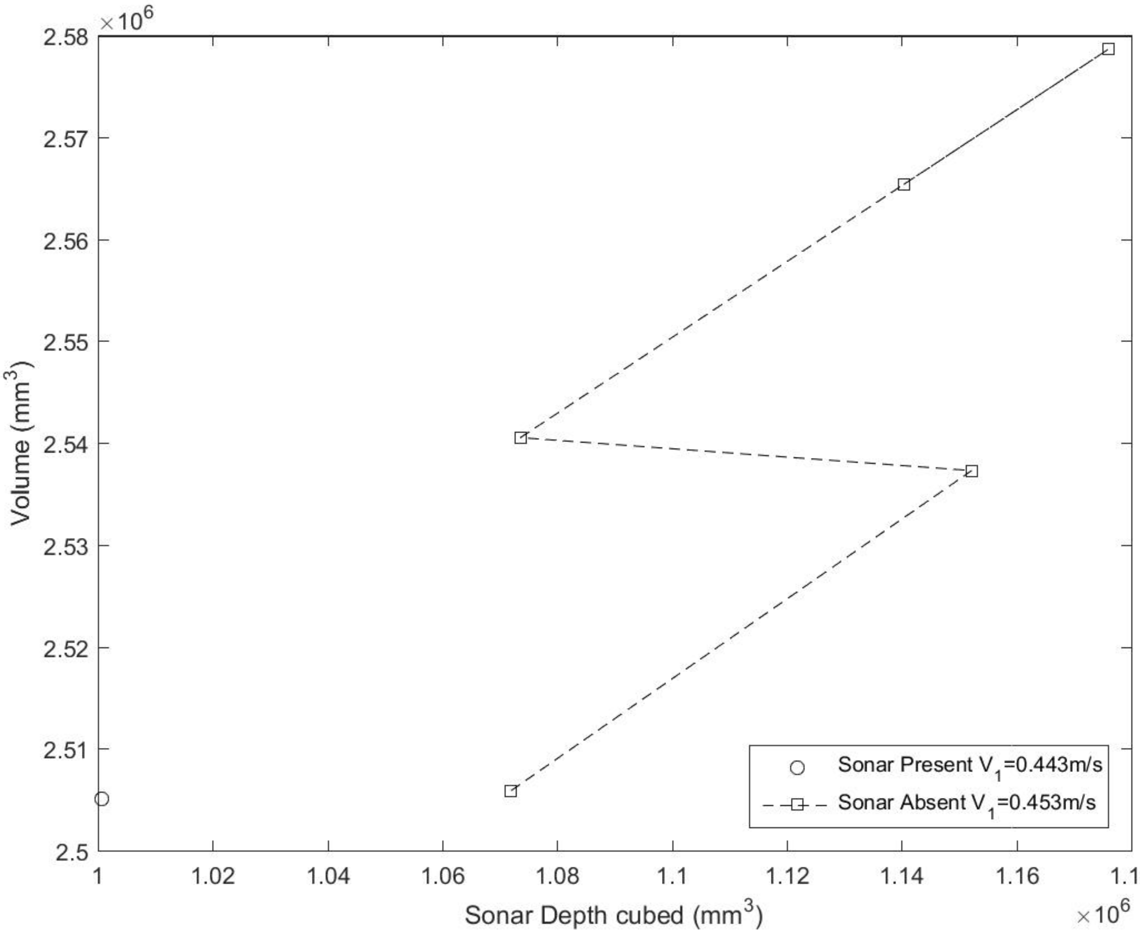

Figure 4.11 Variations in scour hole volume and depth measured for the same scoured bed.

4.4.3 Slider Scanning Configuration

The Konova stepper motor was configured to move the mounted sonar steadily as it performed continuous acoustic swaths of the underlying bed surface (this continuous procedure is referred to as *Automatic* scanning from hereon in). However, the sonar is unable to complete a single transverse swath and receive its acoustic return instantaneously, meaning that outputs from each

---

[29] The (%) volume error is relative to the initial flat-bed condition (i.e. $V_{ol} = 0$), whilst the (%) scour depth is relative to the flow depth within the scour hole.

individual swath profile may not have been measured perfectly transverse to the sonars motion. To eradicate concerns that the assumption of uniform longitudinal spacing may not be appropriate, the speed of the steady continuous motion was calibrated pre-trial to match a baseline measurement scanned manually (moving the sonar in pre-defined steps for static scanning[30]) over a flat-bed surface around the test pier. The calibrated speed was then verified for measuring scour surfaces by interspersing manual and automatic scans during a single trial. An overlain comparison between the computed scour volume and the corresponding maximum scour depth profiles using both scanning configurations are given in Figure 4.12 and Figure 4.13, respectively.

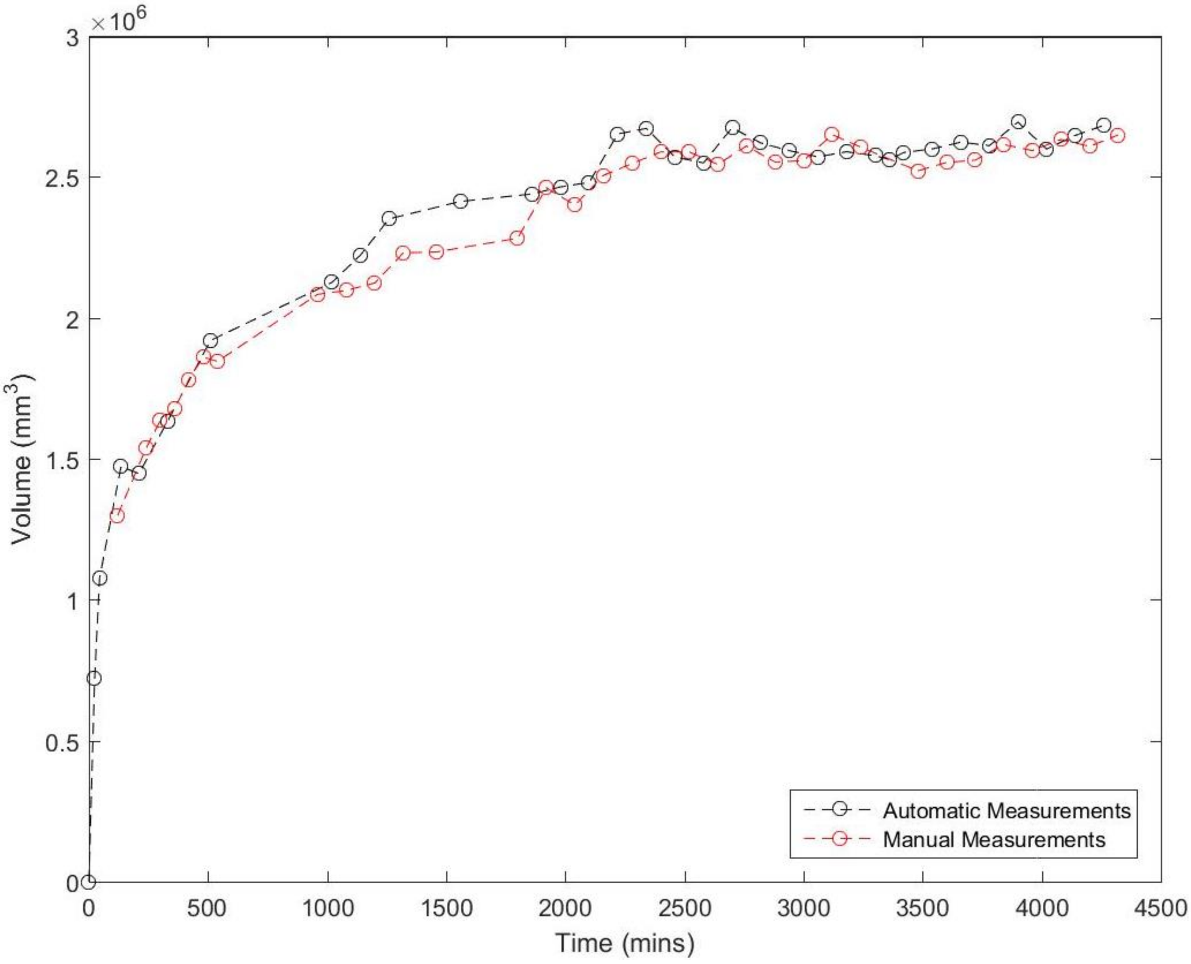

Figure 4.12 Example of volume variation using automatic and manual slider configurations.

---

[30] Each manual scan covered; several measurements of the upstream reference plate, high-density scanning (5mm stream-wise resolution) of the scour hole front, and medium-density scanning (1cm stream-wise resolution) upstream of the scour hole and downstream of the test pier.

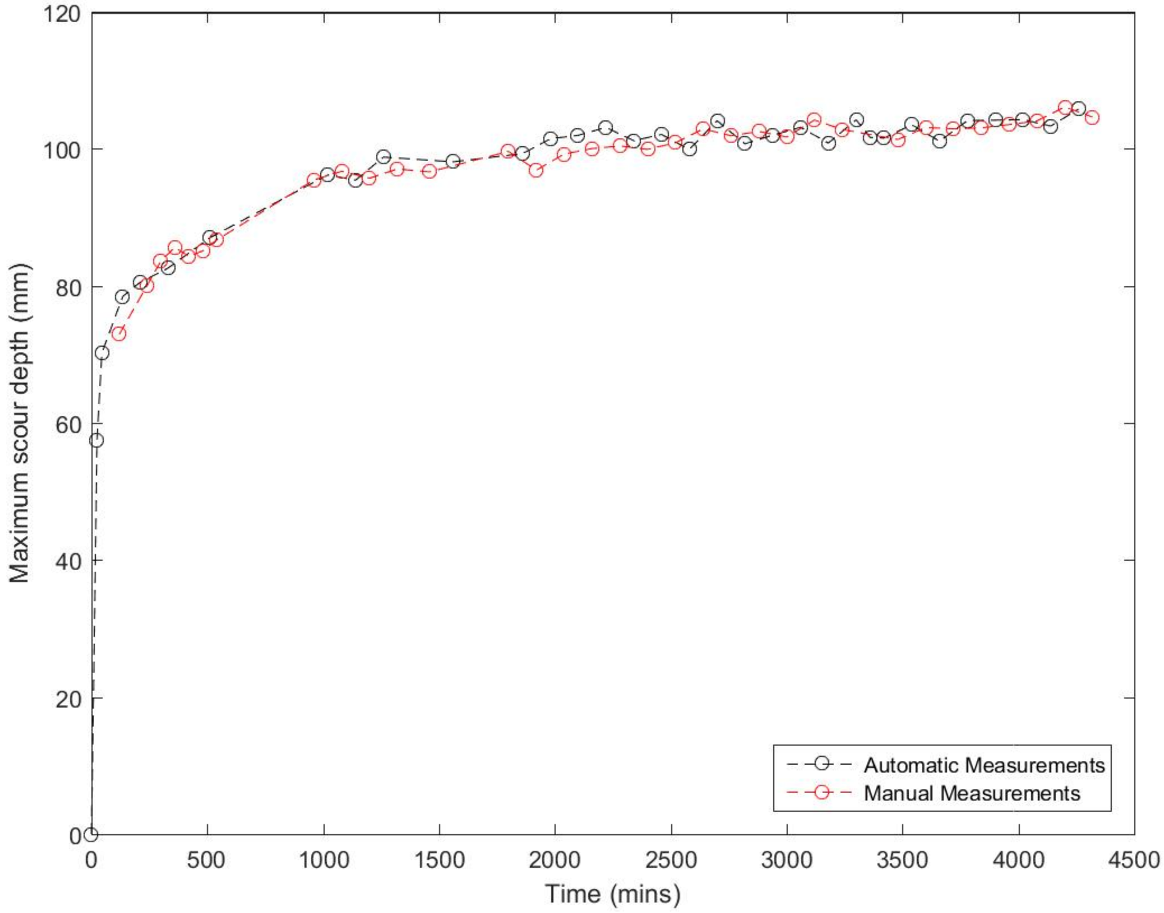

Figure 4.13 Example of depth variation using automatic and manual slider configurations.

Both figures show excellent agreement on the magnitude of the scour hole geometry, outlining the consistency between the automated and manual measurement techniques. For each time-step, the applied measuring technique was alternated, meaning that outputs from either technique are attributed to different periods in time. The level of agreement between the two techniques was therefore statistically tested by considering bulk elevation errors relative to the gauged measurements (PG2 and PG3). The bed elevation errors at both locations are shown using a notched box-plot in Figure 4.14 and Figure 4.15, respectively.

The notch provides a 95% confidence interval of the median that is used for assessing the statistical similarity between two variables. For both measurement locations, the notches of the plot clearly overlap, meaning that a null hypothesis can be accepted with an approximate 95% confidence (Chambers *et al.*, 1983). The null hypothesis considers the two variables being compared are statistically similar, suggesting data resulting from automated scanning can be considered true and an accurate representation of the underlying bed.

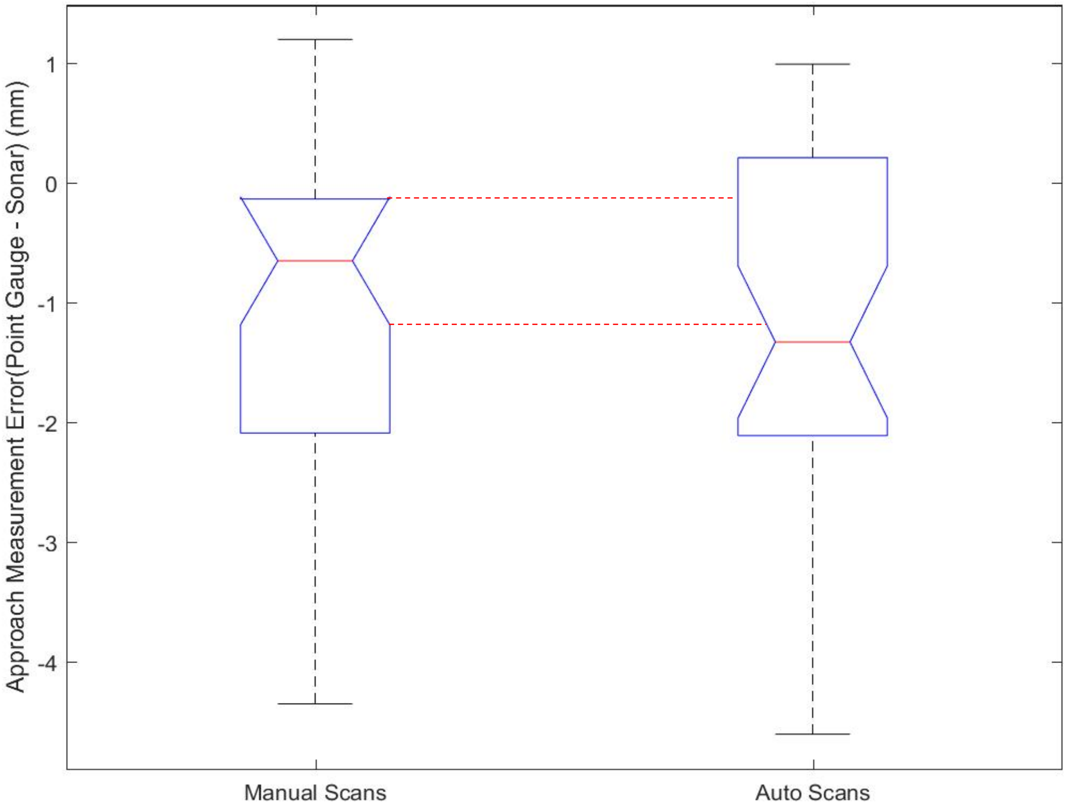

Figure 4.14 Notched box plots of approach elevation errors using manually- and automatically-generated surface profiles.

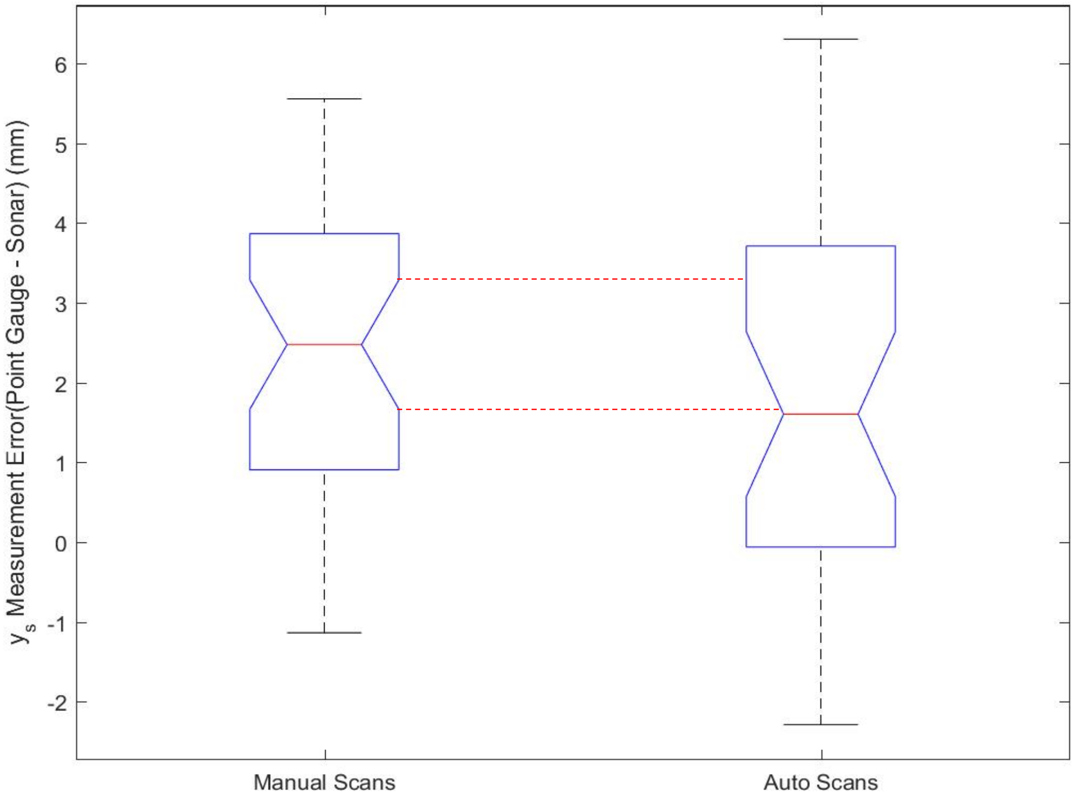

Figure 4.15 Notched box plots of maximum depth elevation errors using manually- and automatically- generated surface profiles.

4.5 Summary

The performance of the sonar scanning technique was assessed as a means to measure the development of the scour hole with time. The validation has shown the sonar to be non-invasive in practice (having a negligible effect on the scour development process) and repeatable (the measurements are accurate as replicated outputs are notably consistent). Whilst it is acknowledged that issues with invasiveness of the equipment may be experienced for shallower flow depths, identification of a flow shallowness lower bound was not investigated in this study. The accuracy of the bed elevation measurements were recorded to be within 1% relative to the flow depth, provided that lower bound limits for the test pier diameter $a > 5$cm and the flow intensity $V_1/V_c > 0.6$ are adhered to. These bounds were identified from analysis of four trials (Trials 3, 5, 6 and 10) that were subsequently removed from analysis due to systematic error.

The remaining trials (excluding those repeated for validation) provide a comprehensive recording of a developing scour hole in both time and space for different flow conditions that will be used to analyse the development of scour geometry in time with confidence.

Chapter 5: Geometric Development of Scour Holes

5.1 Introduction

In the previous Chapter, the performance of the technique used to measure the development of the scour hole in comprehensive detail over time and space was addressed. The assessment identified minimal and consistent errors when using the technique to scan both profiled and flat-bed surfaces. Moreover, repeated trials with and without the equipment showed that the measurement method is non-invasive to vortex development which drives the scour process and is repeatable. The outputs from the temporal studies can, therefore, be used to interpret both the development and similarity of the scour hole geometry with confidence.

The analysis of all 11 experiment trials is presented. As discussed in Chapter 3, the experiments were conditioned by adjusting the pier and sediment diameter to variate the condition of the flow regime within the scour hole. The variables and end-of-trial outputs for these trials are presented in Table 5.1. All trials were completed for a minimum period of 36 hours.

Table 5.1 Characteristic key variables and end-trial outputs. The validation in Chapter 4 reduced the number of valid trials for analysis. The Trial numbers have therefore been adjusted (the superseded Trial number given in brackets) and are used in the subsequent text. t_{end}, $y_{s,\ end}$, $V_{ol,\ end}$ *= time, maximum scour depth and scour hole volume recorded at trial termination;* η *= Kolmogorov length scale, computed using* $(\upsilon^3 a/C_d V_1^3)^{0.25}$ *as per Manes & Brocchini (2015) (see Section 2.5). The coloured Trial column distinguishes between fully-rough (black), transitionally rough (green), transitionally smooth (blue) and hydraulically smooth (red) flow regimes.*

Trial	a (mm)	d_{50} (mm)	$y_{s,\ end}$ (mm)	$V_{ol,\ end}$ ($\times 10^{-3}\ m^3$)	t_{end} (hrs)	a/d_{50}	$y_{s,end}$ /a	V_1/V_c	Re*	d_{50}/η
1 (1)	51	2.62	63.3	0.349	36	19.5	1.24	0.71	75.2	90.6
2 (2)	101	2.62	109.2	2.648	72	38.5	1.08	0.71	73.7	75.3
3 (4)	76	2.62	82.8	1.064	36	29.0	1.09	0.71	80.6	86.4
4 (7)	101	1.61	100.5	1.940	36	62.7	1.00	0.81	41.1	45.3
5 (8)	101	1.61	65.2	0.603	36	62.7	0.65	0.63	30.9	36.6
6 (9)	76	1.61	78.6	0.958	50	47.2	1.03	0.80	43.1	50.4
7 (13)	101	0.86	95.8	2.073	36	117.4	0.95	0.93	15.8	20.2
8 (14)	76	0.86	87.5	1.234	36	88.4	1.15	0.99	17.6	23.5
9 (15)	51	0.86	65.1	0.500	36	59.3	1.28	0.95	17.1	25.4
10 (17)	101	0.28	95.0	1.861	36	360.7	0.94	0.99	3.8	6.0
11 (18)	76	0.28	81.0	0.906	36	271.4	1.07	0.98	4.4	7.1

5.2 Scour Geometry – Volume

The experiments allowed the geometric development of the entire scour hole to be measured, as a function of time. The initial focus is on two key geometrical properties of it, namely, the scour hole volume (V_{OL}) and the maximum scour depth (y_s). Here, the scour hole volume is defined as the volume of sediment removed upstream of the piers' diameter perpendicular to the flow direction. The downstream boundary of the scour hole volume was selected to coincide with the maximum scour hole width W to enable a direct assessment between the geometric size and boundaries of the scour hole. This is covered later in this Chapter. The variation of the volume and scour depth as a function of time are presented in Figure 5.1 and Figure 5.2, respectively.

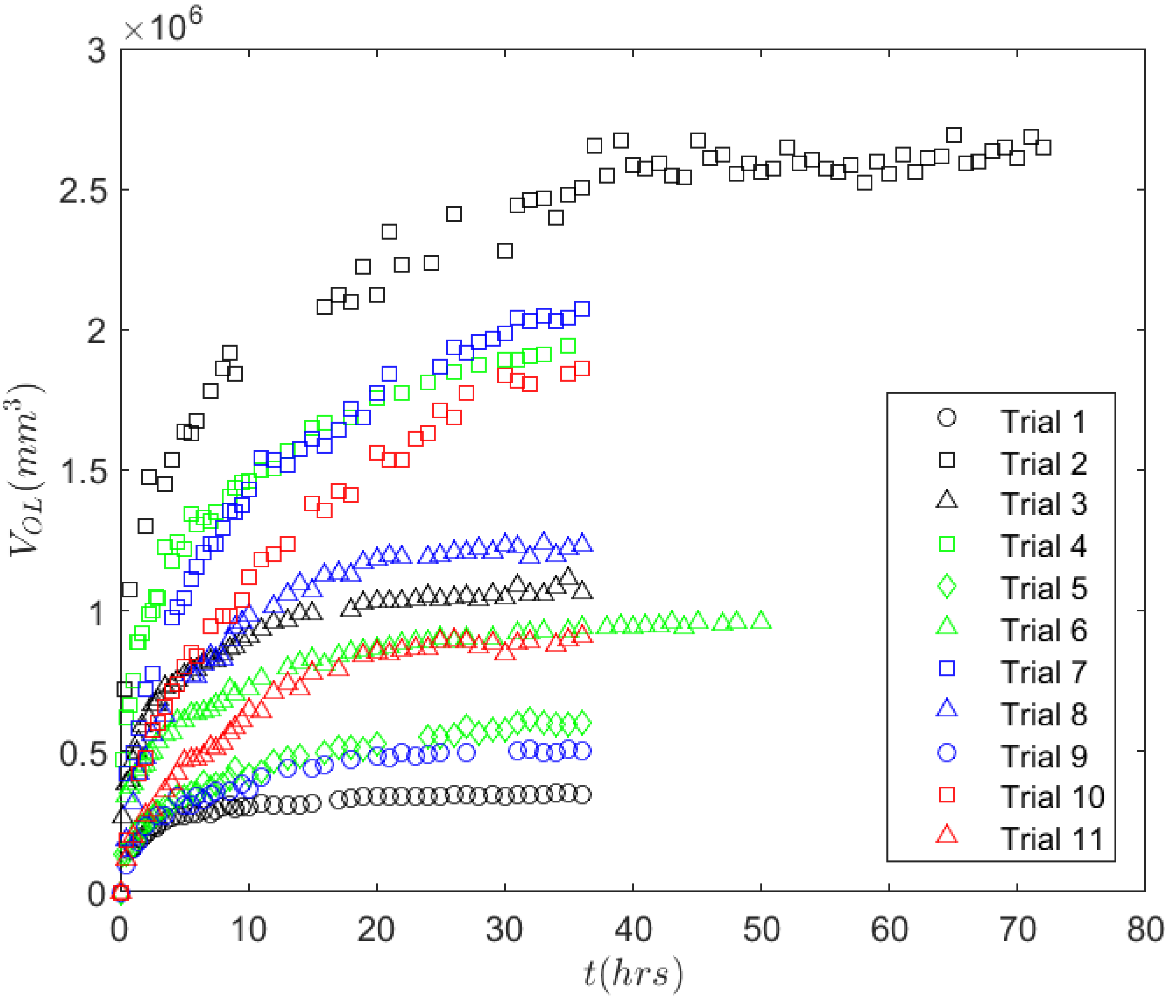

Figure 5.1 Development of the scour hole volume with time for all trials. Symbol colour differentiates the trial flow regime into fully-rough (black), transitionally rough (green), transitionally smooth (blue) and hydraulically smooth (red). The trial pier diameter is also distinguishable by shape, with circles representing a=51mm, triangles representing a=76mm and a square or diamond ($V_1/V_c = 0.6$) symbolising a=101mm. These are used consistently from hereon in for experiment comparison.

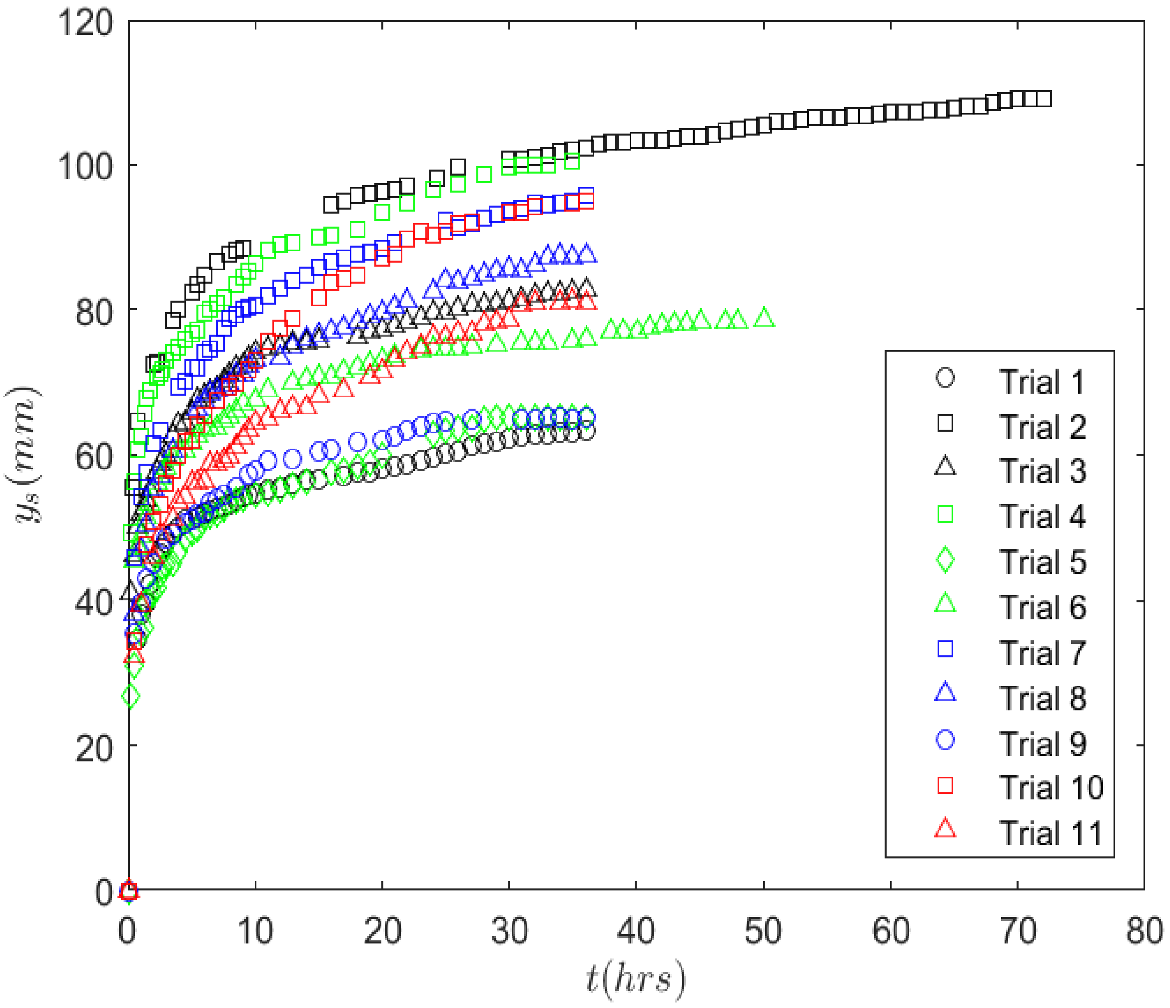

Figure 5.2 Maximum scour depth development with time for all trials.

The variation in the scour hole volume with time shows a striking agreement with the corresponding development in maximum scour depth for all trials. During the first 20% of the trial duration[31], the volume develops rapidly to more than half of the end-trial scour hole volume. Beyond this, the rate of volumetric scour progressively decreases approaching a plateau. Interestingly, the rate of early volumetric scouring is dependent on the flow regime within the scour hole. For fully-rough datasets, the scoured volume after only 20% of the trial duration was observed to be 75-80% of the scour volume measured after 36 hours. For the same development stage, the equivalent scour volume for trials in the hydraulically smooth regime is 55%[32], implying the rate of volumetric scour development decreases more gradually as the regime becomes more influenced by viscosity.

The transitionally smooth and hydraulically smooth datasets were operated at a flow intensity that was higher than the rough trial flow conditions. Experiments operated at a higher flow

---

[31] A reference duration of 36 hours for all trials.

[32] For transitionally rough and smooth cases the magnitude of scour is 66-70% and 63-65%, respectively.

intensity are characterised by a sharper, more immediate increase in the rate of scour during the early stages of scour (Melville and Chiew, 1999). Accordingly, the observed rates of early scouring for the smooth trials are likely higher than expected if the same flow intensity as the rough trials had been used. This highlights the increased differential between the rates of volumetric scour with regime.

5.2.1 Similarity Analysis

As a first step, the analysis of the scour hole is restricted to the simplest case concerning experimental data pertaining to the fully-rough regime only, namely trials 1-3 in Table 5.1. In these trials, the undisturbed flow is in the fully-rough regime (i.e. $Re^{*} > 70$) and, following Manes and Brocchini (2015), the ratio d_{50}/η is very large (i.e. between 75.3 and 90.6).

The effects of viscosity add further complexity to the problem (e.g. Lança *et al.*, 2016) and will be discussed in the sections that follow this initial analysis.

The scaling of the developing scour hole volume (V_{OL}) and the maximum scour depth cubed (y_s^3) is shown for all three trials separately in Figure 5.3(a-c). For all three trials, there is striking evidence that the scoured volume develops with the scour depth cubed through three linear regimes, whose origin may be interpreted as follows. The first regime represents the initial formation of the scour hole, where scour presumably initiates in the flanks and transfers round to the front of the scour hole. This movement coincides with the generation and full development of the HS vortex (Dargahi, 1990). The second regime is associated with the scour hole developing geometrically as an inverted frustum of a cone, with the volume of the HS scaling steadily over time. The presence of a third regime signifies a stage in the volume development process where the gradient of the linear scaling reduces significantly. Observations of scour hole volume stabilisation after significant scour development period corroborates findings of an inflection point in the scaling $V_{OL} \sim y_s$ from Link (2008), although a direct comparison to the data reported here is invalid due to differing definitions of the scour volume region.

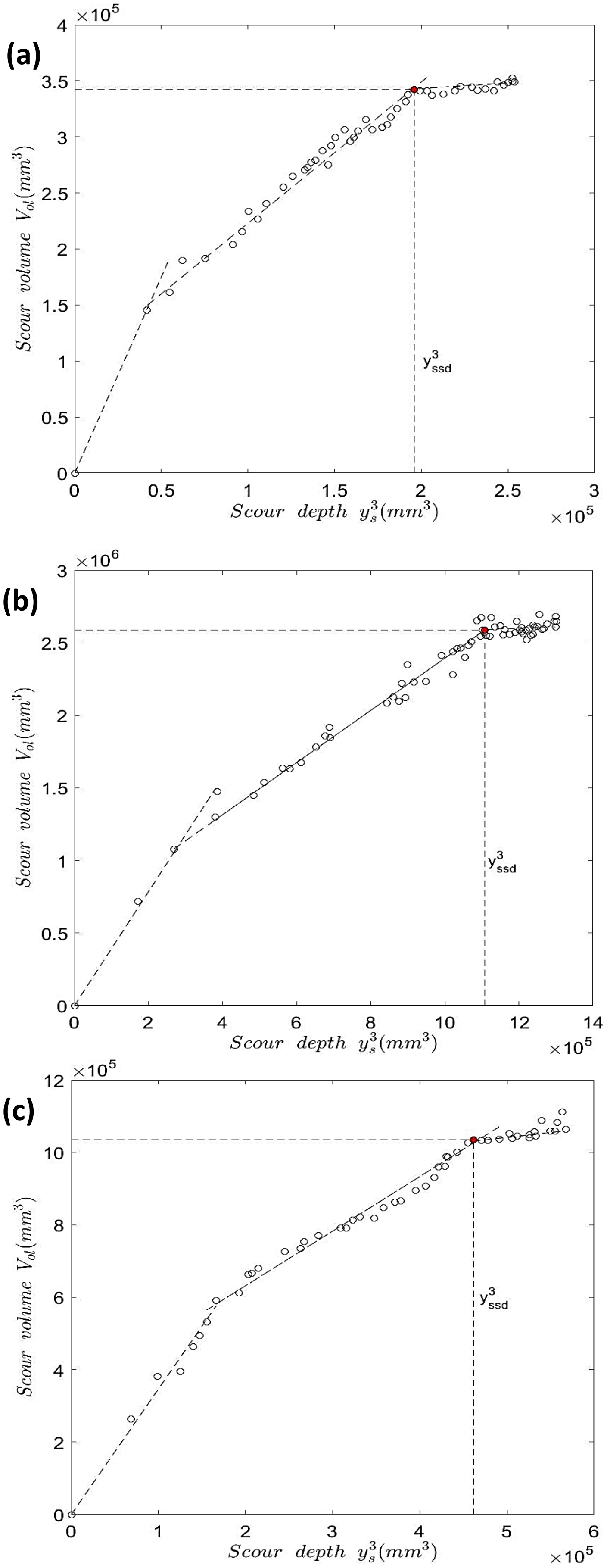

Figure 5.3 Development of scour hole volume with the cubic of the maximum scour depth for (a) 51mm, (b) 101mm and (c) 76mm diameter test pier in the fully-rough regime

The ratio between the scour hole volume (V_{OL}) and maximum scour depth cubed (y_s^3) for all the fully-rough-regime experiments with respect to time is captured in Figure 5.4, where time is normalised by the crossover time ($\mathrm{t_{ssd}}$) which, as shown in Figure 5.3, identifies the point of crossover between the second and third regimes. Figure 5.4 shows a change between the development before and after the crossover point. Pre-crossover, the magnitude of $\mathrm{V_{OL}/y_s^3}$ shows an initially rapid decrease followed by a plateau, which is associated with the development of regime 2. The transition from the second regime to the third regimes is characterised by a notable change in gradient of the $\mathrm{V_{OL}/y_s^3}$ with time which is owing to a step change in the relationship $\mathrm{V_{OL}/y_s^3}$ that is consistent with observations in Figure 5.3(a-c) of an increasing scour depth with respect to a more stable scour hole volume.

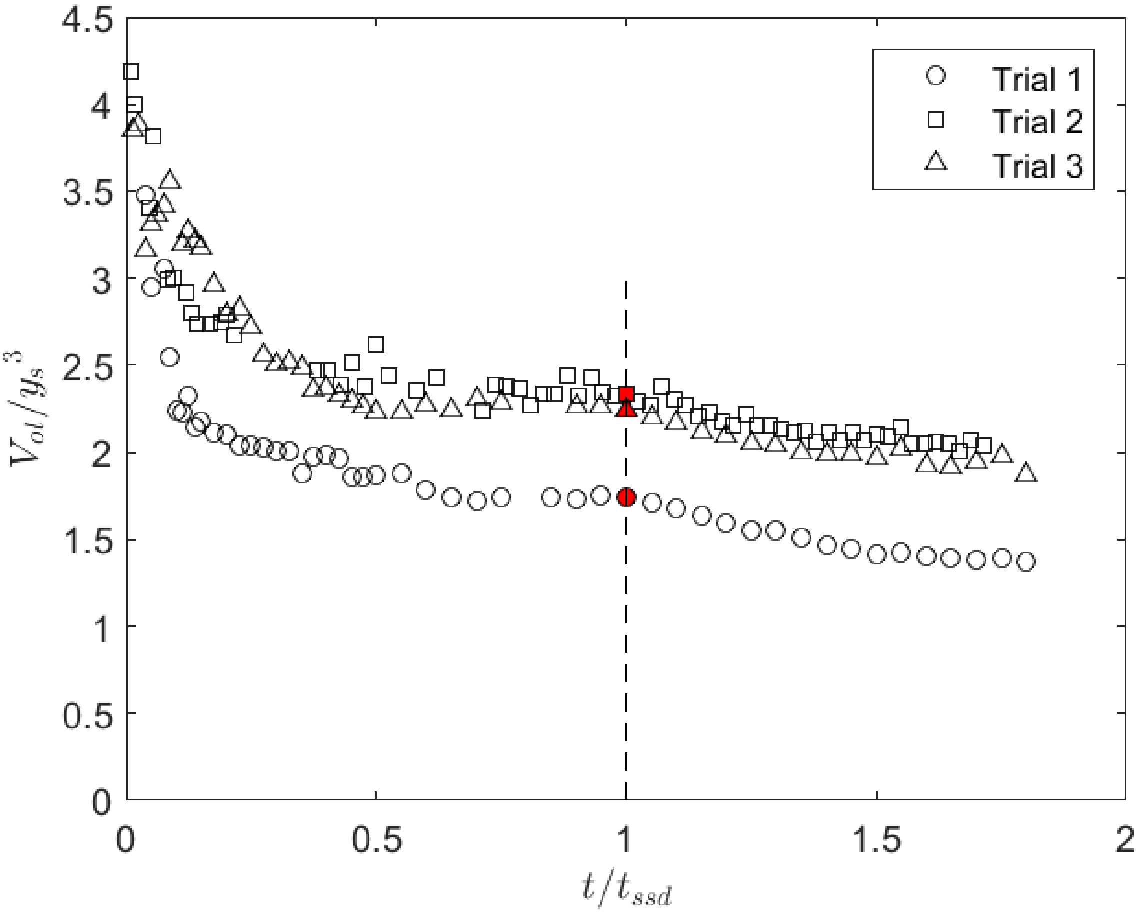

Figure 5.4 *Normalised scour hole volume with time (normalised by the crossover timescale).*

Table *5.2* shows the results that stemmed from an unconstrained multiple-linear regression analysis that was applied to the data for all three trials to identify the crossover point characteristics for transition to the third regime. The observed change, denoted as the crossover point in the subsequent text, characterises a change in the physics of clear water local scour evolution which is herein interpreted using two approaches: one based on the phenomenological theory of turbulence, which follows the line of thought developed by Manes and Brocchini (2015)

(Section 5.2.2), and; another based on topography analysis of the erosion and deposition rates measured within the scour hole (Section 5.2.3).

Table 5.2 *Crossover characteristics.* t_{ssd}, y_{ssd} *and* $V_{ol,\ ssd}$ *= time, maximum scour depth in front of the pier and scour hole volume within the vicinity of the HS vortex, at the point of crossover between the second and third regimes.*

Trial	t_{ssd} (hrs)	y_{ssd} (mm)	$V_{ol,ssd}$ $(10^{-3}m^3)$
1	20	58.1	0.342
2	42	103.5	2.589
3	20	77.3	1.035

5.2.2 Linking Turbulence Phenomenology with Scour Dynamics

The crossover point between the second and third regimes characterises a stabilisation in the bulk scour volume development, relative to the steadily-increasing maximum scour depth. This regime can be interpreted within the context of the phenomenological theory proposed by Manes and Brocchini (2015), where fully-rough conditions were an important hypothesis. Accordingly, the power of the HS vortex P (i.e. the turbulent kinetic energy produced/dissipated by the HS vortex) per unit mass M can be quantified as (see Section 2.5.3):

$$\epsilon = \frac{P}{M} \sim \frac{\frac{1}{2}\rho C_D a L V_1^3}{\rho V_{OL}} \tag{5.1}$$

where C_D is the piers' drag coefficient, and aL is the frontal area of the cylinder exposed to scouring. Using the scaling assumption $L \sim y_s$, Eq. (5.1) converts to

$$\epsilon \sim \frac{C_D a V_1^3}{2} \frac{y_s}{V_{OL}}. \tag{5.2}$$

Therefore, the rate of turbulent kinetic energy (ϵ) production scales with the ratio between the maximum scour depth and its corresponding scour hole volume. Figure 5.5 shows $\epsilon \sim y_s/V_{OL}$ as a function of a normalised time t/t_{ssd}, where t_{ssd} is the time when the crossover occurs.

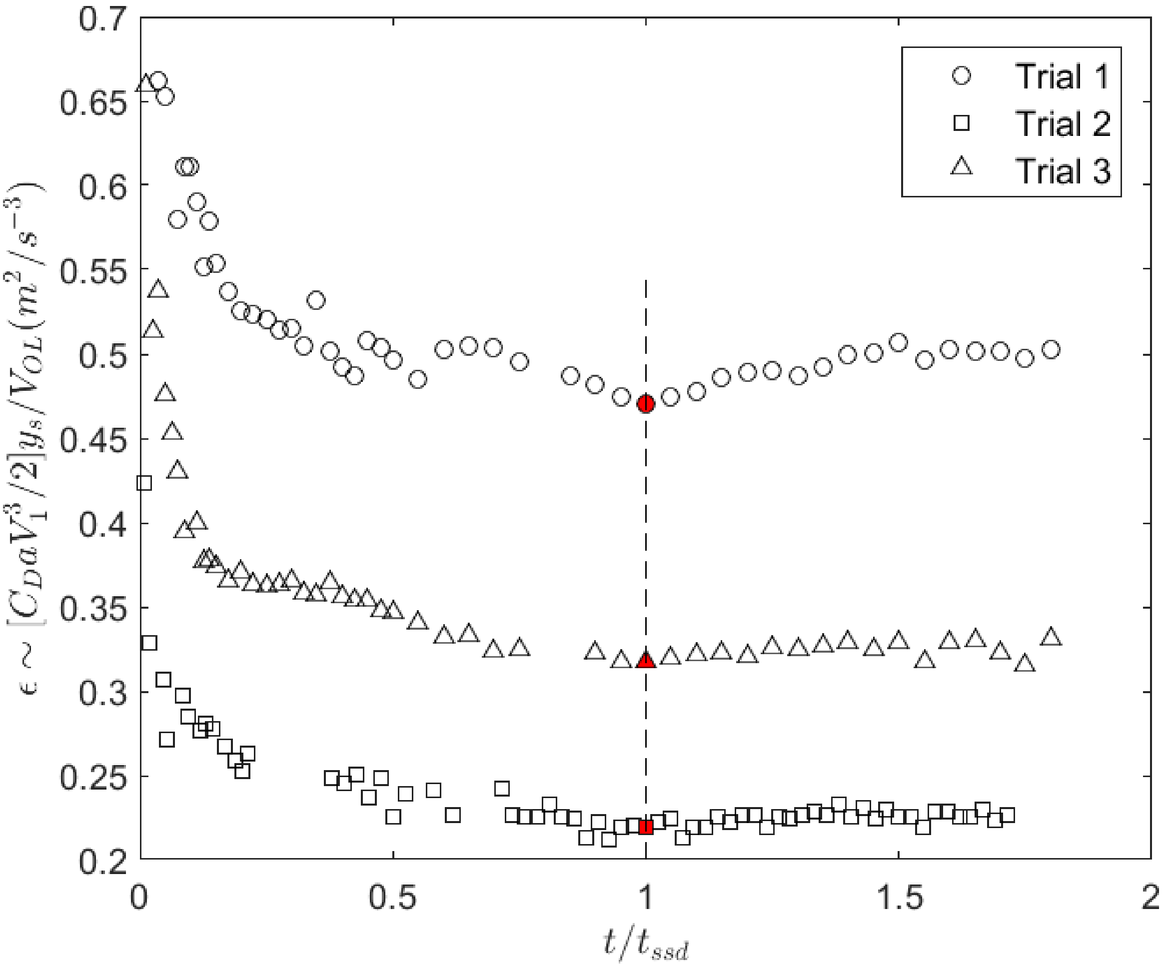

Figure 5.5 Variation in the rate of turbulent kinetic energy (TKE) production (computed using Eq. 3) with time, normalised by the crossover time (t_{ssd}), for all three trials.

Figure 5.5 indicates that before the crossover point, the production of turbulent kinetic energy (TKE) reduces over time and is consistent for all three trials, indicating that the HS vortex progressively weakens. Interestingly, beyond the crossover point (i.e. for t/t_{ssd}>1), the TKE production seems to reach a plateau. Consistently with the Manes and Brocchini (2015) approach, this suggests that the crossover indicates a point in time after which the erosive power of the HS vortex (quantified by means of ϵ) stays constant.

Looking at Figure 5.3(a-c) a question comes naturally. How is it possible that, after the crossover point, the scour hole experiences an increase in y_s while its volume stays essentially constant? The next section provides an answer to this question.

5.2.3 Erosion and Deposition Patterns for the Fully-Rough Trials

A corresponding physical interpretation of the occurrence of the crossover point was assessed by computing the erosion-deposition patterns of the scoured footprint in the second and third regimes defined in Section 5.2.1. For a direct comparison between the two regimes, the erosion-deposition patterns were calculated relative to the scoured surface measured at the point of crossover. Two- and three-dimensional erosion and deposition patterns pre- (second regime) and post- (third regime) crossover are shown for Trial 3 in Figure 5.6. Note that the pink area reflects differences in elevation between the two surfaces that are within the error measured in Chapter 4.

The erosion and deposition patterns show that the scour evolution is very uniformly distributed prior to the crossover point (Figure 5.6a, left) and can be reasonably well represented geometrically by the frustum of a cone (Figure 5.6a, right). However, beyond the crossover point, whilst continued erosion is still observed upstream and far away from the cylinder on the upper slopes of the scour hole, there is notable sediment build-up locally in the pier flanks that appears unable to be entrained and removed (Figure 5.6b). This observation is consistent with the development in the cross-sectional profiles at different angles around the scour hole beyond the crossover (Figure 5.7). The profiles show the development of erosion around the front with time which transitions to a build-up of sediment as the profile angle transfers to around the pier sides. The post-crossover profiles of the scour surface development over time show that this deposition of sediment along the sides of the pier is a steady build-up of sediment over time and not the result of avalanche-type collapses of the scour hole slope. While it is acknowledged that avalanche-type collapses of the scour hole slope may increase the volume of sediment deposited in the pier sides for a snapshot of the scour profile, this does not influence the long-term development of sediment deposition in the pier sides that is observed.

The difference between the crossover and post-crossover outputs exceed the measurement error (as shown in Figure 5.6, left) and can therefore be considered significant. These observations are consistent for all three inviscid trials. The geometric scaling linking V_{OL} with y_s presented in Section 5.2.1 can thus be inferred as a trade-off between erosion and deposition, which combine to nullify any further significant change in the scour volume.

(a) Pre crossover

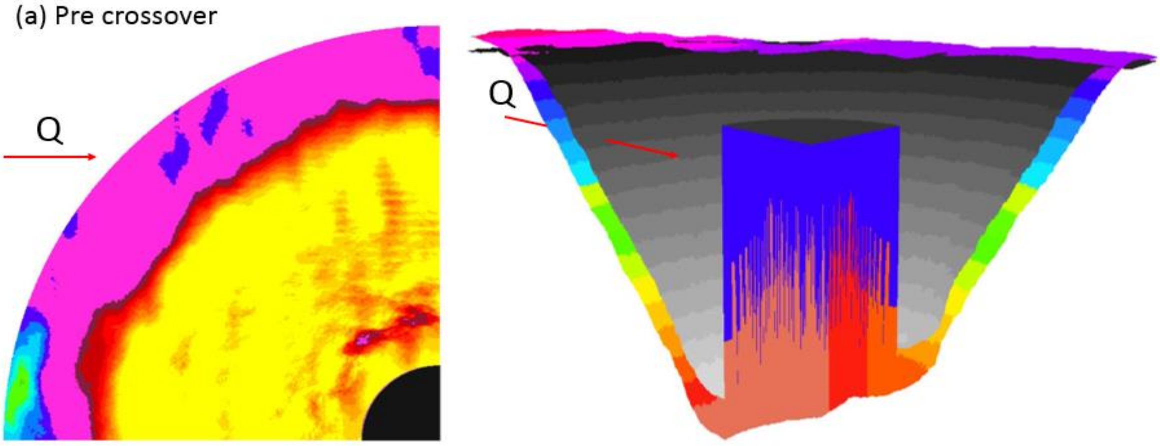

(b) Post crossover

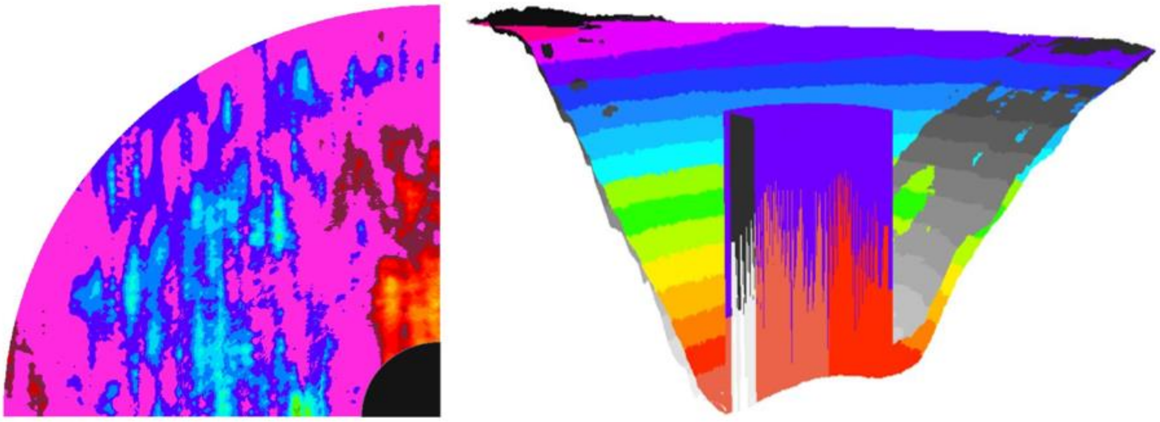

(Left) Elevation of crossover bed surface relative to surface at time t

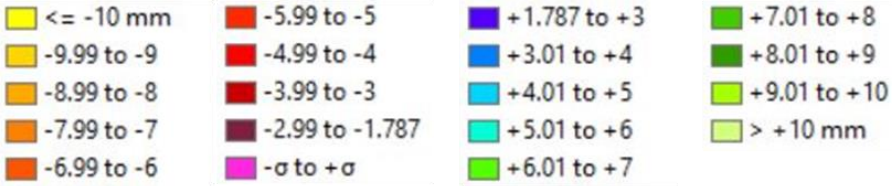

Figure 5.6 Erosion and deposition patterns in the (a) second and (b) third regimes. (Left) A plan view of the scour hole; here, the red (≈+1.8mm) to yellow (>+10mm) colour scaling denotes areas of higher bed level relative to the crossover bed surface, whilst blue (≈-1.8mm) to light green (<-10mm) denote areas of relative lower bed level. The pink zone reflects insignificant elevation differences between the two surfaces, engulfed by the standard deviation of the measurement error for all trials identified in Chapter 4 of ≈1.79mm. The black circle represents the test pier. (Right) A three-dimensional equivalent of the scour hole profile; here, the coloured profile represents the crossover surface, whilst the greyscale profile is the surface at the same time t in the pre or post crossover regime, as stated. Direction of flow (Q) is indicated in the figure.

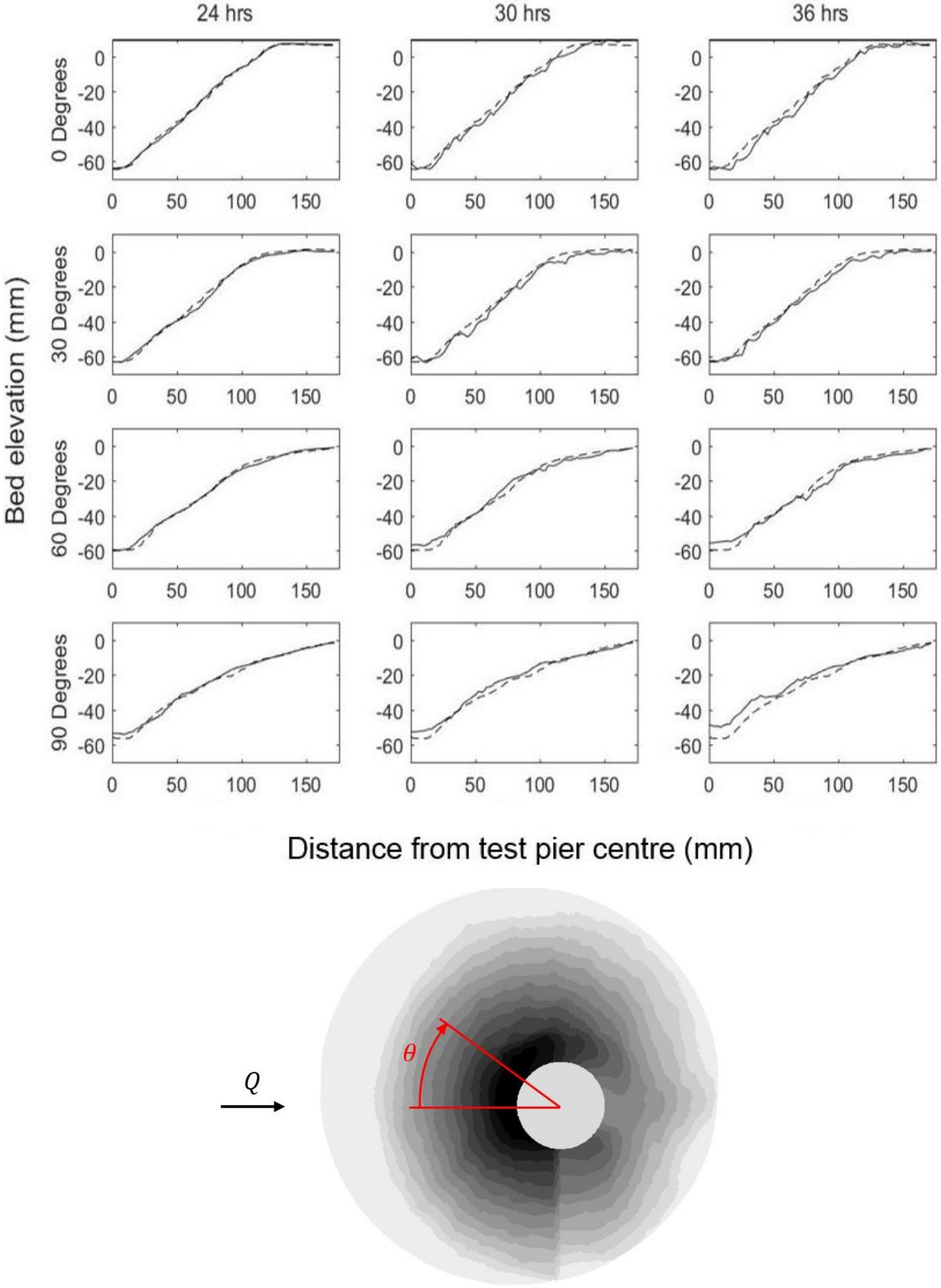

Figure 5.7 Cross-sectional profiles of the developing scour hole at 0°, 30°, 60° and 90° from the upstream axis of the scour hole (above). The bed elevation is measured relative to the flat-bed surface datum. The dashed line (- -) represents the crossover profile, whilst the solid line (-) represents the post-crossover surface at time t as stated. (Below) Definition of the upstream axis. Note that the maximum scour depth is captured within the 0° transect. The apparent shift in bed elevation along the 270° profile results from measurement error resulting from acoustic blanking (see Appendix B).

The build-up of sediment around the sides of the pier (along with continued erosion in front) beyond the crossover point is well captured by considering the scour volume evolution in front and around the sides of the pier, as shown in Figure 5.8. The volumetric scour development shows that, beyond the crossover depth (y_{ssd}), the magnitude of the scoured volume around the sides of the pier reduces steadily over time, owing to the deposition of eroded sediment from upstream. Conversely, the volumetric evolution in the region in front of the pier beyond y_{ssd} shows continued bed erosion and a continually increasing scoured footprint, albeit at a rate that is significantly reduced relative to the rapid development seen in the second linear regime. It is likely that, beyond the crossover point, the scouring process continues to erode sediment from around the front of the pier and transport entrained sediment to the sides, where they deposit, presumably because the HS vortex is unable to move them further downstream. Interestingly, and in keeping with an overall physical change in the local scouring process beyond the crossover time (t_{ssd}), Figure 5.8 shows that the crossover point is reached independent of region selection.

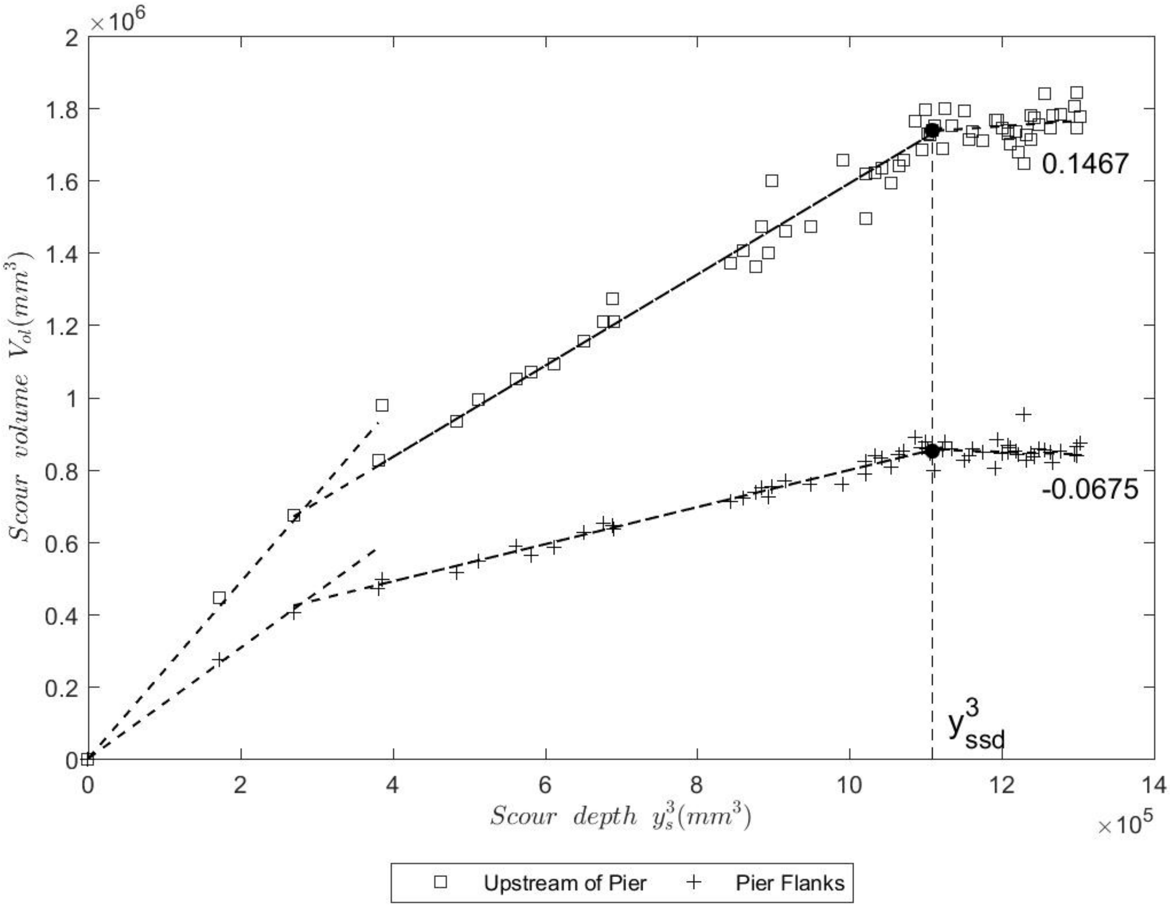

Figure 5.8 Development of the scour volume upstream of the test pier (shown as diagonal lines in the plan view of the scour hole footprint) and the corresponding development around the pier flanks (horizontal lines). The values shown are the gradients of the third linear regime for each plot.

5.2.4 Viscosity-Dependent Flow Regimes

The similarity analysis is now extended to all trials. Here, the aim is to identify to what extent the physical behaviour observed for the fully-rough regime shows consistencies with that observed for trials associated with viscosity dependent flow regimes. Towards this end, the same analysis approach is used. Plots of $V_{ol} \sim y_s^3$ are shown for the remaining trials in Figure 5.9.

High-level observations of Trials 6, 8, 9 and 11 (black – Figure 5.9) show evidence of a well-defined crossover point consistently with the observations from trials in the fully-rough regime. The remaining trials (red – Figure 5.9) do not show clear evidence of a crossover, presumably because they were not carried out for a long enough duration owing to the timescale of scour and experimental test constraints. These four trials (Trials 4, 5, 7 and 10) assessed the development of scour around the largest test pier, and smaller sediment relative to the fully rough trials. The time scale of scour is well known to scale as $\sim a/V_1$ (e.g. Melville and Chiew, 1999), which identifies larger piers requiring a longer time duration in order to reach the same development stage as that of a smaller pier. This is evidenced by the higher crossover timescale for the large pier (Trial 2) recorded for the fully-rough flow cases. The critical velocity for smaller sediments is also reduced, lowering the maximum flow velocity that can be used while still maintaining clear water scour conditions. Accordingly, these four trials were discarded from further analysis.

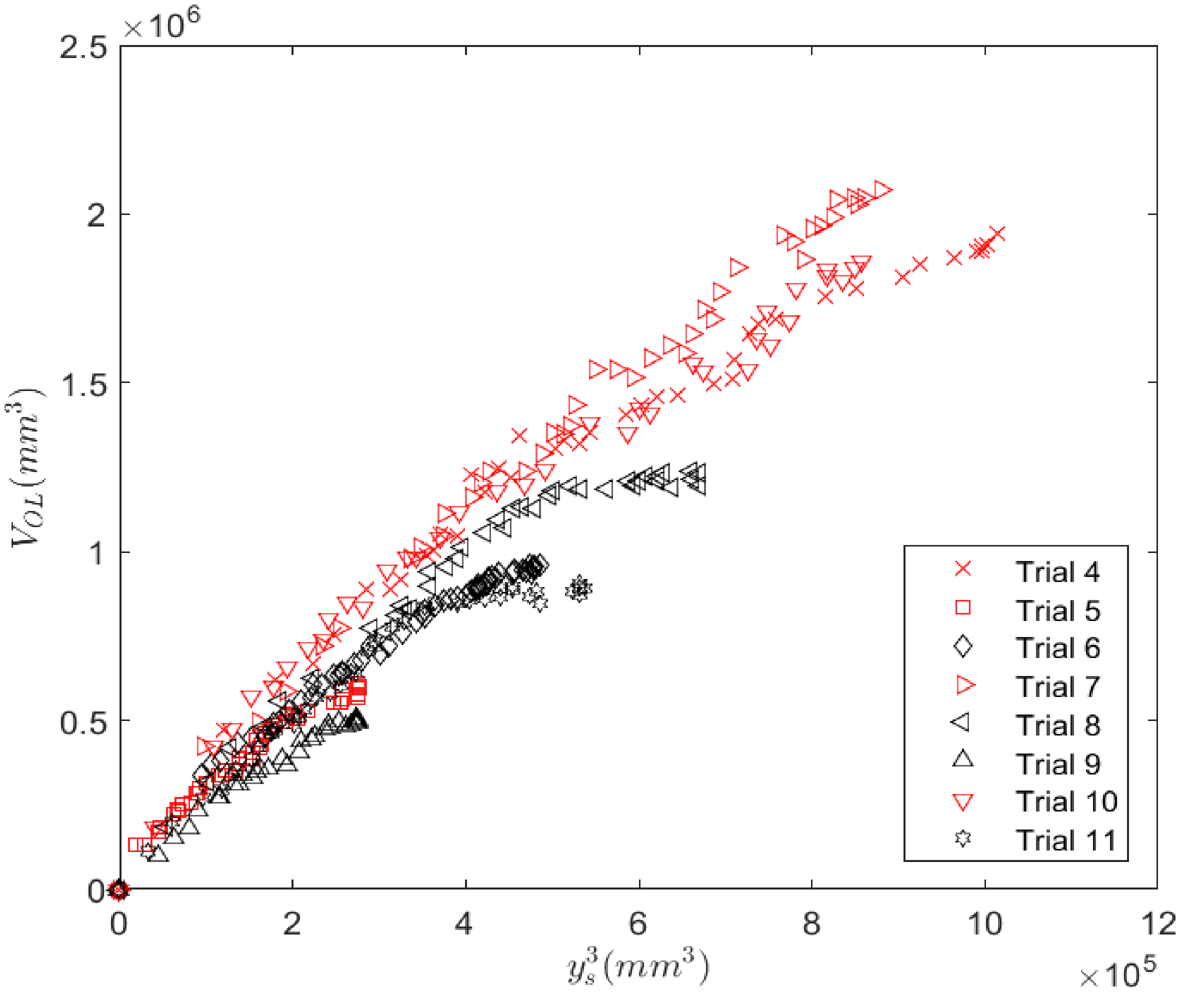

Figure 5.9 Development of scour volume as a function of depth for the transitionally rough, transitionally smooth and hydraulically smooth flow regimes. The trials in black are those observed as showing evidence of a point of crossover consistent with the fully-rough datasets. Black and red symbols, together with a change in symbol shape from previous plots, are used here for the purposes of visual clarity.

An unconstrained multiple-linear regression analysis was applied to the data for all four trials (Trials 6, 8, 9 and 11) displaying evidence of a crossover consistent with the fully-rough datasets. These are presented in Figure 5.10(a-d). Similar to the fully-rough flow regimes, there is consistent evidence that the scour volume develops with the scour depth cubed through three linear regimes. Although the regression analysis identifies a third linear regime for all the trials, it is fair to say that for Trial 6 and 9, this is not so evident (Figure 5.10a,c). However, it should be also noted that, as discussed for the fully-rough experiments, the identification of the third regime (and consequently of the crossover point) can be supported and corroborated through the analysis of the figure displaying V_{OL}/y_s^3 vs time.

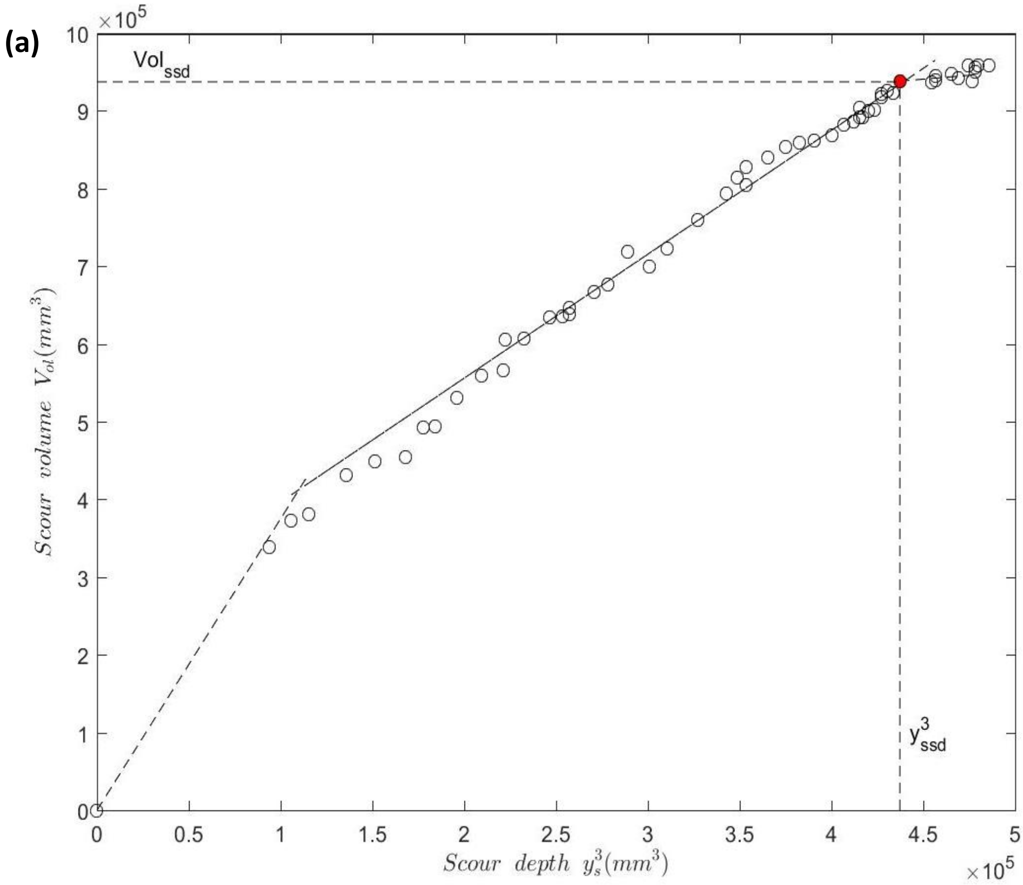
(a)
×10^5
Vol_ssd
y^3_ssd
Scour volume $V_{ol}(mm^3)$
Scour depth $y_s^3(mm^3)$
×10^5
0
1
2
3
4
5
6
7
8
9
10
0
0.5
1
1.5
2
2.5
3
3.5
4
4.5
5

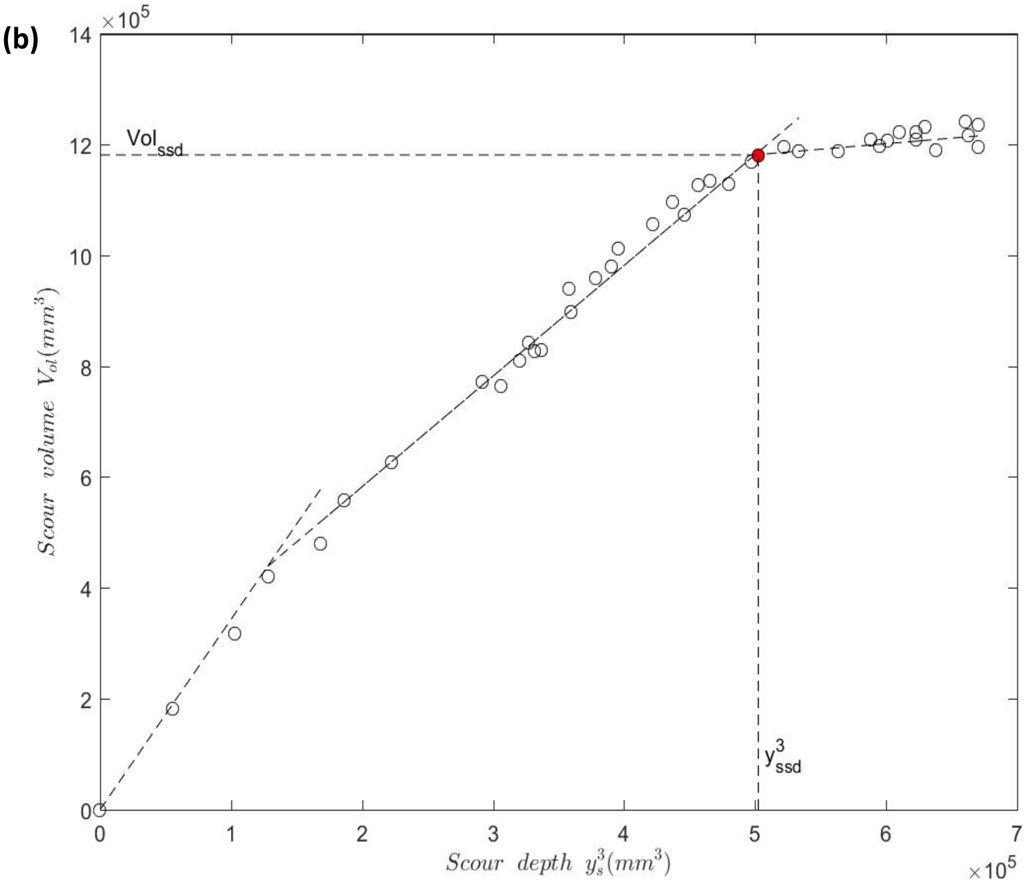
(b)
×10^5
Vol_ssd
y^3_ssd
Scour volume $V_{ol}(mm^3)$
Scour depth $y_s^3(mm^3)$
×10^5
0
2
4
6
8
10
12
14
0
1
2
3
4
5
6
7

(c)

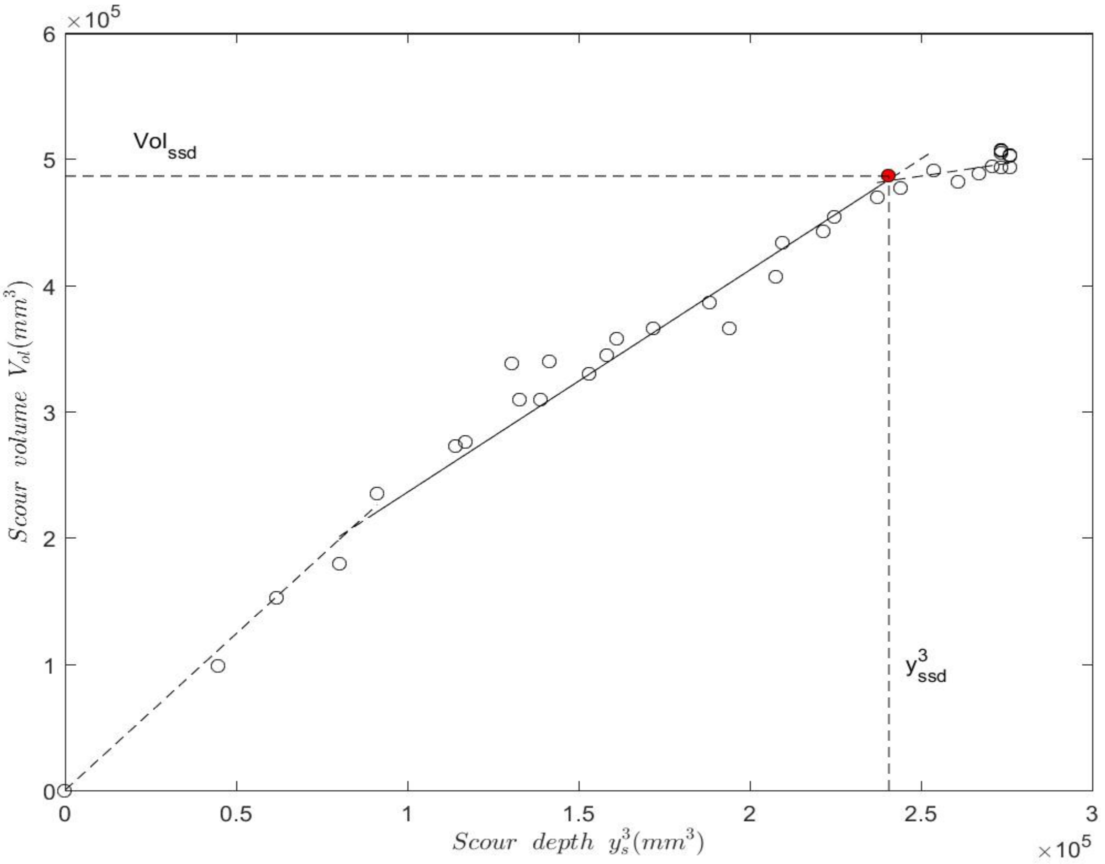

(d)

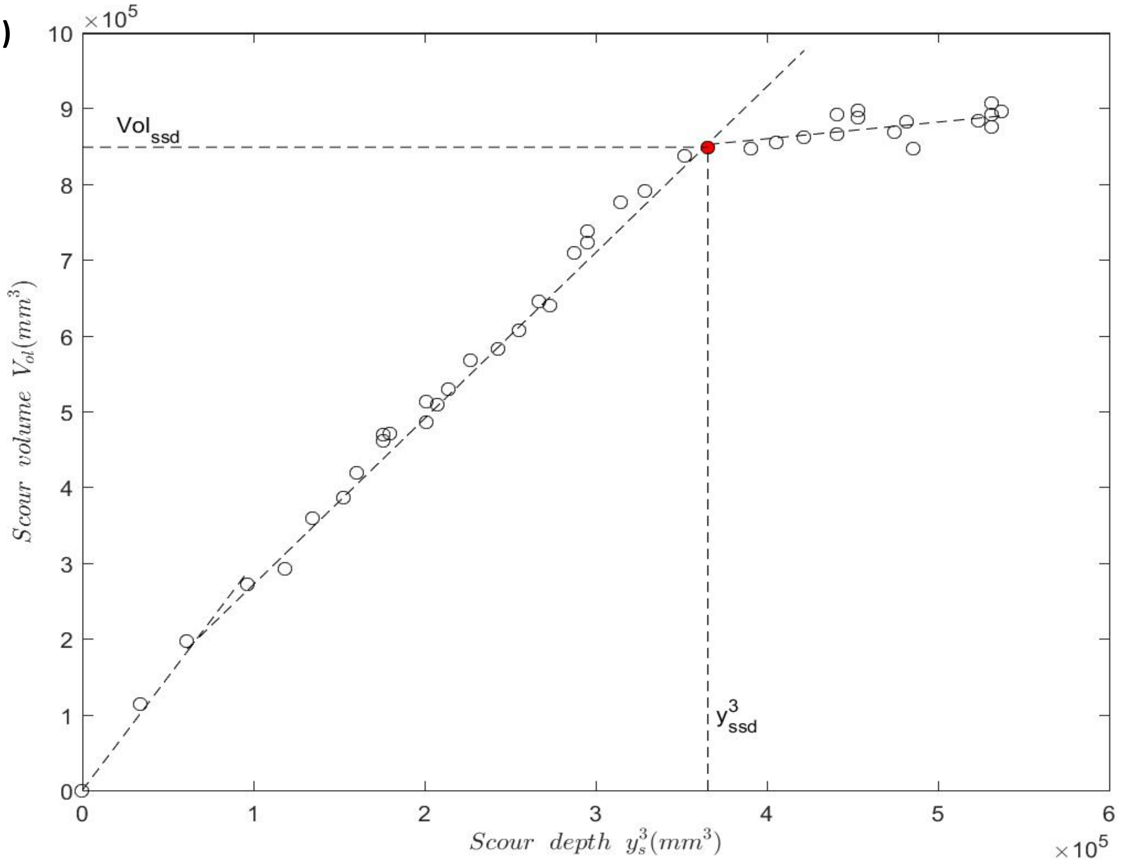

Figure 5.10 Multiple linear regression analysis on scour volume as a function of depth cubed for (a) Trial 6, (b) Trial 8, (c) Trial 9 and (d) Trial 11.

Here, time is normalised by the crossover time (t_{ssd}) as derived from Figure 5.10 and the ratio between the scour volume and depth-cubed is normalised by the equivalent value at the point of crossover. All trials show that, pre-crossover, the ratio between volume and depth cubed reduces and approaches a plateau as the point of crossover is reached. Beyond the crossover point, all values show a striking deviation below the horizontal plane (identifying the crossover point) which shows a differential change in development between the scour depth and bulk scour volume beyond this point. This further corroborates the occurrence of a well-defined third regime (and hence of a well-defined crossover time scale) for all the trials.

Interestingly, the post-crossover deviation below the horizontal plane over time is more significant when the flow regime is more viscosity-dominated. This observation identifies the physical characteristics of scour development in the third linear regime must be influenced by the flow regime. This influence is herein interpreted by considering both energetic principles based on the phenomenological theory of turbulence, and topography analysis of the erosion and deposition rates measured within the scour hole to enable direct comparisons with the fully-rough outputs.

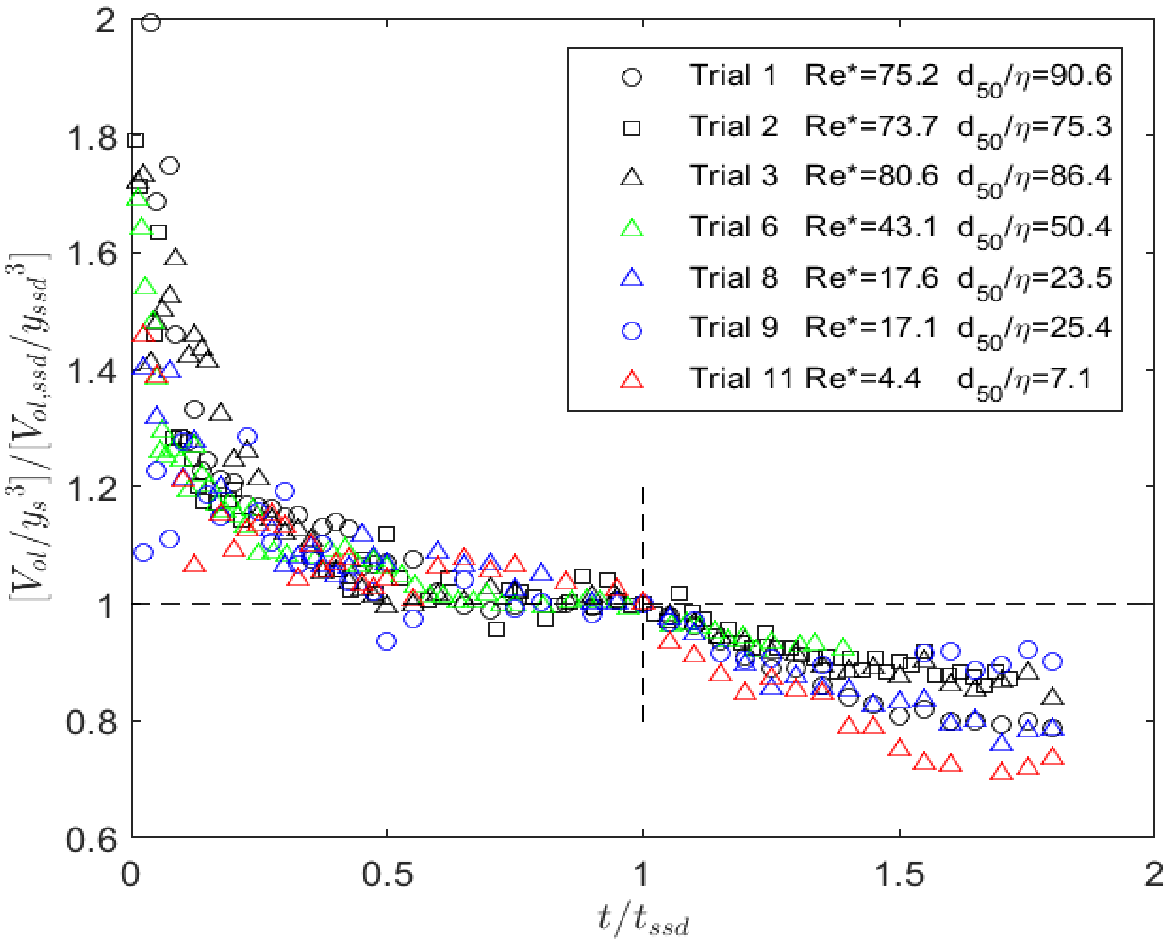

Figure 5.11 Ratio of volume to maximum depth cubed as a function of time, both normalised with the crossover equivalents.

5.2.5 Turbulence Phenomenology and Scour Dynamics

The energetic idealisation that the rate of TKE production scales as the power of the HS vortex P (i.e. the turbulent kinetic energy produced/dissipated by the HS vortex) per unit mass M as derived by Manes and Brocchini (2015) (see Eq.'s 5.1 and 5.2) applies to any flow regime and therefore it is herein explored to interpret the scour dynamics of the viscosity-dependent experiments.

The rate of turbulent kinetic energy (ϵ) production, which scales as $\sim y_s/V_{OL}$, is presented in Figure 5.12 as a function of the normalised time t/t_{ssd}, where t_{ssd} is the time when the crossover occurs as given in Table 5.3. Consistently with the fully-rough cases, the production of turbulent kinetic energy reduces over time. The point of crossover, where $t/t_{ssd} = 1$, indicates the transition where weakening of the HS vortex (as defined by TKE dissipation) plateaus and its erosive power stays approximately constant with time. The experiments (shown in black) used an identical pier diameter which allows for the variation of TKE dissipation with pier diameter to be observed. As such, the equivalent trial from the fully-rough regime (Trial 3) is included in Figure 5.12 for comparison. Interestingly, the magnitude of the TKE dissipation plateau beyond the crossover point notably increases as the impact of viscosity from the flow regime reduces.

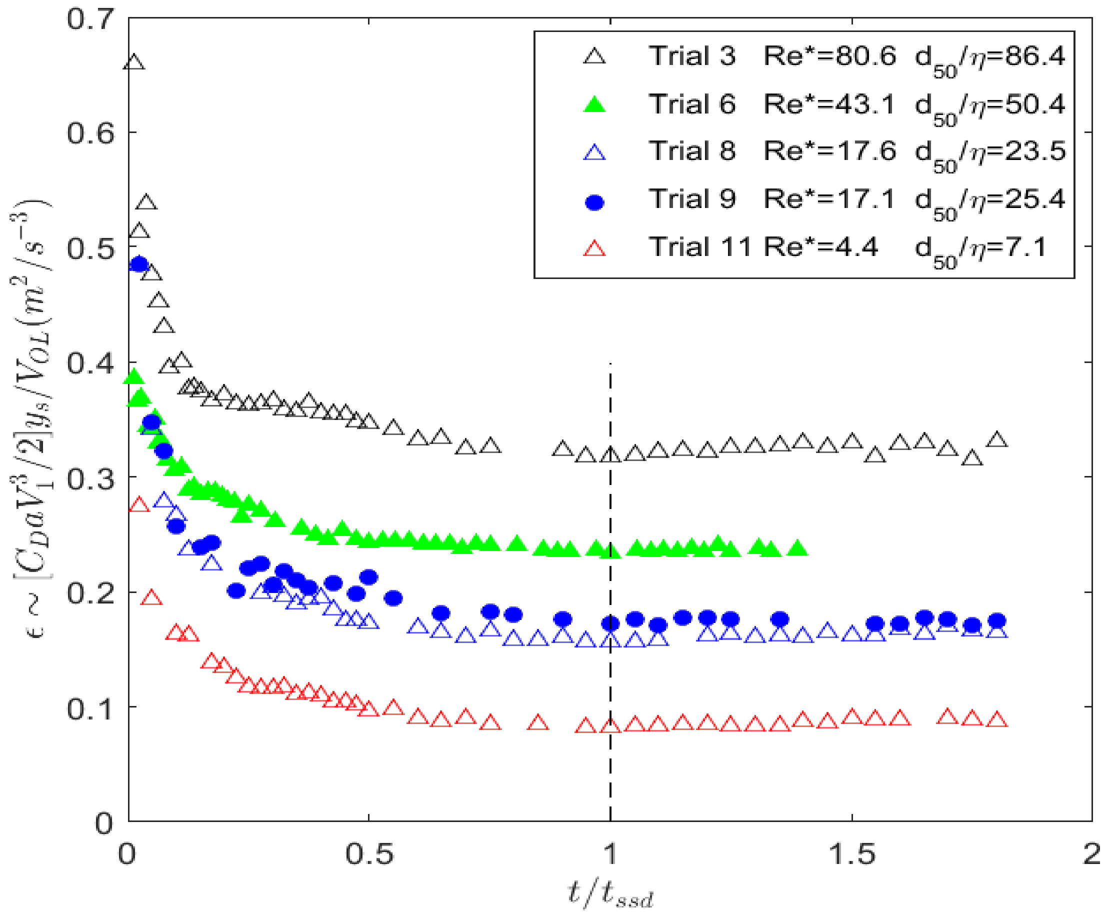

Figure 5.12 Rate of TKE dissipation with time, normalised with the crossover time. Note: Trial 6 and 9 are infilled due to questionable reliability in identifying the crossover point.

Table 5.3 Crossover characteristics (t_{ssd}, y_{ssd} and $V_{ol,\ ssd}$) for trials in the transitionally rough, transitionally smooth and hydraulically smooth flow regime.

Trial	t_{ssd} (hrs)	y_{ssd} (mm)	$V_{ol,ssd}$ $(10^{-3}m^3)$
6	36	75.9	0.937
8	20	79.5	1.181
9	20	62.2	0.485
11	20	71.5	0.849

To assist comparisons between all trials independent of regime, the rate of turbulent kinetic energy production with time (as shown in Figure 5.12) was normalised by the corresponding crossover characteristics. This is presented in Figure 5.13. This plot essentially shows the dissipation of turbulent kinetic energy normalised with the dissipation at the crossover point, as a function of time. As is the case for all trials, upon reaching the point of crossover the production of TKE plateau's. This denotes a point in the scour development process, after which the bulk erosive-power of the HS vortex (where bulk means independently of the specific point in the scour hole) remains constant. It is interesting to note, however, that the early rate of dissipation in turbulent kinetic energy (i.e. pre-crossover dissipation) is more gradual as the flow regime within the scour hole becomes more viscosity-dominated.

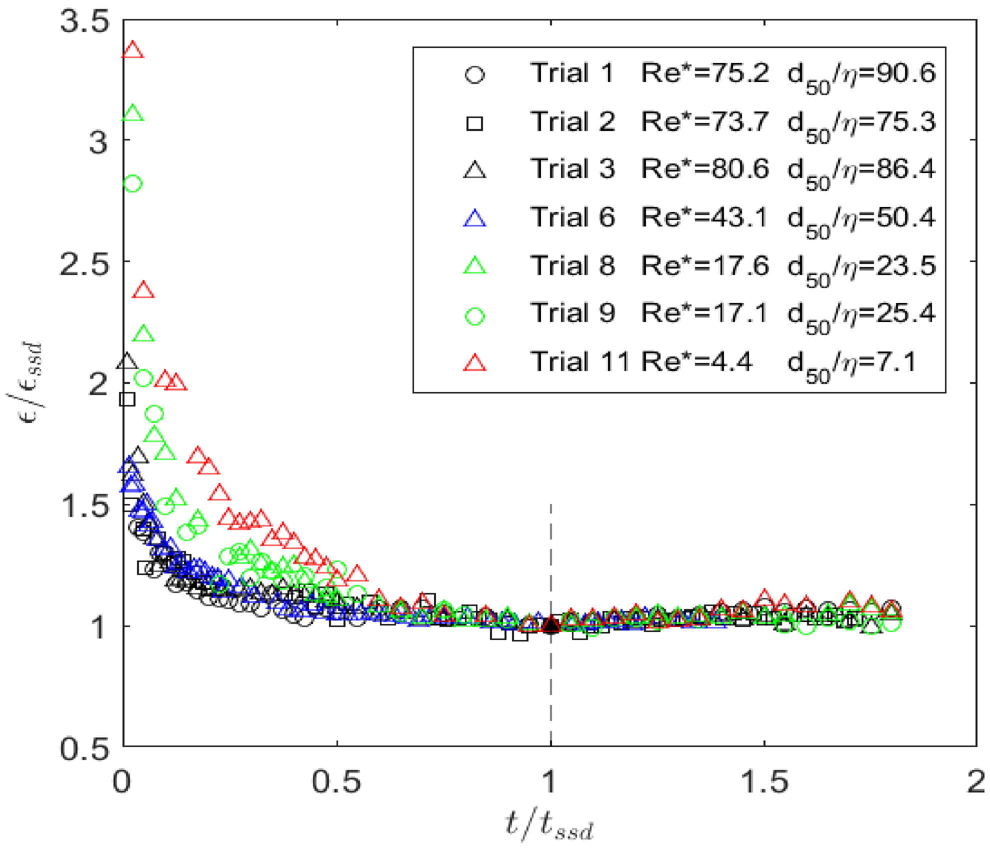

Figure 5.13 TKE dissipation, normalised with the dissipation at the crossover, as a function of time normalised with the crossover timescale for all crossover trials.

5.2.6 Erosion and Deposition Patterns

A corresponding physical interpretation is now presented to assess the consistency of erosion-deposition patterns with respect to those observed in Section 5.2.3 for the fully-rough trials. The two- (left) and three-dimensional (right) erosion and deposition patterns pre-crossover are shown for Trials 6 (transitionally rough), 8 (transitionally smooth) and 11 (hydraulically smooth) in Figure 5.14. Topography patterns for Trial 9 are discounted at this stage owing to possible unreliability in the extracted crossover values.

The figures (left) show the differences in surface elevation between the crossover surface and a sample surface pre-crossover (second regime). The elevation differences are consistent for all three trials, which implies that the development of the scour hole is geometrically similar (i.e. the scour hole scales consistently with time) independent of regime. The three-dimensional profile of the scour hole shows that the development is well represented by a cone frustum, a simplifying geometry typically adopted by many researchers to idealise the shape of a developing scour hole. This simplified geometric profile is consistent with erosion-deposition patterns observed for the fully-rough regime, and can therefore be reasonably well assumed as the universal shape of a scour hole within the second linear regime.

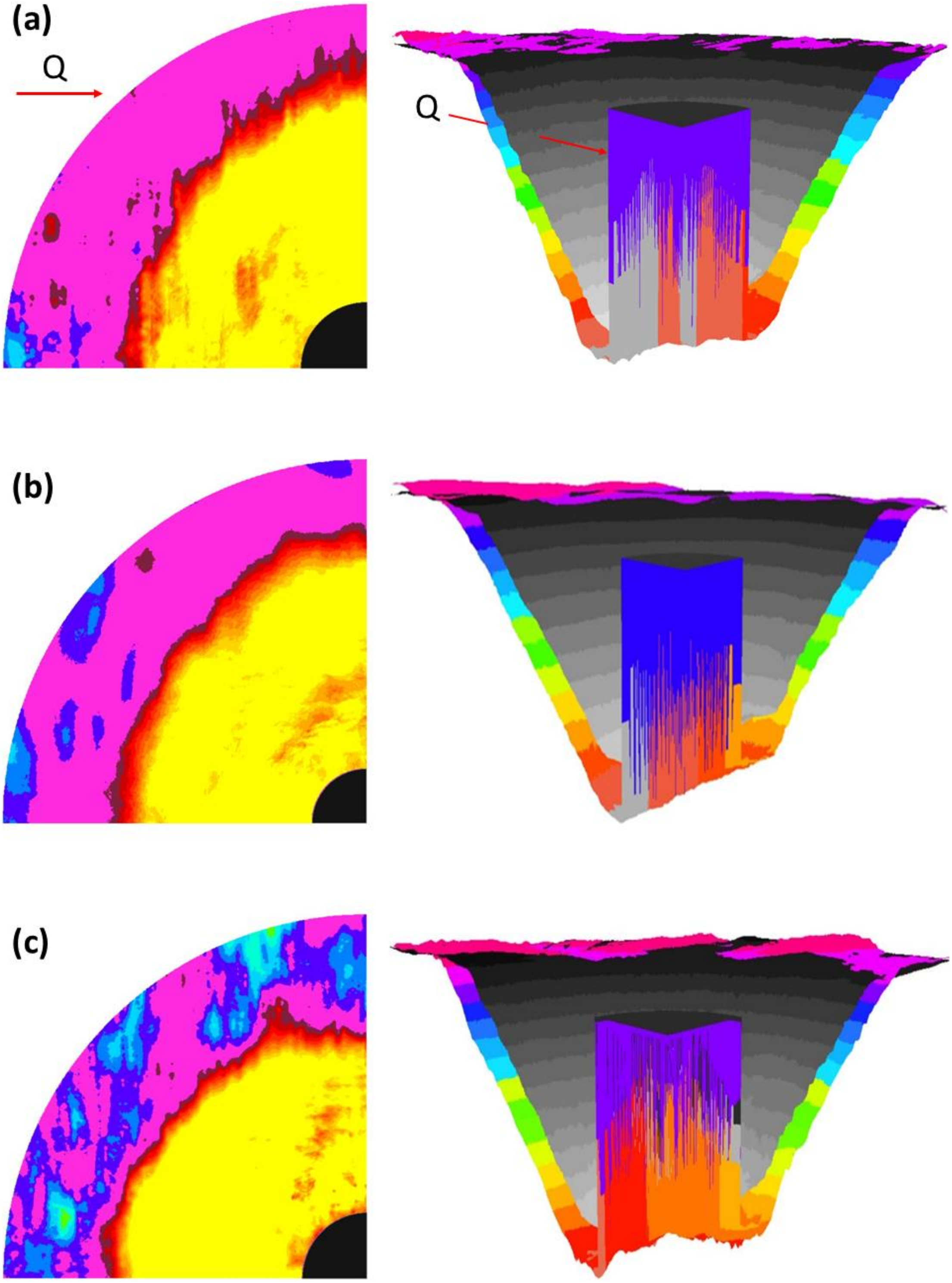

Figure 5.14 Erosion and deposition patterns pre-crossover for the (a) transitionally rough, (b) transitionally smooth and (c) hydraulically smooth flow regimes. (Left) Scour hole plan view; here, the red (≈+1.8mm) to yellow (>10mm) colour scaling denotes areas of higher bed level relative to the crossover bed surface, whilst blue (≈-1.8mm) to green (<-10mm) denote areas of relatively lower bed level. Pink areas signify insignificant elevation differences between the surfaces, engulfed by the standard deviation of the measurement error for all trials identified in Chapter 4 (≈1.79mm). (Right) A three-dimensional equivalent of the scour hole profile; here, the coloured profile represents the crossover surface, whilst the greyscale profile is the surface at the same time t *in the pre crossover regime, as stated. Direction of flow (*Q*) is indicated in the figure.*

The equivalent erosion and deposition patterns post-crossover are shown in Figure 5.15 for the same trials. To remind the reader; it was observed for the fully-rough regime that, beyond the crossover point, evidence of continued erosion upstream of the test pier coincided with a notable localised build-up of sediment around the pier flanks (Figure 5.15a). This trade-off between erosion and deposition combines to nullify any further change in the scour hole volume that was observed. This observation was consistent for all three fully-rough trials in the absence of viscosity.

For the experiment characterised by the lowest Re^{*} and d_{50}/η values (and presumably in the hydraulically-smooth regime, Figure 5.15d), the erosion and deposition patterns show a striking contrast relative to the fully-rough case. Whilst a point of crossover is reached which signifies a physical change in the scour development process, continued erosion is instead observed in the pier flanks rather than upstream of the pier. Moreover, erosion around the sides is coupled with partial sediment build-up observed around the front adjacent to the location of maximum scour depth. The plateau of the scour hole volume within the third linear regime is therefore owing to a trade-off between erosion and deposition which are, physically, a complete reverse to those observed for the fully-rough regime. The transitionally rough (Figure 5.15b) and smooth (Figure 5.15c) regimes provide, naturally, a transition between these two “extreme” cases. Considering the three-dimensional profiles, the transitionally rough case showcases a surface elevation difference post-crossover that has physically similar attributes to the fully-rough case; with sediment build-up in the flanks. However, the sediment build-up in the pier flanks is less pronounced which is matched by a lower magnitude in erosion around the pier front. This presents a similar erosion-deposition trade-off, albeit due to less significant sediment redistribution patterns.

The transitionally smooth regime shows only minor changes in scour development beyond the crossover point that cannot be underwritten by measurement error. The geometric scaling linking V_{OL} with y_s presented for this regime can thus be inferred as a trade-off between negligible erosion and deposition that occurs post-crossover. However, significant erosion is observed locally around the flanks of the pier which signifies the transition into the observations made for the hydraulically smooth regime shown in Figure 5.15d.

A physical interpretation of the erosion-deposition patterns for the viscosity-dependent trials is difficult as they are an effect of many interlinked mechanisms related to the mean and fluctuating properties of the flow which would require a dedicated experimental campaign. This is beyond the scope of this thesis.

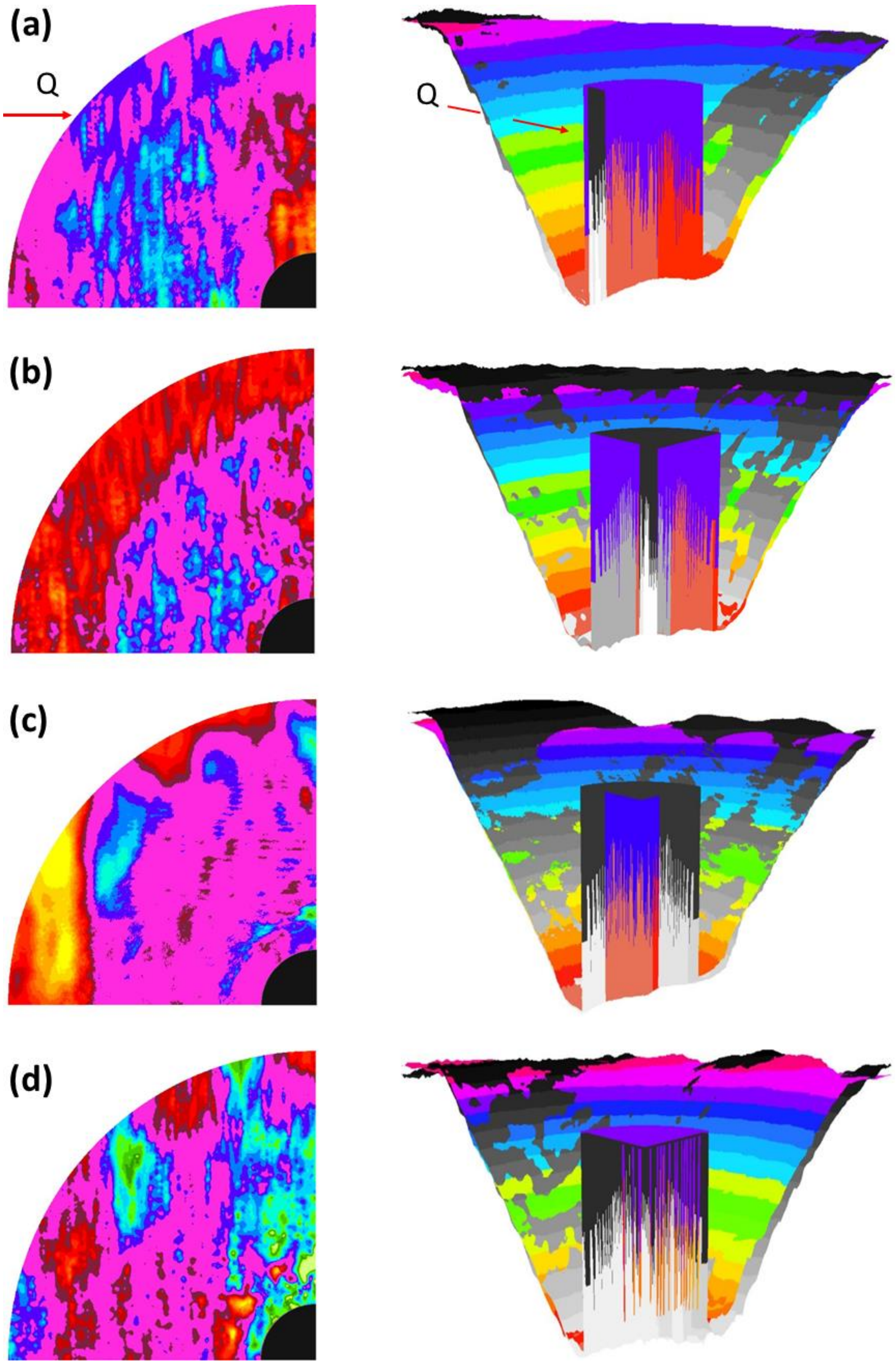

Figure 5.15 Equivalent erosion and deposition patterns post-crossover for the (a) fully-rough [$Re^*=80.6$, $d_{50}/\eta=86.4$], (b) transitionally rough [$Re^*=43.1$, $d_{50}/\eta=50.4$], (c) transitionally smooth [$Re^*=17.6$, $d_{50}/\eta=23.5$] and (d) hydraulically smooth [$Re^*=4.4$, $d_{50}/\eta=7.1$] flow regimes. Colour scale is as defined in Figure 5.6.

5.3 Scour Hole Boundaries

For completeness, the analysis is now extended to the development of other key geometric properties with time, namely, the scour hole length (L), width (W), and the area of the scour footprint (A_f). These properties are physically defined in Figure 5.16. The scour hole length refers to the distance from the edge of the pier diameter to the upstream scour hole apex (along the 0° transect), while the width is the transverse distance between the scour hole edge and the edge of the pier diameter measured on either side. The scour footprint characterises the scoured region projected on a horizontal plane. The footprint is restricted to the area upstream of the pier to be consistent with the restrictions imposed on the scour volume.

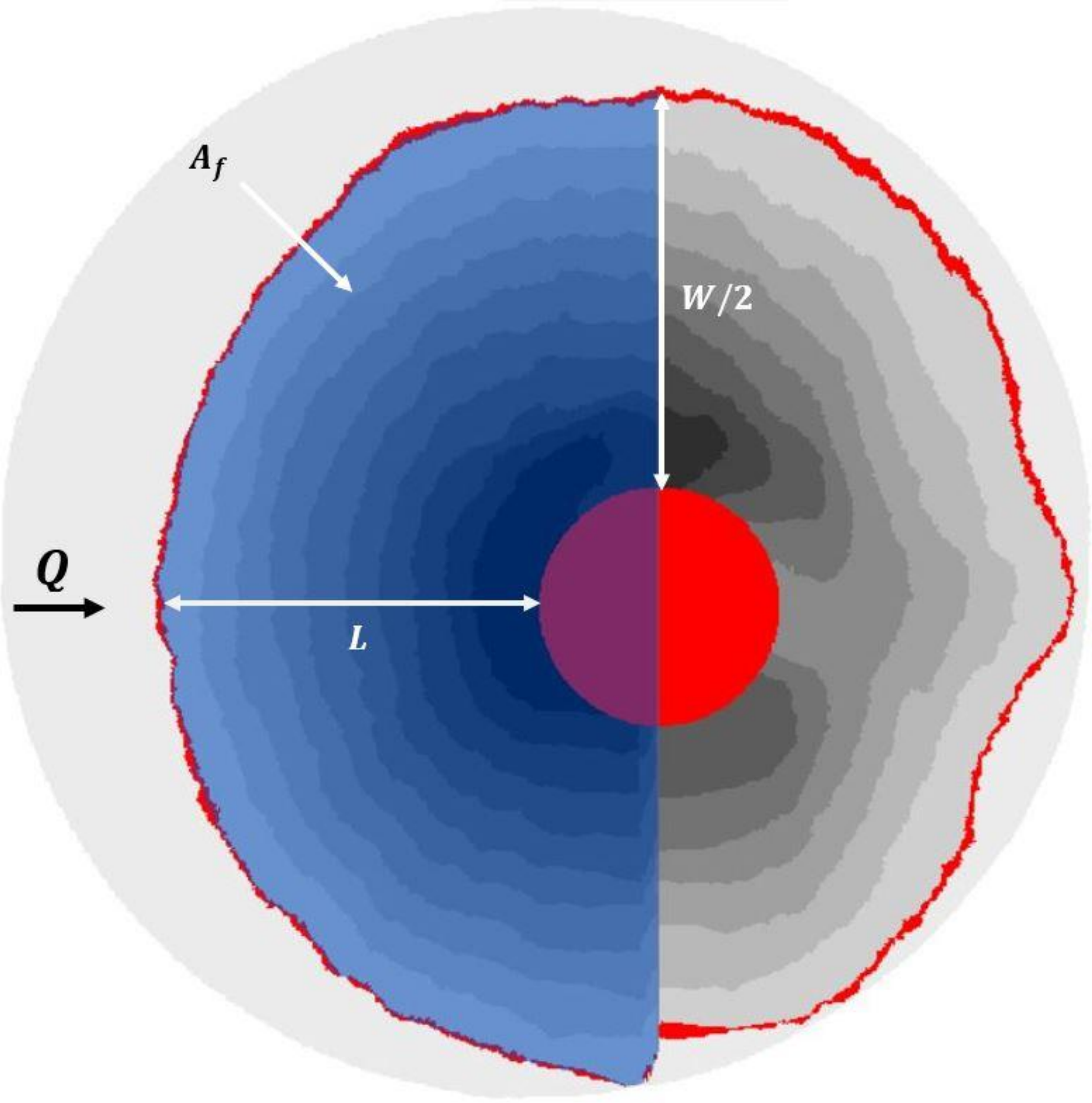

Figure 5.16 Plan view of scour hole physical boundaries. Q denotes the direction of flow.

Collectively, these terms define the main axis of the scour hole extents. Their interlinked development with time is particularly crucial, for example, in the calibration of boundary conditions for numerical models and validation of the outputs. The developments of the scour hole length and width, as a function of time, are presented in Figure 5.17. Generally speaking, the geometric boundaries of the scour hole are strikingly similar to the development in maximum scour depth, with a rapid initial increase followed by a deteriorating continued increase as the scour hole becomes well developed. Both the physical length and width of the scour hole are also observed to increase with an increasing pier diameter, as can be reasonably expected.

The development of the scour hole width and length are now put in the context of interlinked correlations with the maximum depth (y_s). Issues with invasiveness and measurement accuracy has restricted much of our understanding of scour hole boundary development to post-experiment measurements of a drained scoured surface (Khwairakpam *et al.*, 2012; Das *et al.*, 2014a; Das *et al.*, 2014c). Das *et al.* (2014c) observed that the end-of-trial (used interchangeably with *equilibrium* in the literature) scour length and width can be loosely characterised by a linear scaling with the magnitude of the equivalent maximum scour depth. Their baseline stipulated that these three length scales are linearly related[33], i.e. $L_e \propto W_e \propto y_{se}$. However, the use of end-of-trial conditions often considers experiments that are at varying stages of the scour development process, owing to the lack of a general definition for clear-water equilibrium conditions (e.g. Lança *et al.*, 2013) and consideration of the general timescale of scour (Melville and Chiew, 1999). As such, an understanding of the scour boundary development with time is useful for two reasons. First, observed end-of-trial relations between the scour hole geometry observed in past research can be put into context with the development stage of the scour hole. Secondly, these properties are physically relatable to the maximum depth with time, which is very relevant as the variation of this property is well researched as a primary parameter governing scour risk assessments and foundation design.

The ratio of width and length to depth as a function of time is presented in Figure 5.18. The geometric relations are modelled as a function of two different timescales; the crossover time, and the timescale of scour as defined by Melville and Chiew (1999). The figure shows that both the development of W/y_s and L/y_s are well defined through two distinct regimes. The first regime is an initially rapid reduction in both ratios which, presumably, coincides with the formation of the scour hole and full development of the buried HS vortex. The second regime is characterised by proportional growth of both scour boundaries with the scour depth that is independent of time. Evidence of the crossover point observed in Section 5.2.1 is notably absent for these scaling relations (Figure 5.18 a, b) as its occurrence is physically defined by sediment

---

[33] L_e, W_e refer to the equilibrium scour hole length and width, respectively.

redistribution patterns localised around the base of the pier. As such, a negligible impact on the development of the scour boundaries can be reasonably expected.

Beyond initial formation of the scour hole, the similarity scaling between the geometric scour hole boundaries with depth is independent of time (Figure 5.18c,d), irrespective of flow regime. Accordingly, the scour hole length and width can be approximated using the following functions of the maximum scour depth for any time t;

$$W \approx 3 \div 4y_s, \tag{5.3}$$

$$L \approx 1.3 \div 1.8y_s. \tag{5.4}$$

These ranges are now verified using literature data. Das *et al.* (2014c) measured end-of-trial values of L/y_s and W/y_s for 15 independent trials involving similarly-sized cylindrical pier diameters to those used in this study. The variation of the ratios L/y_s and W/y_s were observed to be 1.37÷1.80 and 3.26÷4.44, respectively, which are strikingly consistent with the ranges quoted in Eq. (5.3) and (5.4).

For the fully-rough trials (Figure 5.18a), that is, for a constant sediment diameter (d_{50}), the ratio of W/y_s increases with an increasing pier diameter (a). In other words, scour holes that form around smaller piers are typically narrower. The value of L/y_s is also observed to increase with pier diameter. However, the end-of-trial ratios measured by Link *et al.* (2008a) for a 0.2m diameter pier are consistent with the upper bound of the ranges quoted in Eq. (5.3) and (5.4) (L/y_s ≅1.76 and W/y_s ≅4.26). This is also supported by Dey and Raikar (2007), who measured values of L/y_s ≅1.83 and W/y_s ≅ 3.78 for a 0.12m diameter pier. Based on this information, it is plausible that the effects of pier diameter have only a measurable effect when using very small pier diameters relative to field scales. The ranges presented in Eq. (5.3) and (5.4) can therefore be used to provide a good estimation of the scour hole boundaries for a given maximum depth, independent of time.

Interestingly, the stabilising value of W/y_s with time is influenced by the flow conditioning within the scour hole (Figure 5.18c), with a viscosity-dominated regime producing a lower ratio of W/y_s relative to the fully-rough equivalents. In contrast, this dependency is not observed as clearly in L/y_s (Figure 5.18d). This shows that the effects of viscosity have more of a measurable impact around the sides of the pier rather than upstream.

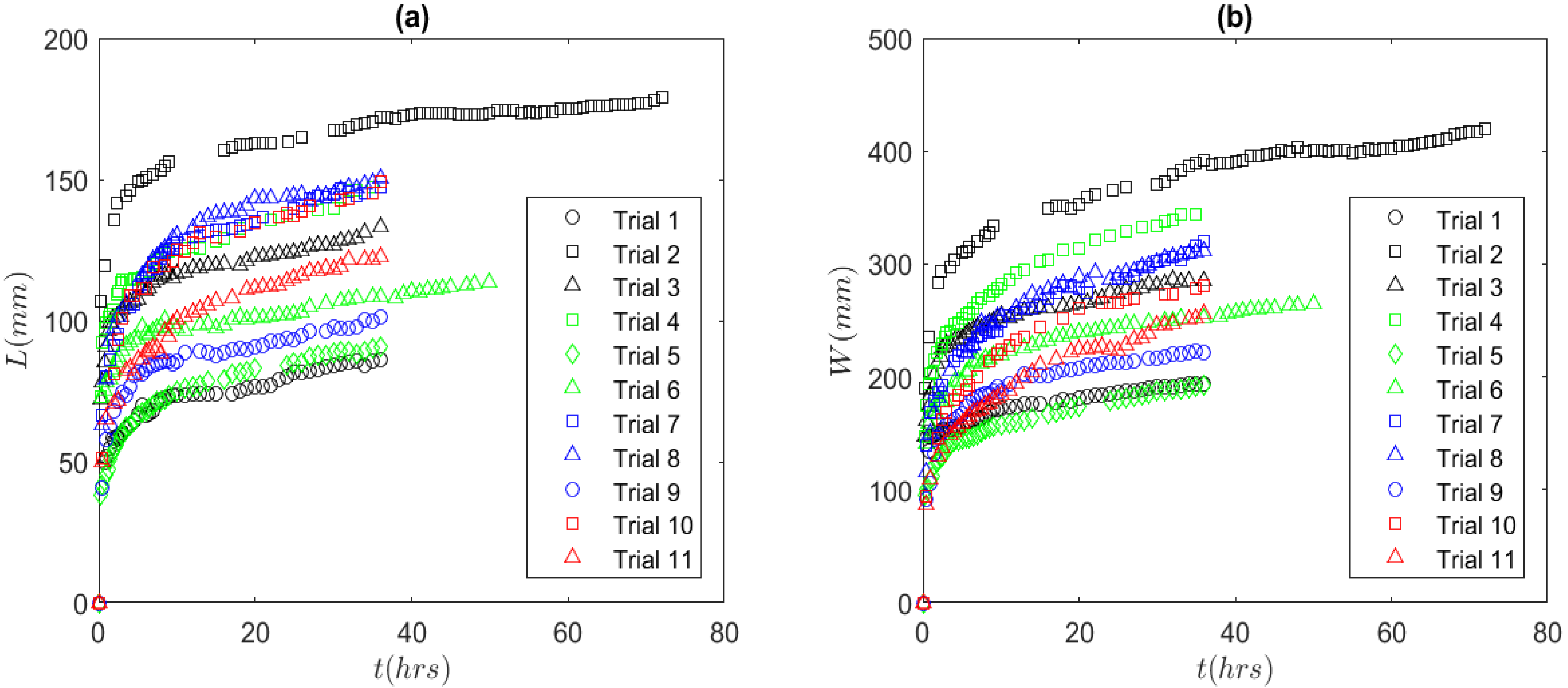

Figure 5.17 Variation of scour hole (a) length and (b) width as a function of time.

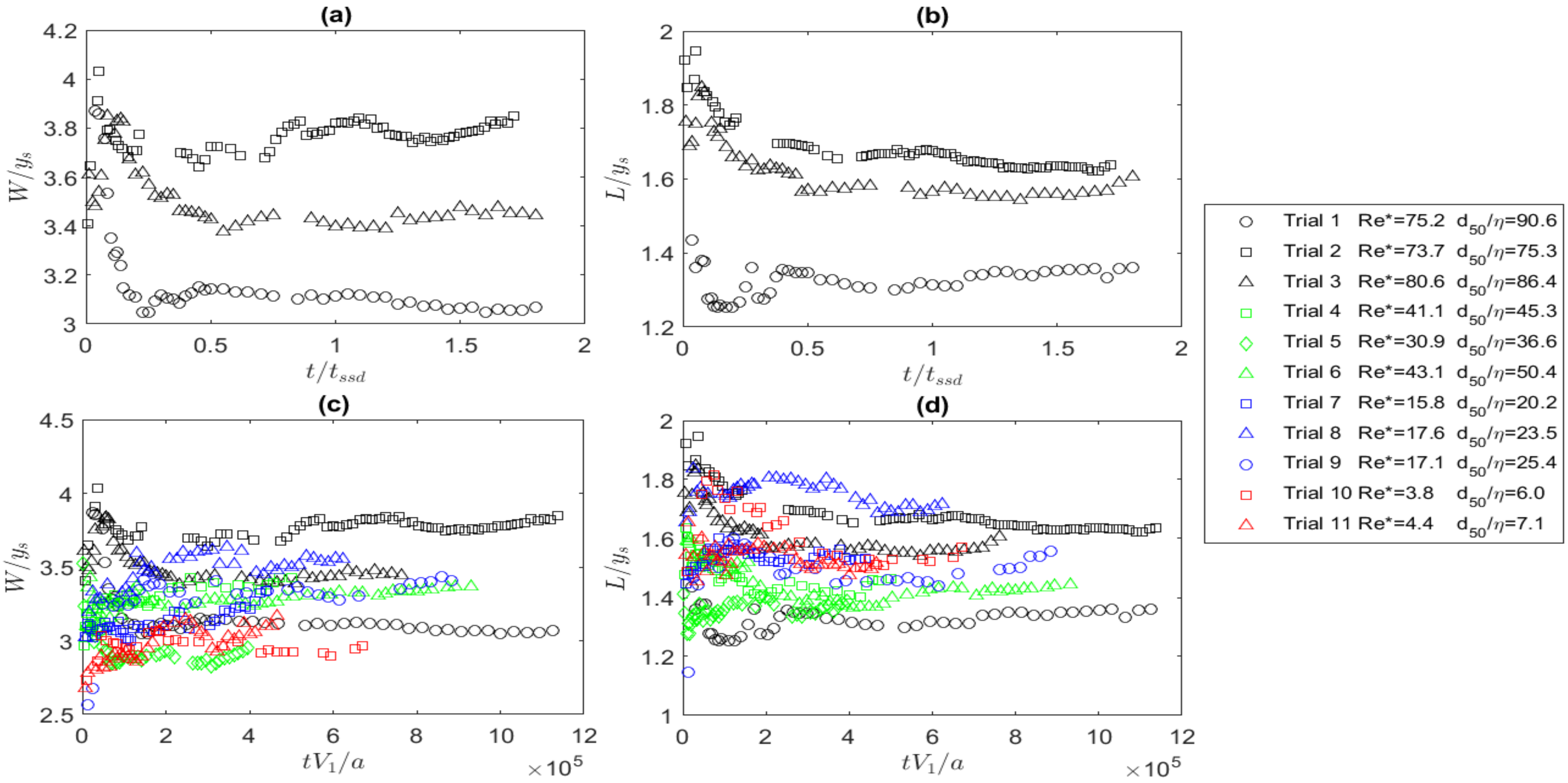

Figure 5.18 Development of scour hole length and width. (a) and (b) Fully-rough scaling (Trials 1-3) of the scour hole width and length, respectively, normalised with the maximum scour depth as a function of time (normalised with the crossover time); (c) and (d) Development of scour hole width and length, respectively, for all trials as a function of the timescale of scour.

5.3.1 Scour Footprint

The scour hole footprint describes the area of the scour hole projected on a horizontal plane. An understanding of its development with respect to the scour depth provides critical information for quantifying the physical extents of the scour hole boundary that can be useful, for example, in identifying the coverage area for riprap countermeasure placement. The scour footprint (A_f), normalised with the corresponding maximum scour depth (y_s) squared, is presented in Figure 5.19 as a function of the same two timescales used previously.

The ratio appears to vary with time through two regimes that are consistent with those observed in Figure 5.18. The variation of A_f/y_s^2 is independent of the crossover timescale (Figure *5.19*a) which is logical as the nature of the crossover point is physically defined by the scour depth and locally around the pier base. The scour hole footprint is observed to grow steadily with the maximum scour depth squared, independently of time, given by

$$A_f \cong 5 \div 8y_s^2. \tag{5.5}$$

Observations of an influence of flow regime (Figure 5.19b) on the stabilisation value of A_f/y_s^2 is attributed to the effects of viscosity in the pier flanks, as discussed previously. Eq. (5.5) can be used for application as a good estimation of the scour hole footprint as a function of depth, independent of time.

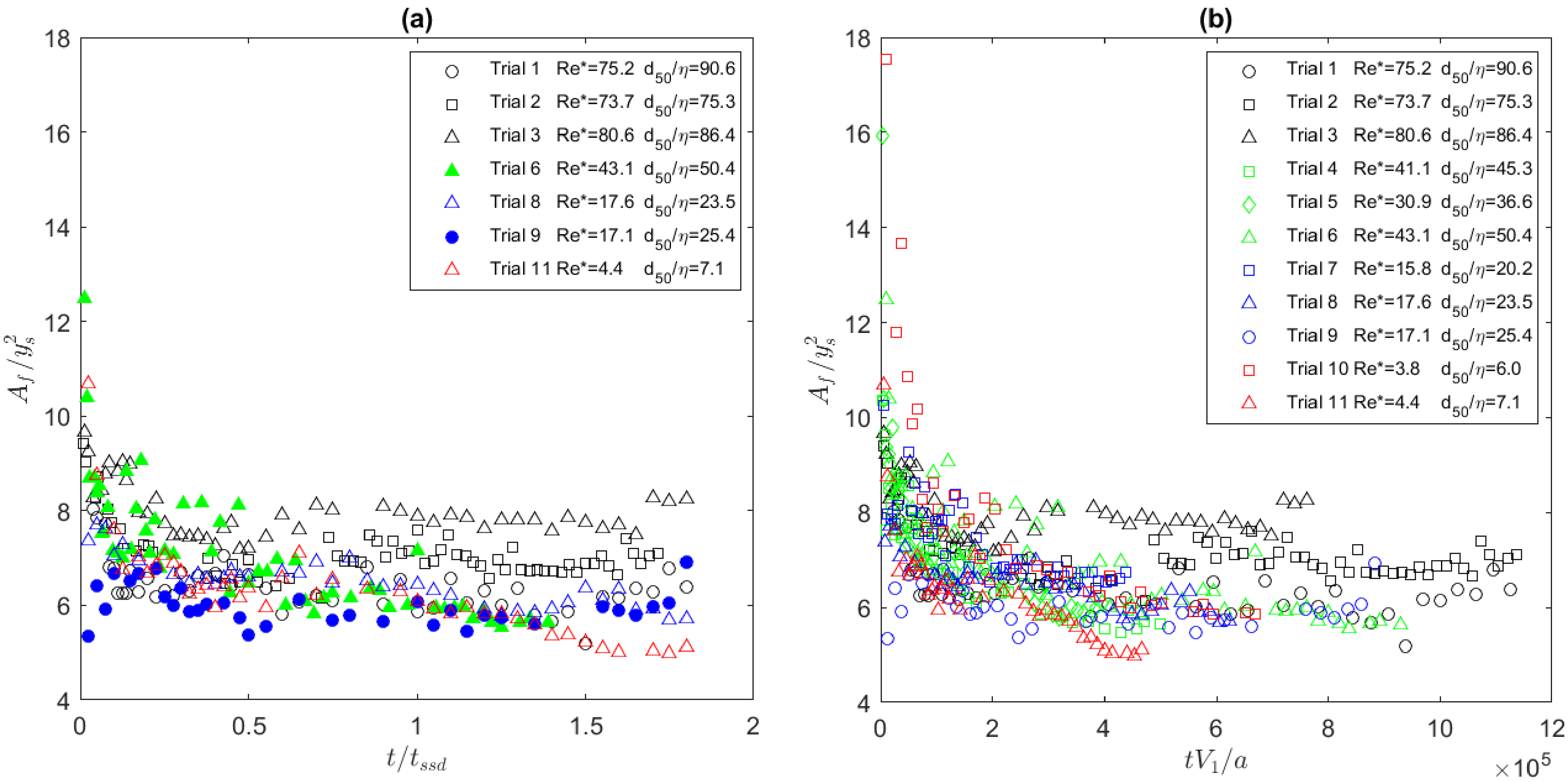

Figure 5.19 Variation of scour hole footprint as a function of (a) time normalised with the crossover timescale, and (b) the timescale of scour for all trials. In panel (a), Trials 6 and 9 are infilled due to questionable reliability in identifying the crossover point.

5.4 Summary

By deploying the measuring technique for experimental trials, the development of the scour hole volume, within vicinity of the HS vortex, was found to scale linearly with the maximum scour depth cubed . Whilst the first and second regimes are attributable to the initial generation and steady growth of the HS vortex, respectively, a third regime observed after significant scour development signifies a change in the physics of clear-water local scour evolution. By considering turbulence phenomenology, the transition from the second to third regime can be interpreted as a plateauing of turbulent kinetic energy production. The plateau coincides with a stabilisation of the bulk scour volume, relative to the steadily-increasing maximum scour depth. The stabilisation in the volume is the result of a trade-off between erosion and deposition characteristics from in-front and around the sides of the pier, which combine to nullify any further significant change in the scour volume.

Interestingly, the sediment erosion and deposition trade-off in the third regime was found to be influenced by the flow regime within the scour hole. For the fully-rough regime beyond the crossover point, the trade-off of sediment movement can be characterised by continued erosion upstream of the test pier coinciding with a local build-up of sediment around the pier flanks. However for the viscosity-dominated hydraulically-smooth regime, the erosion and deposition patterns are completely reversed, where erosion within the flanks and minor deposition upstream of the scour hole is observed to continue post-crossover. As such, the presence of a crossover point identifies a significant change in the physics of clear-water scour development that is physically underwritten by sediment redistribution which varies as a function of viscosity.

The similarity analysis was extended to defining the development of the scour hole boundaries with time. Relationships between the scour boundaries, namely L, W and A_f, were related to the development in scour depth due to this property being extensively-researched. The variation of the scour boundaries was found to grow in proportion with depth and independent of time. The scaling relationships presented within the text are suitable for engineering applications as a good estimation of the scour major axes and footprint for a given scour depth.

Chapter 6: Predictive Method for Scour Hole Geometry

6.1 Introduction

In Chapter 5 the scaling of the scour hole geometry with time was presented. Most notably, it was observed that the relationship between scour hole volume and the maximum depth cubed scales through three linear regimes. The phenomenon of the crossover point and transition into the third regime after significant scour development was physically explained using an energetic interpretation and consideration of sediment redistribution patterns. In this Chapter, quantitative analysis of the relationship $V_{ol} \sim y_s^3$ is presented. The focus is on deriving a predictive model for the crossover depth that can be used as a scaling parameter to define geometric properties of the scour hole at the crossover for engineering applications.

6.2 Modelling the Crossover Depth

The crossover defines a point in time when the development in scour volume significantly changes and essentially plateaus. It is herein argued that at this point in time the shear stress acting on the scour hole surface approaches the value of the critical shear stress i.e. $\tau \approx \tau_c$, beyond which the shear stress and critical shear stress are approximately equal. Following energetic considerations, it was identified that the crossover identified the point at which the power of the HS vortex goes constant. The HS vortex is well known to drive the scour development process (e.g. Dargahi, 1990) and, as such, beyond the crossover only localised changes in sediment movements are observed. Hence, the assumption that $\tau \approx \tau_c$ at the point of crossover is very plausible at least in a "bulk" sense, where "bulk" implies the average condition over the scour hole surface within vicinity of the HS vortex

The framework of $\tau \approx \tau_c$ was used in the theoretical approach by Manes and Brocchini (2015). As such, their approach is exploited to initially model the crossover depth, y_{ssd}. To be consistent with the derivation by Manes and Brocchini (2015), only the fully-rough cases are initially modelled. Accordingly, the equilibrium scour depth (y_{se}) – as derived in the original equation by Manes and Brocchini (2015) (see Section 2.5.3) – is replaced by the new scaling depth y_{ssd},

$$\frac{y_{ssd}g}{V_1^2} \sim \frac{\rho}{(\rho_s - \rho)} {C_D}^{2/3} \left(\frac{a}{d_{50}}\right)^{2/3} \tag{6.1}$$

The predictive formula in Eq. (6.1) is presented for the fully-rough cases in Figure 6.1. For completeness, the corresponding crossover data from the remaining flow regimes are also included.

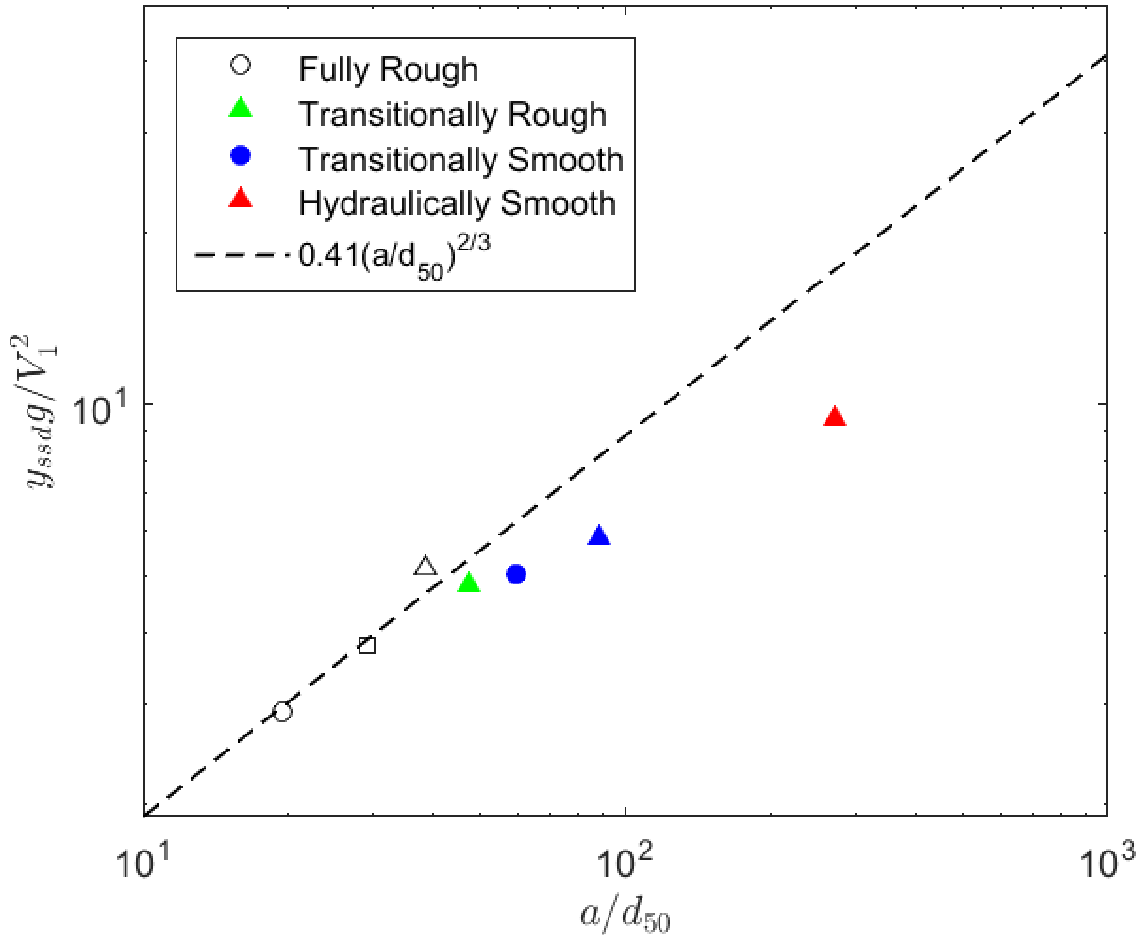

Figure 6.1 Crossover depth modelled using the predictive formula given in Eq. (6.1). The infilled symbols are included for context but do not adhere to the idealisations used in the formula. The colours and symbols are consistent with those used in Chapter 5, representing the fully-rough [Re^*=73.7÷80.6, d_{50}/η=75.3÷90.6], transitionally rough [Re^*=43.1, d_{50}/η=50.4], transitionally smooth [Re^*=17.1÷17.6, d_{50}/η=23.5÷25.4] and hydraulically smooth [Re^*=4.4, d_{50}/η=7.1] flow regimes.

Modelling the crossover depth using Eq. (6.1) gives two important observations. Firstly, the scaling of the crossover depth for the fully-rough trials shows excellent agreement with the 2/3 power line. This corroborates application of the approach by Manes and Brocchini (2015) for modelling the crossover depth for trials within this regime. Conversely, the scaling of crossover trials at transitional regimes shows poor scaling with the power law, with deviation from the line observed to increase with a decrease in Re^*. This is owing to the original approach by Manes and Brocchini (2015) who simplified their derivation to ignore the effects of viscosity owing to a change in flow regime inside the scour hole.

6.2.1 Viscosity Effects

In the literature on local scour, the effects of viscosity have often been disregarded. The reasons for this are typically accredited to the pier Reynolds number (Re_p), quantified by the ratio between inertial and viscous forces aV_1/υ, having a negligible effect on the scour process for large values of Re_p where flows are highly turbulent. However, early work by Shen *et al.* (1969) identified that the equilibrium scour depth has some dependency on Re_p, owing to its effect on the size and strength of the HS vortex. Ettema *et al.* (2006) observed Re_p to also have some effect on the vorticity associated with the wake vortices and their ability to move sediment from the sides and behind the test pier, highlighting that smaller cylinders generate wake vortices of increased vorticity when considering large-scale turbulence intensity. More recently, Lança *et al.* (2016) isolated the effects of viscosity by means of adimensional analysis approach that differs from the approach set out in Section 2.3 to derive a dimensionless sediment diameter defined by $d_* = \sqrt[3]{g\Delta d_{50}^3/\upsilon^2}$ for quantifying viscosity effects, where Δ is the ratio between sediment and fluid density i.e. $(\rho_s - \rho)/\rho$. The unconventional approach, using a bespoke set of data, was used to identify that the end-of-trial scour depth increased with a decrease in d_*. Furthermore, it was observed in Chapter 5 that the nature of sediment redistribution within the third linear regime is influenced by the effects of viscosity characterised by a trade-off in sediment erosion and deposition around the pier sides which changes with viscosity-dependency inside the scour hole. The work by Shields (1936) also implies that the condition of incipient motion of a sediment is dependent on the effects of viscosity, quantified by the particle Reynolds number i.e. $\tau_c \sim (\rho_s - \rho) g d_{50} \sim f(Re^*) = \rho U_*/\upsilon$.

Clearly, the effect of viscosity negligibly influences the scouring process if the flow inside the scour hole is in the fully-rough flow regime (Ettema *et al.*, 1998; Lança *et al.*, 2016), where the variability of the critical shear stress saturates to the scaling law defined as $\tau_c \sim (\rho_s - \rho) g d_{50}$, as according to the Shields curve. However, fully-rough conditions are associated with high Boundary Reynolds number which are only applicable to very coarse sands and gravels (Shields, 1936; Miedema, 2010). These sizes are often larger than bed sediments (often consisting of sand or finer materials) commonly used in laboratory studies and found at field sites which are characterised by the transitionally-rough or transitionally-smooth regime.

Therefore, viscosity effects must be accounted for both in the computation of the critical shear stress and the shear stress acting on the surface of the scour hole. Within this context, the theoretical approach used to derive Eq. (6.1) is now extended to account for the effects of viscosity.

6.2.1.1 Incorporating the Effects of Viscosity

The assumptions of fully-rough flow conditions in the Manes and Brocchini (2015) formula are now relaxed by considering the effects of viscosity. This is addressed in two ways; (a) in the formulation of the shear stress acting on the scour hole, and (b) adding a dependency of the critical shear stress on viscosity, as discussed through consideration of Shields criteria. These are addressed in turn.

We first seek to incorporate the effects of viscosity within the computation of τ. As defined by Eq. (6.7), application of the framework by Manes and Brocchini (2015) is valid so long as the sediment diameter d_{50} belongs to the inertial range of turbulent scales. The second-order structure function, $D(l)$, that describes turbulence phenomena in the inertial and dissipation range range is well described by the Batchelor formula given by (e.g. Lohse and Muller-Groeling, 1994)

$$\frac{D(l)}{\upsilon^2} = \frac{l^2}{3\eta^4\left[1+\left(\frac{1}{3b}\right)^{3/2}\left(\frac{l}{\eta}\right)^2\right]^{2/3}}. \tag{6.2}$$

where l is a characteristic length scale in the inertial range and b = 5.834. Considering Kolmogorov's scaling, within the inertial range of scales the second order structure function can be converted to (e.g. Gravanis and Akylas, 2015)

$$D(l) = \overline{[u_l(r_1) - u_l(r_2)]^2} = C_2(\epsilon l)^{2/3}. \tag{6.3}$$

where r_1, r_2 denote the location of velocity measurements separated by the vector **r**, and C_2 is the Kolmogorov constant arising from Kolmogorov's two-thirds law. Accordingly by exploiting Kolmogorov and Obukhov's law (see Eq. (2.4)), the characteristic velocity of eddies at a characteristic length scale, l, can be modelled using $D(l)$ as

$$u_l \cong \sqrt{D(l)}, \tag{6.4}$$

Where $D(l)$ is defined in Eq. (6.2).

As Eq. (6.2) can reproduce turbulence phenomena in the inertial and dissipation range very well, it is used to model the effects of viscosity as the characteristic length scale l approaches the order of magnitude of the Kolmogorov length scale, η. According to Gioia and Chakraborty (2006), the momentum transfer of near-wall eddies in any flow regime, is dominated by eddies of characteristic length scale

$$l \cong d_{50} + a\eta, \tag{6.5}$$

where a = 5 (i.e. 5η is estimated to be the thickness of the viscous sublayer over the bed sediment). As η becomes very small relative to d_{50}, it is clearly apparent that sediment roughness re-establishes dominance in near-wall momentum transfer and fully-rough conditions result. As such, the combination of Eq.'s (6.2), (6.4) and (6.5) converts the definition of shear stress given by $\tau \sim \rho u_{d50} V$ into a more general function of the form

$$\tau \sim \rho u_{d50} V \sim \rho \sqrt{D(l)} V. \tag{6.6}$$

Eq. (6.6) can be used to define the effects of viscosity on τ as l approaches the order of magnitude of the Kolmogorov length scale η.

The effect of viscosity on the critical shear stress is now addressed. To this end, the principle of incipient motion first introduced by Shields (1936) is exploited to define the dependency of τ_c on viscosity using the particle Reynolds number, Re^*. In keeping with the phenomenological approach used throughout the derivation, Re^* is defined as the ratio between mean sediment size and the Kolmogorov length scale (i.e. d_{50}/η). As such, the dependency of τ_c on viscosity is captured by

$$\frac{\tau_c}{(\rho_s - \rho) g d_{50}} \sim f\left(\frac{d_{50}}{\eta}\right). \tag{6.7}$$

The dependency of τ_c on d_{50}/η saturates to a constant at fully-rough turbulent flow conditions as used in the current approach. Eq. (6.6) and (6.7) can be integrated within Eq. (6.1) to model the effects of viscosity on τ and τ_c. At equilibrium, Eq. (6.1) therefore converts to the form

$$\frac{\tau_c}{(\rho_s - \rho) g d_{50}} \sim f\left(\frac{d_{50}}{\eta}\right) \sim \rho V_1 \sqrt{D(l)} \left(\frac{C_d a}{L}\right)^{1/3}, \tag{6.8}$$

which is solvable if the empirical function $f\left(\frac{d_{50}}{\eta}\right)$ can be quantified.

6.2.1.2 Validation

Here, experimental data presented previously is exploited to assess to what extent the theoretical framework used to model the crossover depth in Section 6.2 is influenced by viscosity effects. To this end, the contribution to τ and τ_c as a function of flow regime (i.e. d_{50}/η) are addressed in isolation.

The dependency of τ on flow regime (and therefore the effects of viscosity relative to inertial forces) can be quantified by considering the ratio between the shear stress modelled using Eq. (6.6), where viscosity effects are integrated within the second order structure function $\sqrt{D(l)}$, and the shear stress modelled using the Manes and Brocchini (2015) idealisation for $\tau \sim \rho u_{d50} V$(6.2), which represents the simplified fully-rough condition. Accordingly, this ratio is reduced to u_l/u_{d50}, which is presented as a function of d_{50}/η in Figure *6.2*. Note that the trials with infilled symbols (i.e. Trials 6 and 9) are those with uncertain crossover data. As presented in Figure *6.2*, the ratio u_l/u_{d50} shows very little variation (at most 5%). As such, within the range $6 < d_{50}/\eta < 90$, viscosity effects on the computation of τ can be reasonably neglected.

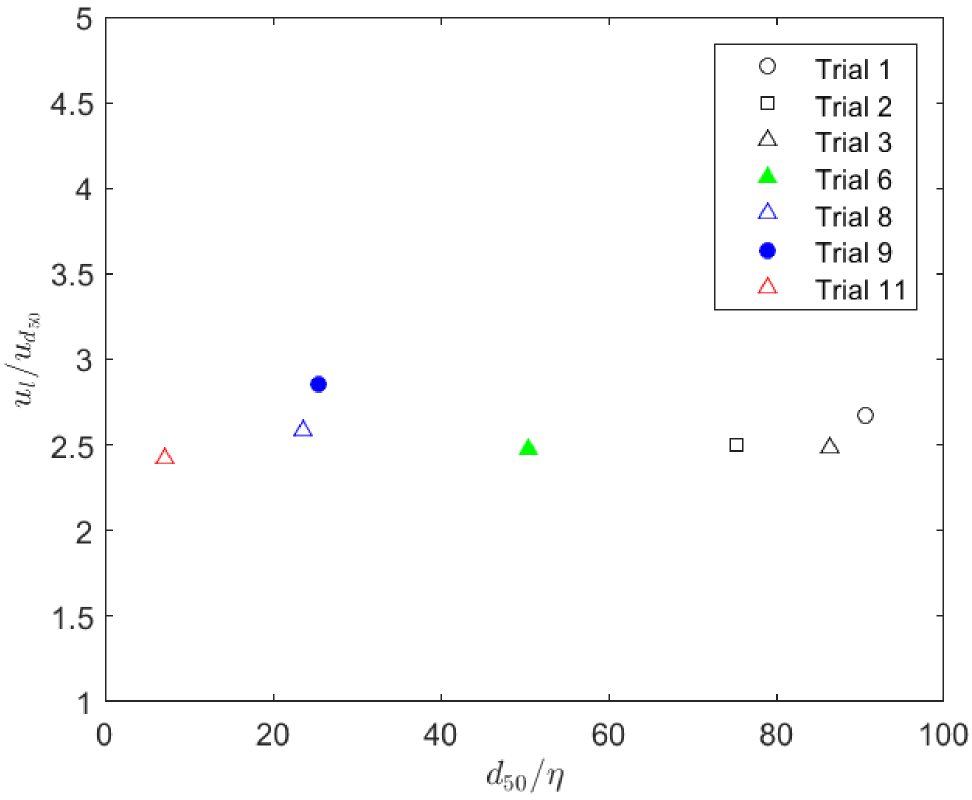

Figure 6.2 Effect of viscosity on τ (modelled by the ratio u_l / u_{d50}) as a function of the flow regime modelled by d_{50} / η. The infilled symbols are those that have questionable reliability in their evidence of a crossover point.

Accordingly, the condition $\tau \approx \tau_c$ (as in Eq. (6.8)) at the crossover can be reasonably replaced by

$$(\rho_s - \rho) g d_{50} f\left(\frac{d_{50}}{\eta}\right) \sim \rho V_1^2 \left(\frac{C_d a}{L}\right)^{2/3} \left(\frac{d_{50}}{L}\right)^{1/3}, \tag{6.9}$$

which, after rearranging, gives

$$\frac{y_{ssd} g}{V_1^2} \sim \frac{1}{f\left(\frac{d_{50}}{\eta}\right)} \frac{\rho}{(\rho_s - \rho)} {C_D}^{2/3} \left(\frac{a}{d_{50}}\right)^{2/3}. \tag{6.10}$$

Due to the dependency of τ on viscosity being reasonably ignored, Eq. (6.10) essentially takes the form of the fully-rough solution given in Eq. (6.1) modulated by the dependency of τ_c on viscosity which is captured by the function $f\left(\frac{d_{50}}{\eta}\right)$.

The function f embodies the variation of the critical shear stress with the flow regime as per Shields criteria for incipient motion. This variation of τ_c with regime, modelled by d_{50}/η, is regarded by many to be reproduced well by the Brownlie (1981) equation which reads as follows

$$f = 0.22\left(\frac{d_{50}}{\eta}\right)^{-0.6} + 0.06e^{-17.77\left(\frac{d_{50}}{\eta}\right)^{-0.6}}. \tag{6.11}$$

The data captured at the point of crossover is now exploited to empirically calibrate Eq. (6.11) for application. The function $f(d_{50}/\eta)$ given by Eq. (6.11) is presented in Figure 6.3a as a fit to the measured data[34]. Note that a coefficient C is applied to the Brownlie equation given in Eq. (6.11) to shift the curve vertically to be reproduced within the range of the experimental data i.e.

$$f = C\left\{0.22\left(\frac{d_{50}}{\eta}\right)^{-0.6} + 0.06e^{-17.77\left(\frac{d_{50}}{\eta}\right)^{-0.6}}\right\}. \tag{6.12}$$

The solution pertaining to the curve presented in Figure *6.3*a is Eq. (6.12) with C=52. The Kolmogorov length scale is estimated using Eq. (2.12) with the assumption that $L{\sim}a$ as discussed extensively in Manes and Brocchini (2015).

Figure *6.3*a shows that the crossover data used in the computation of $f(d_{50}/\eta)$ resembles a Shields-type curve which appears to be modelled well by the adjusted Brownlie equation given by Eq. (6.12). For comparison, the figure also includes a dashed curve which represents an ad-hoc tuned version of the Brownlie equation coefficients[35] derived by Manes *et al.* (2018) to fit a curve to the function $f(d_{50}/\eta)$ for equilibrium scour depth data taken from the literature. They found that the main difference in the two curves (i.e. the original Brownlie and their adjusted version) was a steeper rise in the transitionally rough branch after the minimum that separates the transitionally-smooth and the transitionally-rough regimes. However, modelling the function using the crossover data as the scaling parameter is well represented by the original Brownlie (1981) equation in absence of any adjustments to the equations' coefficients. This suggests that the crossover provides a good alternative to the equilibrium scour depth as a scaling parameter, which is likely owing to the timescale of the latter being poorly defined within the literature

---

[34] The value of *f* calculated using measured data is given using Eq. (6.10).

[35] The tuned version of the Brownlie equation is of the form $f = C\left\{0.22\left(\frac{d_{50}}{\eta}\right)^{-0.6} + 0.09e^{-17.77\left(\frac{d_{50}}{\eta}\right)^{-0.6}}\right\}$ (Manes et al., 2018), where coefficient C is a function of the definition of equilibrium scour depth timescale.

(Lança *et al.*, 2013; Manes and Brocchini, 2015). The good agreement of $f(d_{50}/\eta)$ modelled using a modified Brownlie equation (Eq. (6.12)) for the crossover data is promising, but should be further supported by more data for higher values of d_{50}/η.

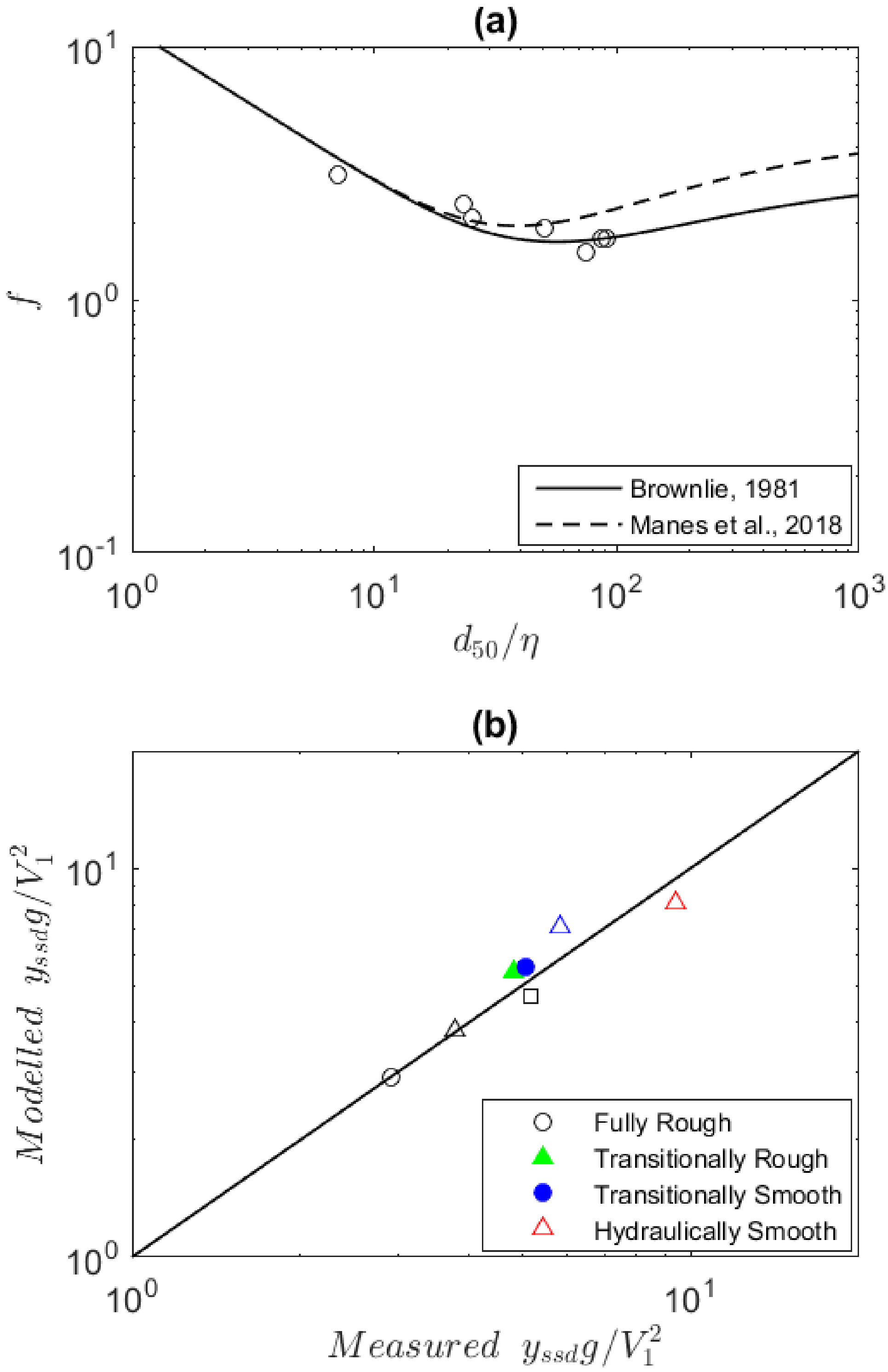

Figure 6.3 (a) Variation of the function f(d/η) estimated using equations by Brownlie (1981) and Manes et al. (2018). The Brownlie (1981) curve is vertically shifted by a factor C to reproduce the curve within the experimental data range. (b) Crossover depth modelled using the original Brownlie equation to derive f and the predictive formula presented in Eq. (6.10). The solid line defines theoretical equality. The infilled symbols are those that have questionable reliability in their evidence of a crossover point.

The calibrated solution to the function $f(d_{50}/\eta)$ can be used in Eq. (6.10) to explore the implications of adjusting Eq. (6.1) to account for viscosity effects in the computation of τ_c. The measured and modelled values for the normalised scour depth are shown in Figure *6.3*b. In comparison with the fully-rough idealised form presented in Figure *6.1*, the viscosity-adjusted linear curve shows a much improved agreement between the measured values and those modelled using Eq. (6.10), with a maximum error in the abscissa of 16.7%. Accordingly, Eq. (6.10) and (6.3) may be used for application to estimate the crossover depth, y_{ssd} subject to further support from data covering a wider range of d_{50}/η.

6.3 Modelling Scour Hole Characteristics at the Crossover

In Section 6.2, the experiment data weres used to successfully derive a predictive model for the crossover scour depth y_{ssd} which accounts for a change in flow regime (and therefore the relative importance of viscosity effects). Here, the experimental dataset is further exploited to derive empirical relations using the scaling depth as a proxy to estimate other geometrical properties at the point of crossover that are important for local scour assessment.

The scaling of the measured crossover depth with corresponding measurements of the scour hole crossover (a) width, (b), length, (c) footprint and (d) volume are presented in Figure 6.4. The scaling of the crossover depth in each panel is excellent, with a maximum discrepancy between the predicted and measured values of 7.4%, 10.2%, 11.3% and 9.6% for the crossover width, length, footprint and volume, respectively[36]. The proposed relations are very promising for engineering applications, using the crossover depth which is quantifiable using the predictive model given in Section 6.2. These results should be further supported by data covering a wider range of hydrodynamic conditions.

---

[36] The errors were quantified by computing the difference between the modelled and measured values of each geometric property at the abscissa given by the measured crossover depths.

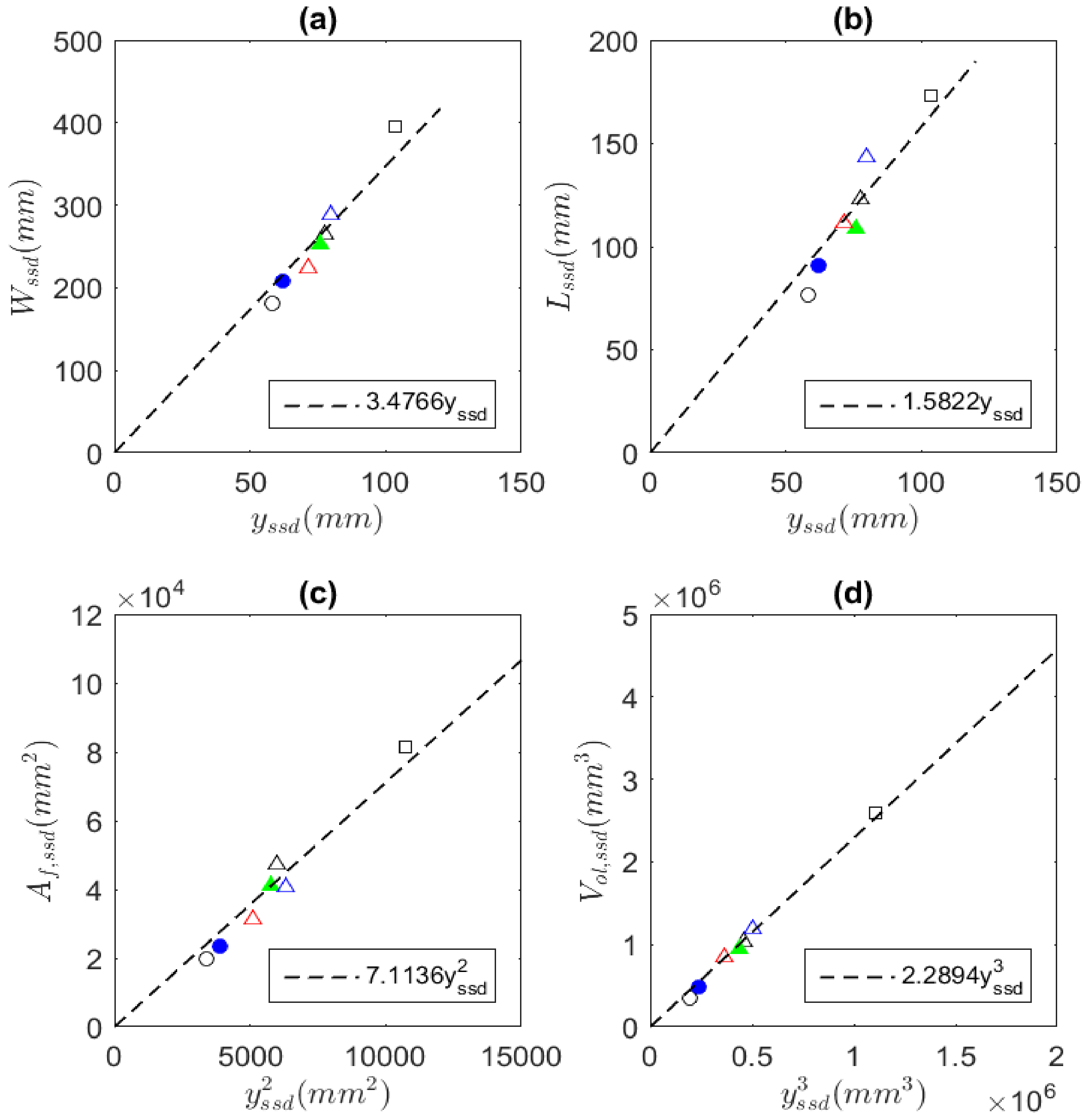

Figure 6.4 Scaling of the crossover depth with the corresponding crossover (a) width, (b) length, (c) scour footprint and (d) scour volume. Trial 6 and 9 are infilled to highlight reliability issues.

For completeness, the pier diameter was also modelled as the scaling parameter to compute the same crossover geometric properties of the scour hole. This is presented in Figure 6.5. The discrepancy between the measured and predicted values is 10.7%, 10.6%, 15.4% and 22.8% for the crossover width, length, footprint and volume, respectively, which is greater relative to the equivalent errors using the crossover depth as the scaling parameter.

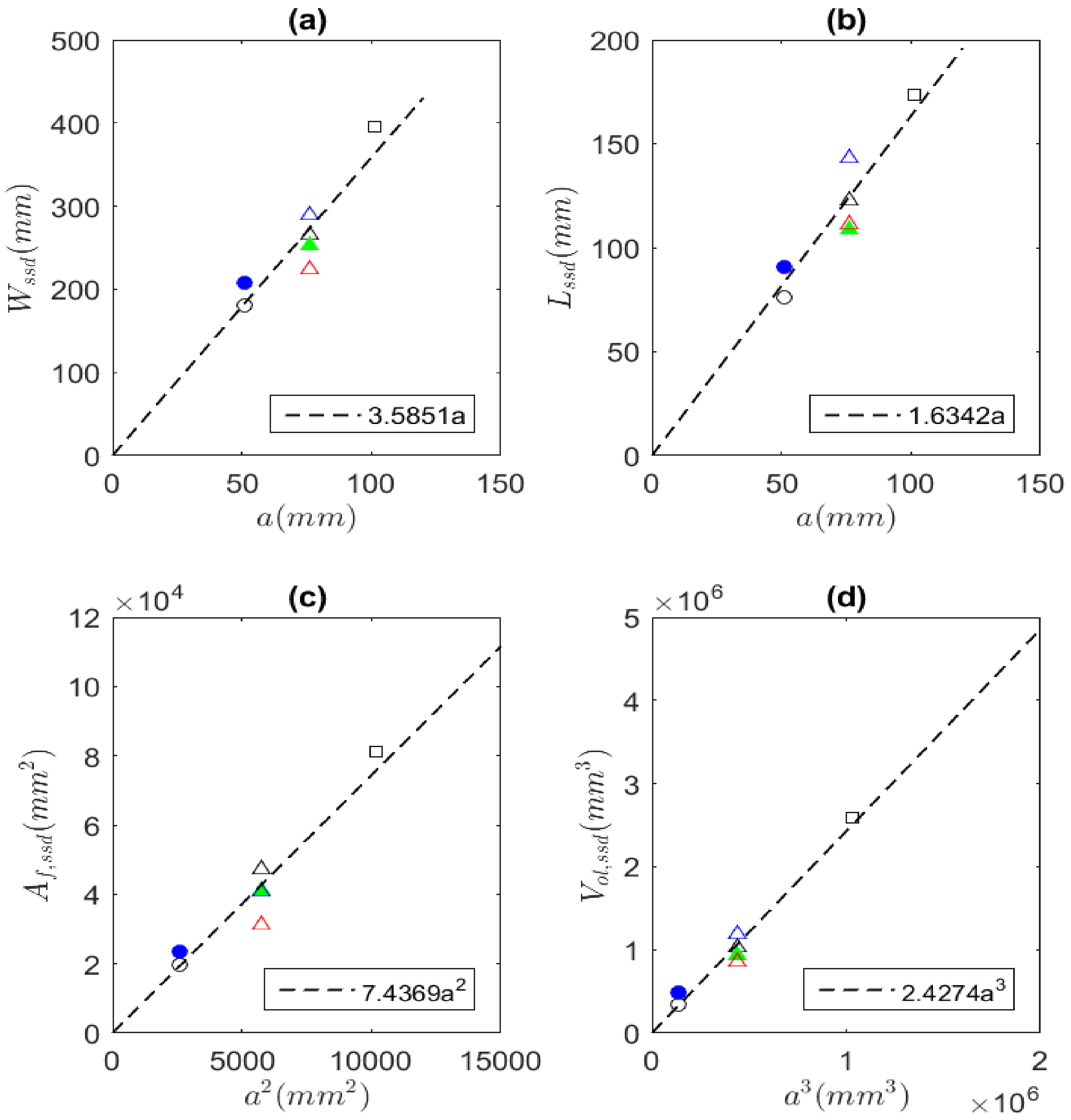

Figure 6.5 Scaling of the pier diameter with the crossover (a) width, (b) length, (c) scour footprint and (d) scour volume.

6.4 Timescale to Crossover

In Section 5.2, the crossover point was found to represent a point in scour development process where the rate of increase in eroded volume of the scour hole, with vicinity of the HS vortex, significantly reduces. As such, the crossover is somewhat closely related to the equilibrium scour depth in that it characterises the point in time at which the scour volume reaches an almost "equilibrium state", with scour evolution beyond this point dictated by sediment redistribution patterns, as observed previously. As discussed extensively within the literature review, the timescale to the equilibrium scour depth is arbitrarily defined (e.g. Lança *et al.*, 2013). Therefore, the existence of a physically-defined crossover point represents a potentially excellent length and time scale parameter that may be more suited for calibrating models that describe local scour dynamics and evolution in time.

The crossover trial data is shown in Table 6.1. The timescale to the crossover point has, presumably, some dependence on both the pier diameter and flow velocity; the parameters often used to model the timescale to the equilibrium depth. This is a reasonable assumption. The former of these parameters dictated the removal of four trials due to the absence of a clearly-defined crossover point. The flow intensity parameter, and therefore the critical bed shear stress, is also well-known to have an influence on the equilibrium timescale (e.g. Melville, 2008). However, it has been shown in Section 5.2 that the nature of the scour hole evolution post-crossover is somewhat critically dictated by the flow regime inside the scour hole, and therefore has at least some dependence on the effects of viscosity. As the purpose of this thesis was to investigate the geometric development of the scour hole within the framework of Manes and Brocchini (2015), the effect of each test parameter on the crossover timescale was not tested in isolation.

The scour development process is driven by the effect of many interlinked mechanisms related to the mean and fluctuating properties of the flow which influence the interaction of the HS vortex with the sediment bed. The crossover point represents the point at which the rate of TKE production within vicinity of the HS vortex reaches a plateau. Therefore, modelling of the crossover timescale requires a dedicated experimental campaign that provides a much more complex view on the behaviour of the HS vortex covering a wide range of hydrodynamic regimes around the crossover point.

Table 6.1 Crossover trial parameters and measured crossover characteristics.

Trial	**a (mm)**	**d_{50} (mm)**	**$y_{s,\,ssd}$ (mm)**	**$V_{ol,\,ssd}$ ($\times10^{-3}\,m^3$)**	**t_{ssd} (hrs)**	**a/d_{50}**	**V_1/V_c**	**Re***
1	51	2.62	58.1	0.342	20	19.5	0.71	75.2
2	101	2.62	103.5	2.589	42	38.5	0.71	73.7
3	76	2.62	77.3	1.035	20	29.0	0.71	80.6
6	76	1.61	75.9	0.937	36	47.2	0.80	43.1
8	76	0.86	79.5	1.181	20	88.4	0.99	17.6
9	51	0.86	62.2	0.485	20	59.3	0.95	17.1
11	76	0.28	71.5	0.849	20	271.4	0.98	4.4

6.5 Summary

This aim of this Chapter was to provide a quantitative analysis of the relationship between scour hole volume and the corresponding depth cubed, which was identified in the previous Chapter to vary through three linear regimes. In particular, the transition into the third regime after significant scour development highlighted a point in time when the physics of the scour process changes significantly. Towards this end this crossover depth was modelled using a theoretical approach by Manes and Brocchini (2015), which was found to provide an excellent fitting to the crossover data under the baseline assumption that, at that point, $\tau \approx \tau_c$. The predictive model, originally idealised for fully-rough conditions only, was extended to account for viscosity effects by considering the dependency of τ and τ_c on the flow regime in turn. The dependency of τ was derived under the assumption that momentum transfer across the wetted surface parallel to the peaks of the viscous layer is dominated by eddies of a size quantified by the sum of the bed sediment diameter and the thickness of the viscous sub-layer, which can be assumed to scale with the Kolmogorov length scale (Gioia and Chakraborty, 2006). For eddies of this characteristic size, the characteristic velocity was estimated using the second-order structure function proposed by Batchelor. The equivalent dependency of τ_c on flow regime (and therefore viscosity effects) for the crossover data was captured by the function $f(d_{50}/\eta)$ which was found to resemble a Shields-type curve that was modelled well using a modified version of the Brownlie (1981) equation. .

Under these principles, the theoretical framework was found to provide an excellent model for the crossover depth using the measured experiment data. Moreover, this crossover depth was found to be an excellent scaling parameter for quantifying other geometric properties of the scour hole at the point of crossover using empirical data-fitting. The final formulae presented in Eq. (6.10), Eq. (6.12) and Figure 6.4 are very promising for engineering applications but should be further supported by data covering a wider range of hydrodynamic conditions.

As a side-note, the scaling relationship between $\mathrm{V_{ol}}$ and $\mathrm{y_s^3}$ at the crossover, as presented in Figure 6.4d, is excellent. This has particular relevance as it can be used to validate an underlying assumption of the Manes and Brocchini (2015) approach that, at equilibrium, the volume of the characteristic large-scale eddy $\mathrm{V_{ol}} \sim \mathrm{y_{se}^3}$, where $\mathrm{y_{se}}$ is the aforementioned equilibrium scour depth. The evidence presented in Figure 6.4d suggests that, at least as far as the crossover point is concerned, this scaling is valid. Therefore, using this theoretical framework for modelling the crossover depth is strengthened where the assumption $V_{ol} \sim y_s^3$ has been proven here to hold true.

Chapter 7: Conclusion

The aim of this thesis was to address the issue of designing and implementing an experimental methodology for measuring the geometry of a developing local scour hole in a quasi-non-invasive manner. Towards this end, a novel technique that involved fixing a swath-scanning sonar profiler to a fully-programmable longitudinal slider was developed. The methodology was extensively validated using independent gauge measurements of the bed surface that identified minimal and consistent errors when using the technique to scan both profiled and flat-bed surfaces. Moreover, repeated trials with and without the equipment showed that the measurement method is non-invasive to vortex development which drives the scour process and is repeatable (Obj. 1).

By deploying the measuring technique for experiment trials, the geometric similarity of the scour hole as it develops over time could be analysed. The focus was on the relationship between the scour depth, length, width, footprint and volume, as each of these geometric properties play an important role in modelling and predicting scour behaviour (Obj. 2).

The development of the scour hole volume in time, within the vicinity of the HS vortex, was found to scale with respect to the maximum scour depth cubed through three linear regimes. Whilst the first and second regimes are attributable to the initial generation and steady growth of the HS vortex, respectively, a third regime observed after significant scour development signifies a change in the physics of clear-water local scour evolution. The transition from the second to third regime was termed the *crossover point*. By considering turbulence phenomenology, the occurrence of the crossover point corresponds to a point in the scour development process where the production of turbulent kinetic energy plateaus. The plateau coincides with a stabilisation of the bulk scour volume, relative to the steadily-increasing maximum scour depth.

The stabilisation in the scour volume after the crossover point is dependent on the flow regime inside the scour hole. By considering sediment redistribution patterns through observing the changes between the scoured surface at the crossover point and those pre- and post- crossover, the stabilisation in volume is owing to a trade-off between erosion and deposition in front and around the sides of the pier which combine to nullify the magnitude of the scour volume. For the fully-rough regime beyond the crossover point, the trade-off of sediment movement can be characterised by continued erosion upstream of the test pier coinciding with a local build-up of sediment around the pier flanks. However for the viscosity-dominated hydraulically-smooth regime, the erosion and deposition patterns that are observed post-crossover are completely reversed. As such, the presence of a crossover point identifies a significant change in the physics of clear-water scour development that is physically underwritten by sediment redistribution which varies as a function of flow regime, highlighting the relative importance of viscosity effects (Obj. 3).

The remaining geometric properties of the scour hole were correlated with the development of the maximum scour depth, as the development of this property is extensively published in the literature. By considering their development in time, the scour length and width were observed to grow consistently with the maximum depth beyond initial formation of the scour hole, independently of time. This was interpreted as the major axes of the scour hole showing geometric proportionality. The scaling relationships presented in Chapter 6 were validated using data available from the literature and can be used in engineering applications to estimate the scour length and width for a given scour depth (Obj. 4). Interestingly, the effects of viscosity on the major axes were found to notably influence the scour width, with viscosity-dependent regimes associated with narrower scour holes (Obj. 2).

7.1 Significance of the Crossover Depth

A means of quantifying the occurrence of the crossover point was provided in Chapter 6 using the baseline assumption that, at least in a "bulk" sense across the scour hole on average, $\tau \approx \tau_c$. This was found to be plausible owing to the rate of turbulent kinetic energy within vicinity of the HS vortex essentially plateauing beyond this point in time. Modelling the crossover depth using the theoretical approach by Manes and Brocchini (2015) provided an excellent fit to the crossover details derived from the fully-rough experiment data. The model was subsequently extended to account for the effects of viscosity by considering the dependency of both τ and τ_c on the flow regime (Obj. 3). With the viscosity extension applied to the model, the predicted crossover depth provided striking agreement with the experimental data. The corresponding geometric properties at the crossover point scale very well with crossover depth which is very promising for engineering applications, but should be further supported by data covering a wider range of hydrodynamic conditions (Obj. 4). As a side note, the scaling of $V_{ol,ssd} \sim y_{ssd}^3$ is excellent and provides strong evidence that, at least as far as the crossover point is concerned, the scaling of these two geometric properties ($V_{ol,ssd}$ and y_{ssd}) is cubic. This validates an underlying assumption of the Manes and Brocchini (2015) approach that $V_{ol} \sim y_s^3$ which is highly relevant in that this framework was used as the basis to model the crossover depth itself (Obj. 4).

The occurrence of the crossover point denotes a significant point in the scour process where a switch in the physics of scour development occurs. As such, the crossover depth is a length scale that, essentially, embodies a close relative to the equilibrium scour depth in the sense that it is characterised by the point at which the development in scour volume plateaus to an "equilibrium" state, and evolution beyond it is dictated by the redistribution of sediment in front and around the sides of the pier. A condition of bulk equilibrium is evidenced by the excellent modelling of the data under the assumption that $\tau \approx \tau_c$. Accordingly, the existence of a well-defined crossover point presents itself as an excellent candidate for defining length and time scales that may effectively describe local scour dynamics and evolution in time. This is extremely relevant because, especially in clear-water conditions, the definition of such scales is still elusive as the equilibrium scour depth and time are well known to be arbitrarily defined.

7.2 Final Discussion and Suggested Further Work

The stabilisation of the scour volume beyond the crossover point was found to be the result of a trade-off between sediment erosion and deposition patterns around the front and sides of the pier. Whilst a plausible physical explanation for the behaviour in fully-rough conditions is provided within the text, a corresponding interpretation of the sediment redistribution patterns in the viscosity-dependent flow regimes remain elusive in this thesis. A physical interpretation of the erosion-deposition patterns for the viscosity-dependent trials is difficult as they are an effect of many interlinked mechanisms related to the mean and fluctuating properties of the flow which would require a dedicated experimental campaign. In order to disentangle the problem, accurate flow measurements within the vicinity of the scour hole must be carried out as the scour hole develops as sediment incipient motion conditions (an hence so-called equilibrium conditions in the scour hole) are dictated by turbulent fluctuations, mean flow properties and the scour hole geometry (i.e. local bed slopes).

Furthermore, the sediment redistribution patterns, along with the identification of a physically-defined crossover point and associated scaling relations, should be further supported with more data covering a wider range of hydrodynamic regimes and variations in flow intensity. This would provide a much more complete view on the behaviour of the function f across a wider range of d_{50}/η and hence further validation towards the application of these results for engineering practice.

Appendix A Laboratory Structural Drawings

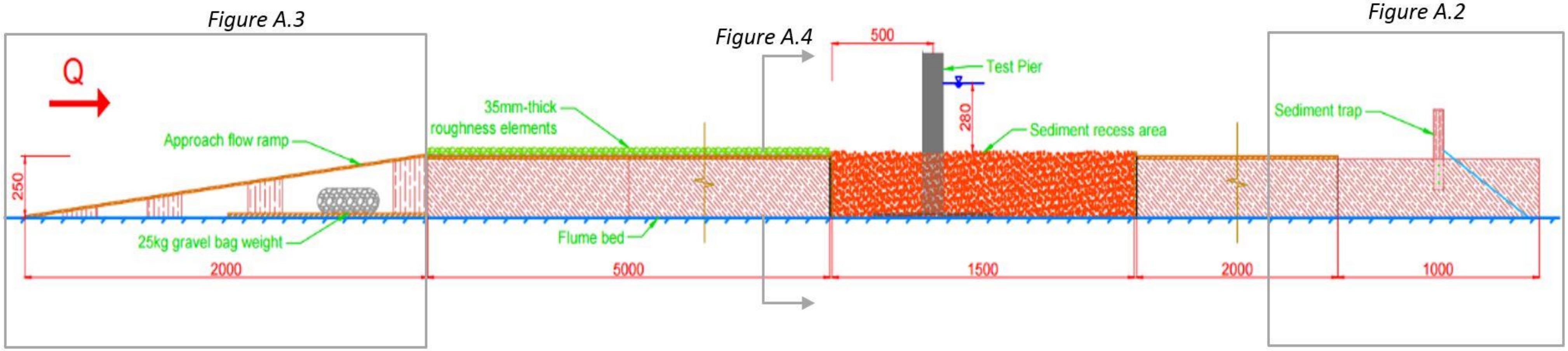

Figure A.1 Full elevation of laboratory structural platform.

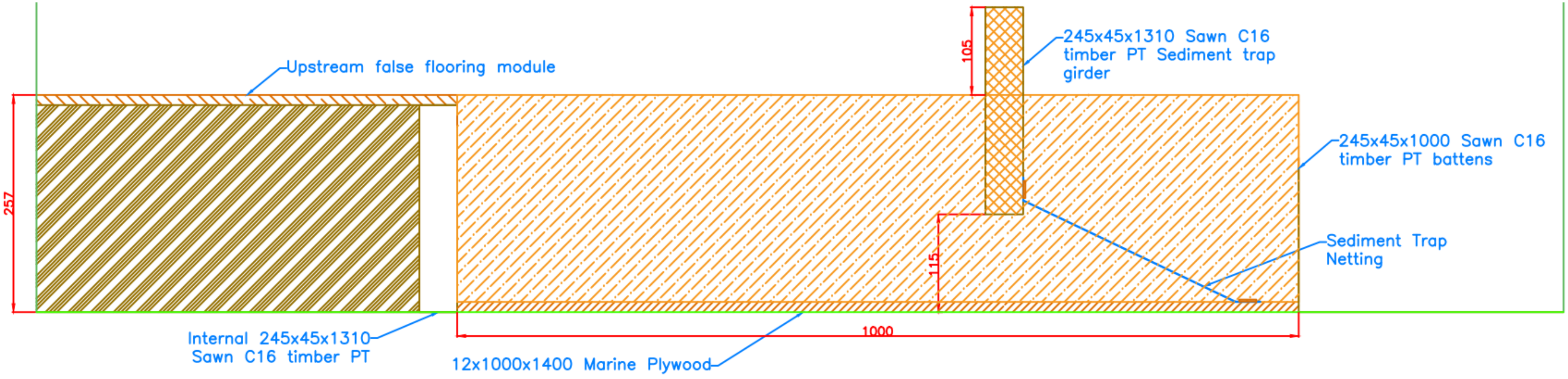

Figure A.2 Section through downstream sediment trap.

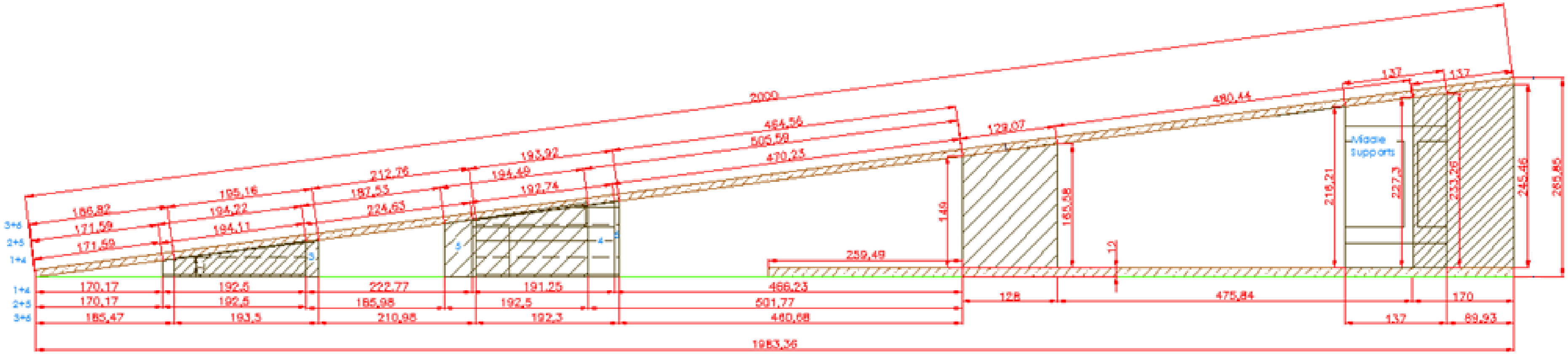

Figure A.3 Elevation of upstream approach ramp (Measurements relate to available off-cuts).

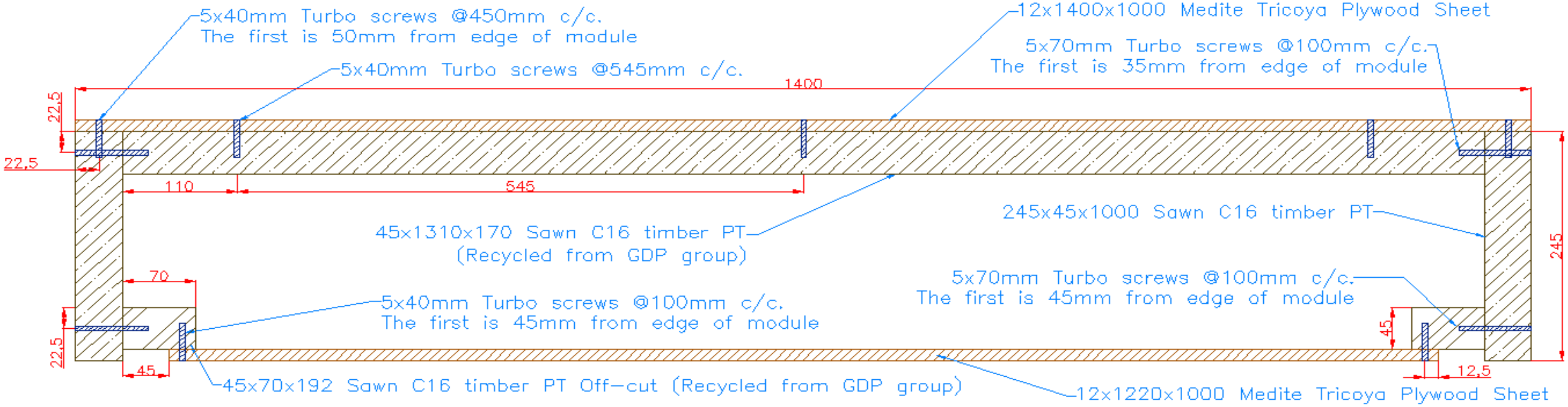

Figure A.4 Typical cross-section of false flooring module.

Figure A.5 *Downstream sediment trap.*

Appendix B Laboratory Data Processing Method

B.1 Introduction

The processing method used to convert the raw data from the sonar measuring technique (described in Chapter 3) into an interpolated raster surface of the scour hole for geometric analysis is presented here. The processing covers the following steps: (a) raw image data conversion and formatting, (b) filtering and smoothing of the sonar data, (c) surface interpolation and (d) analysis approach.

B.2 Raw Data Extraction

For a single sweep of the underlying surface, the sonar produces a raw image file (.img2 file format) representing the acoustic returns received by the sonar's transducer. Each image file is processed by converting the raw serial output of acoustic responses into a surface outline using the sonar's associated Pipe Profiler E software. The Pipe Profiler E software uses playback of the raw image files to remove weak acoustic noise signals and background noise through applying an acoustic intensity threshold before generating a bathymetry outline from the acoustic response. A blanking radius, which sets the starting range from which the two-dimensional line profile is captured, can also be applied to filter acoustic reflections that result from suspended sediment in the water column. The final outline for each line scan is an ASCII comma-delimited text file in two-dimensions.

B.2.1 Intensity Threshold

A threshold signal return intensity is programmed so that weaker acoustic returns (i.e. background noise) can be filtered to isolate the return signal of the bed. The threshold setting is defined as a minimum raw acoustic intensity beyond which the acoustic signals are considered for surface profile outline (Lepot *et al.*, 2014). The value of the threshold is set as a percentage of the maximum intensity received from the surface for that single swath.

The threshold was calibrated by considering a line scan taken of a well-developed scour hole profile for each of the three test piers. The optimal threshold setting was identified initially through visual assessment of the scour hole profiles, and additionally supplemented by comparisons of the surface outputs with physical measurements using the three point gauges (locations defined in Chapter 4). Initially, threshold values within the range 50 – 100% were trialled in increments of 5% (threshold intensity values below a 50% limit produced outlines influenced by significant background noise). Intervals of 1% either side of the calibrated value were then used to verify any sensitivity to minor variations in the proposed threshold. Figure B.1 shows a generated scour hole line profile using an 80, 90 and 100% acoustic threshold value. The outline blanking radius was set to 0.27m in all cases.

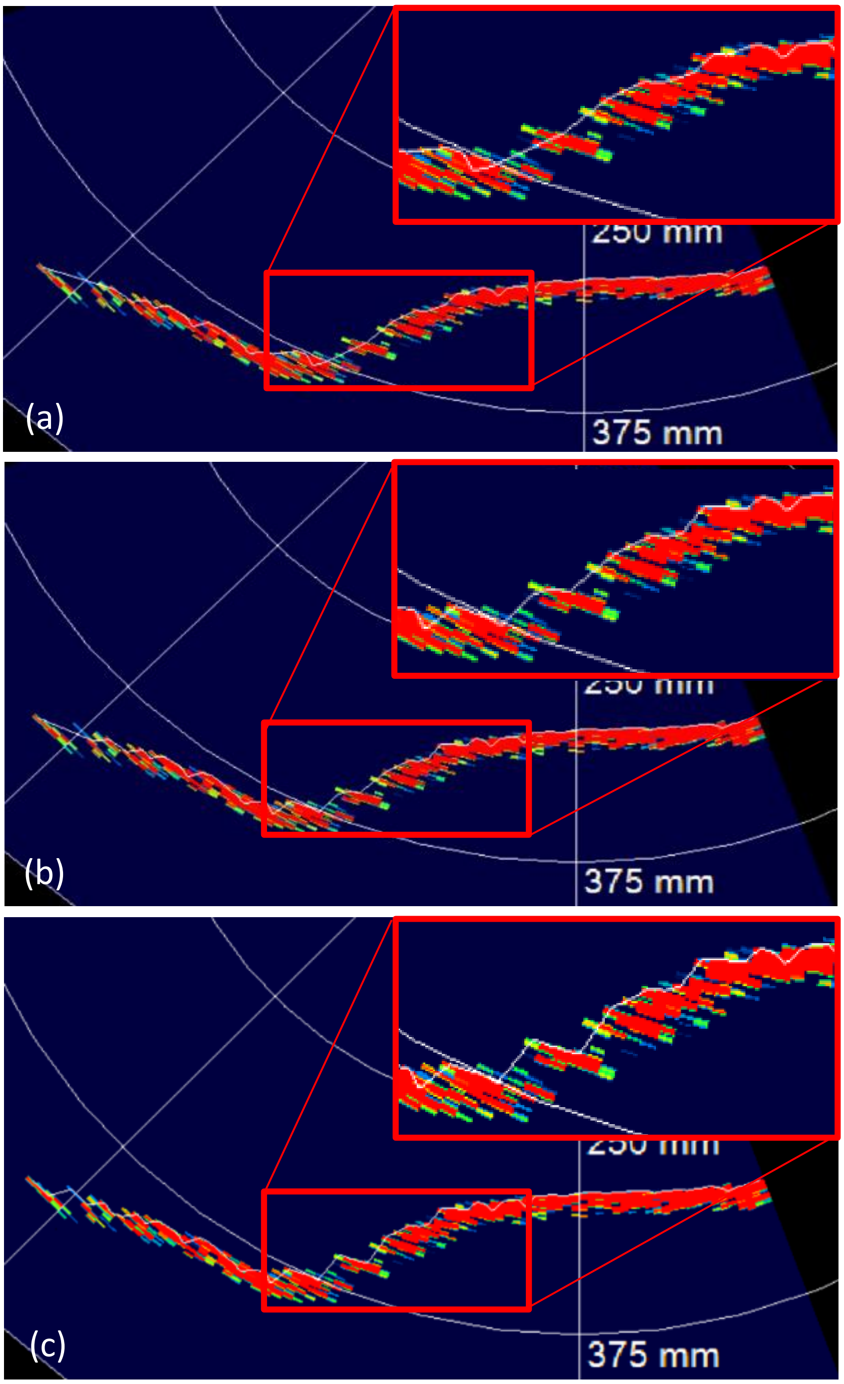

Figure B.1 Profile outline using an intensity threshold of (a) 100%, (b) 90%, and (c) 80% for a 51mm diameter test pier.

For all three piers, the surface outline of the underlying bed was best represented using a 90% acoustic intensity threshold (Figure B.1b). This is also the recommended value of the sonar's supplier. Applying a higher acoustic intensity (i.e. 100%, Figure B.1a) resulted in an overly smoothed bed outline, owing to the output being produced from considering only acoustic returns that are essentially equal to the maximum acoustic intensity return from that swath. Conversely, a lower threshold (80%, Figure B.1c) naturally generated outputs influenced by lower intensity acoustic responses, resulting in a rough scour hole topography and an undulating upstream approach bed that masks the true surface profile. This was verified using comparisons with point gauge readings at key locations. A representative value of 90% was therefore used for all trials.

B.2.2 Roll Offset

The sonar transducer functions by performing a rapid swath of the surface through a pre-defined angle in incremental steps, before returning to the initial position to repeat the process. Therefore, it is vital that the origin of the transducer's beam is accurately referenced to a perfectly horizontal plane so that scans of a flat surface are not reproduced on acoustic playback as a shallow incline.

Calibration of the sonar roll offset was conducted prior to experiment trials. The sonar was securely strapped to a horizontal lever arm to perform scans of a large flat-bottomed hydraulic-modelling tank through a vertical-facing 90° swath motion. The sonar was located 0.3m above the tank base to match the depth used in the experiments. The roll offset was adjusted until the converted outline produced an identical elevation across its surface. From this calibration exercise, a roll offset of -5.3° was identified. This was configured within the Pipe Profiler E software and later verified in the laboratory prior to experimentation. The effect of the adjustment factor on the received acoustic responses are shown in Figure B.2.

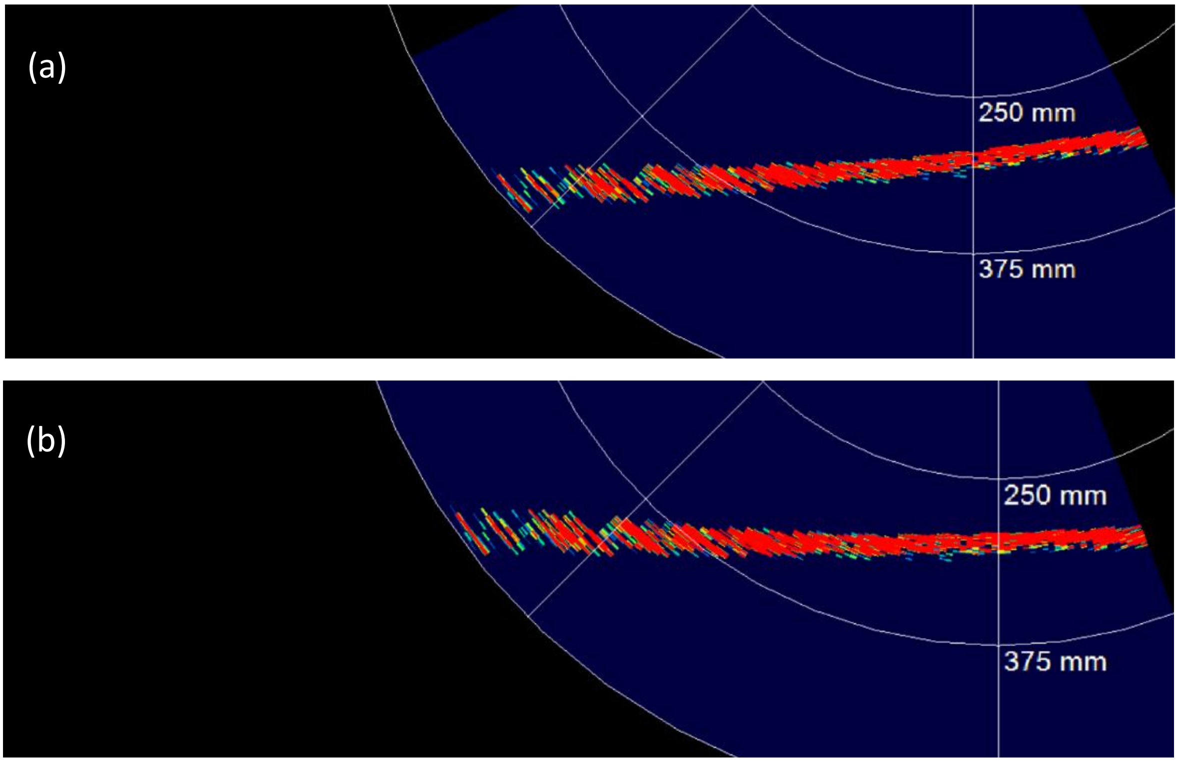

Figure B.2 Roll effects on sonar output of a flat-bed, illustrating (a) the original sloping output, and (b) the effect of applying a calibrated -5.3° roll offset.

B.2.3 Formatting XYZ Data

Each line scan outline represents a two-dimensional output characterising its relative cross-stream position (y-data) and associated surface elevation (z-data). A full scan of the scoured bed is made of multiple line scans that are scanned by continuous steady motion of the sonar. In order to concatenate these scans of the scoured surface into a single XYZ point cloud, the stream-wise distance between line scans was required. The stream-wise distance between adjacent line scans was computed by considering the total stream-wise scan length and the associated number of line scans recorded. By considering the automated movement of the continuous-scanning sonar, equidistant stream-wise spacing between individual line profiles could be assumed and was used for all trials. Automated scanning is validated in Section 4.4.3.

The stream-wise location of each line scan is quantified on a cumulative basis to represent the distance relative to the scan origin (Figure B.3).

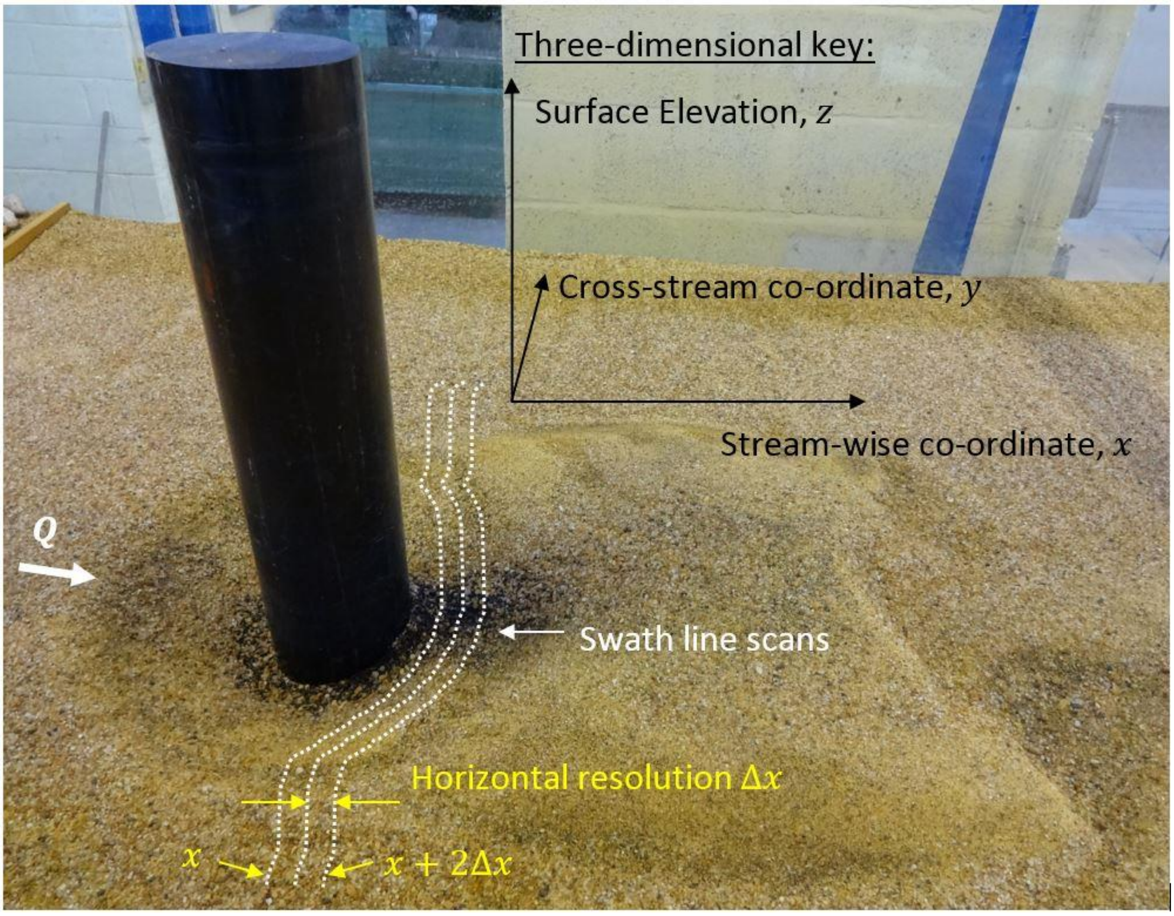

Figure B.3 Spatial co-ordinate system and calculation of stream-wise data co-ordinates.

B.3 Data Filtering

Filtering and smoothing of the raw acoustic data was applied using both two- and three-dimensional methods to further minimise the effects of acoustic noise on the data (see Figure B.4). First, a locally weighted polynomial regression function (an in-built MATLAB *loess* function) was used to smooth the data in two-dimensions across each line scan. The function considers each point on the surface line in turn. A local subset of neighbouring points, within a set radius from that point, are identified and assigned a regression weight (w_i) (ranging from 0 to 1) based on their abscissa distance from the point of interest using a tri-cube weight function (Cleveland and Devlin, 1988)

$$w_i = \left(1 - \left|\frac{x - x_i}{d(x)}\right|^3\right)^3,$$

where x and x_i are the abscissa values of the point of interest and the nearest neighbours, respectively, and $d(x)$ is the abscissa distance of the point of interest to the furthest away point within the defined span (Cleveland and Devlin, 1988). A local weighted quadratic least-squares polynomial is then fitted to each subset to calculate a smoothed elevation value at the point of interest. The loess output for each line scan is complete after all data points have been considered and a smoothed value obtained (Figure B.4)[37].

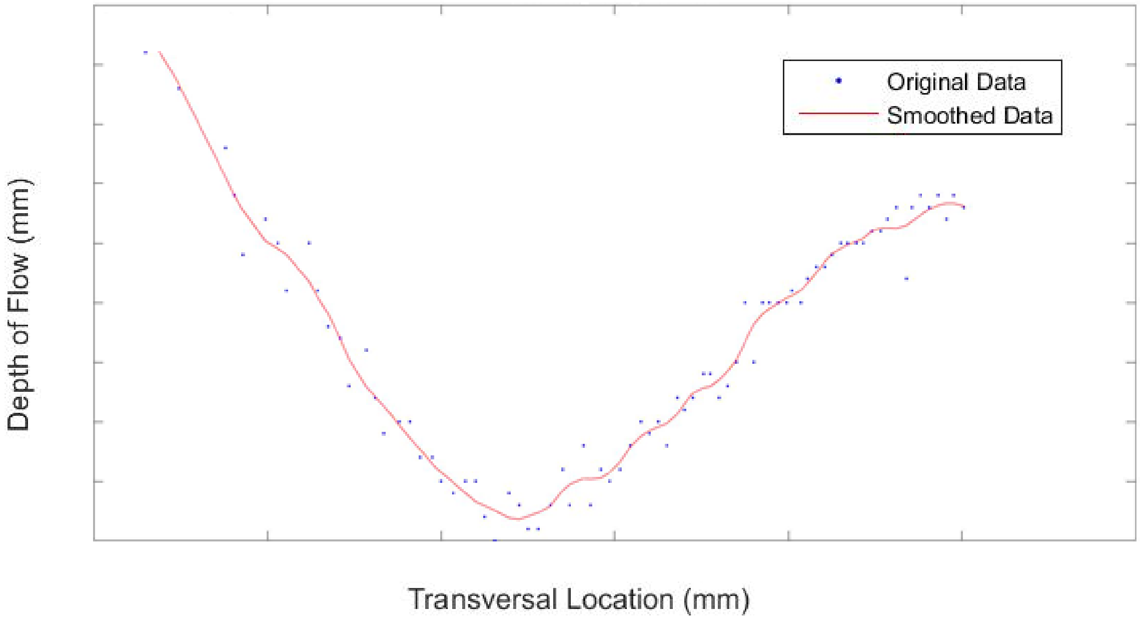

Figure B.4 Quadratic regression model used to smooth the raw sonar data.

The radius used to define the subset was determined through trial and error. The optimal value was identified when the fluctuation due to noise was minimised, whilst ensuring that the elevation discrepancies at key locations against the original data cloud surface and physical gauge measurements were negligible. The optimal value was set as 0.15 (15% of the total data within the two-dimensional profile). Values set below this value over-captured the fluctuation in data caused by acoustic noise within the smoothed output (Figure B.5a). Conversely, higher values were found to significantly oversimplify the geometric profile of the scour hole and misrepresent key characteristics of the scour surface (Figure B.5b).

---

[37] Several alternative regression functions were trialled; however, their applications were found to cause either a substantial impact on the natural profile of the scour hole, or inadequate smoothing of acoustic noise.

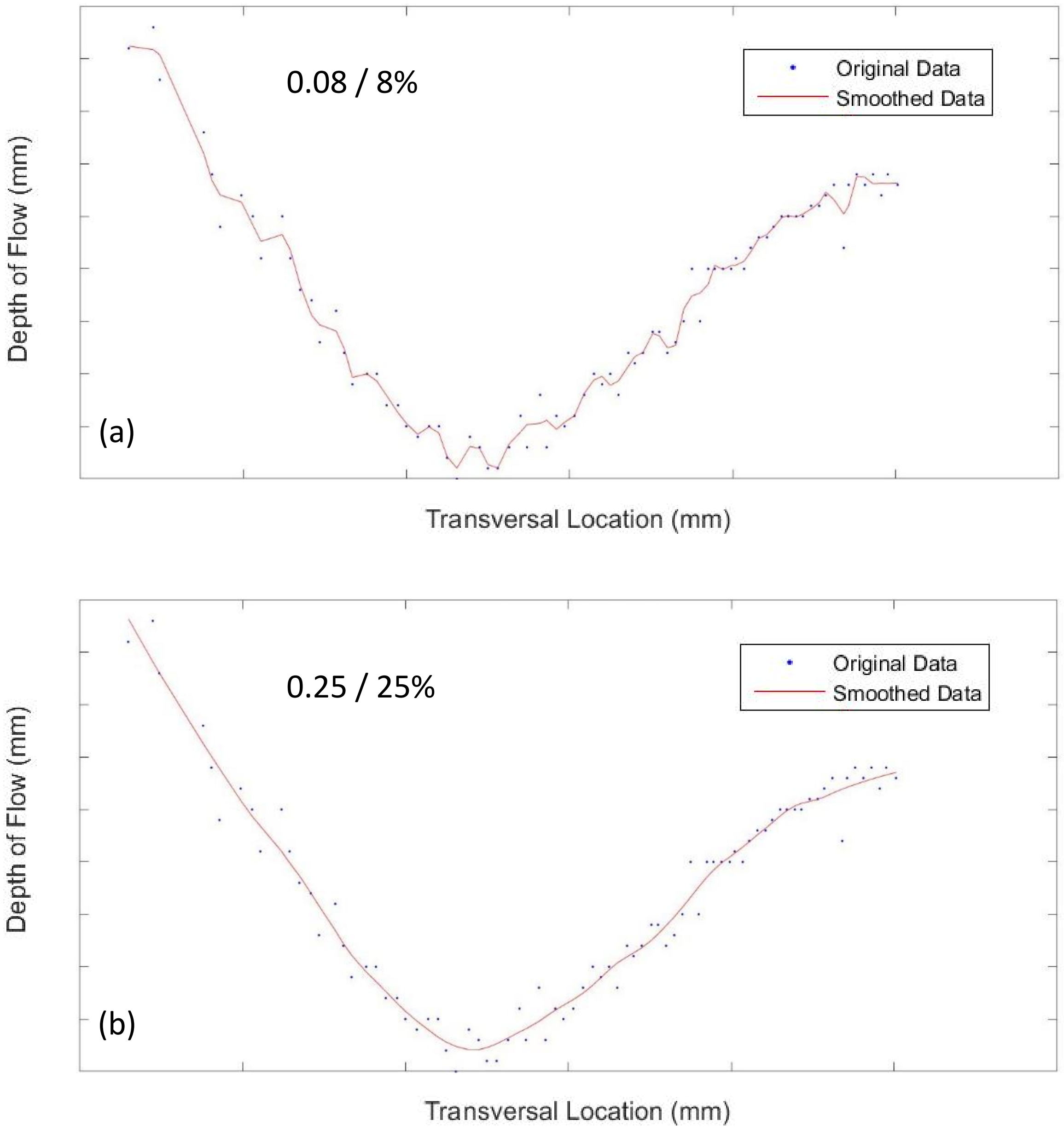

Figure B.5 Percentage of line scan points employed within the regression model subset to smooth each individual raw data point; (a) 8%, and (b) 25%.

Following two-dimensional smoothing, three-dimensional data filtering was performed using weighted Kernel convolution. This was used to address any outstanding outlier acoustic responses remaining within the dataset.

Kernel filtering works by considering a pre-determined radius of points surrounding the point of interest. A triangular-weighted system is then applied to the elevation of all points within that radius and assigns weights based on x-y radial distances when viewed in plan. A normalised weighted-average value for the point of interest is then able to be computed (Weinhaus, 1978). i.e. for points within a Kernel radius, r

$$w_i = \left| \sqrt{(x_P - x_i)^2 + (y_P - y_i)^2} - (r + 1) \right|,$$

and

$$z_{w,av} = \sum_{0}^{r} w_i z_i \Big/ \sum w_i .$$

Here, w_i is the elevation weight of point i within the radius r; x_P and x_i are the abscissas for the point of interest and point i; y_P and y_i are the ordinates for the point of interest and point i; z_P, z_i, and $z_{w,av}$ are the elevations of the point of interest, point i, and the large-Kernel weighted-average, respectively. If the original elevation at the point of interest was found to be outside a specified distance from the weighted average elevation (referred to as the *bound limit* from hereon in), it was considered an outlier. The outlier was then subject to an additional smaller Kernel convolution to calculate a new weighted average that replaced the original elevation at the point of interest. i.e. If $\left|z_{w,av} - z_P\right| > L_l$, where L_l is the bound limit, then a reduced-Kernel radius, r_r is applied to calculate a new weighted average at the point of interest, z_{nP}

$$w_i = \left|\sqrt{(x_P - x_i)^2 + (y_P - y_i)^2} - (r_r + 1)\right|,$$

and

$$z_{nP} = \sum_{0}^{r_r} w_i z_i \Big/ \sum w_i ,$$

where z_{nP} is the small-Kernel weighted-average elevation that replaces the original elevation at the point of interest. The values of r, r_r and L_l were determined using extensive trial and error analysis for all three values simultaneously. Throughout, the outputted bed elevations were compared at key points to those measured using point gauges. The criteria for selecting optimum filtering parameters was not only to provide adequate filtering of data outliers, but also to avoid changes to the elevation and profile of the scour hole surface. The optimal performance of the first and second Kernels was found with $r = 7$mm and $r_r = 3$mm, respectively. The apparent small stature of these Kernels reflects the effect of larger Kernel sizes on attenuating both the scour hole depth and profile extents. The bound limit (L_l) was calibrated by varying its value in multiples of the coarse sediment diameter (i.e. 2.62mm). Accordingly, a value of $L_l = 10.48$mm was found to provide the best filtering limit for all tests, inclusive of changes in sediment diameter.

B.4 Point Cloud Surface Generation

Filtered XYZ point clouds of the scoured surface were converted into raster surfaces using Geographic Information Systems (GIS) software. Three-dimensional raster surfacing involves estimating intermediary values at unsampled locations using a continuous interpolation model based on known values. The interpolation model can either be deterministic (considering natural neighbours to determine the smoothness of the projected surface) or geostatistical (stochastic models considering the spatial variation of the point cloud by calculating the spatial autocorrelation between points in distance and direction). The latter methodology, *kriging*, is typically applied to regularly-scattered bathymetric or geological point cloud data as these data forms can be expected to have spatial correlation or directional bias. Kriging interpolation was deemed suitable for application as directional bias reflects the profile of a scour hole.

Kriging interpolation estimates the bed elevation at unsampled locations using a continuous model of stochastic spatial variation (Webster and Oliver, 2007). Spatial variation of the bed is taken into account through a semi-variogram model, which measures the strength of statistical correlation between data points around the intermediary point of interest. The statistical correlation is realised by fitting the semi-variogram with a spherical mathematical function that compares the intersection between pairs of spheres (in three-dimensions) separated by a lag vector. The length of this vector is increased incrementally to identify the overall spatial variance within a finite range. The computed semivariogram model, fitted with a spherical mathematical function, describes the spatial continuity of the data and is applied to estimate the spatial co-ordinates and elevation of an intermediary point of interest using unbiased weights of the neighbouring data.

B.4.1 Application of Kriging Interpolation: Assumptions

Ordinary Kriging Method

The ordinary kriging method used here for interpolation is a linear estimation method based on the ability to detail the spatial structure of the data point cloud using a variogram. The availability of a detailed data cloud is vital for modelling the spatial correlation of a data series reliably. Here, the output of each time series dataset is characterised by a dense and regularly-spaced network of elevation points. Lag vectors between the XYZ spatial data points are regular in both direction and distance and provide a comprehensive account of the spatial variance over the surface.

The lag vectors used to derive the variogram cover only local distances as the ordinary kriging method can accommodate for possible variation in the mean. This characteristic is highly desirable for scour hole surface interpolation as the scoured profile, and therefore the mean, is highly variable. Thus in this instance modelling using a variogram approach, and hence application of ordinary kriging as the preferred kriging method, is well suited.

Stationarity

Applying a variogram to describe spatial variability assumes stationarity in the data. Stationarity assumes that the spatial distribution of the dataset has certain attributes that are the same everywhere up to a stabilisation value (a *sill*), beyond which the spatial variation is said to be practically uncorrelated (Kitanidis, 1997). The spatial variability derived from the variogram is then assumed to be representative of the entire scoured surface.

Strictly speaking, the ordinary kriging method is confined to a small radius and as such the computed variogram around the intermediary point of interest is highly localised. This means that local stationarity (quasi-stationarity) can be more accurately assumed (Kitanidis, 1997; Webster and Oliver, 2007). Quasi-stationarity infers that the spatial variation over large spatial distances is of little consequence, allowing kriging to consider the values at different locations when forming the semivariogram as though they are different realisations of the same bed surface. This is of particular importance to the scoured surfaces, as the bed is characterised by an upstream flat-bed superseded by an irregular rapid variation in bed elevation around the test cylinder. By placing a restriction on the finite boundary from which the variogram is computed, quasi-stationarity can reasonably be assumed without violating the interpolation method.

Spherical Model

So that an unbiased weighted value for the intermediary point can be determined, the estimated variogram was modelled using a spherical mathematical function. The intrinsic spherical model is the most frequently used in geostatistics and is well known to fit three-dimensional spatial variability very well (Webster and Oliver, 2007). The spherical model function curves more gradually than bounded-linear or circular model equivalents (one and two dimensional, respectively) as the function can represent sources of variation at other scales. In contrast, a three-dimensional negative exponential model is typically better suited to describing the spatial variation of data that have random extents within the data field (Kitanidis, 1997). Random extents are not applicable to a naturally scoured surface. Moreover, the exponential model function approaches its sill asymptotically, meaning that stationarity of the whole surface must apply. This is an assumption that does not hold due to the significant spatial variation of the scoured bed surface around the test cylinder relative to upstream.

Lag Size Increment

The semivariance is computed by considering paired sets of outputs separated by a given lag size and identifying their spatial variance. The lag size is increased in set increments to derive an estimate for the data semivariance for each bin used to compute the final semivariogram model.

The lag size increment influences the amount of spatial autocorrelation that is incorporated into the semivariogram. While the average lag distance between neighbouring points (i.e. ~1.8mm) is recommended (Kitanidis, 1997; Webster and Oliver, 2007), the increment was reduced by an order of magnitude as the resultant interpolation generated a substantially smoothed surface that failed to account for key details in the spatial variation of the bed surface.

Each calculated semivariance for a given lag is only an estimate of the mean semivariance for that lag and therefore subject to error arising from sampling fluctuation. However, the assumption of quasi-stationarity means that the variogram is only of interest very locally, and is suited to smaller lag distances and increments where the variogram is best estimated (Webster and Oliver, 2007). A lag size increment of 0.1mm was found to best represent the data that minimised mean square estimation errors. This increment is large enough that the semivariogram did not produce erratic outputs caused by empty bins or small sample bins that produced unrepresentative averages, whilst optimising computational time. The lag size was coupled with a search radius of 12 points from which the spherical function (fitted to the variogram) that produces a variable range and is used to compute the weighted average elevation at the intermediary point of interest. The nearest measured points are those that carry the most weight and therefore the assumed radius of points considered is reasonable.

B.4.2 Acoustic Shadowing

Point cloud data overlapped with kriging interpolation using assumptions stated in Section B.4.1 is shown in Figure B.6. The unnatural raised areas within the scour hole is the resultant of acoustic shadowing caused by the test cylinder which minimises data sampling from the sonar in that region.

The minimal data in this area essentially produces significant sample fluctuation in the computed mean semivariance over a given lag. Spatial variation is critical for estimating the semivariogram, but with minimal data the mean square estimation errors are significant (Figure B.7). For a majority of the surface where the sonar is unimpeded by acoustic shadowing, the dense sample produces a consistent spatial variance that is well modelled by the spherical function fitted to the variogram. To minimise such estimation errors impacting calculations of the scour hole volume, only half the scour hole visible to the sonar was used for analysis. This is very appropriate as it is well known that the scour hole is symmetrical with respect to the x-z plane through the pier's centre (see Figure B.3).

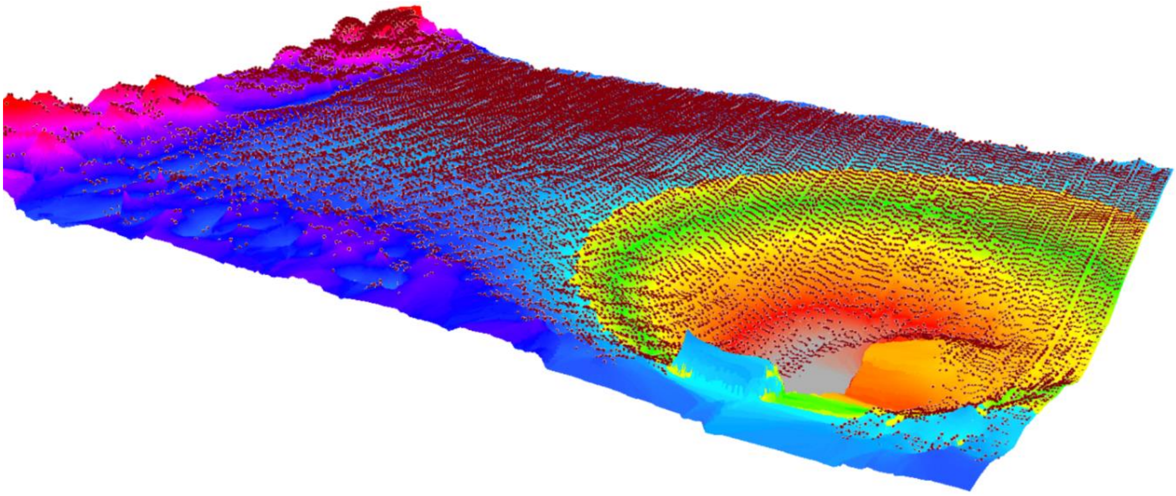

Figure B.6 Kriging interpolation performed on a sample point cloud. The scoured bed surface embodies a smooth three-dimensional profile.

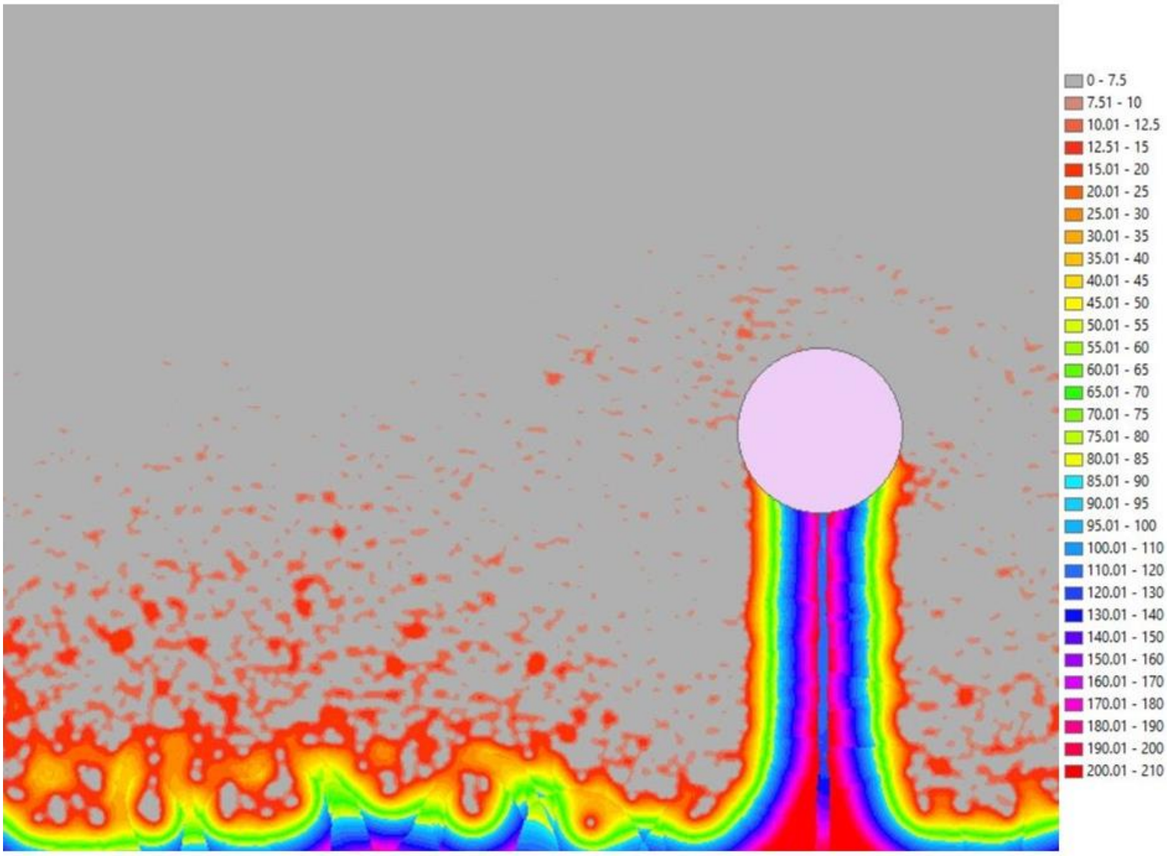

Figure B.7 Estimated semi-variance values for all intermediary locations. Unnaturally high values of semivariance are estimated for the region covered from the sonar by the test cylinder due to minimal sampled values amplifying the mean estimation errors present within the semivariogram.

B.4.3 Incorporation of Test Pier

The stream-wise and cross-stream location of the test pier, for incorporation into the interpolated surface, was measured before each experiment. Stream-wise distances were measured relative to the sonar transducer, taking into account the offset of the transducer disc (Figure B.8). The test pier was integrated into each surface after interpolation (Figure B.9).

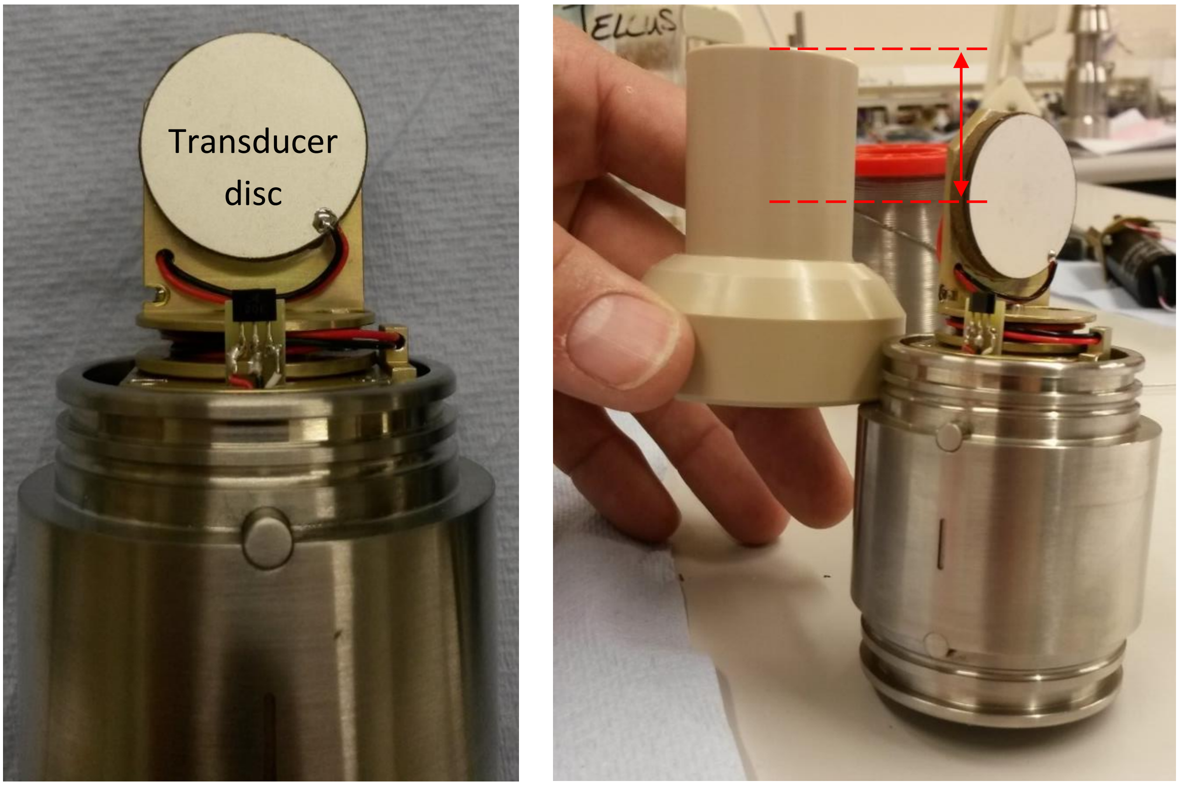

Figure B.8 Internal structure of the mini pipe profiler 2512 sonar.

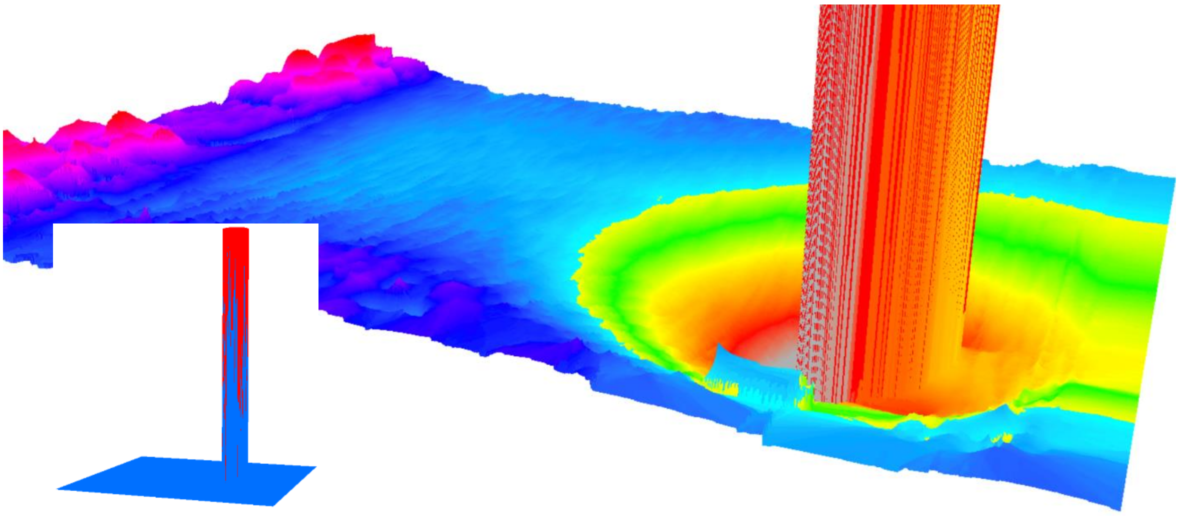

Figure B.9 Example Kriging surface with test pier.

B.5 Computing the Scour Hole Geometry

The spatial coverage of the interpolated surface was reduced in size to just the vicinity of the scour hole. For each pier diameter, the clipping extent was calculated by finding the intersection between the scour hole boundary of the end-of-trial scoured profile and the initial undisturbed flat-bed surface. The same clipping extent was then applied to measurements in that trial, independent of the stage of development. Application of the "clipping radius" used to reduce the bed surface to leave only the scour hole profile is shown in Figure B.10.

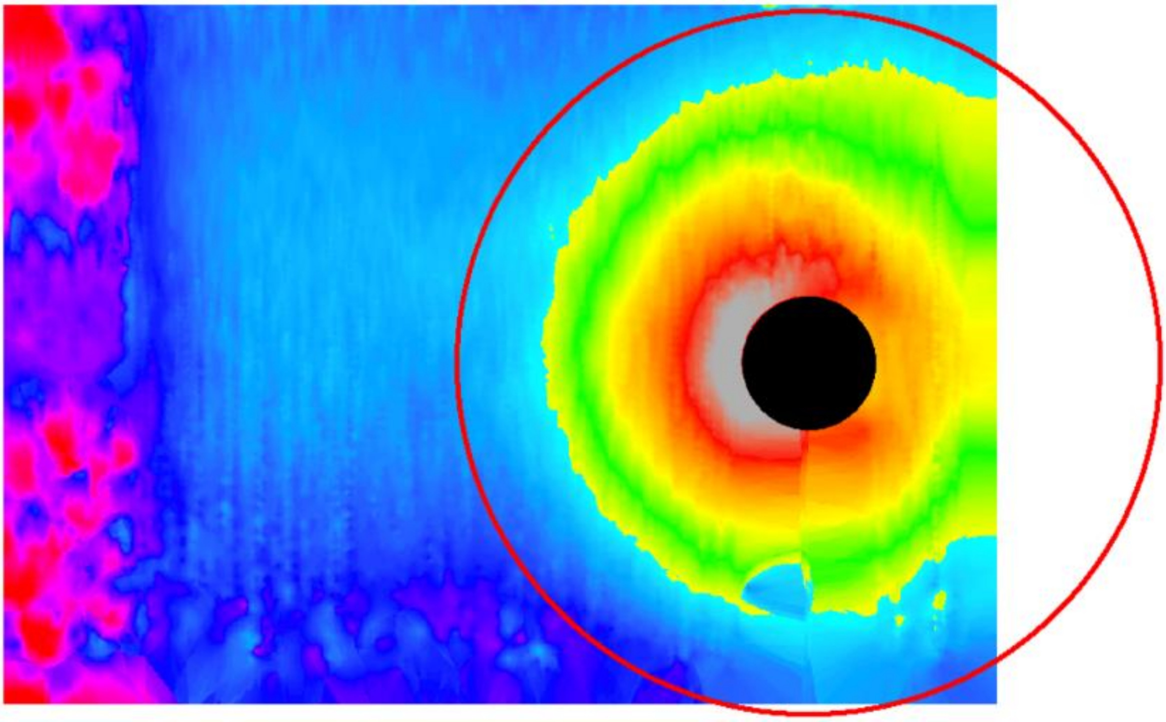

Figure B.10 Visual of scour hole clipping extent for 101mm test pier.

The experiments allowed for the measurements of the temporal development of the entire scour hole. Here, an important simplifying hypothesis is made about the topology of the horseshoe (HS) vortex forming at the base of the pier and its relation with the scour hole volume and shape. Manes and Brocchini (2015) argued that the characteristic size of the HS vortex (i.e. L) scales with the maximum scour depth (i.e. y_s) and that the volume of the HS vortex would scale as $\sim L^3$ and hence as $\sim {y_s}^3$. It is herein argued that, since after only a short period of erosion the HS vortex is well known to be fully buried within scour hole (Dargahi, 1990; Unger and Hager, 2007; Dixen *et al.*, 2012), the scour hole volume can be used as a proxy to quantify the volume of the HS vortex itself. Within this context, it should be noted that only a portion of the entire scour hole volume containing the HS vortex was taken into consideration. This region is assumed to coincide with the hole generated upstream of the piers' diameter perpendicular to the flow direction. Downstream of this position the HS vortex loses its coherence and is essentially replaced by wake vortices.

However for completeness, three different sector sizes (Figure B.11) were used to calculate the scour hole volumes and allow an examination of the output sensitivity to region selection. This is briefly covered in Section 5.2.

Real-time characteristics (i.e. y_s, L, W, A_f, V_{OL}) of the developing scour hole (for each sector defined in Figure B.11) were computed for each trial using the difference between bed elevations at time interval t and the corresponding flat-bed condition at time $t = 0$.

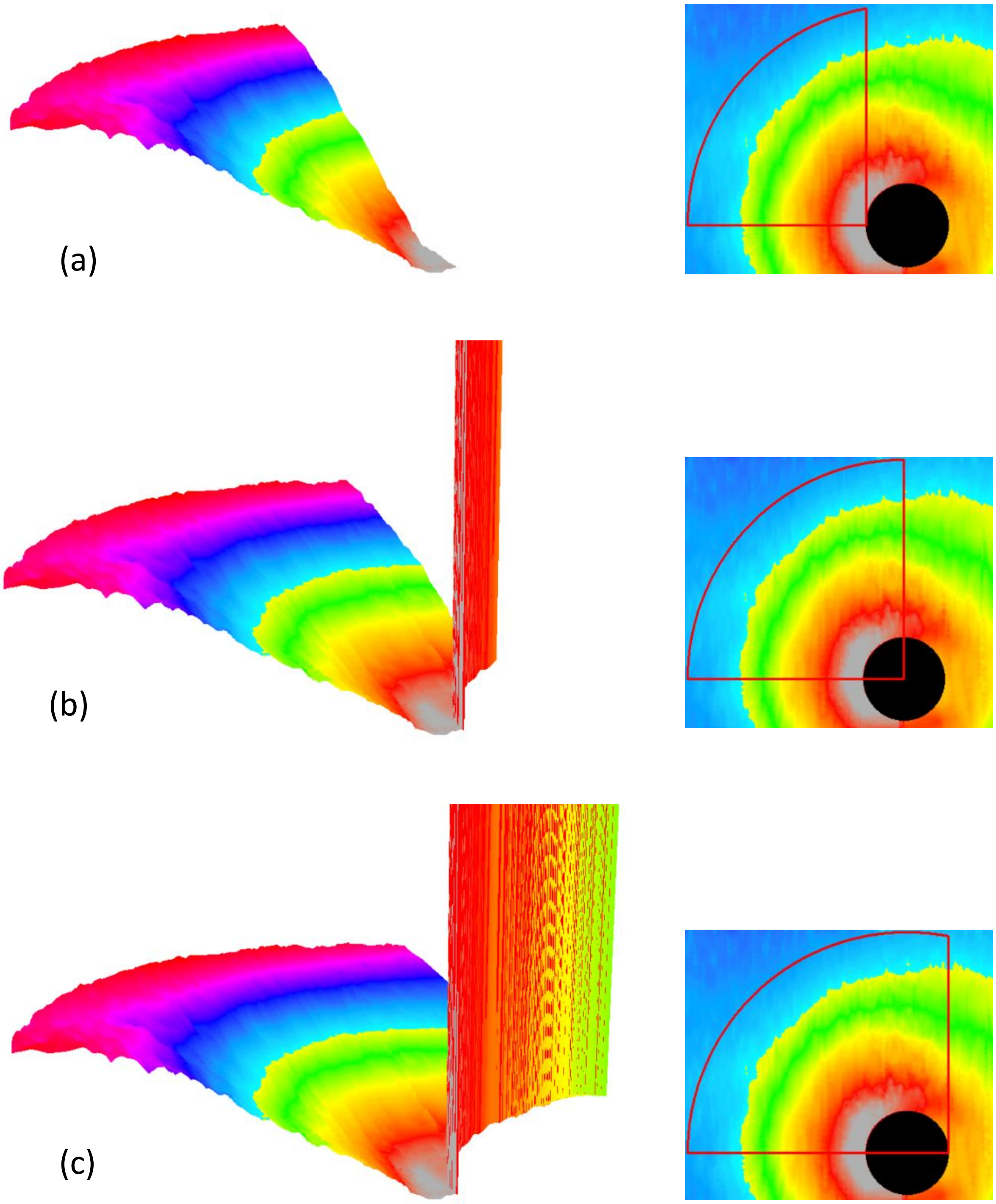

Figure B.11 Sectors of the scour hole used to calculate volume. (a) In front of the test pier only. (b) Inclusive of half of the test pier, and (c) the entire test pier.

Bibliography

Alemi, M. and Maia, R.J. (2018) Numerical simulation of the flow and local scour process around single and complex bridge piers. *International Journal of Civil Engineering,* 16, 475-487.

Arneson, L.A., Zevenbergen, L.W., Lagasse, P.F. and Clopper, P.E. (2012) *Evaluating scour at bridges - Fifth edition*. Springfield, Publication No. FHWA-HIF-12-003.

Atherton, M.W. (2011) *Echoes and images: The encyclopedia of side-scan and scanning sonar operations*. Seattle, United States of America: OysterInk Publications.

Baker, C.J. (1980a) Theoretical approach to prediction of local scour around bridge piers. *Journal of Hydraulic Research,* 18 (1), 1-12.

Baker, C.J. (1980b) The turbulent horseshoe vortex. *Journal of Wind Engineering and Industrial Aerodynamics,* 6, 9-23.

Barenblatt, G.I. (1996) *Scaling, self-similarity, and intermediate asymptotics*. Cambridge, UK: Cambridge University Press.

Benn, J. (2013) Railway bridge failure during flooding in the UK and Ireland. *Proceedings of the Institution of Civil Engineers,* 166 (FE4), 163-170.

Benn, J., Mantz, P., Mountain, A., Green, T., Bryant, R., Gubbin, A. and Reed, D. (2004) *Impact of scour and flood risk on railway structures: Final Report (Report No. T112)*. London: Rail Safety and Standards Board (RSSB).

Bland, J.M. and Altman, D.G. (1999) Measuring agreement in method comparison studies. *Statistical Methods in Medical Research,* 8 (2), 135-160.

Bombardelli, F.A. and Gioia, G. (2006) Scouring of granular beds by jet-driven axisymmetric turbulent cauldrons. *Physics of Fluids,* 18 (8).

Bomminayuni, S. and Stoesser, T. (2011) Turbulence tatistics in an open-channel flow over a rough bed. *Journal of Hydraulic Engineering,* 137 (11), 1347-1358.

Bonetti, S., Manoli, G., Manes, C., Porporato, A. and Katul, G.G. (2017) Manning's formula and Strickler's scaling explained by a co-spectral budget model. *Journal of Fluid Mechanics,* 812, 1189-1212.

Brownlie, W.R. (1981) *Prediction of flow depth and sediment discharge in open channels*, PhD Thesis.

Buffington, J.M. and Montgomery, D.R. (1997) A systematic analysis of eight decades of incipient motion studies, with special reference to gravel-bedded rivers. *Water Resources Research,* 33 (8), 1993-2029.

Chabert, J. and Engeldinger, P. (1956) *Etude des affonillements author des piles des ponts*. Chatou, France (In French).

Chambers, J.M., Cleveland, W.S., Kleiner, B. and Tukey, P.A. (1983) Comparing data distributions *Graphical methods for data analysis*. California, United States: Wadsworth International Group.

Chang, W.Y., Constantinescu, G., Lien, H.C., Tsai, W.F., Lai, J.S. and Loh, C.H. (2013) Flow structure around bridge piers of varying geometrical complexity. *Journal of Hydraulic Engineering,* 139 (8), 812-826.

Chiew, Y.M. (1984) *Local scour at bridge piers*, PhD Thesis, Auckland University.

Chow, V.T. (1959) *Open-channel hydraulics*. McGraw-Hill Book Company.

Cleveland, W.S. and Devlin, S.J. (1988) Locally weighted regression: An approach to regression analysis by local fitting. *Journal of the American Statistical Association,* 83 (403), 596-610.

Dargahi, B. (1990) Controlling mechanism of local scouring. *Journal of Hydraulic Engineering,* 116 (10), 1197-1214.

Das, S., Das, R. and Mazumdar, A. (2013a) Circulation characteristics of horseshoe vortex in scour region around circular piers. *Water Science and Engineering,* 6 (1), 59-77.

Das, S., Das, R. and Mazumdar, A. (2013b) Comparison of characteristics of horseshoe vortex at circular and square piers. *Research Journal of Applied Sciences, Engineering and Technology,* 5 (17), 4373-4387.

Das, S., Das, R. and Mazumdar, A. (2014a) Variations in clear water scour geometry at piers of different effective widths. *Turkish Journal of Engineering and Environmental Sciences,* 38 (1), 97-111.

Das, S., Das, R. and Mazumdar, A. (2014b) Vorticity and circulation of horseshoe vortex in equilibrium scour holes at different piers. *Journal of The Institution of Engineers (India): Series A,* 95 (2), 109-115.

Das, S., Ghosh, R., Das, R. and Mazumdar, A. (2014c) Clear water scour geometry around circular piers. *Ecology, Environment and Conservation,* 20 (2), 479-492.

Das, S., Midya, R., Chatterjee, B., Ghosh, R., Das, R. and Mazumdar, A. (2014d) Bed shear stresses past a flat plate under clear water equilibrum scour state. *Journal of the Association of Engineers, India,* 84 (1&2), 27-36.

Deng, L. and Cai, C.S. (2010) Bridge scour prediction, modelling, monitoring and countermeasures - Review. *Practical Periodic of Structural Design and Construction,* 15 (2), 125-134.

Deng, L., Wang, W. and Yu, Y. (2015) State-of-the-art review on the causes and mechanisms of bridge collapse. *Journal of Performance of Constructed Facilities,* 30 (2).

Dey, S. (1996) Sediment pick-up for evolving scour near circular cylinders. *Applied Mathematical Modelling,* 20 (7), 534-539.

Dey, S. and Ali, S.Z. (2017) Mechanics of sediment transport: Particle scale of entrainment to continuum scale of bedload flux. *Journal of Engineering Mechanics,* 143 (11).

Dey, S. and Bose, S.K. (1994) Bed shear in equilibrium scour around a circular cylinder embedded in a loose bed. *Applied Mathematical Modelling,* 18 (5), 265-273.

Dey, S. and Raikar, R.V. (2007) Characteristics of horseshoe vortex in developing scour holes at piers. *Journal of Hydraulic Engineering,* 133 (4), 399-413.

Diab, R., Link, O. and Zanke, U. (2010) Geometry of developing and equilibrium scour holes at bridge piers in gravel. *Canadian Journal of Civil Engineering,* 37 (4), 544-552.

Dixen, M., Lohmann, I.P. and Christensen, E.D. (2012) Method to predict long time span of scour around offshore wind turbine structures. *Coastal Engineering Proceedings,* 1 (33), 88.

Eddowes, M.J., Waller, D., Taylor, P., Briggs, B., Meade, T. and Ferguson, I. (2003) *Railway safety implications of weather, climate and climate change: Final Report (Report No. T096)*. London: Rail Safety and Standards Board (RSSB).

Ettema, R. (1980) *Scour at bridge piers*, PhD Thesis, Auckland University.

Ettema, R., Constantinescu, G. and Melville, B.W. (2011) *Evaluation of bridge scour research: Pier scour processes and predictions. NCHRP Research Results Digest 378.* Washington D.C.: National Cooperative Highway Research Program, Transportation Research Board

Ettema, R., Kirkil, G. and Muste, M. (2006) Similitude of large-scale turbulence in experiments on local scour at cylinders. *Journal of Hydraulic Engineering,* 132 (1), 33-40.

Ettema, R., Melville, B.W. and Barkdoll, B. (1998) Scale effects on pier-scour experiments. *Journal of Hydraulic Engineering,* 124 (6), 639-642.

Gioia, G. and Bombardelli, F.A. (2002) Scaling and Similarity in Rough Channel Flows. *Physical Review Letters,* 88 (1).

Gioia, G. and Bombardelli, F.A. (2005) Localized turbulent flows on scouring granular beds. *Physical Review Letters,* 95 (1), 014501-014501:014504.

Gioia, G. and Chakraborty, P. (2006) Turbulent friction in rough pipes and the energy spectrum of the phenomenological theory. *Physical Review Letters,* 96 (4).

Gobert, C., Link, O., Manhart, M. and Zanke, U. (2010) Discussion of "Coherent Structures in the Flow Field around a Circular Cylinder with Scour Hole" by G. Kirkil, S. G. Constanintinescu, and R. Ettema. *Journal of Hydraulic Engineering,* 136 (1), 82-84.

Graf, W.H. and Altinakar, M.S. (1998) *Fluvial hydraulics*. Chichester, England: J. Wiley and Sons Ltd.

Gravanis, E. and Akylas, E. (2015) Generalized Batchelor functions of isotropic turbulence. *Physics of Fluids,* 27 (1).

Guan, D., Chiew, Y.M., Wei, M. and Hsieh, S.C. (2019) Characterization of horseshoe vortex in a developing scour hole at a cylindrical bridge pier. *International Journal of Sediment Research,* 34, 118-124.

Hager, W.H. (2007) Scour in hydraulic engineering. *Proceedings of the Institution of Civil Engineers - Water Management,* 160 (3), 159-168.

Harris, J., Whitehouse, R.J. and Benson, T. (2010) The time evolution of scour around offshore structures: The scour time evolution predictor (STEP) model. *Proceedings of the Institution of Civil Engineers - Maritime Engineering,* 163 (1), 3-17.

Jenkins, G., Perry, M. and Prior, J. (2009) *UKCIP The climate of the United Kingdom and recent trends*. Oxford, United Kingdom.

Khwairakpam, P., Ray, S.S., Das, S., Das, R. and Mazumdar, A. (2012) Scour hole characteristics around a vertical pier under clearwater scour conditions. *ARPN Journal of Engineering and Applied Sciences,* 7 (6), 649-654.

Kirby, A.M., Roca, M., Kitchen, A., Escarameia, M. and Chesterton, O.J. (2015) *Manual on scour at bridges and other structures*. London, United Kingdom.

Kirkil, G. and Constantinescu, G. (2012) A numerical study of the laminar necklace vortex system and its effect on the wake for a circular cylinder. *Physics of Fluids,* 24 (7).

Kirkil, G., Constantinescu, G. and Ettema, R. (2008) Coherent structures in the flow field around a circular cylinder with scour hole. *Journal of Hydraulic Engineering,* 134 (5), 572-587.

Kirkil, G., Constantinescu, G. and Ettema, R. (2009) Detached eddy simulation investigation of turbulence at a circular pier with scour hole. *Journal of Hydraulic Engineering,* 135 (11), 888-901.

Kironoto, B.A. and Graf, W.H. (1994) Turbulence characteristics in rough uniform open-channel flow. *Proceedings of the Institution of Civil Engineers Water - Maritime and Energy,* 106, 333-344.

Kitanidis, P.K. (1997) *Introduction to geostatistics: Applications of hydrogeology*, 1st ed. The Edinburgh Building, Shaftesbury Road, Cambridge: Cambridge University Press.

Kolmogorov, A.N. (1941) The local structure of turbulence in incompressible viscous fluid for very large Reynolds numbers. *Cr Acad. Sci. URSS,* 30 (4), 301-305.

Kothyari, U.C., Hager, W.H. and Oliveto, G. (2007) Generalized approach for clear-water scour at bridge foundation elements. *Journal of Hydraulic Engineering,* 133 (11), 1229-1240.

Kuhnle, R.A., Alonso, C.V. and Shields Jr, F.D. (1999) Geometry of scour holes associated with 90° spur dikes. *Journal of Hydraulic Engineering,* 125 (9), 972-978.

Lagasse, P.F., Ghosn, M., Johnson, P.A., Zevenbergen, L.W. and Clopper, P.E. (2013) *Risk-based approach for bridge scour prediction. NCHRP Project 24-34*. National Cooperative Highway Research Program, Transportation Research Board.

Washington D.C., United States of America.

Lança, R.M., Fael, C.S., Maia, R.J., Pego, J.P. and Cardoso, A.H. (2013) Clear-water scour at comparatively large cylindrical piers. *Journal of Hydraulic Engineering,* 139 (11), 1117-1125.

Lança, R.M., Simarro, G., Fael, C. and Cardoso, A.H. (2016) Effect of viscosity on the equilibrium scour depth at single cylindrical piers. *Journal of Hydraulic Engineering,* 142 (3).

Landau, L.D. and Lifshitz, E.M. (1959) *Fluid mechanics: Course of theoretical physics*. Institute of Physical Problems, USSR Academy of Sciences, Moscow: Pergamon Press.

Laursen, E.M. and Toch, A. (1956) *Scour around bridge piers and abutments: Final Report (Bulletin No. 4, PB-C-8314)*. Iowa Institute of Hydraulic Research, Iowa, United States.

Lee, S. and Sturm, T.W. (2009) Effect of sediment size scaling on physical modelling of bridge pier scour. *Journal of Hydraulic Engineering,* 135 (10), 793-802.

Lee, S., Sturm, T.W., Gotvald, A. and Landers, M. (2004) Comparison of laboratory and field measurements of bridge pier scour *Proceedings of the 2nd International Conference on Scour and Erosion 2004*, Singapore. 231-239.

Lepot, M., Pouzol, T., Aldea Borruel, X. and Bertrand-Krajewski, J.-L. (2014) Monitoring sediments in sewer with sonar technology: From laboratory experiments to in situ tests. Paper presented at 13th International Conference on Urban Drainage, Sarawak, Malaysia.

Link, O. (2008) Measurement on spatio-temporal development of scour around a cylinder in coarse sand. *Ingeniería Hidráulica en Mexico,* 23 (2), 59-74.

Link, O., Castillo, C., Pizarro, A., Rojas, A., Ettmer, B., Escauriaza, C. and Manfreda, S. (2017) A model for bridge pier scour during flood waves. *Journal of Hydraulic Research,* 55 (3), 310-323.

Link, O., Gobert, C., Manhardt, M. and Zanke, U. (2008a) Characteristics of developing scour-holes at a sand-embedded cylinder. *International Journal of Sediment Research,* 23 (3), 258-266.

Link, O., Pfleger, F. and Zanke, U. (2008b) Characteristics of developing scour-holes at a sand-embedded cylinder. *International Journal of Sediment Research,* 23, 258-266.

Link, O. and Zanke, U. (2004) On the time-dependent scour-hole volume evolution at a circular pier in uniform coarse sand *Proceedings of the Second International Conference on Scour and Erosion 2004*, Meritus Madarin, Singapore. 207-215.

Lohse, D. and Muller-Groeling, A. (1994) Anisotropy and scaling corrections in turbulence. *Physical Review Letters,* 74 (10), 1747.

Manes, C. and Brocchini, M. (2015) Local scour around structures and the phenomenology of turbulence. *Journal of Fluid Mechanics,* 779, 309-324.

Manes, C., Coscarella, F., Rogers, A. and Gaudio, R. (2018) Viscosity effects on local scour around vertical structures in clear-water conditions. Paper presented at 9th International Conference on Fluvial Hydraulics - River Flow 2018, Lyon-Villeurbanne, France.

Marczak, W. (1997) Water as a standard in the measurements of speed of sound in liquids. *Journal of Acoustical Society of America,* 102 (5, Pt. 1), 2776-2779.

May, R.W.P., Ackers, J.C. and Kirby, A.M. (2002) *Manual on scour at bridges and other hydraulic structures*. Westminster, London: Ciria, CIRIA C551.

Mcmanus, J. (1988) Grain size determination and interpretation *Techniques in sedimentology*. Oxford, UK: Blackwell, 63-85.

Melville, B.W. (1975) *Local scour at bridge sites*, PhD Thesis, University of Auckland.

Melville, B.W. (1984) Live-bed scour at bridge piers. *Journal of Hydraulic Engineering,* 110 (9), 1234-1247.

Melville, B.W. (1997) Pier and abutment scour: Integrated approach. *Journal of Hydraulic Engineering,* 123 (2), 125-136.

Melville, B.W. (2008) The physics of local scour at bridge piers. Paper presented at Fourth International Conference on Scour and Erosion 2008.

Melville, B.W. and Chiew, Y.M. (1999) Time scale for local scour at bridge piers. *Journal of Hydraulic Engineering,* 125 (1), 59-65.

Melville, B.W. and Coleman, S.E. (2000) *Bridge scour*. Water Resources Publications: Highlands Ranch, CO. United States: .

Melville, B.W. and Raudkivi, A.J. (1977) Flow characteristics in local scour at bridge piers. *Journal of Hydraulic Research,* 15 (4), 373-380.

Melville, B.W. and Raudkivi, A.J. (1996) Effects of foundation geometry on bridge pier scour. *Journal of Hydraulic Engineering,* 122 (4), 203-209.

Met Office, Department for Environment Food and Rural Affairs, Environment Agency and Department for Business Energy & Industrial Strategy (2018) UKCP18 headline findings. *UK Climate Projections 2018 (UKCP18)*.

Miedema, S.A. (2010) Constructing the Shields curve, A new theoretical approach and its applications. Paper presented at World Dredging Conference XIX, Beijing, China.

Monin, A.S. and Yaglom, A.M. (2007) *Statistical fluid mechanics: Mechanics of turbulence*. Mineola, NY, USA: Dover Publications Inc.

Moser, R.D. (1994) Kolmogorov inertial range spectra for inhomogeneous turbulence. *Physics of Fluids,* 6 (2), 794.

Muzzammil, M. and Gangadhariah, T. (2003) The mean characteristics of horseshoe vortex at a cylindrical pier. *Journal of Hydraulic Research,* 41 (3), 285-297.

Nikuradse, J. (1950) *Law in flow in rough pipes: Technical Memorandum (No. 1292)*. Washington D.C., United States: National Advisory Committee for Aeronautics.

Oliveto, G. and Hager, W.H. (2002) Temporal evolution of clear-water pier and abutment scour. *Journal of Hydraulic Engineering,* 128 (9), 811-820.

Oliveto, G. and Hager, W.H. (2005) Further results to time-dependent local scour at bridge elements. *Journal of Hydraulic Engineering,* 131 (2), 97-105.

Olsen, N.R.B. and Melaaen, M.C. (1993) Three-dimensional calculation of scour around cylinders. *Journal of Hydraulic Engineering,* 119 (9), 1048-1054.

Porter, K., Simons, R. and Harris, J. (2014) Comparison of three techniques for scour depth measurement: photogrammetry, echosounder profiling and a calibrated pile. *Coastal Engineering Proceedings,* 1 (34), 64-75.

Qi, Z.X., Eames, I. and Johnson, E.R. (2014) Force acting on a square cylinder fixed in a free-surface channel flows. *Journal of Fluid Mechanics,* 756, 716-727.

Raudkivi, A.J. (1986) Functional trends of scour at bridge piers. *Journal of Hydraulic Engineering,* 112 (1), 1-13.

Raudkivi, A.J. and Ettema, R. (1983) Clear-water scour at cylindrical piers. *Journal of Hydraulic Engineering,* 109 (3), 338-350.

Schanderl, W., Jenssen, U. and Manhart, M. (2017a) Near-Wall Stress Balance in Front of a Wall-Mounted Cylinder. *Flow Turbulence Combust,* 99, 665-685.

Schanderl, W., Jenssen, U., Strobl, C. and Manhart, M. (2017b) The structure and budget of turbulent kinetic energy in front of a wall-mounted cylinder. *Journal of Fluid Mechanics,* 827, 285-321.

Shen, H.W., Schneider, V.R. and Karaki, S.S. (1966) *Mechanics of local scour*.

Shen, H.W., Schneider, V.R. and Karaki, S.S. (1969) Local scour around bridge piers. *Journal of the Hydraulics Division,* 95 (6), 1919-1940.

Sheppard, D.M., Jones, J.S., Odeh, M. and Glasser, T. (2000) Local sediment scour model tests for the Woodrow Wilson Bridge piers. Paper presented at Joint Conference on Water Resource Engineering and Water Resources Planning and Management 2000, Minneapolis, MN, United States of America.

Sheppard, D.M. and Melville, B.W. (2011) *Scour at wide piers and long skewed piers. NCHRP Report No. 682*. Washington: National Cooperative Highway Research Program, T.R.B.

Sheppard, D.M., Melville, B.W. and Demir, H. (2014) Evaluation of existing equations for local scour at bridge piers. *Journal of Hydraulic Engineering,* 140 (1), 14-23.

Sheppard, D.M. and Miller Jr, W. (2006) Live-bed local pier scour experiments. *Journal of Hydraulic Engineering,* 132 (7), 635-642.

Sheppard, D.M., Odeh, M. and Glasser, T. (2004) Large scale clear-water local pier scour experiments. *Journal of Hydraulic Engineering,* 130 (10), 957-963.

Shields, I.A. (1936) Application of similarity principles and turbulence research to bedload movement. Pasadena, California: California Institute of Technology.

Soulsby, R. (1997) *Dynamics of marine sands: A manual for practical applications*. Thomas Telford.

Stevens, M.A., Gasser, M.M. and Saad, M.B.a.M. (1991) Wake vortex scour at bridge piers. *Journal of Hydraulic Engineering,* 117 (7), 891-904.

Sturm, T.W., Ettema, R. and Melville, B.W. (2011) *Evaluation of bridge-scour research: Abutment and contraction scour processes and prediction. NCHRP Web-Only Document 181*. National Cooperative Highways Research Program, Transportation Research Board.

Sumer, B.M., Peterson, T.U., Locatelli, L., Fredsoe, J., Musemeci, R.E. and Foti, E. (2013) Backfilling of a scour hole around a pile in waves and current. *Journal of Waterway, Port, Coastal, and Ocean Engineering,* 139 (1), 9-23.

Tafarojnoruz, A., Gaudio, R., Grimaldi, C. and Calomino, F. (2010) Required conditions to achieve the maximum local scour depth at a circular pier. Paper presented at XXXII Convegne Nazionale di Idraulica e Costruzioni Idrauliche, Palermo.

Tritton, D.J. (1988) *Physical fluid dynamics* 2nd ed. New York: Oxford University Press Inc.

Tubaldi, E., Macorini, L., Izzuddin, B.A., Manes, C. and Laio, F. (2017) A framework for probabilistic assessment of clear-water scour around bridge piers. *Structural Safety,* 69, 11-22.

Umbrell, E.R., Young, K., Stein, S.M. and Jones, J.S. (1998) Clear-water contraction scour under bridges in pressure flow. *Journal of Hydraulic Engineering,* 124 (2), 236-240.

Unger, J. and Hager, W.H. (2007) Down-flow and horseshoe vortex characteristics of sediment embedded bridge piers. *Experiments in Fluids,* 42 (1), 1-19.

Vanoni, V.A. (1964) *Measurements of critical shear stress for entraining fine sediments in a boundary layer*. Pasadena, California: California Institute of Technology.

Von Leeuwen, Z. and Lamb, R. (2014) *Flood and scour related failure incidents at railway assets between 1846 to 2013*. North Yorkshire, United Kingdom: Jba Trust.

Voulgaris, G. and Trowbridge, J.H. (1998) Evaluation of the Acoustic Doppler Velocimeter (ADV) for turbulence measurements. *Journal of Atmospheric and Oceanic Technology,* 15 (1), 272-289.

Webster, R. and Oliver, M.A. (2007) *Geostatistics for environmental scientists*, 2nd ed. Chichester, UK: John Wiley & Sons Ltd.

Weinhaus, F. (1978) *Digital image filtering*. Available from: fmwconcepts.com/imagemagick/digital_image_filtering.pdf [Accessed 28th August].

Whitehouse, R.J., Harris, J.M., Sutherland, J. and Rees, J. (2011) The nature of scour development and scour protection at offshore windfarm foundations. *Marine Pollution Bulletin,* 62 (1), 73-88.

Yanmaz, A.M. and Altinbilek, H.D. (1991) Study of time-dependent local scour around bridge piers. *Journal of Hydraulic Engineering,* 117 (10), 1247-1268.